A STUDY OF UNSTABLE ROCK FAILURES USING FINITE DIFFERENCE AND DISCRETE ELEMENT METHODS

by

Ryan J. Garvey

A thesis submitted to the Faculty and the Board of Trustees of the Colorado School of Mines in partial fulfillment of the requirements for the degree of Doctor of Philosophy (Mining and Earth Systems Engineering).

Golden, Colorado

Date _____

Signed: _____
Ryan J. Garvey

Signed: _____
Dr. Ugur M. Ozbay
Thesis Advisor

Golden, Colorado

Date _____

Signed: _____
Dr. Hugh B. Miller
Associate Professor and Provisional Department Head
Department of Mining Engineering

ABSTRACT

Case histories in mining have long described pillars or faces of rock failing violently with an accompanying rapid ejection of debris and broken material into the working areas of the mine. These unstable failures have resulted in large losses of life and collapses of entire mine panels. Modern mining operations take significant steps to reduce the likelihood of unstable failure, however eliminating their occurrence is difficult in practice. Researchers over several decades have supplemented studies of unstable failures through the application of various numerical methods. The direction of the current research is to extend these methods and to develop improved numerical tools with which to study unstable failures in underground mining layouts.

An extensive study is first conducted on the expression of unstable failure in discrete element and finite difference methods. Simulated uniaxial compressive strength tests are run on brittle rock specimens. Stable or unstable loading conditions are applied onto the brittle specimens by a pair of elastic platens with ranging stiffnesses. Determinations of instability are established through stress and strain histories taken for the specimen and the system.

Additional numerical tools are then developed for the finite difference method to analyze unstable failure in larger mine models. Instability identifiers are established for assessing the locations and relative magnitudes of unstable failure through measures of rapid dynamic motion. An energy balance is developed which calculates the excess energy released as a result of unstable equilibria in rock systems. These tools are validated through uniaxial and triaxial compressive strength tests and are extended to models of coal pillars and a simplified mining layout.

The results of the finite difference simulations reveal that the instability identifiers and excess energy calculations provide a generalized methodology for assessing unstable failures

within potentially complex mine models. These combined numerical tools may be applied in future studies to design primary and secondary supports in bump-prone conditions, evaluate retreat mining cut sequences, asses pillar de-stressing techniques, or perform backanalyses on unstable failures in select mining layouts.

TABLE OF CONTENTS

ABSTRACT iii

LIST OF FIGURES ix

LIST OF TABLES xix

NOTATIONS xx

ACKNOWLEDGMENTS xxii

DEDICATION xxiv

CHAPTER 1 MODELING UNSTABLE FAILURES IN MINING 1

1.1 Problem Statement 1

1.2 Research Objectives 2

1.3 Scope of Work 3

1.4 Thesis Overview 3

CHAPTER 2 LITERATURE REVIEW OF NUMERICAL METHODS FOR STUDYING UNSTABLE ROCK FAILURES 7

2.1 Common Terms 8

2.2 Review of Unstable Failure Theory 9

2.3 Literature Review of Numerical Methods Used to Study Unstable Failures . . 13

2.4 Conclusions 18

CHAPTER 3 DISCRETE ELEMENT MODELS OF ROCK FAILURE IN COMPRESSION 20

3.1 Micromechanics of Rock Failure in Compression 20

3.2 PFC^{3D} Modeling of Micromechanical Failure 27

3.3 Unstable UCS Tests in PFC^{3D} 30

3.3.1 Calibration of PFC^{3D} 30

3.3.2 UCS Test Procedure 36

3.3.3 UCS Test Results 38

3.3.4 Dynamic Loading Effects on Model Response 42

3.3.5 Conclusions 44

3.4 Discussion of Bonded-Particle Method for Simulating Unstable Failure in Rock 47

CHAPTER 4 FINITE DIFFERENCE MODELS OF ROCK FAILURE IN COMPRESSION 49

4.1 Mohr-Coulomb Rock Strength with Weakening Properties 50

4.2 $FLAC^{3D}$ Modeling of Macroscopic Failures 53

4.3 Unstable UCS Tests in $FLAC^{3D}$ 58

4.3.1 Calibration of Mohr-Coulomb Strain-Softening Model 58

4.3.2 UCS Test Procedure 60

4.3.3 UCS Test Results 62

4.3.4 Conclusions of Unstable UCS Tests 64

4.4 Triaixial Compressive Strength Tests in $FLAC^{3D}$ 66

4.4.1 Triaxial Test Procedure 66

4.4.2 Results of Triaxial Tests 67

4.5 Dynamic Loading Effects on Model Response 69

4.6 Discussion of Finite Difference Method for Simulating Unstable Compression Failure in Rock 71

CHAPTER 5 IDENTIFIERS OF UNSTABLE FAILURE IN FINITE DIFFERENCE MODELS 75

5.1 FDM Identifiers of Instability in UCS Tests . . . 77
5.1.1 Testing Procedure . . . 78
5.1.2 Identifier Results of UCS Tests . . . 81
5.1.3 Conclusions on Unstable Failure Identifiers in UCS Tests . . . 88
5.2 FDM Identifiers of Instability in Triaxial Compressive Strength Tests . . . 90
5.2.1 Identifier Results of Triaxial Tests . . . 90
5.2.2 Conclusions on $FLAC^{3D}$ Identifiers of Unstable Failure in Triaxial Tests . . . 98
5.3 Discussion of Dynamic Identifiers of Unstable Failure . . . 99
CHAPTER 6 ENERGY BALANCE OF UNSTABLE FAILURES IN CONTINUUM MODELS . . . 100
6.1 Extension of Energy Balance to FDM . . . 104
6.2 UCS Test with Energy Balance . . . 106
6.2.1 UCS Test Energy Balance Results . . . 108
6.3 Discussion on Energy Balance in Explicit Models of Unstable Failure . . . 113
CHAPTER 7 COAL PILLAR MODELS . . . 115
7.1 Coal Pillar Strength Characteristics . . . 115
7.2 $FLAC^{3D}$ Calibration Procedure . . . 119
CHAPTER 8 2D MODEL OF LOCAL LOADING STIFFNESS . . . 130
8.1 Test Procedure . . . 130
8.2 Results of 2D Pillar Behavior . . . 133
8.2.1 Conclusions . . . 154
CHAPTER 9 3D MODEL OF GLOBAL LOADING STIFFNESS . . . 156
9.1 Test Procedure . . . 157

9.2 Results of 3D Pillar Behavior 159
9.3 Conclusions 166
CHAPTER 10 CONCLUSIONS 169
10.1 Summary of Conclusions 169
10.2 Contributions 175
10.3 Future Work 176
REFERENCES CITED 177
SELECTED BIBLIOGRAPHY 191
APPENDIX A - EXCESS ENERGY OF FLAC3D UCS TESTS 215
APPENDIX B - SUPPLEMENTAL ELECTRONIC FILES 221

LIST OF FIGURES

Figure 2.1 Demonstration of physical instability between an elastic loading system and a brittle rock during failure. 11

Figure 2.2 Force-displacement plots of loading system and brittle rock in compression 12

Figure 2.3 Example of a crush-type unstable failure of a Crandall Canyon coal pillar after massive bump event. Void space can be seen where coal was ejected from the original pillar 15

Figure 3.1 (a) A dogbone-shaped model specimen containing a preexisting flaw. (b) Stable crack growth under axial compression 24

Figure 3.2 (a) A barrel-shaped model specimen containing a preexisting flaw. (b) Unstable crack growth under axial compression 25

Figure 3.3 (a) A laboratory specimen failing in macroscopic shear after the coalescence of tensile cracks. (b) Diagram of crack extension and fracture initiation 26

Figure 3.4 Particle contact logic 28

Figure 3.5 PFC^{3D} general calculation steps. 29

Figure 3.6 UCS specimen generated from BPM and the resulting calibrated stress-strain curve after using the genetic algorithm. 31

Figure 3.7 Structure of genetic algorithm routine for calibrating BPM samples. . . . 34

Figure 3.8 Fitness values of each specimen tested by genetic algorithm over 500 trials and 47 generations. 35

Figure 3.9 Maximum fitness of elite survivors after 500 trials. 35

Figure 3.10 Stress-strain history of calibrated PFC^{3D} specimen during uniaxial compressive loading applied at a strain rate of 0.01/sec. 36

Figure 3.11 Configuration of uniaxial compressive strength test system with elastic platens (red) and a brittle specimen (blue). Strain is applied through walls at the top and bottom of the loading system. 38

Figure 3.12 Specimen stress vs. strain for different sets of platens in UCS tests. . . . 39

Figure 3.13 Stress of system vs. crack number during UCS tests. 40

Figure 3.14 Tensile and compressive forces within bonded particle model after specimen failure for 100 GPa platen test. 41

Figure 3.15 Tensile and compressive forces within bonded particle model after specimen failure for 10 GPa platen test. 41

Figure 3.16 Tensile and compressive forces within bonded particle model after specimen failure for 0.5 GPa platen test. 42

Figure 3.17 Specimen stress vs. strain during 100 GPa platen loading with three applied system strain rates of 0.1, 0.01, and 0.001 sec^{-1}. 43

Figure 3.18 Tensile and compressive forces within bonded particle model after specimen failure for 0.5 GPa platen test. 44

Figure 3.19 Tensile and compressive forces within bonded particle model after specimen failure from the very slow 0.001 sec^{-1} system strain rate. 45

Figure 3.20 Tensile and compressive forces within bonded particle model after specimen failure from the intermediate 0.01 sec^{-1} system strain rate. . . . 45

Figure 3.21 Tensile and compressive forces within bonded particle model after specimen failure from the very fast 0.1 sec^{-1} system strain rate. 46

Figure 4.1 Triaxial compressive strength test with Mohr-Coulomb shear plane along which failure occurs. 51

Figure 4.2 Mohr-Coulomb shear strength envelope as a function of principal stresses. 51

Figure 4.3 Example of a continuum grid generated in $FLAC^{3D}$. 54

Figure 4.4 A $FLAC^{3D}$ volume element, or "zone", showing numbered faces and gridpoints. 54

Figure 4.5 $FLAC^{3D}$ general calculation procedure. 55

Figure 4.6 Tetrahedral volumes used for stress and strain calculations in zones. . . . 56

Figure 4.7 Stable stress-strain response of $FLAC^{3D}$ UCS specimen showing a detail of local post-peak slopes. 60

Figure 4.8 Cohesion, internal friction angle, and dilation angle values as functions of plastic shear strain for the calibrated $FLAC^{3D}$ Mohr-Coulomb strain-softening constitutive model. 61

Figure 4.9 $FLAC^{3D}$ model of uniaxial compressive strength test specimen for research into unstable failure. 62

Figure 4.10 $FLAC^{3D}$ specimen response with superimposed load lines to represent 1.5 GPa (Soft), 10 GPa (Semi-Stiff), and 100 GPa (Stiff) platens. 63

Figure 4.11 $FLAC^{3D}$ system stress-strain response for varying platen stiffnesses. . . . 64

Figure 4.12 $FLAC^{3D}$ specimen stress-strain response for varying platen stiffnesses. . 65

Figure 4.13 Stable-unstable-stable failure case of 10 GPa platens failing a specimen while using modified testing procedure with pauses during failure. The drop in strength corresponds to the duration of unstable failure in the $FLAC^{3D}$ model. 66

Figure 4.14 Stress-strain responses of triaxially confined brittle coal specimens undergoing failure under unstable (2 GPa) and stable (100 GPa) platen loading conditions. 68

Figure 4.15 Stress-strain responses of triaxial compressive strength tests on plastic Mohr-Coulomb specimens under 2 GPa and 100 GPa platen loading conditions. 69

Figure 4.16 Labels applied to vertical stress measurement sections of the model which correspond with the numbering of plot Figure 4.17. 71

Figure 4.17 Specimen stress vs. strain plot with detailed assessment of stress in principal loading direction for unstable UCS test. 72

Figure 4.18 The internally measured specimen stress strain response in static vs. unstable (2 GPa) UCS tests. 73

Figure 5.1 Representation of unbalanced force equilibrium which may develop at point O in uniaxial compression case. 76

Figure 5.2 Uniaxial compressive strength test configuration in $FLAC^{3D}$ model. . . . 78

Figure 5.3 UCS specimen stress-strain response of Mohr-Coulomb Strain-Hardening/-Softening (MCSS) and Mohr-Coulomb (MC) models. . 80

Figure 5.4 Stress-strain behavior of specimen showing rebound along elastic modulus of platens for unstable tests. 81

Figure 5.5 Stress vs. strain of Mohr-Coulomb strain-softening specimen during stable (40 GPa platens) and unstable (2 GPa platens) failures with corresponding histories of maximum unbalanced forces. 82

Figure 5.6 Maximum gridpoint unbalanced force (N) within specimen over a range of platen stiffnesses for both plastic Mohr-Coulomb and brittle Mohr-Coulomb strain-softening models. 83

Figure 5.7 Maximum gridpoint accelerations (m/step^2) within specimen over range of platen stiffnesses for plastic Mohr-Coulomb and brittle Mohr-Coulomb strain-softening models. 84

Figure 5.8 Maximum gridpoint velocity (m/step) within specimen over range of platen stiffnesses for plastic Mohr-Coulomb and brittle Mohr-Coulomb strain-softening models. 84

Figure 5.9 Maximum zone shear strain rate (step^{-1}) within specimen over range of platen stiffnesses for plastic Mohr-Coulomb and brittle Mohr-Coulomb strain-softening models. 85

Figure 5.10 Histogram of maximum zone shear strain rate (step^{-1}) within specimen for 2 and 100 GPa platen tests of a brittle Mohr-Coulomb strain-softening model. 86

Figure 5.11 Maximum unbalanced forces (N) from 2 GPa UCS test that were in excess of stable unbalanced forces from 100 GPa test. 87

Figure 5.12 Maximum accelerations (m/step^2) from 2 GPa UCS test which were in excess of stable accelerations from 100 GPa test. 88

Figure 5.13 Maximum velocities (m/step) from 2 GPa UCS test which were in excess of stable velocities from 100 GPa test. 89

Figure 5.14 Maximum shear strain rates (step^{-1}) from 2 GPa UCS tests which were in excess of maximum stable shear strain rate from 100 GPa test. 89

Figure 5.15 Stress-strain responses of triaxially confined brittle coal specimens undergoing failure under unstable (2 GPa) and stable (100 GPa) platen loading conditions. 91

Figure 5.16 Stress-strain responses of triaxial compressive strength tests on plastic Mohr-Coulomb specimens under 2 GPa and 100 GPa platen loading conditions. 91

Figure 5.17 Maximum unbalanced forces (N) at gridpoints for triaxial strength tests ranging from 1 to 6 MPa confinement. 92

Figure 5.18 Maximum accelerations (m/step^2) at gridpoints for triaxial strength tests ranging from 1 to 6 MPa confinement. 93

Figure 5.19 Maximum velocities (m/step) at gridpoints for triaxial strength tests ranging from 1 to 6 MPa confinement. 93

Figure 5.20 Maximum shear strain rate (step^{-1}) in zones for triaxial strength tests ranging from 1 to 6 MPa confinement. 94

Figure 5.21 Histogram of maximum shear strain rates (step^{-1}) recorded for Mohr-Coulomb strain-softening zones for stable (100 GPa) and unstable (2 GPa) failures. 95

Figure 5.22 Maximum unbalanced force (N) recorded in MCSS specimen for 2 GPa platens at 6 MPa confinement. 96

Figure 5.23 Maximum accelerations (m/step^2) recorded in MCSS specimen for 2 GPa platens at 6 MPa confinement. 96

Figure 5.24 Maximum velocities (m/step) recorded in MCSS specimen for 2 GPa platens at 6 MPa confinement. 97

Figure 5.25 Maximum shear strain rates (step^{-1}) recorded in MCSS specimen for 2 GPa platens at 6 MPa confinement. 97

Figure 5.26 Specimen strain increment at which each respective zone reached its maximum shear strain rate for triaxial strength test with 2 GPa platens and 6 MPa confinement. 98

Figure 6.1 Probing forces applied onto a predefined volume of rock or soil. From . 101

Figure 6.2 Demonstration of unstable failure energy balance in uniaxial compressive strength test. 102

Figure 6.3 Uniaxial compressive stress vs. strain for Mohr-Coulomb (plastic) and Mohr-Coulomb strain-softening (brittle) material responses. 107

Figure 6.4 Specimen stress vs. strain for UCS test with 2 GPa platens, overlayed with the energy terms used to calculate excess energy. 109

Figure 6.5 Specimen stress vs. strain for UCS test with 4 GPa platens, overlayed with the energy terms used to calculate excess energy. 109

Figure 6.6 Specimen stress vs. strain for UCS test with 6 GPa platens, overlayed with the energy terms used to calculate excess energy. 110

Figure 6.7 Specimen stress vs. strain for UCS test with 100 GPa platens, overlayed with the energy terms used to calculate excess energy. 110

Figure 6.8 Specimen stress vs. strain for UCS test on Mohr-Coulomb specimen with 2 GPa platens, overlayed with the energy terms used to calculate excess energy. 112

Figure 6.9 Specimen stress vs. strain for UCS test on Mohr-Coulomb specimen with 100 GPa platens, overlayed with the energy terms used to calculate excess energy. 112

Figure 7.1 ARMPS database of pillar collapses and squeezes . Note that no pillar collapses were found to occur at widths greater than 3:1. 118

Figure 7.2 $FLAC^{3D}$ 2D pillar calibration model. 120

Figure 7.3 $FLAC^{3D}$ quarter-symmetry pillar calibration model. 121

Figure 7.4 Cohesion drop rate as a method to control brittleness in the MCSS constitutive model 122

Figure 7.5 Stress-strain results of calibrated 2D pillar model. 123

Figure 7.6 Ultimate strengths of 2D pillar model from calibration tables in $FLAC^{3D}$. 124

Figure 7.7 Pillar strengths of calibrated $FLAC^{3D}$ model compared to Mark-Bieniawski strength formula. 124

Figure 7.8 Cohesion input values for MCSS pillar models. 125

Figure 7.9 Friction angle input values for MCSS pillar models. 125

Figure 7.10 Dilation angle input values for MCSS pillar models. 126

Figure 7.11 Stress-strain results of calibrated 3D pillar model. 126

Figure 7.12 Calibrated strength values of pillars from 1:2 to 5:1 width-to-height as compared to empirical formulae. 127

Figure 7.13 Wagner post-failure modulus from with overlayed $FLAC^{3D}$ results at 0.5, 1, and 2. The range of post-failure moduli from Wagner represents the maximum and the average post-failure modulus while the $FLAC^{3D}$ results show the maximum modulus only. 128

Figure 8.1 Two-dimensional pillar model with inset showing detail of pillar and entry. 132

Figure 8.2 W:H=1, Pillar stress-strain response. 134

Figure 8.3 W:H=1, Maximum velocities, accelerations, and shear strain rates. . . . 134

Figure 8.4 W:H=1, Maximum velocities, accelerations, and shear strain rates. . . . 135

Figure 8.5 W:H=1, Pre-filtered histories of excess energy. 136

Figure 8.6 W:H=1, Cumulative excess energy. 137

Figure 8.7 W:H=1, Maximum excess energy. 138

Figure 8.8 W:H=2, Pillar stress-strain response. 138

Figure 8.9 Maximum principal strains in W:H 2 pillar after stable failure in 20 GPa rock. 139

Figure 8.10 Maximum principal strains in W:H 2 pillar after unexpected unstable failure in 40 GPa rock. 140

Figure 8.11 W:H=2, Maximum velocities, accelerations, and shear strain rates. . . . 140

Figure 8.12 W:H=2, Maximum velocities, accelerations, and shear strain rates. . . . 141

Figure 8.13 W:H=2, Cumulative excess energy. 142

Figure 8.14 W:H=2, Maximum excess energy. 142

Figure 8.15 W:H=3, Pillar stress-strain response during failure. 143

Figure 8.16 Maximum principal strain of 3:1 pillar in 0.5 GPa rock. Localized failure is observed at the pillar rib in the soft loading conditions. 144

Figure 8.17 Maximum principal strain of 3:1 pillar in 40 GPa rock. A distributed failure extends over 3 m into the pillar in the stiff loading conditions. . 144

Figure 8.18 W:H=3, Maximum velocities, accelerations, and shear strain rates. . . . 145

Figure 8.19 W:H=3, Maximum velocities, accelerations, and shear strain rates. . . . 146

Figure 8.20 W:H=3, Cumulative excess energy after 0.002 pillar strain had been reached. 146

Figure 8.21 W:H=3, Maximum excess energy. 147

Figure 8.22 W:H=4, Pillar stress-strain response. 148

Figure 8.23 W:H=4, Maximum velocities, accelerations, and shear strain rates. . . . 148

Figure 8.24 W:H=4, Maximum velocities, accelerations, and shear strain rates. . . . 149

Figure 8.25 W:H=4, Cumulative excess energy. 149

Figure 8.26 W:H=4, Maximum excess energy. 150

Figure 8.27 W:H=5, Pillar stress-strain response. 150

Figure 8.28 W:H=5, Maximum velocities, accelerations, and shear strain rates. . . . 151

Figure 8.29 W:H=5, Maximum velocities, accelerations, and shear strain rates. . . . 152

Figure 8.30 W:H=5, Cumulative excess energy. 152

Figure 8.31 W:H=5, Maximum excess energy. 153

Figure 8.32 Excess energy released as a function of pillar width-to-height. 153

Figure 9.1 3D global pillar model. Full model and zoomed view of pillar. 158

Figure 9.2 Stress vs. strain behavior of pillars under global loading. 160

Figure 9.3 Excess energy of systems under global loading. 160

Figure 9.4 1:1 pillar failing from global loading. Stress and excess energy are plotted against the pillar strain. The applied global load is also shown. 161

Figure 9.5 4:1 pillar failing from global loading. Stress and excess energy are plotted against the pillar strain. The applied global load is also shown. 162

Figure 9.6 Peak magnitudes of excess energy. 162

Figure 9.7 Peak magnitudes of excess energy per m^2 of development. 163

Figure 9.8 Excess energy released per square meter of development under global loading. 164

Figure 9.9 (a) Records of stress and strain for global loading models. (b) Maximum accelerations, velocities, and shear strain rates in the pillar plotted against pillar strain. 165

Figure 9.10 Projected elevation view of side of 3:1 pillar after unstable failure by gravitational loading. Zones colored by maximum shear strain rate show areas of highest instability. 166

Figure 9.11 Internal view of innermost 3:1 pillar core after unstable failure by gravitational loading. Zones colored by maximum shear strain rate show areas of highest instability. 166

Figure 9.12 View of rib corner of 3:1 pillar after unstable failure by gravitational loading. Zones colored by maximum shear strain rate show areas of relative instability. 167

Figure A.1 Specimen stress vs. strain for UCS test with 8 GPa platens, overlayed with the energy terms used to calculate excess energy. 215

Figure A.2 Specimen stress vs. strain for UCS test with 10 GPa platens, overlayed with the energy terms used to calculate excess energy. 216

Figure A.3 Specimen stress vs. strain for UCS test with 12 GPa platens, overlayed with the energy terms used to calculate excess energy. 216

Figure A.4 Specimen stress vs. strain for UCS test with 14 GPa platens, overlayed with the energy terms used to calculate excess energy. 217

Figure A.5 Specimen stress vs. strain for UCS test with 16 GPa platens, overlayed with the energy terms used to calculate excess energy. 217

Figure A.6 Specimen stress vs. strain for UCS test with 18 GPa platens, overlayed with the energy terms used to calculate excess energy. 218

Figure A.7 Specimen stress vs. strain for UCS test with 20 GPa platens, overlayed with the energy terms used to calculate excess energy. 218

Figure A.8 Specimen stress vs. strain for UCS test with 40 GPa platens, overlayed with the energy terms used to calculate excess energy. 219

Figure A.9 Specimen stress vs. strain for UCS test with 60 GPa platens, overlayed with the energy terms used to calculate excess energy. 219

Figure A.10 Specimen stress vs. strain for UCS test with 80 GPa platens, overlayed with the energy terms used to calculate excess energy. 220

LIST OF TABLES

Table 3.1 Results from demonstration calibration after 100 and 500 trials. 33

Table 3.2 Macroproperty inputs for particles and bonds in PFC^{3D} BPM. 37

Table 3.3 Resultant material properties of calibrated PFC^{3D} specimen. 37

Table 3.4 Microparameter inputs of platens in PFC^{3D}. 38

Table 4.1 Input parameters of calibrated $FLAC^{3D}$ coal specimen. 59

Table 4.2 Input parameters of Mohr-Coulomb (plastic) $FLAC^{3D}$ coal specimen. . . . 67

Table 6.1 Total excess energy (E_e) released during UCS tests on Mohr-Coulomb strain-softening (MCSS) and Mohr-Coulomb (MC) coal specimens. 111

Table 7.1 Steepest post-failure modulus (E_{pp}) of calibrated $FLAC^{3D}$ pillar trials. . . 128

Table 8.1 Loading velocities applied to top and bottom of system for varying rockmass Young's moduli. 131

Table 8.2 Peak excess energy of 2D pillar studies. 153

Table 9.1 Excess energy released for global loading conditions, normalized by the development area being modeled. 163

NOTATIONS

Stress and Strain Conventions

The stress and strain convention used for all mathematical derivations in this text follows the standard mechanical convention of negative stresses and strains to represent compression. Plots which display stress or strain histories adhere to the geomechanical convention of compression taking positive values.

Symbols

applied loading system stiffness (N/m) . . . . . k

local slope of force-displacement curve (N/m) . . . . . λ

Young's modulus (Pa) . . . . . E

post-peak failure modulus (Pa) . . . . . E_{pp}

Poisson ratio . . . . . υ

material density (kg/m^3) . . . . . ρ

crack half-length (m) c

friction coefficient . . . . . μ

virtual probing force (N) . . . . . $\overline{P}_i$

virtual displacements (m) . . . . . $\overline{U}_i$

force damping coefficient . . . . . α

average stress (Pa) . . . . . $\bar{\sigma}$

average stress from previous timestep (Pa) . . . . . $\bar{\sigma}'$

Mohr-Coulomb friction angle (deg.) . . . . . ϕ

Mohr-Coulomb dilation angle (deg.) . . . . . ψ

plastic strain . . . . . ε_p

excess energy (J) . . . . . E_e

boundary work (J) . . . . . W_b

gravitational potential energy (J) . . . . . W_g

elastic strain energy (J) . . . . . U

plastic work (J) . . . . . W_r

kinetic energy (J) . . . . . E_k

damped kinetic energy (J) . . . . . W_k

strength of pillar (Pa) . . . . . S_p

cubic compressive strength of rock (Pa) . . . . . S_1

height of pillar (m) . . . . . h

length of pillar (m) L

width-to-height ratio of pillar . . . . . W/H, $W{:}H$

ACKNOWLEDGMENTS

This dissertation marks the conclusion of a three year research project conducted at the Colorado School of Mines. The research and my doctoral education was funded by the National Institute of Occupational Safety and Health whose financial assistance made this entire process possible. I would also like to acknowledge Itasca International Inc. for their Educational Partnership program which enabled access to the range of Itasca software and associated training courses. I would also like to thank the Itasca staff for providing incredibly valuable feedback on advanced modeling techniques in PFC^{3D} and $FLAC^{3D}$. A special thanks goes to Dr. Matt Pierce who implemented the energy tracking module in $FLAC^{3D}$ which contributed significantly to my research.

More than anyone, I would like to thank my advisor Dr. Ugur Ozbay for the time and energy he has committed to the helping me complete my research and my degree. I can not overstate how valuable his recommendations and insights have been through this process, and I know that this research would not have been possible without his guidance. I would also like to thank the Colorado School of Mines for providing the facilities and exceptional teaching staff that I have come to rely on. I have been especially grateful for the support and feedback given to me by my thesis committee: Drs. John Grubb, Vaughan Griffiths, Graham Mustoe, and Cameron Turner. It was a true pleasure to learn in their classrooms and I have gained a tremendous respect for their specialized knowledge across the range of topics in this research.

And finally, I would like to say just how grateful I am to my family, friends, and colleagues who have never stopped believing in me through this process. There were times when I did not think that I could go on emotionally or physically, but your support is what carried me through to the end. Thank you Mom, Dad, and Richard for your unwavering love and kindness, and for encouraging a lifelong pursuit of knowledge. To my brothers

Michael, Andrew, Brian, and Zach, we're going to get through this thing together! To my colleagues Evan Kias, Ruixiang Gu, and Ugur Ozbay, with whom I have had the most incredible discussions ranging from the minutia of rock mechanics theory to all-encompassing philosophies of existence. And to Shannon, thank you for never losing faith in me through this process. I love you all and I cannot imagine a more perfect bundle of humanity with which to travel through life. Thank you.

To my wife, Shannon, who has always encouraged me to seek out genuine sources of happiness. To our cats Gray and L.B., who provide much needed furry support. And to all of my family, friends, and colleagues who I am so blessed to know and to have in my life. May we work together to receive the exponential gains which come from the coordinated efforts of a dedicated few.

CHAPTER 1
MODELING UNSTABLE FAILURES IN MINING

Case histories in mining have long described pillars or faces of rock failing violently with an accompanying rapid ejection of debris and broken material into the working areas of the mine [88, 94]. These unstable failures have resulted in large losses of life and total collapses of entire mine panels [21, 134]. Locally violent failures also occur in isolated pillars or sidewalls which do not affect the general stability of the mine but which pose a great threat to miners in the area.

Modern mining operations take significant steps to reduce the likelihood of unstable failures. Eliminating their occurrence is difficult in practice due to the uncertainty of rock stresses, strains, strengths, stiffnesses, and micromechanical characteristics. The failure mode of rock during highly dynamic loading is also not well understood, which further contributes to the unpredictability of these failures. Researchers over the past several decades have supplemented the study of unstable failures through the application of various numerical methods with mixed success. The direction of the current research is to extend these findings and to develop additional numerical tools with which to study unstable failures in underground mining layouts.

1.1 Problem Statement

Unstable rock failures are low frequency, high magnitude events which pose a serious threat to miners. Numerical methods are well suited to mitigate the likelihood and effects of unstable failures, yet current limitations restrict their usage for effectively studying complex mining geometries.

A review must be made of existing numerical methods regarding their applicability for studying unstable failures. Improved methodologies should be forwarded for qualitatively assessing the onset of unstable failure and for quantifying the effects of instability within

numerical models. With improved methods of analyzing unstable failure comes the ability to issue improved guidelines towards the design of safer mining layouts and the ultimate reduction of rockburst and coal bump events.

1.2 Research Objectives

The goal of this research is to develop improved methods with which to analyze unstable failures in numerical models of underground mines. The steps required to achieve this goal are outlined below:

- Assess existing numerical methods for their suitability in studying unstable failure in realistic mining geometries.
- Select appropriate numerical code(s) and perform elemental tests of idealized unstable failures.
- Study the expression of unstable failure in the models using existing modes of analysis.
- Develop methods for identifying the onset of unstable failures which may be extended to more generalized studies.
- Develop methods for calculating the relative magnitudes of unstable failure and of quantifying their effects within a simulated rock support system.
- Validate instability identifiers and calculations of relative energy magnitudes using simplified tests so that they might be applied to more complex models.
- Extend methodologies for assessing instability to models of coal mines.
- Study the effects of variable loading conditions and pillar size on the expression of unstable failure using the constructed models.
- Compare results between parametric coal bump studies and historical observations of coal behavior during unstable loading conditions and massive collapse.

1.3 Scope of Work

- Review past research on numerical methods which have been used to study of unstable failures.
- Construct discrete element models to represent a micromechanical brittle failure mode of rock in compression.
- Construct continuum finite difference models to represent a macroscopic brittle failure mode of rock in compression.
- Simulate unstable failures in laboratory style uniaxial and triaxial compressive strength tests using the selected numerical methods.
- Explore methods of tracking instability in the micromechanical failure models.
- Explore methods of tracking instability in the macroscopic failure models.
- Develop method to identify unstable failure conditions and calculate their relative magnitudes within a continuum model.
- Develop continuum models of room-and-pillar coal mining layouts in which unstable failure conditions may arise.
- Conduct studies on pillar models to determine trends of energy released and of the expression of rapid motion during unstable loading conditions.
- Summarize findings from this research and present recommendations for future work.

1.4 Thesis Overview

Chapter 2 of this dissertation explores unstable failure theory in idealized representations of failure. Existing literature on numerical models for studying unstable failure are reviewed, with a particular emphasis applied to coal bumps. Deficiencies of these existing methods are presented and areas for advancements and supplemental work are explored.

Chapter 3 presents a view of the micromechanics of rock fracture as is currently understood in rock mechanics theory. The chapter extends this knowledge of rock fracture onto the discrete element method. Uniaxial compressive strength tests are developed using the DEM software PFC^{3D} in order to study unstable failures in compressive tests on brittle rock specimens. A novel approach to calibrating the discrete element method is presented in Section 3.3.1 which employs a hybrid genetic algorithm to iteratively optimize the particle and bond input parameters used in the model. A micromechanical investigation is made on the failure of rock specimens under stable and unstable conditions. A discussion concludes the chapter which frames the results of these studies in the context of studying unstable failures in larger mine models.

A macroscopic, continuum-based view of unstable failure is developed at the beginning of Chapter 4. Uniaxial compressive strength tests are again conducted, but in this instance the simulations are run using the finite difference software $FLAC^{3D}$. Brittle rock specimens are failed under stable and unstable conditions while measurement histories record model behavior. The laboratory style simulations are extended to triaxial compressive strength tests which better represent the confined rock conditions found in underground mines. A final analysis is conducted on the behavior of the finite difference model during dynamic loading and a discussion is presented on the true dynamic response of rock in laboratory tests.

The primary focus of this doctoral research is to develop improved methods for studying the loss of stable equilibrium in numerical models of rock. The first of these improvements is presented in Chapter 5, in which the concept of instability identifiers are developed and validated in the context of the finite difference simulations of laboratory rock testing. Records of maximum unbalanced forces, accelerations, velocities, and shear strain rates are explored for their relation to unstable equilibria in the model. A qualitative assessment of instability is derived from these measurements.

An energy balance is developed in Chapter 6 to track the energy released as a consequence of unstable force equilibria in the finite difference models. In this manner an additional tool is provided for analyzing instability using the definitions of static and dynamic energy. Uniaxial compressive strength tests are again conducted in $FLAC^{3D}$, with the energy balance histories from these tests reported within Chapter 6.

The instability identifiers and excess energy balance presented in Chapters 5 and 6 are later applied to continuum models of full-scale pillar geometries whose material properties are calibrated to match those of *in situ* coal. The calibration process required to achieve these desired model responses is explained in detail within Chapter 7. Two- and three-dimensional calibrated coal pillar models of width-to-height ratios varying from 1:2 to 5:1 are constructed using the Mohr-Coulomb strain-softening constitutive model. The strengths and post-failure moduli of the pillars are compared against empirical formulae and *in situ* coal pillar tests.

Chapter 8 explores a continuum two-dimensional mine model in which an elastic rockmass fails a coal pillar with an applied local loading stiffness which is proportional to the elastic properties of the rockmass. The failure of the pillars is analyzed within the context of stable and unstable loading conditions. Localized unstable failures of the pillar rib are identified in wider pillar geometries and are correlated to outburst bump events.

Chapter 9 incorporates the excess energy balance developed in Chapter 6 to quantify the magnitude of energy released during a simulated massive collapses of room-and-pillar layouts. The studies include three-dimensional models of coal pillars ranging from 1:1 to 5:1 width-to-height ratios. The pillars support simulated overburdens and increasing tributary area loads. Larger pillars are seen to maintain overall stability however localized unstable failures are still observed in large pillars under these global loading conditions.

Concluding remarks of the numerical investigations are found in Chapter 10. Limitations to the proposed methods of analysis are presented and potential areas of future work are identified. A final discussion of the numerical methods for unstable failure analysis is

presented as the culmination of this doctoral research at the end of Chapter 10.

CHAPTER 2
LITERATURE REVIEW OF NUMERICAL METHODS FOR STUDYING UNSTABLE ROCK FAILURES

Unstable failures have been shown to occur in a wide variety of mining environments and mine layouts. The conditions necessary for unstable failure are fairly well defined by past researchers [23, 46, 101, 104, 107], yet mitigating the effects of these failures is difficult in practice due to the complexities of measuring and predicting the interactions between rock strength, rock brittleness, loading system stiffness, and *in situ* ground conditions. Information of the failure process of large underground structures is limited due to a lack of detailed knowledge of how these failures propagate in realistic mining situations. The speed of failure and the substantial damage which typically results has further restricted the amount of information which can be gained about the process of unstable failures in full scale mining scenarios. Numerical models may be applied to further study the propagation of failure during mining processes to attempt to reduce the likelihood of unstable failures. This dissertation describes in detail the developments which were made to existing numerical models in order to aid in the study of unstable failures in rock.

This literature review will first explore a brief overview of the general theory of unstable failure as it pertains to rock. The texts of Cook [23] and Salamon [104] will be relied on heavily as they were instrumental early works in the field. A review of coal bump history will then be made with particular attention being made to room-and-pillar layouts and massive collapses. The final component of the literature review will cover the topic of numerical models which have previously been employed to study unstable failure. This section will identify deficiencies of existing methods for studying unstable failure in large mine models and attempt to determine areas of improvements for the field.

2.1 Common Terms

The terminology to describe failures in mines differs significantly by the context under which they occur. A brief description is provided below for the terms commonly found in studies of failure and more specifically of unstable failure.

- *Unstable failure* or *dynamic failure* both refer to a sudden and violent release of stored potential energy during an accompanying dynamic failure of rock.

- *Rockbursts* are a form of unstable failure in which a violent ejection of rock into a mine or tunnel opening results in injury to personnel or significant damage to equipment or underground workings.

- *Coal bumps* are similar to rockbursts, but occur in coal mines.

- A *crush-type* of unstable failure, also referred to as a *strain-burst*, is used to describe the compressive failure of an underground support structure.

- A *slip-type* of unstable failure is that which initiates along a fault or discontinuity; slip-type events may then cause additional failures in the underground workings through induced seismic waves or by a redistribution of stresses.

- *Longwall mining* is a method of full extraction mining where large movable hydraulic shields are used to temporarily prevent the immediate roof from collapsing while a shearer mines the longwall face. Progressive caving of the roof is allowed as the shields advance. The caved rock forms a pile of disjointed broken material referred to as the *gob*.

- The unintended collapse of large portions of the roof may lead to large *air blasts* in which a sudden increase in air pressures may cause injury and death along with damage to mine seals and ventilation equipment.

- *Room-and-pillar mining* is a method of partial extraction in which an array of rock pillars are left in place throughout mining to support the roof and overburden.

- *Retreat mining* is a form of secondary mining in room-and-pillar layouts in which primary support pillars are mined and the roof is allowed to cave behind the active mining area. This method is prone to unstable failures and massive collapses in deep mining conditions.

- The *rib* refers to the unconfined side of a pillar which is prone to dynamic ejections due to a lack of confinement at the free face.

- *Slabbing* is a form of stable failure in which sections of rock, potentially large, are broken from a rib or sidewall in a typically slow failure taking anywhere from days to decades to occur. Slabbing does pose a crushing hazard for miners, especially in deep mining conditions and weaker support rock, yet is fundamentally different from unstable failures in that no significant excess energy is released as a consequence slabbing.

2.2 Review of Unstable Failure Theory

Rockbursts and coal bumps occur in underground hard rock and coal mines when a volume of brittle rock is stressed beyond its strength by a comparatively soft loading system [23, 46, 104]. This instability is accompanied by a transfer of stored potential energy from the loading system into the failing volume of brittle rock until a static equilibrium is reached within the entire system. The large magnitudes of energy released during unstable failures result in the rapid ejection of rock and debris into the working areas of the mine and present a serious hazard to miners.

The energy required to propagate unstable failure is derived from the excess energy released from a loading system which cannot be stored or dissipated during the failure process. The rates of energy released by the loading system may be large as compared to the

rate of energy dissipated or stored by the failing rock. Excess energy is then released from the system as kinetic energy through fault slip, ejection of debris, or rapid roof-floor convergence. Magnitudes of energy released during unstable failure range from very small unstable crack extensions to extremely large events observed during massive pillar collapses. To unite these wide reaching concepts under a common theme, unstable failure may be generalized to describe any unstable equilibrium in a rock system which results in the deviation of rock behavior from static conditions and introduces dynamic effects from the release of excess energy.

Rock is typically found to behave in a quasi-static, controlled fashion during failure. The failure may, however, take on dynamic characteristics if kinetic energy is applied to the failing rock from an external loading system. If the loading system is shown to release more potential energy than can be stored or dissipated by the failing rock, then the system is said to be in unstable equilibrium. Unstable equilibria exist when a brittle rock is loaded past the point of failure by a comparatively soft loading system. If the loading system stiffness is less than the post-failure stiffness of a rock sample and the peak strength of the sample is exceeded, then potential energy stored in the loading system will be transferred rapidly into the failing sample of rock in the form of an unstable failure.

Cook and Salamon have explored this topic of potential energy initiating unstable failure in rock through simplified representations of unstable equilibria. Figure 2.1 demonstrates physical instability using the concept of the unstable equilibrium that can develop between an elastic loading system and a brittle rock specimen during failure. A downward displacement is applied to point O_1, adding load P to the system until the specimen is caused to fail completely. This system is analogous to a uniaxial compressive strength test on a brittle rock specimen in which the stiffness of the loading system may be manipulated through artificial means.

The spring in the system has a linear elastic force-displacement behavior which is shown in Figure 2.2 where the spring force, F_s, is a function of the spring's stiffness, k, and the

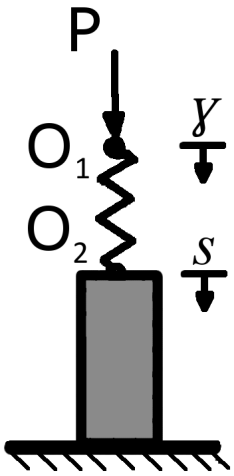

Figure 2.1: Demonstration of physical instability between an elastic loading system and a brittle rock during failure.

change in spring length. The total compression of the spring may be calculated from the displacements at its ends, labeled γ and s.

$$F_s = k \cdot (\gamma - s) \tag{2.1}$$

Any displacement Δs applied to point O_2 would cause a change $\lambda \cdot \Delta s$, if λ is to represent the local slope of theF_r force-displacement curve.

$$\Delta F_r = \lambda \cdot \Delta s \tag{2.2}$$

Displacements may be added to the top of this simple system and a new equilibrium position and force will be found for point O_2. If the system has become compressed to the point that the specimen becomes brittle with increased load (see Point O_1 in Figure 2.1), then the spring has the possibility of releasing excess strain energy into the specimen if the stiffness of the spring is less than the local slope of the rock. This statement may be explored formally through work terms and energy released due to fictitious applications of work.

If a virtual displacement is applied onto the system and results in a release of excess energy from the system, then the system is said to be unstable. Instability may be assessed at any point of compression during the test. For convenience, let a virtual displacement be applied to central point O_2 in the downward direction with the top point in the system being

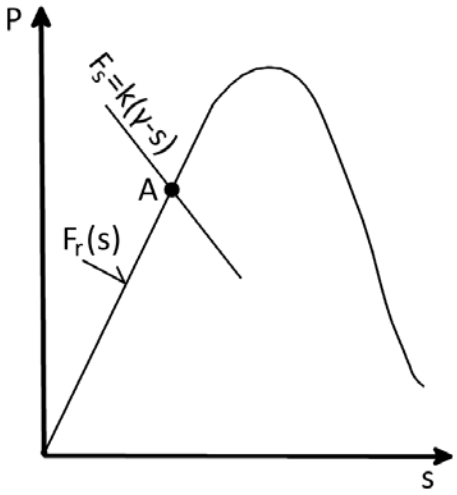

Figure 2.2: Force-displacement plots of loading system and brittle rock in compression [104].

fixed. The virtual displacement will cause a release in energy from the spring and a resistive work term caused by the rock. If the work released by the spring is greater than the work performed by the rock, then excess energy is released and the system becomes unstable.

$$\Delta W_s - \Delta W_r < 0 \quad (unstable) \tag{2.3}$$

For a system in equilibrium, an initial force is applied through the spring and the rock which is equal and opposite. This initial equilibrium force P is shown graphically for point A on the force-displacement curves of the spring and the rock. A virtual displacement applied onto the system will then cause a change in work which may be calculated as a function of the equilibrium force and the change in the spring or rock force, respectively.

$$\Delta W_s = (P + \frac{1}{2}\Delta F_s) \cdot \Delta s \tag{2.4}$$

$$\Delta W_r = (P + \frac{1}{2}\Delta F_r) \cdot \Delta s \tag{2.5}$$

From the definitions of F_s and F_r, these equations may be further reduced to include the relative stiffnesses of the spring and failing rock.

$$\Delta F_s = -k \cdot \Delta s \tag{2.6}$$

$$\Delta F_r = \lambda \cdot \Delta s \tag{2.7}$$

$$\Delta W_s = (P - \frac{1}{2} \cdot k \cdot \Delta s) \cdot \Delta s \tag{2.8}$$

$$\Delta W_r = (P + \frac{1}{2} \cdot \lambda \cdot \Delta s) \cdot \Delta s \tag{2.9}$$

These terms may then be directly substituted into 2.3.

$$\left[P + \frac{1}{2} \cdot (\lambda \cdot \Delta s)\right] \cdot \Delta s - \left[P + \frac{1}{2} \cdot (-k \cdot \Delta s)\right] \cdot \Delta s < 0 \quad (unstable) \tag{2.10}$$

Further reduction leads to an isolation of the unstable failure criterion using only slopes of the force-displacement curves of the spring and rock.

$$\frac{1}{2} \cdot (k + \lambda) \cdot (\Delta s)^2 < 0 \tag{2.11}$$

$$k + \lambda < 0 \quad (unstable) \tag{2.12}$$

Within this system a negative slope would be observed for the brittle rock specimen under failure. The value of the spring constant k is always positive by definition. Therefore, if the negative slope of the rock after failure becomes greater than the stiffness of the spring, then unstable failure will be initiated. In summary, instability may be characterized either from a capacity of the loading system to exert more forces than will be resisted, or through an investigation of the release of excess energy as a result of unstable equilibrium.

2.3 Literature Review of Numerical Methods Used to Study Unstable Failures

Case histories provide invaluable information for preventing unstable failures. Design criteria are established from the historical records which provide guidance on the strength of rock structures and on the post-failure characteristics of supportive rock. Extensive laboratory testing of rock failure properties has also contributed to the knowledge of the failure mode in rock under static and dynamic, stable and unstable loading conditions. These historical repositories of information on unstable failures have paved the way for problems of a more advanced nature to be addressed through numerical methods. Improvements have

been made to numerical methods, computer hardware, and the constitutive material models for capturing rock behavior which provides additional incentive to employ numerical models for the study of unstable failure in more complex mining geometries and *in situ* conditions.

Particular attention has been made in this dissertation to unstable failure in coal. Unstable failures in coal, or coal bumps, have an extensive database of past case histories from which to draw. From 1983 to 2007 at least 187 bump events occurred in coal mines in the United States. These bumps caused 229 injuries and 19 fatalities [20]. The prevalence of unstable failures in coal is due in large part to the physical characteristics of coal, which is a weak brittle rock. These contributing factors make coal an ideal rock in which to study unstable failure.

Coal bumps have been documented extensively in the United States since the 1920s [54]. A large loss of life from bumps occurred as recently as the 2007 Crandall Canyon disaster in which 9 miners and rescuers were killed, and 6 more were injured [36]. During a single bump event, over one-half mile of coal pillars failed within seconds. The sudden release of energy was observed as a 3.9 Richter magnitude event as over half of a million tons of coal were crushed in an instant. Factors known to contribute to bump events include deep cover [86, 126], hard competent roof strata [66, 117, 122], retreat mining [75], and unfavorable stress concentrations from multiple seam [74] or longwall mining [27, 44]. The majority of these factors were found to contribute to the Crandall Canyon disaster [92] with the exception being multiple seam mining. Computer models had been used in the design of the Crandall Canyon mine prior to the collapse, however these models were shown to overestimate the strength of the coal pillars in the mine and disregarded the potential for unstable failures [116]. Poor mine planning and faulty numerical analyses directly led to the disaster and highlighted why recommendations need to be made for assessing the threat of unstable failure within numerical models.

Extensive research has previously been conducted on the general causes of coal bumps and on methods of mitigating their effects. Countless researchers and numerous regulatory

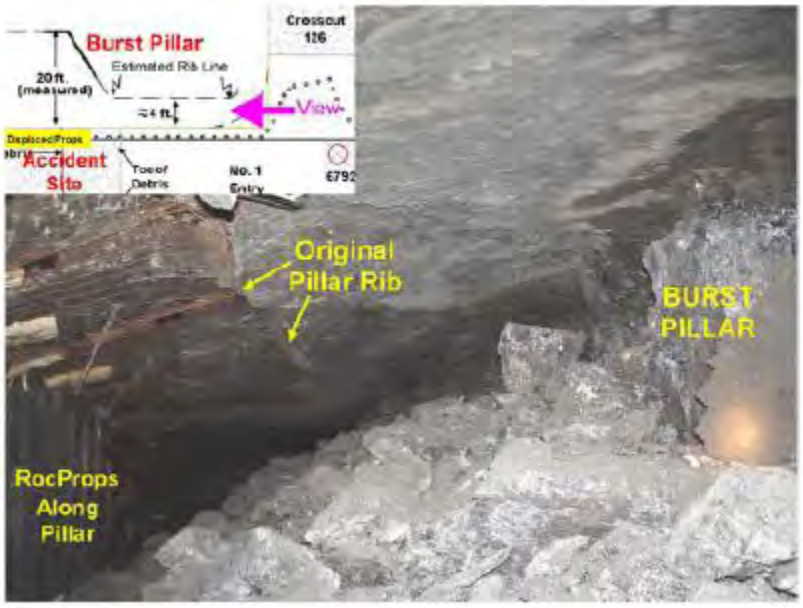

Figure 2.3: Example of a crush-type unstable failure of a Crandall Canyon coal pillar after massive bump event. Void space can be seen where coal was ejected from the original pillar [116].

agencies have made design recommendations for underground room-and-pillar and longwall mining layouts regarding sizing of pillars, support types, mining sequences, and appropriate geometries [44, 53, 66, 72, 73, 135]. Numerical models have taken a more direct role in studying bumps as these methods become more advanced [22, 82, 123]. Researchers have conducted studies using finite element, boundary element, and discrete element methods [50, 65, 93, 95, 98], which have been applied to simulate the micromechanical behaviors of unstable failures [34, 43, 45, 87, 109, 132]. A range of theories have been presented on the micromechanics of unstable failures which explore a variety of potential failure modes. These include the stick-slip mechanism [136], material superbrittleness [113], and surface buckling [5]. A cusp-type catastrophe theory explores the energy released during these events and makes predictions as to the durations of unstable and stable failures [123].

Unstable failure research has recently been applied towards using larger models of multiple pillars and realistic mine layouts to identify potentially unsafe mining conditions [31, 70, 134]. Modern advances in computing technology have dramatically increased the possi-

ble size and complexity of these models. Comparable advances in computer software have enabled more realistic constitutive behavior to be applied to represent rock as it fails. The behavior of brittle rock such as coal has been accurately captured within a continuum model using a strain-softening constitutive model [105, 129]. For added detail at the micromechanical level, discrete element models have been inserted within a continuum framework to reduce overall run time of the simulation while still maintaining a high degree of resolution at the scale of a single pillar [19].

These numerical tools have led to several design recommendations in coal and hard rock mines [29, 52]. Some studies have been conducted specifically on the prediction and prevention of unstable failures, with the majority of this research being conducted on reducing high stress concentrations [67, 133]. Some numerical analyses have been conducted on the post-failure characteristics of support pillars. A major area of study in recent years was the sizing of yield pillars in longwall mining layouts to reduce bump events and roof falls. A number of numerical analyses were conducted to accurately capture the post-failure process when using smaller sized yield pillars [89]. This design and sizing of yield pillars was investigated through a stress and strain analysis of sequential mining steps taken in a longwall excavation [90]. The role of loading stiffness was disregarded within these studies, although it is a vital aspect to understanding the occurrence of bumps [30]. In order to better understand and predict the conditions which lead to unstable failure, additional research should be made on the combination of brittle rock and the potentially unstable loading conditions.

Researchers have aimed to definitively identify unstable failure conditions within the numerical models using a number of analysis techniques. The primary method of identifying instability is through detailed analyses of stress behaviors in the models [22, 61, 123, 124]. Some investigations have attempted to classify unstable failure from records of acoustic emissions in dynamic models [68]. However, acoustic emissions are generated as a consequence of failure in the models and are not a direct assessment of stability. Similar approaches have made similar errors in analysis when classifying a failure as stable or unstable. The

studies which define instability through the number of acoustic emissions or zone failures are inherently flawed in that they are only capable of identifying magnitudes and locations of *failure,* while being unable to apply a rigorous assessment of *stability* to a modeled system.

Research has been conducted by Wang to quantify the excess energy released in a finite element program with failable linear-elastic elements as an ultimate assessment of system stability [124]. The release of excess energy was calculated from the local loading system stiffness applied onto an element at the time of failure. While this is a good application of theory to quantify energy release during unstable failure, the program which was used in these studies does not provide a time-dependent representation of the progression of failure due to the implicit calculation mode being applied. Additionally, an elasto-brittle model for the elements does not accurately account for plastic deformations which occur during failure or for the plastic work required to perform these deformations. One additional consequence of a perfectly brittle failable element on the proposed calculation of energy release is that regardless of the conditions present in the model, excess "unstable" energy would be recorded for any failures of any element in the models. Relative magnitudes of energy released may be compared between tests as an assessment of unstable failure, however it is incorrect to assume an instability condition for all failure within the models. The research conducted by Wang et al. holds promise for future studies on unstable brittle rock failures in ground, however the proposed finite element formulations make the approach undesirable for assessing unstable failures until these numerical modeling limitations are addressed.

Exhaustive methods for determining stability do exist in numerical models. One method developed by Schofield and Wroth [107] applies small probing forces at every point in the model at every state of loading. If the probing force results in a greater magnitude of energy released from the system than what was added in work done by the probe, then the system is unstable in that direction of loading [104]. Finite element, finite difference, and boundary element simulations have been conducted which have incorporated the force-probe stability analysis, however as one might expect this approach becomes increasingly difficult to apply

with the increasing size and complexity of model being studied [17]. No analyses are known which have incorporated this rigorous determination of instability in complex mining layouts. The exhaustive approach outlined by Schofield and Wroth is prohibitively difficult to perform in numerical models which have many gridpoints, make many explicit timesteps, or which experience non-uniform loading directions.

One promising area of research is in the field of advanced constitutive modeling of the combined tensile-shear failure mode which is thought to be exhibited during dynamic failure of rock. Wu et al. [128] have forwarded a tensile-shear failure criterion and demonstrated its capacity for elementary research on the progression of failure in tunneling applications if unstable equilibrium conditions are present. The authors carefully explored the calculation of energy dissipation within a continuum model using Griffith's theory of crack propagation. The adherence of the models to strict definitions of energy storage and consumption permitted the authors to make an assessment on the energy consumed and released during rock failures. The preliminary tests conducted in $FLAC^{3D}$ showed that the combined tensile-shear constitutive relation has the potential to consume less energy during failure than a shear-only model. The reduced consumption of energy during failure led to more available energy for propagating the failure. A tensile-shear constitutive model holds the promise of more accurately simulating the failure of brittle rock in unstable conditions than the existing shear-based brittle failure models like the Mohr-Coulomb strain-softening model. At the time of writing this dissertation, no follow up studies had been conducted on the constitutive model presented by Wu et al. Additional testing of the proposed tensile-shear failure criterion and further development of a flow rule is required to validate the method for use in detailed studies of unstable failure.

2.4 Conclusions

Numerical studies have historically had great success in addressing unfavorable stress concentrations in the design of underground mines. Modern advances in constitutive modeling techniques have provided improved methods for simulating brittle rock failures and

the unstable failures which may result. Concurrent improvements made to numerical modeling of large scale underground mining layouts show that existing numerical models may be calibrated to match expected behavior for roof and floor deformations. These parallel advancements in numerical modeling techniques allow for the direct simulation of unstable equilibria in geomechanical models of large rock support systems.

A striking limitation exists, however, when combining these numerical tools to study unstable failure. Few methods of analysis have been implemented to identify and quantify the effects of instability on large rock systems. The methodologies which do exist for detecting instability suffer from a number of restrictions which limits their application. Records of acoustic emissions and the release of kinetic energy have been one major area of research in numerical modeling of unstable failures, however existing dynamic models have not been thoroughly evaluated for their accuracy in simulating dynamic rock behavior. A few exhaustive methods exist for assessing stability in explicit numerical models, the most direct being the application of virtual probing forces as demonstrated by Schofield and Wroth, however this approach has been shown to be prohibitively difficult for identifying instability in complex mine models. Currently, there is no method known for effectively assessing unstable failure conditions in complex mining geometries. Further research is required to address these deficiencies and to determine improved methodologies for analyzing the expression of unstable failures using existing numerical methods.

CHAPTER 3

DISCRETE ELEMENT MODELS OF ROCK FAILURE IN COMPRESSION

The discrete element method holds significant promise for studying the evolution of micromechanical damage leading to macroscopic failure in rock [50]. The discrete fracturing of rock plays an integral role in its failure and within the case of unstable failure this point is even more evident. During unstable failures, excess energy from the unstable system is converted into the rapid formation of cracks and free surfaces within the failing rock. The newly formed rock fragments are commonly ejected from the rock face with a sudden release of kinetic energy and extraneous frictional heating. The ejection of broken material exposes the rock underneath thereby causing a removal of confinement and a propagation of the failure even deeper into the rockmass [3].

The exact mode of failure is not well understood for the case of dynamic compressive failure in rock [32, 79]. A complex interaction between shear, tensile, and buckling failures leads to the ultimate loss of strength of the larger rockmass. The evolution of these damage mechanics are critically affected by local stress and strain concentrations, material inhomogeneities in the rock, and dynamic effects on material response. A discrete element model which is capable of capturing the micromechanical material responses within a dynamic context [45] is ideally suited to study the progression of failure in a rockmass during unstable loading conditions.

3.1 Micromechanics of Rock Failure in Compression

Compressive stresses induce failure in rock through a number of stages which originate at the pre-existing flaws found in all rocks. Griffith presented a now commonly accepted hypothesis on crack theory [6, 9, 39] which yields a criterion for fracture initiation based on the principal components of stress as related to the material's uniaxial tensile strength.

Griffith's theories were substantiated with testing performed in tension on materials with pre-formed cracks. The original theory was limited to cracks in tension. McClintock and Walsh extended Griffith's hypothesis to account for crack closure observed during compression [78]. The modification's to Griffith's equations led to 3.1 which includes the term µ as the coefficient of internal friction of the material, while σ_1, σ_3, and σ_t refer to the major principal stress, the minor principal stress, and the uniaxial tensile strength respectively.

$$\sigma_1 = \frac{-4\sigma_t}{(1-\sigma_3/\sigma_1)\sqrt{(1+\mu^2)-\mu(1+\sigma_3/\sigma_1)}} \tag{3.1}$$

Of great significance during these studies was the prediction of whether a fracture was stable or was instead unstable and capable of continued propagation without the need for an increased load. The energy required to crack a material was more fully developed by Irwin [55] who showed that the propagation of the fracture will continue as long as more elastic energy is released from the solid material than is consumed by the increase in surface energy of the crack as new crack faces are formed. The total change in potential energy, ΔP, was put in the form shown in 3.2 for an infinite plate of unit thickness. In this formula c is the half-length of the crack, γ is the specific surface energy of the crack, E is the Young's modulus of the material, and σ is the applied far-field tensile stress.

$$\Delta P = 4c\gamma - \frac{\pi c^2 \sigma^2}{E} \tag{3.2}$$

The first portion of this equation refers to the energy demand required to open new crack faces while the second term is the increase in strain energy due to the introduction of the crack. A negative change in potential energy for an increasing crack length would therefore lead to an unstable tensile rupture. A more complete energy balance was developed to include kinetic energy of the material during rapid propagations of cracks. It was shown that for the case of a moving crack, 3.2 takes the form shown below, where v is the velocity of the moving crack tip, ρ is the density of the material, and k is a constant proportionality factor which was evaluated through additional research [102].

$$\Delta P = 4c\gamma - \frac{\pi c^2 \sigma^2}{E} + \frac{k\rho c^2 v^2 \sigma^2}{2E^2} \tag{3.3}$$

When considering compressive rather than tensile forms of failure a number of complexities are introduced, namely through the frictional sliding along closed cracks. When shearing takes place rather than tensile rupture, the change in strain energy in a flat plate has been shown to fit 3.4 [112].

$$\Delta U = \frac{\pi \tau^2 c^2}{E} \tag{3.4}$$

An effective shear stress term may then be substituted to account for the frictional resistance between crack faces [23]. The idealized crack equation in compression is shown in 3.5 where μ is the coefficient of friction between crack faces and σ_n is the normal compressive stress.

$$\Delta U = \frac{\pi (\tau - \mu \sigma_n)^2 c^2}{E} \tag{3.5}$$

By introducing γ_s as the work of fracture in shear, it can further be derived that instability arises when the inequality shown in 3.6 is met. Note that this instability criterion does not factor in the velocity of rock during dynamic cracking in shear, but will identify the onset of instability conditions and may be used as an assessment of the direction of quasi-static crack growth.

$$(\tau - \mu \sigma_n) \geq \sqrt{\frac{2E\gamma_s}{\pi c}} \quad (unstable) \tag{3.6}$$

The most stable direction of travel for tensile cracks has been shown from the above inequality to be parallel to the major principal stress [23]. This theory matches well with results observed from destructive compressive tests performed on carefully prepared rock specimens. Under purely axial loading it is observed that existing flaws at the boundary extend as cracks grow in the direction of loading. Under confined compression or when loading an existing crack inclined to the direction of loading, shear forces develop across the plane of fracture which result in the nucleation of tensile cracks which then curve towards

the direction of principal compression. These effects can be observed polarized images of cracks in laboratory specimens. Horii and Nemat-Nasser [49] have shown both stable and unstable crack growth towards the direction of principal loading. Figure 3.1 and Figure 3.2 show this effect in a stable, "dogbone" specimen geometry and in an unstable barrel-shaped specimen. In the dogbone specimen the crack did not extend to the ends due to the higher levels of confinement at the specimen ends as compared to specimen center. Tensile cracking was therefore isolated in the center of the specimen. For the barrel shaped specimen the crack nucleated and grew unstably towards to less confined portions of the specimen.

For less idealized materials and conditions such as those found in typical mining applications, a failure is dependent upon the interaction of an array of pre-existing cracks in the rock. Complex networks of microflaws result in the growth and coalescence of tensile cracks from the tips of the existing flaws. These cracks interact most predominantly with one another along a fractured zone which will ultimately fail through macroscopic shearing when the frictional shear resistance of the interlaced discontinuities has been exceeded. These fractured zones are referred to in this text as shear bands or localized shear failures. Figure 3.3 shows a representation of the shear band which develops as tensile cracks coalesce within rock during compression.

The complexity of calculating crack growth is again increased for the case of failure in anisotropic rocks which include coal. Aligned joint sets, bedding planes, cleats or butts, or inherent strength or stiffness inhomogeneities will lead to higher stress concentrations along the boundaries of anisotropy [128]. In their tests, Horii and Nemat-Nasser [49] found that larger flaws caused higher stress concentrations at their tips which resulted in the ultimate failure of a specimen being dominated by the largest existing set of favorably aligned joints or discontinuities.

Unstable crack growth leading to rupture in rock plays an integral role in the underlying failure mechanism which is exhibited during macroscopic unstable failures. The equations utilized above have been shown to approximate the point at which potential energy released

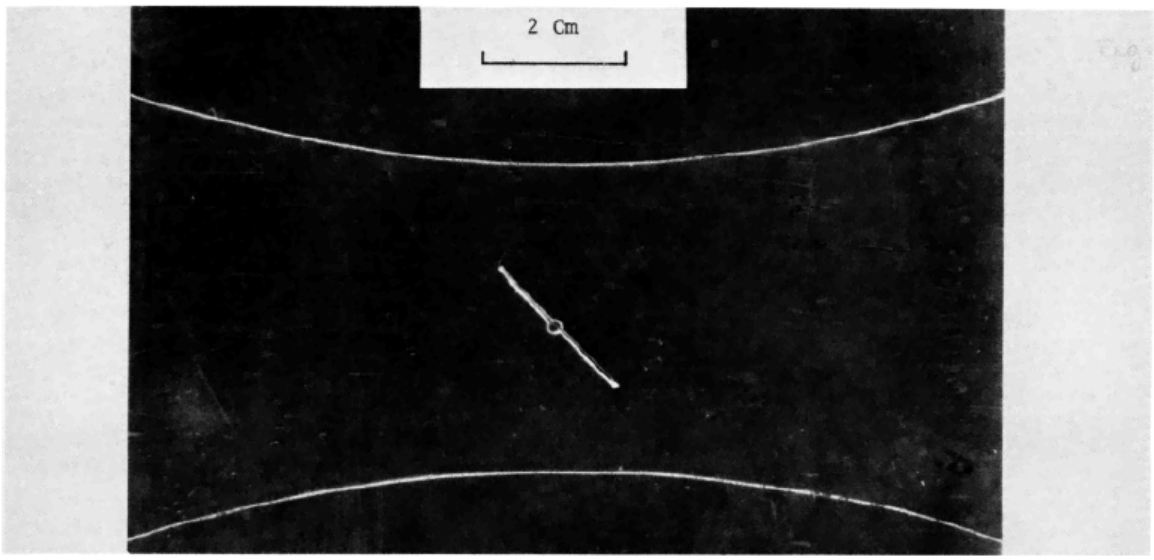

(a)

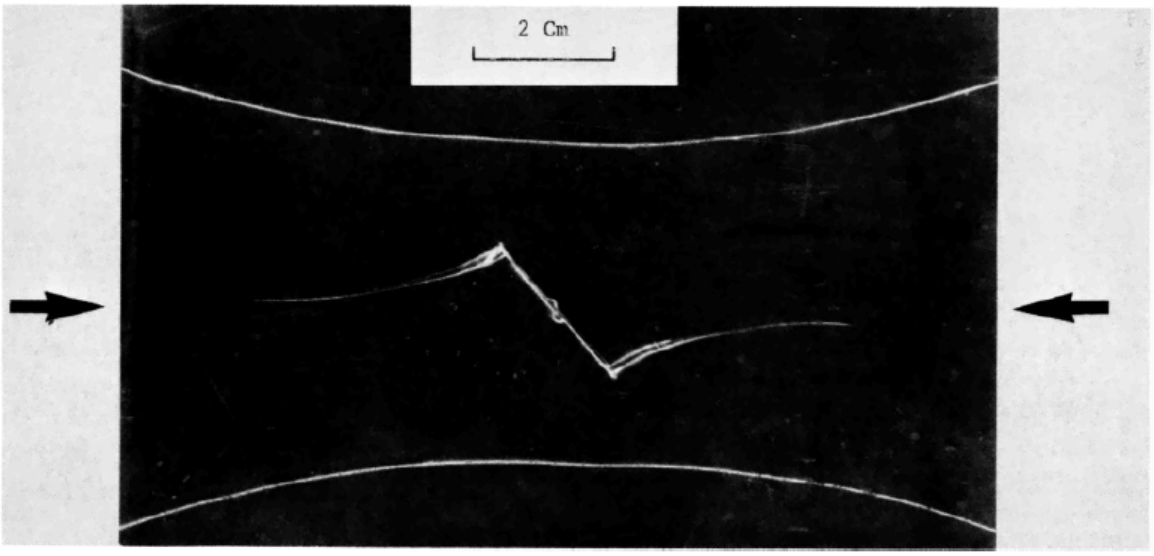

(b)

Figure 3.1: (a) A dogbone-shaped model specimen containing a preexisting flaw. (b) Stable crack growth under axial compression [49].

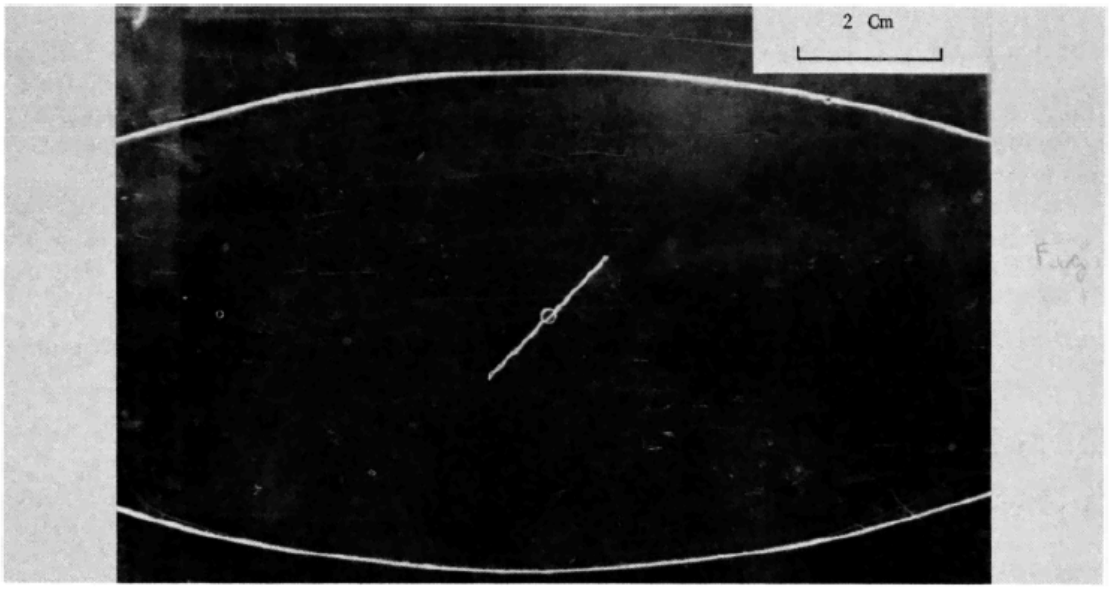

(a)

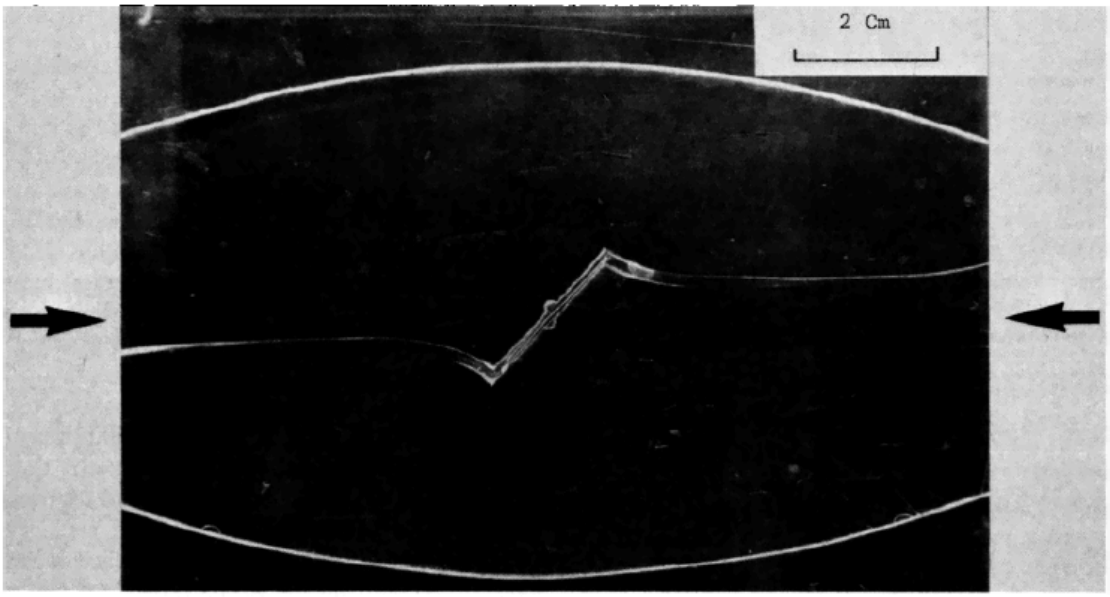

(b)

Figure 3.2: (a) A barrel-shaped model specimen containing a preexisting flaw. (b) Unstable crack growth under axial compression [49].

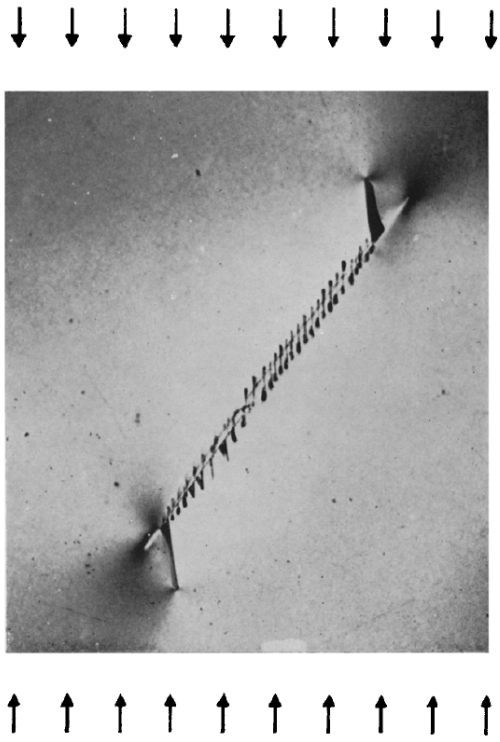

(a)

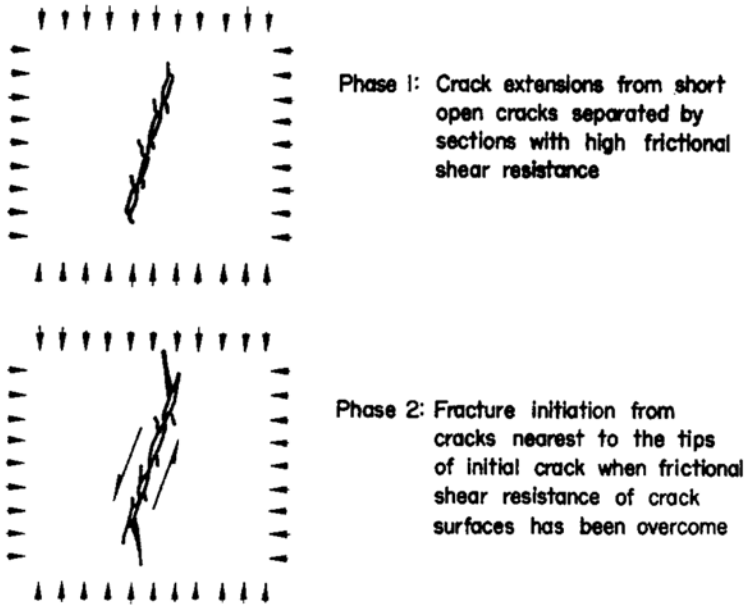

(b)

Figure 3.3: (a) A laboratory specimen failing in macroscopic shear after the coalescence of tensile cracks. (b) Diagram of crack extension and fracture initiation [13].

from the material is sufficient to fuel unstable crack growth [32]. This concept may be extended to study the interaction of the arrays of microcracks and flaws within real rock specimens. Additional consideration may be made to the potential energy which is added to the system through increases of stress or displacements from the surrounding rock. Excess energy introduced from an external loading system may further contribute to unstable crack growth from the existing arrays of microcracks, joints, or other such flaws inherent in the rock, and such external contributions of energy may ultimately dominate the failure behavior observed for macroscopic ruptures or unstable shear failures.

3.2 PFC^{3D} Modeling of Micromechanical Failure

The discrete element method (DEM) may be used to model the progressive fracturing of brittle rock and is well suited for studying dynamic rock behaviors due to its adherence to Newtonian physics. A bonded-particle model (BPM) is one such form of DEM which consists of a close packing of particles bonded together to represent a rock specimen of a specified geometry [93, 98]. The explicit discrete element software PFC^{3D} , or Particle Flow Code in 3D, is capable of simulating bonded-particle models [59] and was selected for further study of the micromechanical nature unstable failures.

The PFC^{3D} calculation scheme simulates particles as rigid bodies with soft-contact overlaps between particles as shown in Figure 3.4. The contact forces are projected onto the particle centers to impart motion. Parallel bonds are generated between particles in contact at the start of the simulation. Shear and normal forces are transmitted through the parallel bonds, along with bending moments at the particle centers. A frictional force also acts between sliding particles.

Forces are determined through the contacts and bonds. A local non-viscous damping scheme is applied to the unbalanced forces acting on the particle centers. A damping coefficient is assumed for the model which is applied to the particle center in the direction opposite the particle's velocity vector. The local damping force is shown in 3.7 as the product of the damping coefficient, α, and the force acting at the particle center.

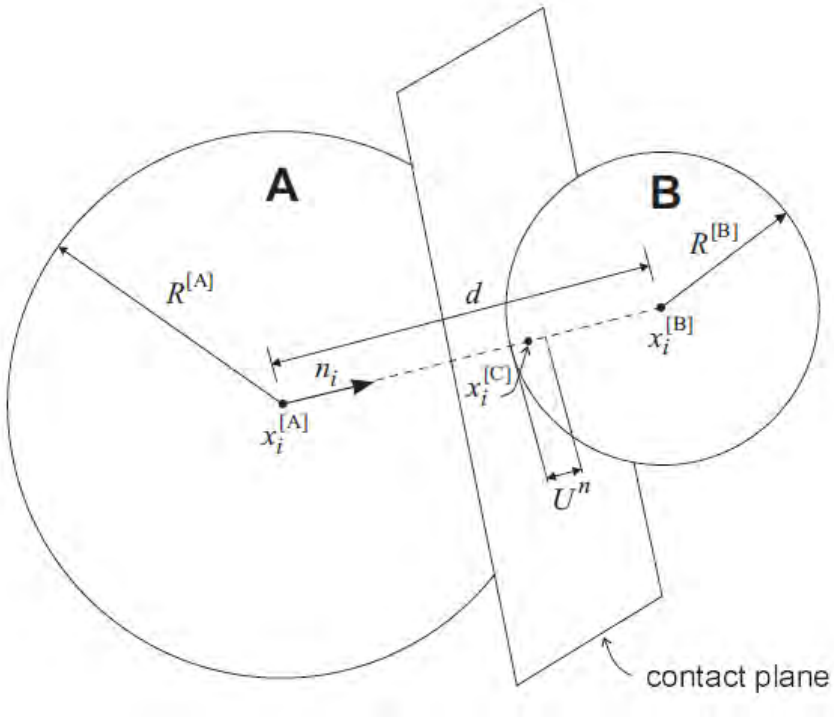

Figure 3.4: Particle contact logic [59].

$$F_d = \alpha \cdot F \tag{3.7}$$

The particle accelerations are determined from Newton's second law after the forces on all particles have been calculated. A critical timestep is determined for the entire system to prevent instability and chaotic motion of the particles. This critical timestep is calculated from the parameters shown in 3.8.

$$t_{crit} = \begin{cases} \sqrt{m/k^{tran}} & (translational\ motion) \\ \sqrt{I/k^{rot}} & (rotational\ motion) \end{cases} \tag{3.8}$$

Particle velocities and positions are then updated in a stepped forward marching scheme with the critical timestep being calculated at each iteration. New forces are calculated from the following step and the process is iterated until the simulation has been completed. Figure 3.5 demonstrates this process.

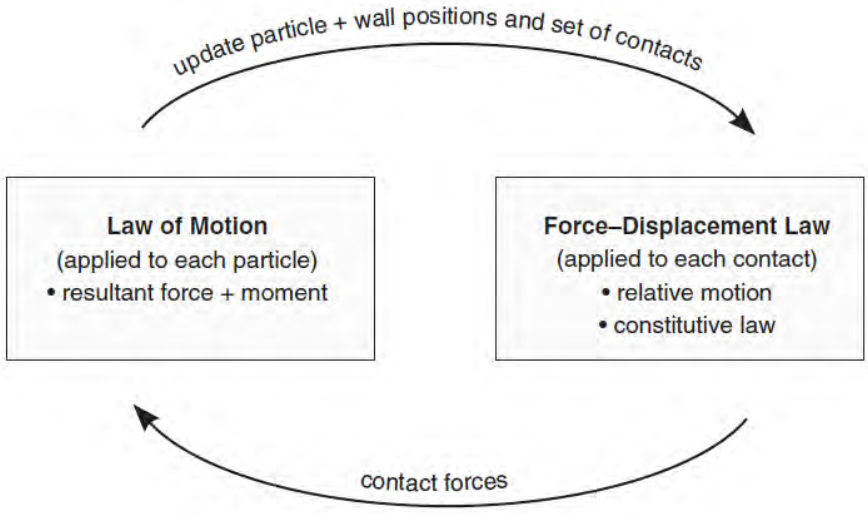

Figure 3.5: PFC^{3D} general calculation steps.

The value in the discrete element method of simulating rock breakage comes from the ability for the bonds between particles to break and thereby represent progressive rock fracturing. The bond parameters may be carefully calibrated so as to represent the desired strength properties for models failing under various forms of loading. The bonds are given ultimate tensile and shear strengths which are multiplied by the total bond areas to determine the bonding strength between particles. If these limits are reached then the bond is deleted and failure is deemed to have occur between the particles.

The formation and propagation of shear and tensile induced cracking occurs through the elimination of particle bonds once local strength limits have been reached. Progressive micromechanical failure leading to macroscopic failure modes of shearing or tensile splitting may then the assessed within model. Naturally observed phenomena such as tensile splitting and ejection of debris in rapid compression are then emergent behaviors in DEM from which analogues may be found for real rock fracture. Of particular interest for study in DEM is the process of confinement loss due to the ejection of discrete material away from a free face of failing rock. A discrete numerical formulation may be used to study the effects of confinement loss on the speed and depth of failure within conditions similar to those found

during unstable failure. The propagation and coalescence of micromechanical failures may then be assessed within the context of unstable failures across a range of material and loading conditions.

3.3 Unstable UCS Tests in PFC^{3D}

A closely packed arrangement of bonded particles was used to represent a slender cylindrical rock specimen of width-to-height ratio 0.5 in a simulated UCS test. A packing scheme was applied through the PFC^{3D} FISHTank routine 'mg_matgen' to generate a cylinder of spherical particles in which a desired isotropic stress state was reached by allowing the particles to interact, rearrange into a new configuration, and then be increased in size until the desired stress was achieved. Parallel bonds are then installed between the centers of particles which are in contact. A parallel bond transmits moments, shear forces, and compressive or tensile forces between bonded particles. Strength limits are assigned for shear and tensile loading. If the strength limit is reached then the bond is removed and the particles no longer interact with one another through the bond, although contact forces including friction are still applied so long as the particles are in contact.

3.3.1 Calibration of PFC^{3D}

PFC^{3D} was used to simulate uniaxial compressive strength specimens with material properties specific to coal. Among these properties was brittleness, which was required for controlled testing of unstable failure. A series of recommended calibration steps have been developed by Itasca and others [16, 83, 121, 130] to provide a sensible means of determining sets of BPM inputs to generate models with appropriate material responses. These steps include guidelines on the relationships between input parameters and macroproperties of the specimen. Some detailed studies have added insight into the effects of input parameters using artificial neural networks [114], statistical central composite design method [130], and dimensional analysis [33]. Due to confounding variables and a complex design space, the difficulty of calibrating a BPM becomes compounded as a greater number of inputs are

considered. Non-linear effects between inputs and their responses only add to the difficulty of developing a calibrated model.

A genetic algorithm was implemented [34] for resolving these issues by iteratively calibrating a simulated specimen with desired values for Young's modulus, Poisson ratio, ultimate compressive strength, and post-failure response (i.e., brittleness). A total of 9 variable inputs were used in PFC^{3D} to calibrate the BPM specimen. These variable inputs consisted of Young's modulus of the particles, Young's modulus of the bonds, the ratio of normal to shear stiffness of the balls, the normal to shear stiffness of the bonds, the bond normal strength, the bond shear shear strength, friction between balls, the ratio of maximum to minimum particle size, and the percentage of pre-failed bonds in the specimen.

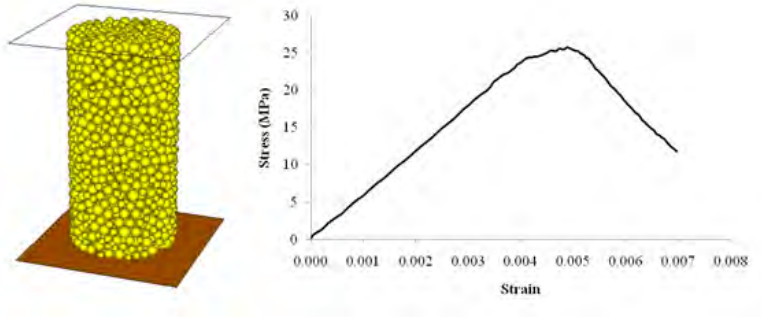

Figure 3.6: UCS specimen generated from BPM and the resulting calibrated stress-strain curve after using the genetic algorithm.

The genetic algorithm routine was written in the FISH programming language to modify these 9 inputs. Several choices were considered during the design of the genetic algorithm to reduce the total number of trials required to obtain a calibrated sample [125]. The final structure of the algorithm took the form of an elite survivor population of best fit individuals performing a hybrid form of crossover and mutation as is described in the process below:

1) Generate initial population. Create forty sets of random inputs and generate forty BPMs from these inputs.

2) Perform uniaxial compressive stress tests on each specimen. Compute E, ν, UCS, and post-peak modulus for each specimen based on these tests. Approximate the post-peak

modulus by finding a linear fit between two points on the stress-strain curve. For convenience these points were taken when the stress in the specimen is reduced by 25% and 50% after failure. Assess the fitness of the population as a measure of relative error of N number of BPM macroproperties. This fitness can be found from the relationship shown in 3.9.

$$Fitness = 1 - \frac{1}{N}\sum_{i=1}^{N} abs\left(\frac{desired - actual}{desired}\right)_i = 1 - abs(avg.\ relative\ error) \tag{3.9}$$

3) Identify three elite survivors which most closely fit the desired macroproperties.

4) Perform crossover between pairs of the survivors to generate sets of inputs for an intermediate generation of 10 new specimens. During crossover the input values for each new specimen are selected randomly from a uniform distribution of values lying between the inputs of the parents.

5) Randomly mutate the newly generated sets of inputs with a frequency determined by 3.10. If the fitness of both parents is high, then the likelihood of mutation will also be higher. A suitable value for the maximum mutation rate [28, 37, 111] was found to be 15% in this equation.

$$Mutation\ Rate = Max\ Mutation - \left[1 - \left(\frac{Fitness_{parent1} - Fitness_{parent2}}{2}\right)\right] \tag{3.10}$$

6) Mutate the randomly selected inputs with a magnitude inversely proportional to the average fitness of the selected pair of parents. This is achieved by creating a Gaussian distribution with a mean equal to the input value prior to mutation and with a standard deviation equal to the relative error of the parents multiplied by the mean.

7) Iterate the process starting on Step 2 until a termination criterion has been reached.

This process of generating new offspring through crossover and mutation of elite survivors was allowed to continue for 1000 total trials before the calibration process was terminated. If successful calibration limits were not reached then the process was restarted using a new random seed for generating the initial population. A flow diagram of this routine can be

found in Figure 3.7.

Over 25,000 bonded-particle models were generated and tested in the development of the genetic algorithm. It was found that a typical calibration required between 500 and 1000 trials to match desired material properties to within 1%. The results of a demonstration calibration are shown below in Figure 3.6 to Figure 3.9. A strain rate of 0.1 sec^{-1} was applied onto the specimen until its strength was reduced to 50% of its recorded peak axial stress. The calibrated BPM is shown in Figure 3.6 with its corresponding stress-strain response after calibration. The results from the calibration after 100 trials and 500 trials are shown in Table 3.1 with the corresponding percent error of each desired macroproperty.

Table 3.1: Results from demonstration calibration after 100 and 500 trials.

Macroproperty	Desired	100 trials	Error (%)	500 trials	Error (%)
Young's modulus	6.00 GPa	5.77 GPa	3.77	5.89 GPa	1.89
Poisson's ratio	0.20	0.21	4.13	0.20	1.15
Peak UCS	25.0 MPa	24.8 MPa	0.82	24.9 MPa	0.39
Post-peak modulus	-6.00 GPa	-6.03 GPa	0.50	-6.02 GPa	0.35

The genetic algorithm was used to calibrate macroscopic material properties of the BPM to match desired results within uniaxial compressive strength tests. The calibration method proved capable of optimizing 9 variable inputs to achieve 4 outputs and also calibrated brittleness of the specimen for a specific rate of loading. Over 25,000 specimens were generated and tested during the development of the genetic algorithm. Future improvements could be made to the heuristic to speed the calibration process. Parallel processing may be adopted to reduce run times for simulations. Coupling the genetic algorithm with an artificial neural network may provide additional methods for reducing the total number of iterations needed to calibrate a particular material property. These advancements to the calibration of bonded-particle models allowed brittleness to be incorporated into the models, a necessary requirement for research on unstable failures using DEM. With little modification the genetic algorithm could be applied to a wide array of technically challenging DEM calibrations with

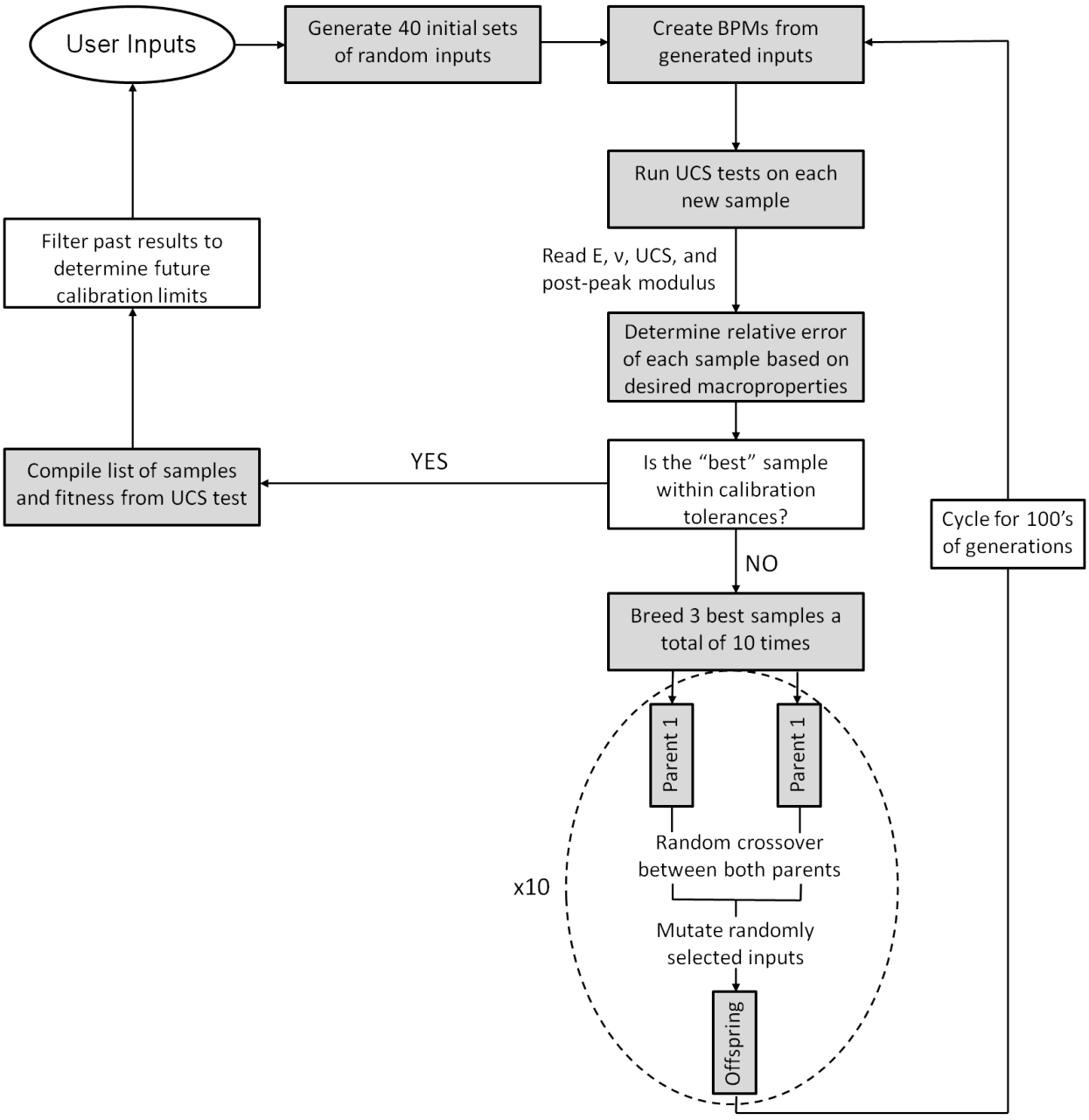

Figure 3.7: Structure of genetic algorithm routine for calibrating BPM samples.

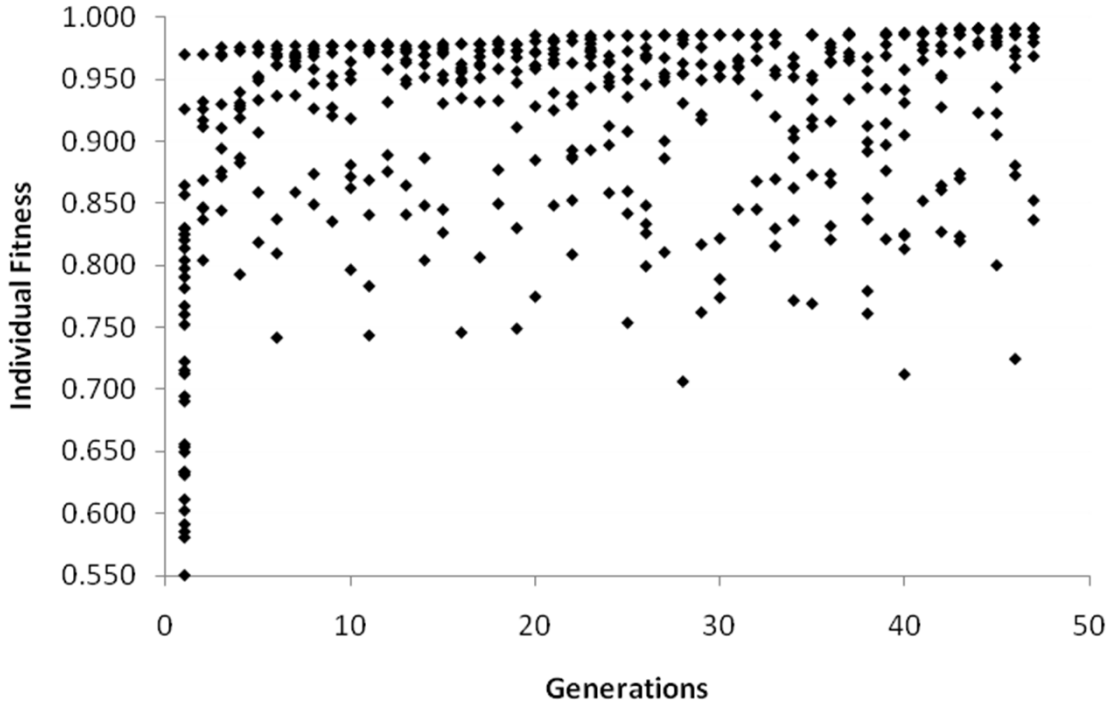

Figure 3.8: Fitness values of each specimen tested by genetic algorithm over 500 trials and 47 generations.

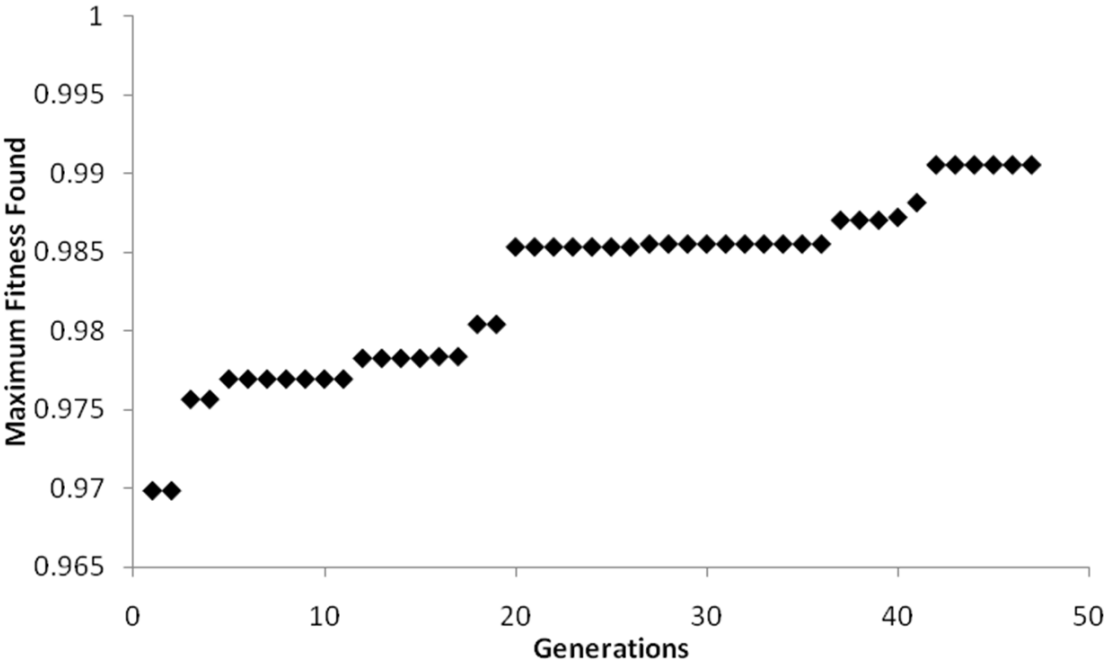

Figure 3.9: Maximum fitness of elite survivors after 500 trials.

little prior knowledge on how to achieve the desired material properties.

3.3.2 UCS Test Procedure

A series of tests were conducted using PFC^{3D} to determine the effect of unstable loading conditions on a bonded-particle discrete element model. Uniaxial compressive strength tests were conducted on cylindrical brittle specimens calibrated to represent a 7.6 MPa cubic strength of coal. The specimen geometry was 1 m in diameter and 2 m in height. The specimen stress-strain behavior shown in Figure 3.10 was calibrated at a specimen strain rate of 0.01 sec^{-1}, or 3.8e-7/step, through the genetic algorithm routine described in the previous section. A quasi-static solution scheme with a damping coefficient of 0.8 was applied locally to the particles. The combination of inputs shown in Table 3.2 were found to yield the desired material properties shown in Table 3.3.

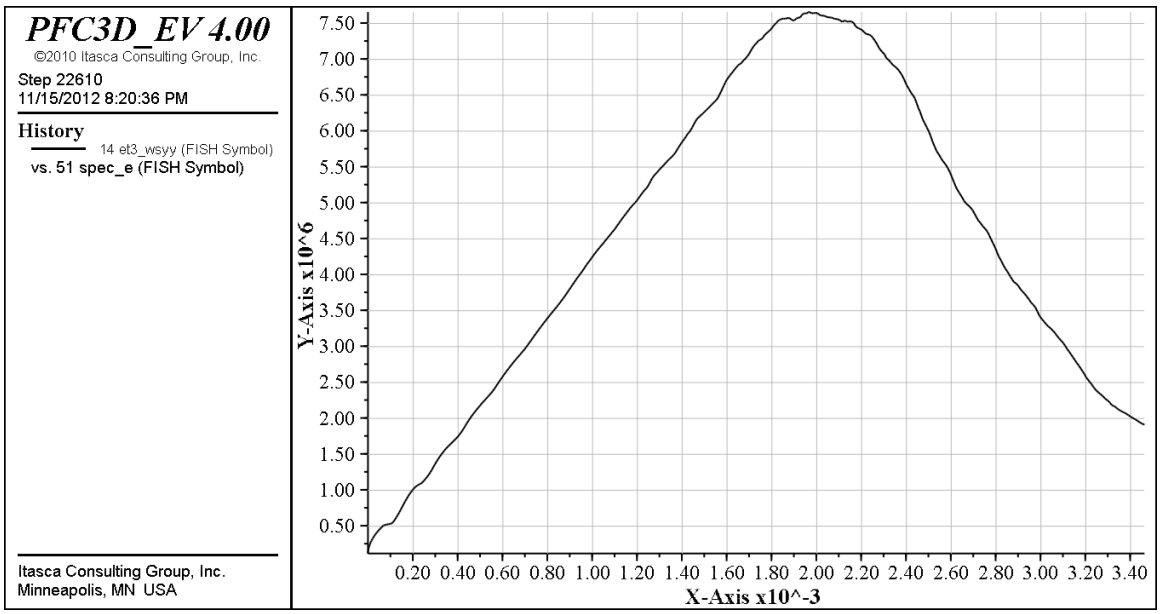

Figure 3.10: Stress-strain history of calibrated PFC^{3D} specimen during uniaxial compressive loading applied at a strain rate of 0.01/sec.

Two cylindrical platens sized 1 m by 1 m were set in series on either end of the specimen. The particle generation procedure was applied to the entire system in a single process using the 'mg_matgen' routine. Bonds were formed between all interacting particles in the system.

Table 3.2: Macroproperty inputs for particles and bonds in PFC^{3D} BPM.

Particle Inputs		Parallel Bond Inputs	
D_{max}/D_{min}	1.94	Radius Multiplier	1.0
Young's Modulus	3.14 GPa	Young's Modulus	4.48 GPa
Normal:Shear Stiffness	1.84	Normal:Shear Stiffness	1.62
Coefficient of Friction	0.49	Normal Strength	6.67 MPa
Density	1313 $\frac{kg}{m^3}$	Shear Strength	7.15 MPa

Table 3.3: Resultant material properties of calibrated PFC^{3D} specimen.

Material Outputs	
Young's Modulus	4.21 GPa
Poisson Ratio	0.19
Peak Strength (UCS)	7.65 MPa
Post-Peak Modulus	-5.17* GPa

* Linear fit between measurements taken at -25% and at -50% of peak stress.

Different strength and elastic properties were assigned to the bonds depending on if they fell within the specimen or platen boundary definitions. Bonds placed across a specimen-platen boundary were assigned either elastic or failable parameters to represent the platen or specimen, respectively. The assignment of these microparameters was determined by the location of the center of the bond which yields a "bonded" and highly frictional interface condition. This configuration of particles is shown in Figure 3.11.

The UCS test procedure was repeated with three different sets of microparameters assigned to the particles and bonds of the system. These inputs are shown in Table 3.4. Elastic values for Young's modulus of the balls and bonds were assigned for each tests as 100, 10, and 0.5 GPa. The possibility for initiating unstable failure conditions arose for loading system stiffnesses less than the post-peak slope of the specimen. Note that for the calibrated specimen, unstable failure conditions should therefore be initiated for platens with Young's modulus less than 5.17 GPa, or for the 0.5 GPa platen case only.

For the UCS tests a strain rate of 0.01 sec^{-1} was applied to the system, however a much more detailed analysis of loading velocity effects may be found at the end of this chapter.

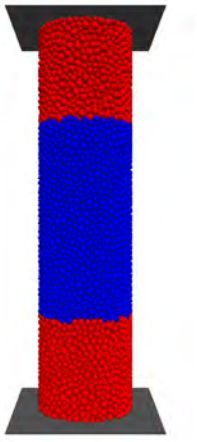

Figure 3.11: Configuration of uniaxial compressive strength test system with elastic platens (red) and a brittle specimen (blue). Strain is applied through walls at the top and bottom of the loading system.

Table 3.4: Microparameter inputs of platens in PFC^{3D}.

Particle Inputs		Parallel Bond Inputs	
D_{max}/D_{min}	1.94	Radius Multiplier	1.0
Young's Modulus	0.5, 10, 100 GPa	Young's Modulus	0.5 GPa
Normal:Shear Stiffness	2.5	Normal:Shear Stiffness	2.5
Coefficient of Friction	0.5	Normal Strength	-
Density	$1313\frac{kg}{m^3}$	Shear Strength	-

Resultant forces were recorded at the velocity boundary such that the axial stress of the system was to be determined and compared against strain measurements recorded for the platens and the specimen.

3.3.3 UCS Test Results

The values of specimen stress and strain recorded during the three uniaxial compressive strength tests are shown in Figure 3.12. These combined results show that the peak strength was reduced from 7.6 MPa to 6.4 MPa in the case of the 0.5 GPa Young's modulus loading platens. Several potential factors could impact the peak strength of the specimen, the primary among these is the reduction in confining boundary effects at the platen-specimen interface due to greater outward expansion for softer platens.

For the unstable case of 0.5 GPa Young's modulus platens the stress-strain behavior of the specimen was a linear post-peak slope of -0.4 GPa. This result was slightly less than the expected elastic rebound of -0.5 GPa for the platens. A much more surprising result was found in the response of the specimen to the two supposedly stable sets of platen stiffnesses during the 10 and 100 GPa tests. Assuming quasi-static failure the post-peak response of a specimen under stable loading conditions should remain consistent for all loading stiffnesses. It was seen that the post-peak response was shifted to have a more brittle response when load was applied through the stiffer 100 GPa platens. It can be seen from the tests that the 10 GPa platens actually elicited a -6.9 GPa post-peak response while the 100 GPa platens resulted in a much steeper -17.4 GPa response.

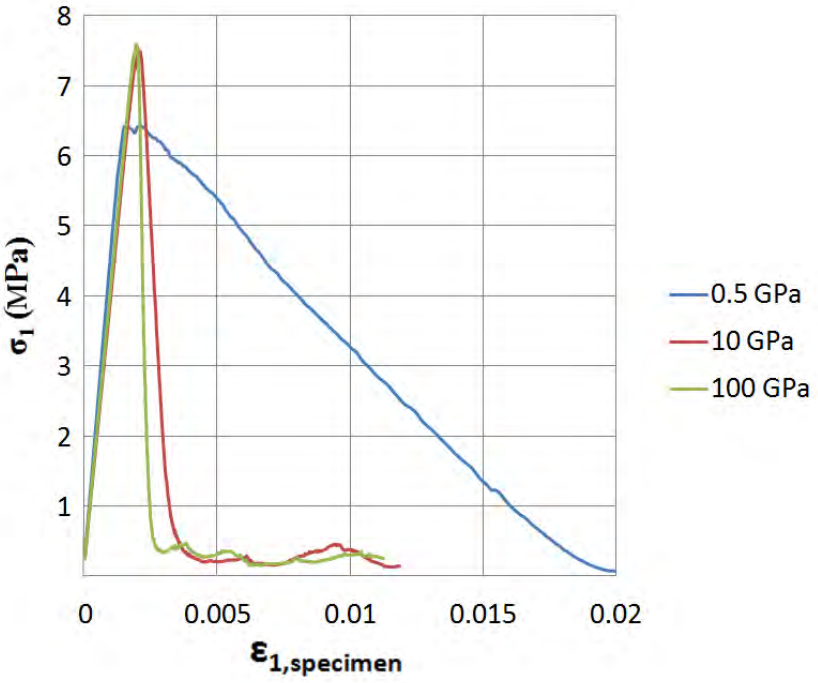

Figure 3.12: Specimen stress vs. strain for different sets of platens in UCS tests.

Further analysis was conducted on the micromechanical development of failure in the specimen in order to identify the cause of discrepancies between stable test conditions. Figure 3.13 plots the uniaxial principal stress recorded within the specimen as a function of the number of parallel bonds broken in the specimen.

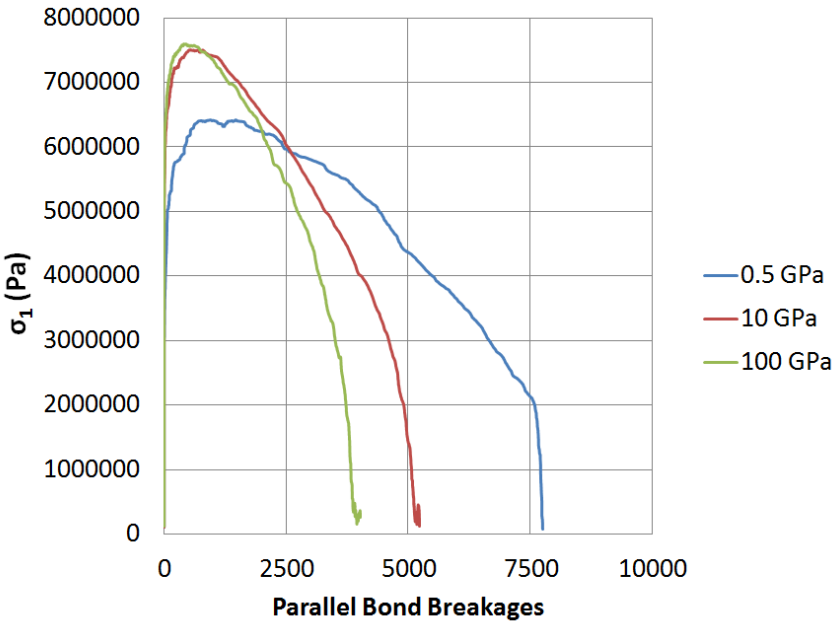

Figure 3.13: Stress of system vs. crack number during UCS tests.

A detailed view of fracturing within the models is shown in Figure 3.14 to Figure 3.16. Red and black lines represent tension and compression within unbroken parallel bonds in the loading system and specimen. Vacant areas indicate affected zones of broken bonds and are a reference for the general degree of fracture which has occurred, yet particles may still be present within these highly failed areas.

The mode of failure was shown to be consistent between the 10 and 100 GPa platen tests. In these tests a clearly defined band of failed bonds separates large sections of unfailed rock moving freely along planes of unbonded particles. The failure mode appears quite different for the unstable failure case with 0.5 GPa platens in that extensive fracturing occurred in a large affected region at the bottom portion of the specimen. This large failed zone is indicative of rupture or the rapid failure of bonds prior to the formation of a clearly defined failure path.

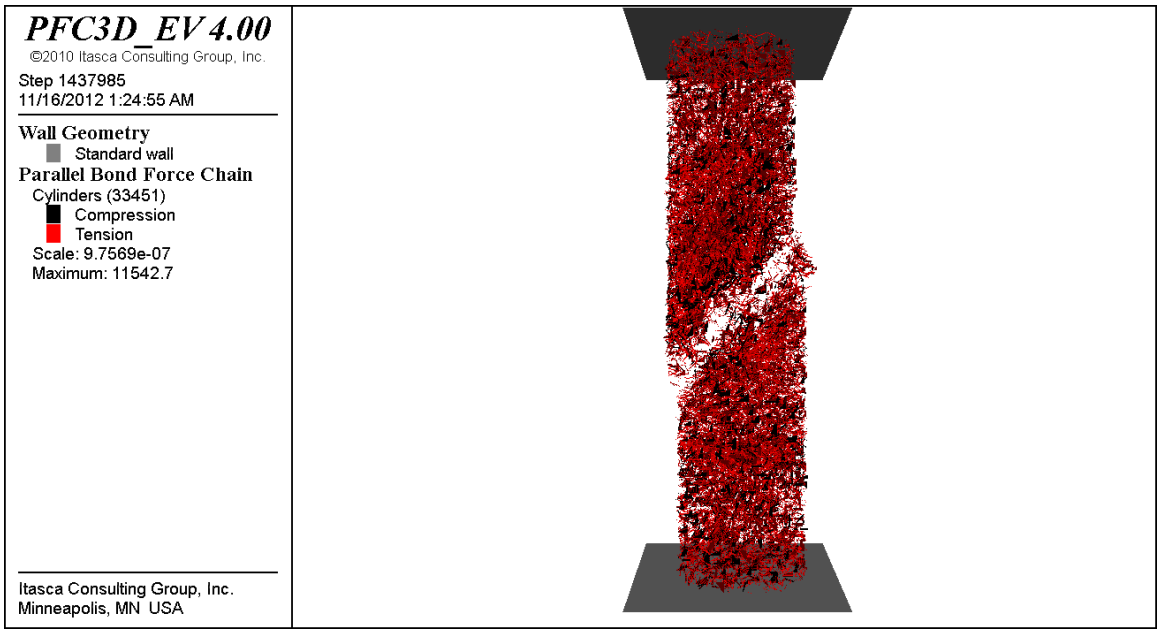

Figure 3.14: Tensile and compressive forces within bonded particle model after specimen failure for 100 GPa platen test.

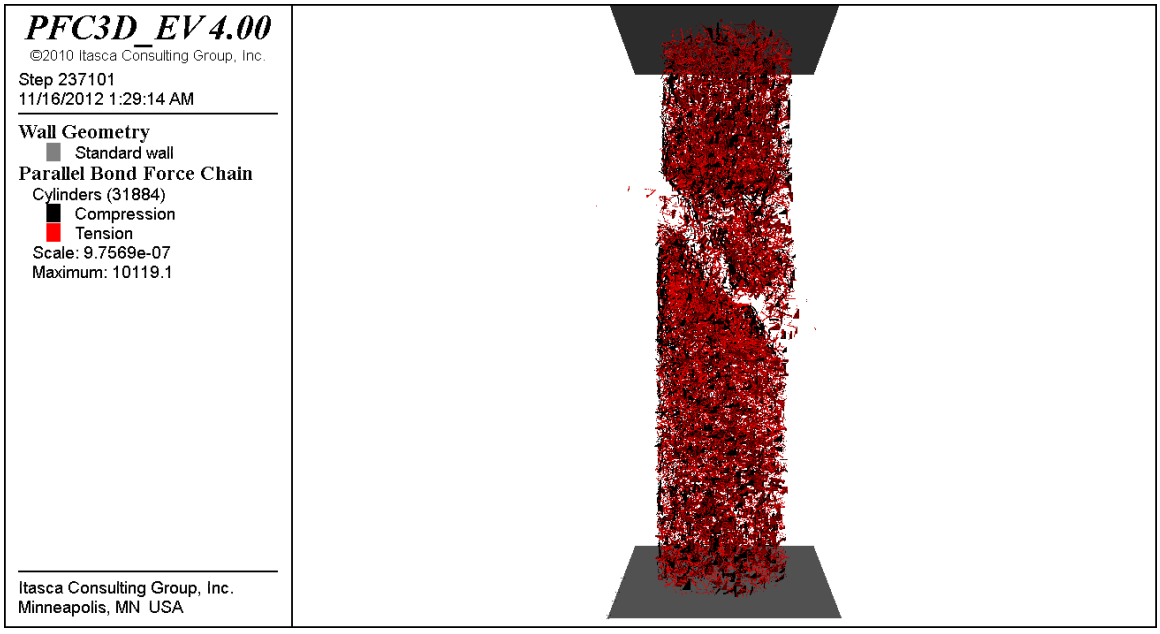

Figure 3.15: Tensile and compressive forces within bonded particle model after specimen failure for 10 GPa platen test.

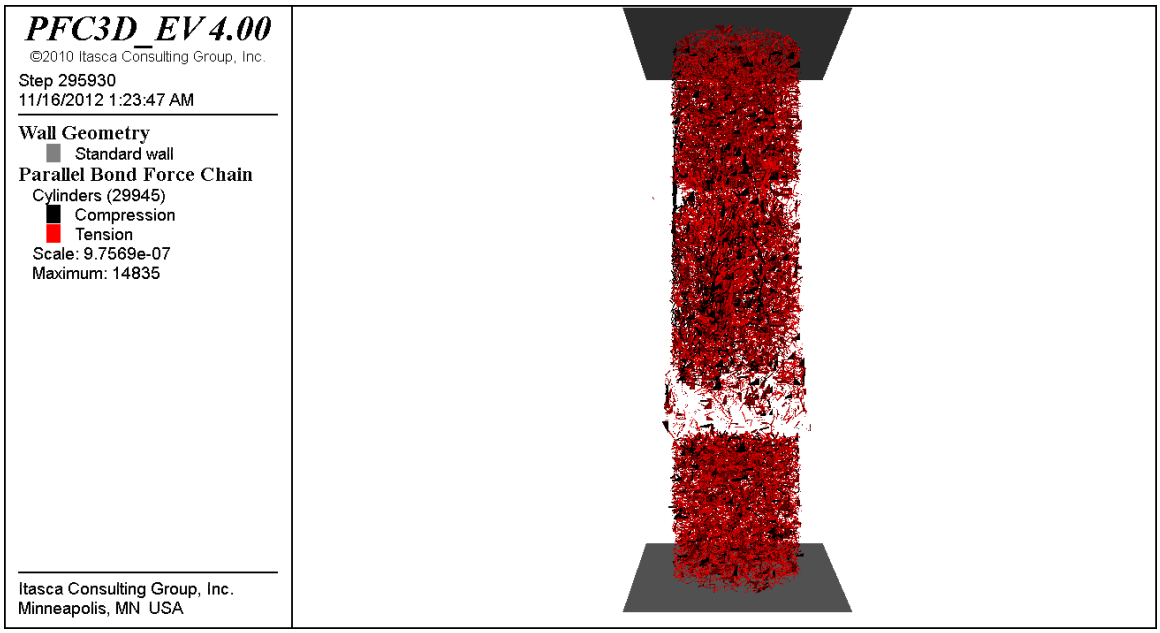

Figure 3.16: Tensile and compressive forces within bonded particle model after specimen failure for 0.5 GPa platen test.

3.3.4 Dynamic Loading Effects on Model Response

Several issues arose from the analysis of results in the uniaxial compressive strength tests. The post-peak material behavior was found to be inconsistent between similarly constructed compressive strength tests under stable loading conditions. The peak strength of the specimen was also found to be reduced in the case of the very soft 0.5 GPa Young's modulus platens. An extended series of tests was therefore run in PFC^{3D} to isolate the origin of these unexpected strength and post-peak material behavior changes under strictly stable loading conditions.

The loading system described in the previous UCS tests was adopted for the extended dynamic analysis, however the Young's modulus of the bonds and particles making up the platens were fixed at 100 GPa. Three strain rates of 0.1, 0.01, and 0.001 sec^{-1} were then applied onto the system. The stress-strain results from the specimen during these three tests is shown in Figure 3.17. For the fast loading case the peak stress was over 9 MPa as compared to the 7.6 and 7.4 MPa peak stress values reached in the subsequent tests. This

large increase in peak recorded stress was a consequence of the large dynamic forces in the model as which were as large as 4 MPa at the onset of loading. However, the tests of slow, quasi-static loading conditions still resulted in disparities between the post-peak responses of the material. The specimen failing from the 0.01 sec^{-1} system strain rate maintained a post-peak modulus of -20.4 GPa while the 0.001 sec^{-1} strain rate case resulted in a -60.9 GPa post-peak modulus for the specimen.

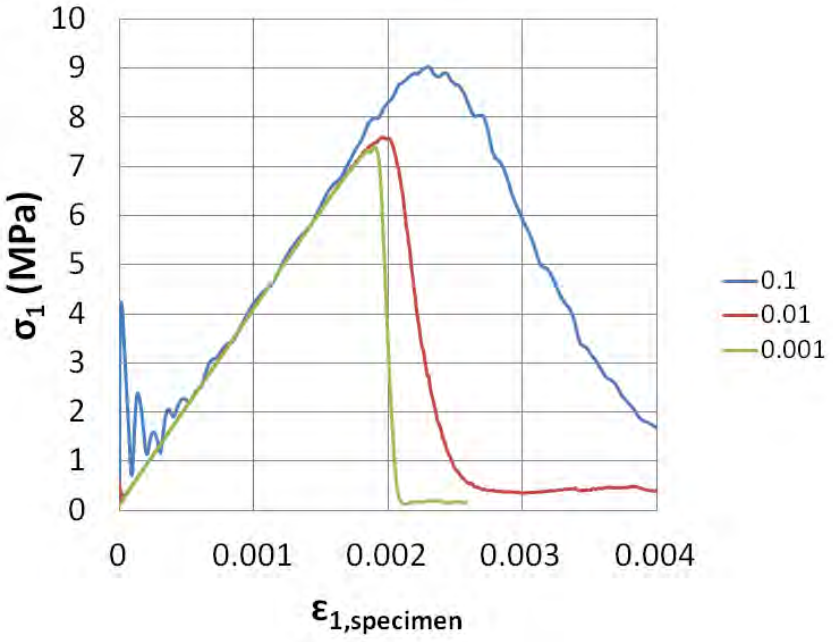

Figure 3.17: Specimen stress vs. strain during 100 GPa platen loading with three applied system strain rates of 0.1, 0.01, and 0.001 sec^{-1}.

An investigation was also made into the development of cracks in the model. More cracking and breaking of bonds was observed for the highly dynamic loading case shown in plot Figure 3.18. This same result is shown graphically in to Figure 3.21 from the breaking of force chains in the specimen

Figure 3.19 through Figure 3.21 show unbroken bonds at the conclusion of each speed test in which red and black lines represent tensile and compressive forces transmitted through parallel bonds. The absence of bonds indicate an area highly affected by failure. For the slowest 0.001 sec^{-1} system strain rate test the failure developed along a localized plane within

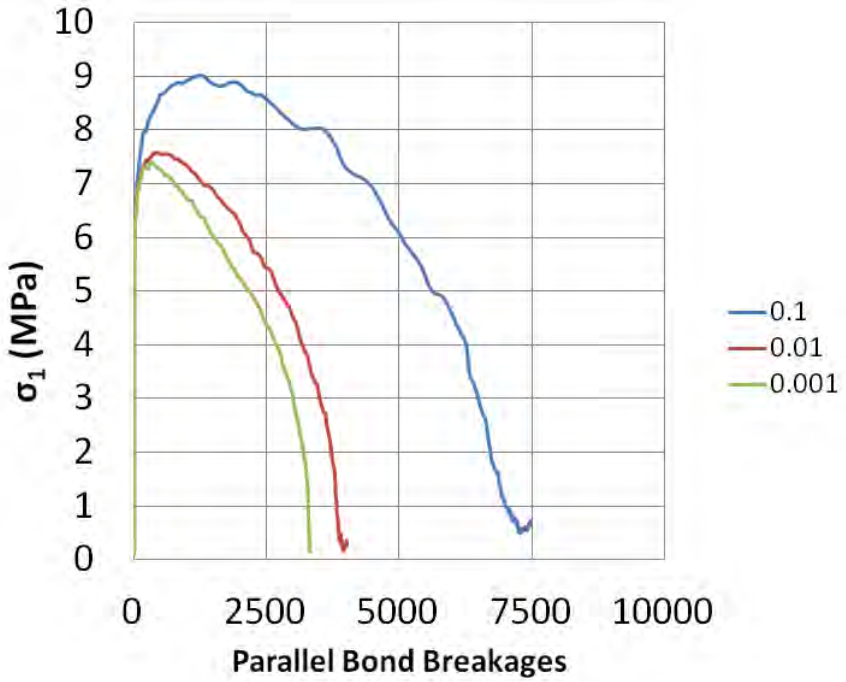

Figure 3.18: Tensile and compressive forces within bonded particle model after specimen failure for 0.5 GPa platen test.

the specimen. This behavior ran in stark contrast to the highly dynamic 0.1 sec^{-1} test in which extensive rupture caused the sudden loss in strength of the specimen. Figure 3.21 shows several large portions of the bonded-particle model which had separated from the center of the specimen due to sudden rupture.

3.3.5 Conclusions

A series of uniaxial compressive strength tests were conducted in PFC^{3D} to study the condition of unstable failure using a discrete element method bonded-particle model. The simulated rock specimen was a slender cylinder of bonded particles whose microproperties were calibrated for a given strain rate to represent the coal macroproperties shown in Table 3.3. Elastic platens were also simulated using PFC^{3D} and were placed on either end of the specimen, with strain then being applied at a constant rate to the system made up of the platens and specimen. The microproperties of the platens' particles and bonds were then modified between tests to apply an effective loading system stiffness onto the specimen

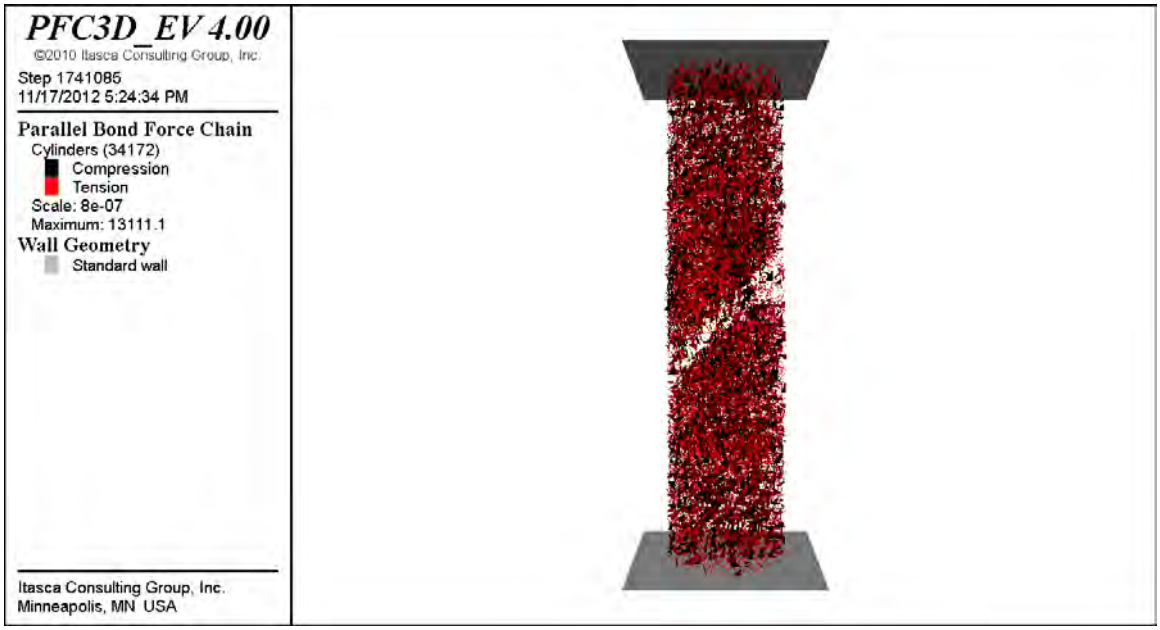

Figure 3.19: Tensile and compressive forces within bonded particle model after specimen failure from the very slow 0.001 sec^{-1} system strain rate.

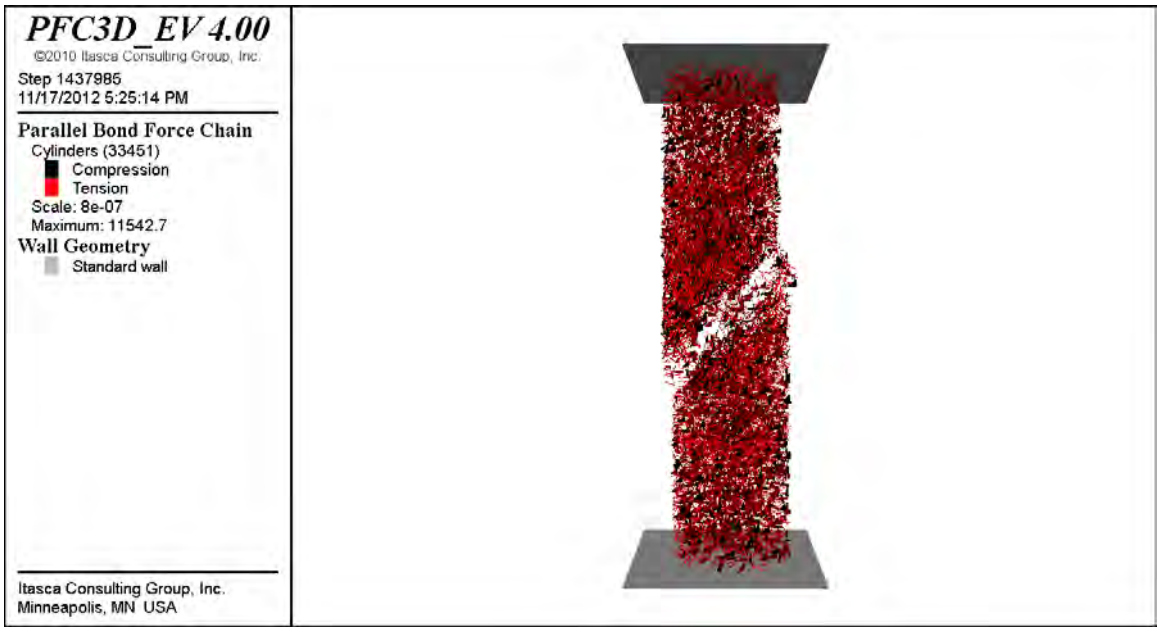

Figure 3.20: Tensile and compressive forces within bonded particle model after specimen failure from the intermediate 0.01 sec^{-1} system strain rate.

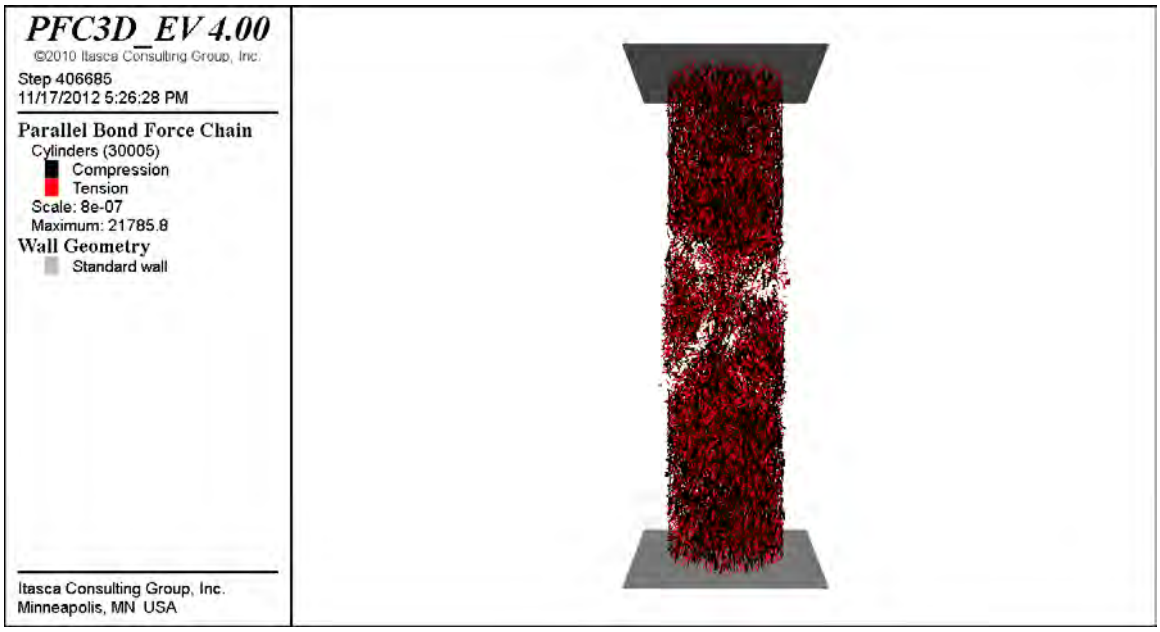

Figure 3.21: Tensile and compressive forces within bonded particle model after specimen failure from the very fast 0.1 sec^{-1} system strain rate.

ranging from fully stable to highly unstable conditions.

The results from these tests showed a clear distinction between the failures of the specimen under soft and stiff loading cases. For the soft platens, or unstable loading case, rupture was observed at the bottom of a heavily fractured specimen. Records of fracture propagation also revealed a higher number of total cracks in the case of unstable failure.

These preliminary investigations on the micromechanics of unstable failure were overshadowed by a number of unintended effects which emerged from the tests. The strength of the specimen was seen to drop by 15% when failed by the 0.5 GPa Young's modulus platens. The reduction in strength was due primarily to the outward expansion of the soft platens under axial compression and the application of tensile loads onto the ends of the specimen. Of more pressing concern for studies of brittle failure came in the form of a shift in the post-peak behavior between stable loading schemes.

An additional series of tests was run to determine the source of variations in the brittleness of the BPM. A constant, stable platen stiffness was used between tests with loading

velocities ranging from quasi-static to highly dynamic being applied onto the system. During dynamic applications of load the propagation of cracks was similar to what was observed for the unstable 0.5 GPa platen loading case. Through these tests it was observed that the intrinsic post-peak behavior of a brittle bonded-particle model was velocity dependent, even for loading velocities within the traditional quasi-static regime of discrete element models.

The specimen behavior was found to be highly dependent on effects from loading velocity. A direct effect was seen on material brittleness even for quasi-static loading velocities in which no other significant dynamic effects are measured. The results from this extended series of uniaxial compressive strength tests revealed significant technical challenges to modeling consistent material behavior for the BPM within static and stable loading tests.

3.4 Discussion of Bonded-Particle Method for Simulating Unstable Failure in Rock

A discrete element method capable of producing realistic fracture paths is ideal for assessing micromechanical effects from material or loading system characteristics. The explicit nature of the method also makes it well suited for studies on the dynamic response of rock. Discrete element models which combine the micromechanical progression of failure with an accurate representation of the macroscopic failure response may then be applied with some extrapolation to studies of rock failure under unstable loading conditions.

A discrete element method bonded-particle model was investigated for its ability to represent brittle failures in unstable compression. A PFC^{3D} bonded-particle model was constructed to first attempt to represent brittle macroscopic failure through the propagation and coalescence of cracks in a simulated rock specimen. An extensive calibration procedure was required to achieve precise material properties for the bonded specimen. A genetic algorithm was developed to aid in this process and the given heuristic was found sufficient for achieving a set of desired material macroproperties at a given loading rate. Destructive uniaxial compressive strength tests were then conducted on the BPM and the results were compared with observations made in physical testing environments such as [13, 40, 48, 49]. Realistic modes

of failure were presented in the bonded-particle models however the behavior of the specimen was found to vary considerably with changes to the applied loading rate. The post-peak material response for the specimen was found to be inconsistent between different loading velocities, even under previously assumed quasi-static loading conditions. Consequently, an extreme level of care was required to calibrate a specimen for a given loading velocity.

Alternative methods for formulating bonded-particle models are currently being developed by researchers to address these significant technical challenges [62]. Recent publications have risen additional concerns when applying the bonded-particle model which include unrealistic values for tensile to compressive strength ratios [3, 4], non-physical releases of energy with the breakage of bonds [16], and large numbers of tensile bond failures as compared to shear bond failures. Methods are being explored to resolve these fundamental issues, such as projecting flat faces between spherical particles to more appropriately model continuous rock [99]. Regardless of the developments being made to the method, the combined difficulties which were introduced by the bonded-particle model made its use infeasible for the current studies on mine layouts and realistic underground mining conditions.

CHAPTER 4

FINITE DIFFERENCE MODELS OF ROCK FAILURE IN COMPRESSION

Unstable failure was presented in Chapter 2 through the axial stress-strain behavior of rock in compression. This method relies on a deterministic approach to solving the stresses and strains which develop within the rock. For typical rock there is no single process through which can fail; inherent complexities introduced by material inhomogeneities, boundary conditions, and dynamic effects all affect the evolution of failure. Microcracks and pre-existing flaws in the rock are the underlying cause of failure [12] and yet the interacting arrays of microflaws and their resulting stress concentrations are a problem of such an advanced nature that it is too complex to deconstruct the macroscopic failure response directly from a knowledge of the micromechanical behavior of the rock [13]. Many different constitutive models have been constructed to describe the strength of rock through a stochastic application of macroscopic material properties.

Numerical methods which apply constitutive relationships to a continuum provide a useful range of predictive tools for the failure of a rockmass. Computational approaches often use boundary element or finite element numerical methods which have been shown to realistically simulate brittle rock response. The finite difference method has also been applied extensively to the field of rock mechanics with great success [57]. The explicit numerical formulation of the finite difference method is of particular interest to the study of unstable failure due to its calculation of dynamic motion as a response to physical instability in the model. For this and additional reasons which will be discussed throughout this dissertation, the explicit finite difference method was employed as the primary numerical tool for the study of rock in unstable compressive failure.

4.1 Mohr-Coulomb Rock Strength with Weakening Properties

The ultimate failure mode of rock under triaxial compression occurs through shearing as microcracks coalesce along a favorably aligned, localized band along which the rockmass bifurcates. A number of failure criteria and flow rules have been developed to represent the effects on ultimate rock strength by variations of confinement conditions. These tools may be combined to develop a constitutive material model to describe the overall macroscopic response of a rockmass, even under conditions found past the point of failure.

The Mohr-Coulomb peak strength criterion is a longstanding and widespread approach in geomechanical applications to determining the shear strength of rock under various levels of confinement. The criterion accounts for a material-specific cohesion of the rock with a friction across an assumed plane of shear failure. The strength envelope is defined by 4.1 where c is the unconfined cohesive strength, σ_n is the normal stress across the shear plane , and ϕ is the angle of internal friction for the material.

$$\tau = c + \sigma_n \tan \phi \tag{4.1}$$

This concept is outlined in more detail in Figure 4.1 for a triaxial compressive strength laboratory test specimen. The maximum shear stress develops along a critical shear plane oriented with angle β found through a transformation of the major and minor principal stresses (intermediate principal stress is typically ignored).

The diagram shown in Figure 4.2 ties these concepts together by projecting the Mohr's circle transformation of a stress state at the point of yield or failure, as defined by 4.1.

A material may be represented by a constitutive model with varying levels of complexity depending on the analysis being performed. Elastic models account for recoverable elastic deformation while peak strength models assign an ultimate strength to the material. Many failure criteria may be used to define the peak strength however the Mohr-Coulomb criterion is selected for additional study due to its relatively good fit to experimental data through a straightforward application of rock mechanics theory.

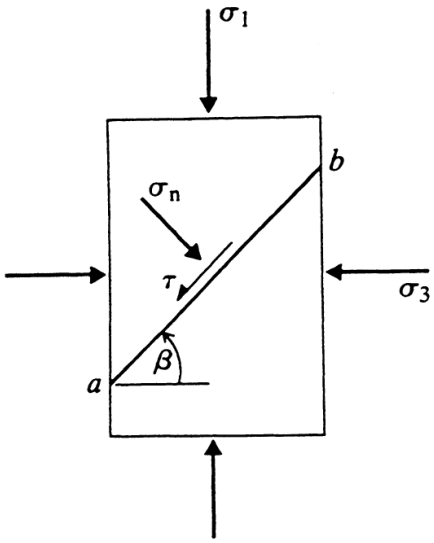

Figure 4.1: Triaxial compressive strength test with Mohr-Coulomb shear plane along which failure occurs.

Additional levels of detail may be incorporated in a constitutive model to assign residual post-failure strengths to a material. For simulating brittle materials a strain-softening strength rule may be incorporated to match the reductions in strength observed in controlled physical tests. Consideration must then be made for the flow of the material past the point of yield. Experimental tests show that rock dilates as it fails [8]. If shear occurs along a plane, asperities will open due to the irregular surface of the plane. These effects may be measured in terms of the dilation angle of the rock, which may be found through 4.2 with

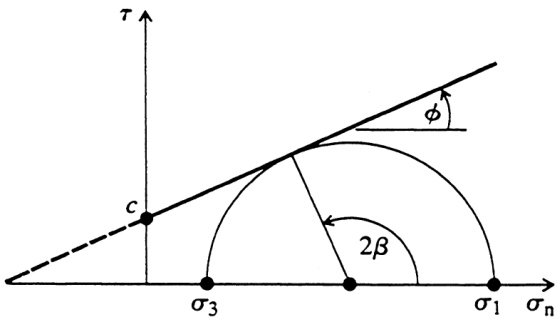

Figure 4.2: Mohr-Coulomb shear strength envelope as a function of principal stresses.

the determination of volumetric rate of strain shown in 4.3.

$$\sin\psi = \frac{\dot{\varepsilon_v^p}}{-2\dot{\varepsilon_1^p} + \dot{\varepsilon_v^p}} \tag{4.2}$$

$$\dot{\varepsilon}_v = \dot{\varepsilon}_1 + \dot{\varepsilon}_2 + \dot{\varepsilon}_3 \tag{4.3}$$

The plastic potential function shown in 4.4 takes on the same shape as the strength envelope from 4.1 and is a type of non-associated flow rule which may be used to represent plastic flow after failure [119]. The only change which is made from 4.1 is the substitution of the dilation angle in place of the friction angle.

$$g = \tau + \sigma_n \sin\psi \tag{4.4}$$

Further control may be brought into modeling brittle failure by varying cohesion, internal friction angle, and dilation angle as functions of plastic strain. A strain-weakening, friction-hardening model is a commonly adopted approach to represent brittle rock [80]. The use of this particular constitutive model has been shown to introduce a number of difficulties in implementation due to grid-dependent localization effects [14, 25, 97, 100, 103], but these issues will be discussed in more detail in subsequent sections.

Constitutive laws describe the elastic, plastic, and brittle failure responses observed in rock. A simplistic approach to studying failure may be taken by calculating peak strength using the Mohr-Coulomb failure criterion and assuming perfectly plastic behavior after failure. Varying levels of complexity may then be adopted into the models to more completely describe the range of observed rock behavior. A Mohr-Coulomb strain-softening model is one approach to defining brittle rock behavior. Difficulties may emerge from the use of these methods in numerical models. However, their careful application provides beneficial tools for analyzing the behavior of brittle rock during failure. The effects of unstable loading conditions on brittle rock supports may then be assessed.

4.2 $FLAC^{3D}$ Modeling of Macroscopic Failures

$FLAC^{3D}$, or Fast Lagrangian Analysis of Continua in 3 Dimensions, is an explicit finite difference numerical model which is commonly applied to the study of rocks or soils in geomechanical simulations [57]. The continuum nature of the model proves beneficial for reducing calculation times and is conducive to modeling larger mine layouts. Contrary to traditional finite or boundary element methods, the explicit numerical formulation is able to account for unstable force equilibria through the application of equations of motion to determine potentially large-strain displacements within the continuum. These calculation steps are necessary for tracking the progression of unbalanced force equilibria which lead to the rapid velocities and displacements observed in unstable rock failures. The following section describes the general numerical methodology used by $FLAC^{3D}$ and the limitations which these formulations may present to the realistic representation of unstable failure.

Rock is simulated in $FLAC^{3D}$ as a Lagrangian (i.e., deformable) mesh of gridpoints whose positions and velocities are updated at discrete timesteps. An example of a mesh generated in $FLAC^{3D}$ is shown in Figure 4.3.

Internal strain and strain rate calculations are then performed within the "zones", or the discrete volumes whose vertices are defined by neighboring gridpoints (see Figure 4.4).

The general calculation scheme outlined in Figure 4.5 is then performed at the gridpoints and within two sets of overlaying tetrahedral subunits which define each zone, as shown in Figure 4.6.

The calculation steps which $FLAC^{3D}$ applies during its explicit iterations are as follows:

1) Forces are calculated at the gridpoints from stresses summed with applied loads and body forces.

2) Equations of motion are used to calculate accelerations, and update velocities and displacements at the gridpoints.

3) Strain rates are calculated from the values of gridpoint velocity.

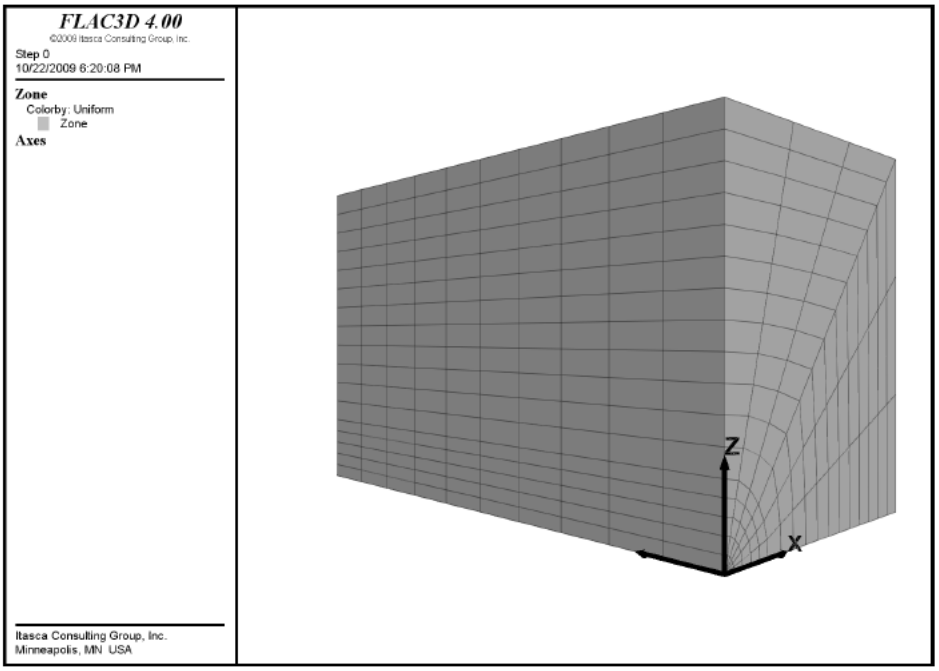

Figure 4.3: Example of a continuum grid generated in $FLAC^{3D}$.

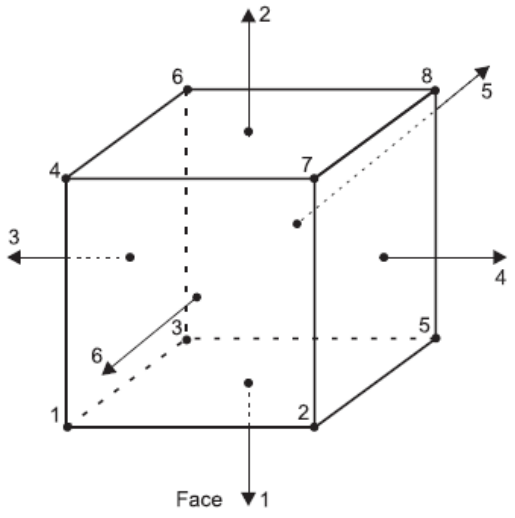

Figure 4.4: A $FLAC^{3D}$ volume element, or "zone", showing numbered faces and gridpoints.

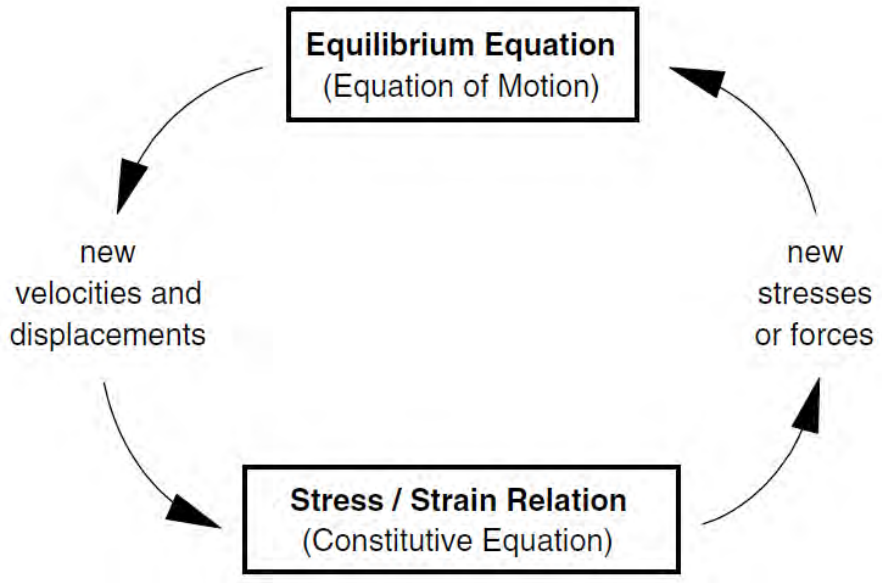

Figure 4.5: $FLAC^{3D}$ general calculation procedure.

4) Stresses are calculated as a function of a constitutive law as a response to strain increments.

Stresses within the polyhedral subunits constitutive the zones are first used to calculate the tractions acting along edges of each polyhedron. Forces acting at the gridpoints are calculated from a summation of these tractions. A local damping force is applied at gridpoints to approach static equilibrium in the model. The damping force in direction i, labeled $F_{d,i}$, is applied proportionately to the force, F_i, acting at the gridpoint in the direction opposite of travel. This relation is shown in 4.5, where α is a constant damping coefficient.

$$F_{d,i} = -\alpha \left|F_i\right| sgn(v_i) \tag{4.5}$$

Mass damping is also applied to reduce potential accelerations and maintain numerical stability. Mass is artificially scaled to increase the inertial mass of gridpoints and resolve any potential accelerations within a single timestep, which is set in the calculations to unity as a matter of convenience. The inertial mass term used in the mass damping mode is found from a summation of minimum mass terms required to maintain numerical stability

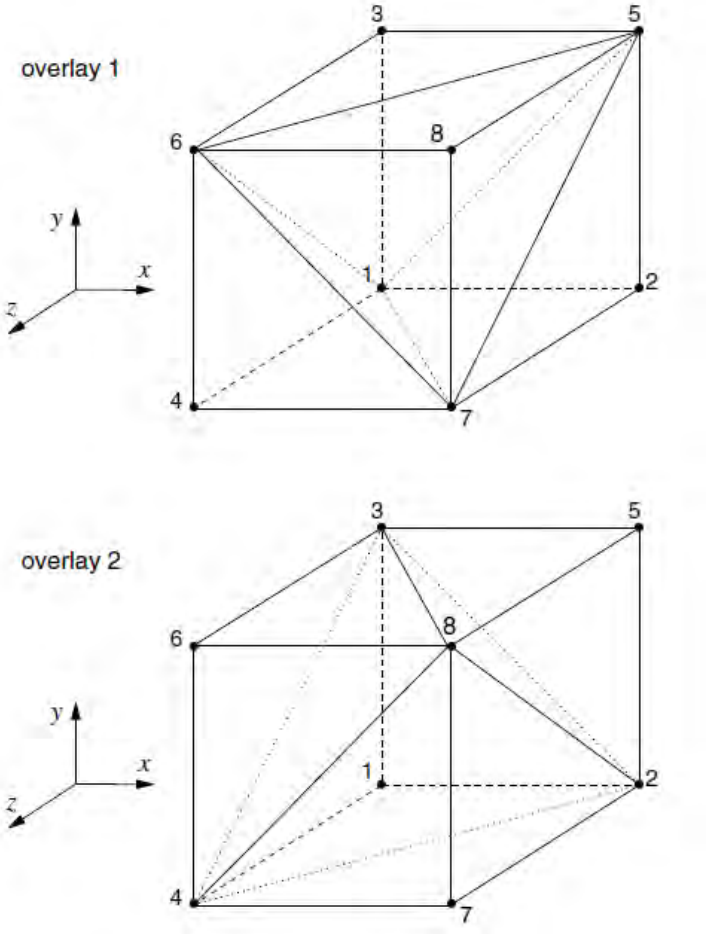

Figure 4.6: Tetrahedral volumes used for stress and strain calculations in zones.

for each polyhedron calculation, as is determined from the stiffness of the polyhedron. The consequence of this static solution form is that the dynamic response of the model does not result in a physically significant representation of mass or time dependent behavior.

After the unbalanced forces have been damped through local and inertial mass damping methods, the resulting gridpoint accelerations are used to calculate updated velocities through a central differencing time marching scheme. Displacements are calculated at the gridpoints and within large-strain mode the gridpoint positions are also updated to reflect significant changes in geometry for subsequent timesteps.

Gauss' theorem is applied to derive the strain rates acting within tetrahedral subunits in the zones. Small deformation theory is then applied to derive strain rates directly from

changes in velocities with an assumed linear spatial variation of velocity across a zone. The strain rates are calculated at gridpoints through a nodal mixed discretization process [28, 77]. This approach is similar to the mixed discretization method and has been adapted for dilatant materials by averaging velocities throughout a volume surrounding each gridpoint. A constitutive law is used to calculate the resulting change in stress caused by an increment in strain. Many different constitutive material behaviors may be applied within$FLAC^{3D}$, however elastic, Mohr-Coulomb (plastic), and Mohr-Coulomb strain-hardening/-softening (brittle/weakening) models are used exclusively within this dissertation.

The elastic constitutive law is a straightforward application of Hooke's law to calculate stress from strain. The Mohr-Coulomb model allows for the possibility of failure and plastic deformation. The ultimate strength of the material remains constant after plastic deformation has occurred which results in non-associated plastic flow and a constant state of stress. Plastic strain increments are calculated from 4.6 where λ is a constant which is calculated from friction and dilation angles, and bulk and shear moduli. The function g^s is the plastic flow equation defined from 4.7 with N_ψ being calculated from the dilation angle, φ, found from 4.8.

$$\Delta\epsilon_i^p = \lambda \frac{\partial g}{\partial \sigma_i} \tag{4.6}$$

$$g^s = \sigma_1 - \sigma_3 N_\psi \tag{4.7}$$

$$N_\psi = \frac{1 + \sin(\psi)}{1 - \sin(\psi)} \tag{4.8}$$

The Mohr-Coulomb strain-softening (MCSS) model allows strength and flow properties to vary as functions of total plastic strains and provides tremendous control over the response of the constitutive model. The user enters tabular values for friction angle, cohesion, and dilation angle which are then used in the standard fashion within the Mohr-Coulomb constitutive law. This complete process is repeated at every timestep through a central differencing scheme with the stress and strain calculations being performed at alternating

half-timesteps.

The explicit finite difference software $FLAC^{3D}$ was selected for simulations of unstable failure conditions due to its dynamic modeling of a continuum and capability to represent physical instability. The three-dimensional nature of the software allows realistic mine models to be constructed for backanalyses or parametric studies. Brittle material behaviors are defined through a Mohr-Coulomb strain-softening model. Plastic deformations are then calculated from a non-associated plastic flow rule with a potentially variable dilation angle.

4.3 Unstable UCS Tests in $FLAC^{3D}$

The numerical methodology incorporated in $FLAC^{3D}$ was assessed for its ability to simulate the onset and propagation of unstable failure through the laboratory-style UCS tests which are described in the following sections. The tests were structured after the idealized case of instability presented in Chapter 1 in which a compressive spring-specimen-spring system becomes unstable if the unloading modulus of the springs is less than the post-peak modulus of the brittle specimen. Through this simplified uniaxial loading condition the analysis of unstable failure is reduced to an idealized one-dimensional test case. The response of the finite difference method could thereby be assessed in the case of uniaxial compression and the appropriateness of representing the failure through a Mohr-Coulomb constitutive model could be evaluated. Unstable failure conditions could then be applied within the model to record the resulting numerical effects caused by physical instability.

4.3.1 Calibration of Mohr-Coulomb Strain-Softening Model

The UCS rock specimen was modeled after idealized coal properties using the Mohr-Coulomb strain-softening (MCSS) constitutive model for capturing brittle failure behavior. The MCSS model requires an intensive calibration of cohesion, friction angle, and dilation angle to elicit varying degrees of brittleness and peak strength from simulated rock specimens. The details surrounding the calibration efforts proved so numerous that this section has been dedicated solely to a description of these efforts, along with the subsequent lessons learned.

The MCSS model uses a Mohr-Coulomb failure criterion that is determined from cohesion, dilation angle, and internal friction angle as functions of plastic strain of a zone. The method for achieving a brittle material response relies on a cohesion-weakening, friction-hardening model [2] in which cohesion decreases and friction increases with the onset of plastic deformation. Elastic properties of Young's modulus and Poisson ratio were applied directly to the zones at the initial stages of the calibration. The input values of dilation angle were next set to match those determined from past numerical modeling of brittle rock [47]. The real control of specimen behavior was then adjusted through the tabular inputs for cohesion and internal friction angle. An iterative, manual calibration process was taken to obtain a desired model response using input values within physically observed ranges.

The initial goal of the calibration was to develop a specimen with a linear post-failure response to represent a characteristic coal behavior with peak strength equal to the 7.6 MPa cubic strength of coal. Tests were conducted on a cylindrical specimen with rigid applications of displacement at its ends. Manual adjustments of constitutive model input parameters made the process difficult for obtaining a precisely controlled failure. This process of manual calibration resulted in a non-linear post-failure response yet the averaged post-peak slope was similar to intended behavior. The details of non-linearity in the specimen's post-peak response is shown in further detail in Figure 4.7.

The final set of MCSS inputs were calibrated for the model and are shown in Figure 4.8. Table 4.1 shows the additional input properties used to define the material in the model. These combination of parameters led to the material behavior displayed in Figure 4.7.

Table 4.1: Input parameters of calibrated $FLAC^{3D}$ coal specimen.

Model Inputs			
Density	1313 $\frac{kg}{m^3}$	Local damping Coefficient	0.8
Young's Modulus	4 GPa	System loading velocity	1.2e-7 $\frac{m}{s}$
Poisson ratio	0.2	Specimen height	2 m
Vertical gridpoint spacing	0.2 m	System diameter	1 m
Radial gridpoint spacing	0.1 m	Total system height	4 m

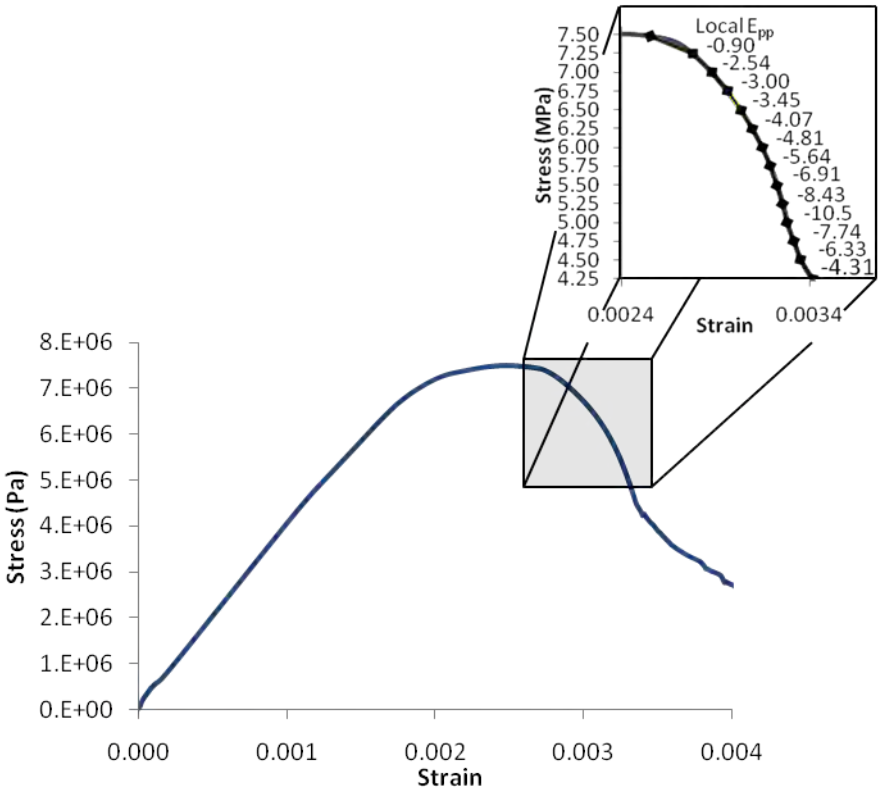

Figure 4.7: Stable stress-strain response of $FLAC^{3D}$ UCS specimen showing a detail of local post-peak slopes.

4.3.2 UCS Test Procedure

A series of simulated uniaxial compressive strength tests were conducted in $FLAC^{3D}$ to study a brittle specimen failing between two elastic platens. The model of the UCS loading system and specimen is shown in Figure 4.9 with cylindrical platens representing spring elements. The resulting testing system is shown in Figure 4.9 along with its idealized representation as a spring-specimen system.

A slow velocity boundary condition of 6e-8 m/step was applied to simulate quasi-static loading of the system. Stress was measured through unbalanced forces at the top and bottom of the model boundaries. Strains were measured both for the specimen and for the entire

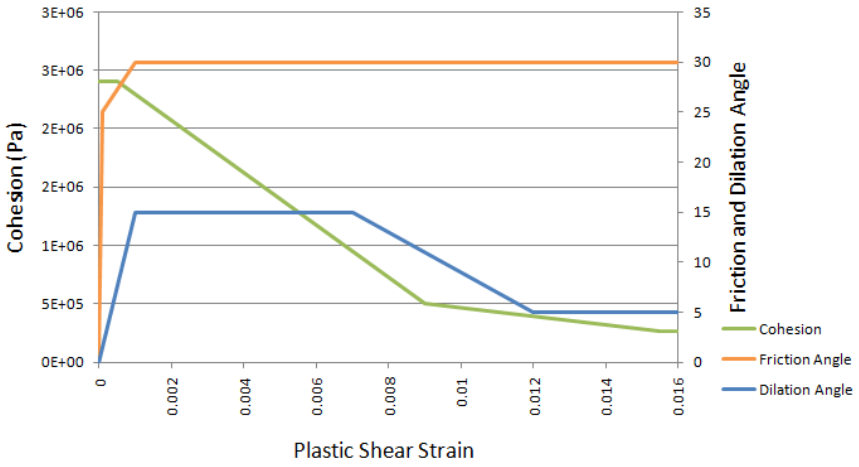

Figure 4.8: Cohesion, internal friction angle, and dilation angle values as functions of plastic shear strain for the calibrated $FLAC^{3D}$ Mohr-Coulomb strain-softening constitutive model.

loading system which included platens.

A plane of interface elements was applied to the top and bottom of the coal specimen between the coal and the platens. A Mohr-Coulomb strength law was applied to the interface, however slip was allowed to occur early along the interface by defining it as a cohesionless plane. These interface elements were introduced to reduce potential confinement of the uniaxial specimen in order to mimic true uniaxial loading conditions of a slender rock specimen.

A series of uniaxial compressive strength tests were run on the calibrated coal specimen while adjusting the Young's modulus of the platens between tests. Values of 1.5, 10, and 100 GPa were assigned for the Young's modulus of the platens. This range of values was selected to provide a case of unstable, stable-unstable-stable, and stable type failures (see Figure 4.10) as determined from the post-peak response of the specimen. Primary studies were conducted on the effects of damping, however it was determined that a default local damping ratio of 0.8 was assumed for the tests.

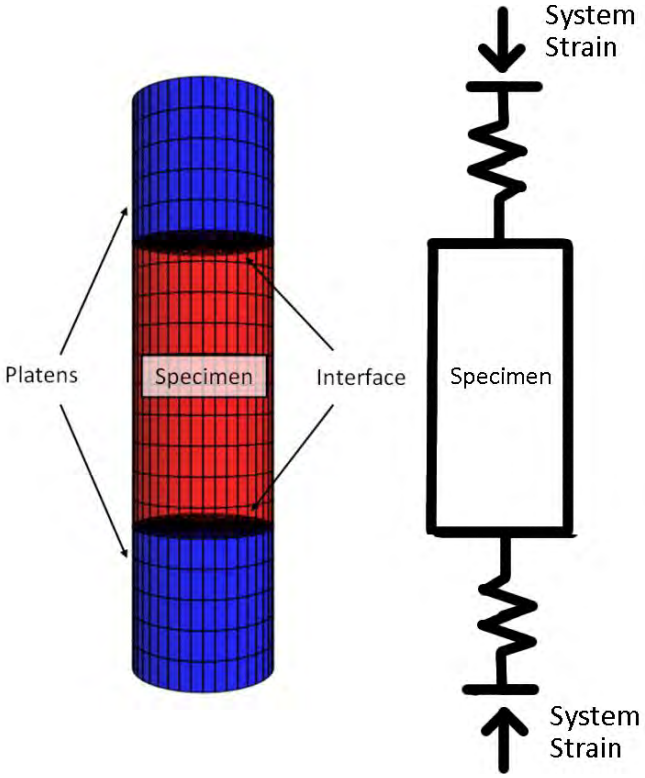

Figure 4.9: $FLAC^{3D}$ model of uniaxial compressive strength test specimen for research into unstable failure.

4.3.3 UCS Test Results

The model platens were assigned elastic material properties with a Young's modulus of 1.5, 10, and 100 GPa. Platens with low elastic moduli should result in an unstable failure in the given loading condition. Platens with high elastic moduli should result in a stable failure. A "high" or "low" moduli is based on the steepest post-failure slope of the brittle coal specimen. From the detailed study of the specimen's material response, it was determined that the most brittle response of the coal specimen achieved a local post-peak modulus of approximately -11 GPa. Any Young's modulus less than 11 GPa for the platens should therefore result in an unstable failure. Under these conditions, the specimen should lose stability if its brittleness exceeds the loading system stiffness, but will then regain stability when it hardens under increased strains. These failures in which stability may be regained will be referred to as stable-unstable-stable failures.

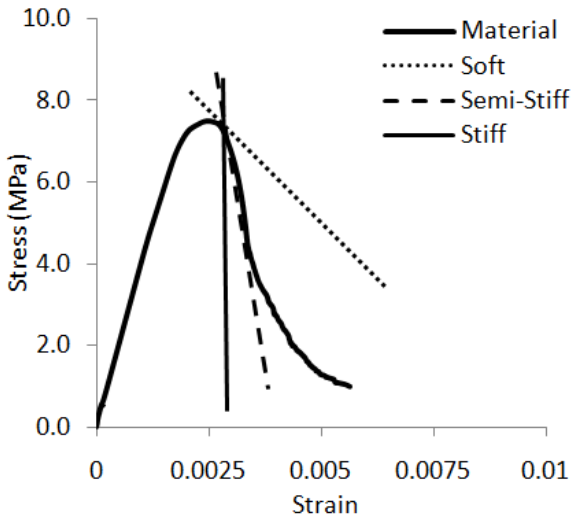

Figure 4.10: $FLAC^{3D}$ specimen response with superimposed load lines to represent 1.5 GPa (Soft), 10 GPa (Semi-Stiff), and 100 GPa (Stiff) platens.

Figure 4.12 and Figure 4.11 show the resulting stress-strain behaviors for specimen and for the system as were recorded during the 1.5, 10, and 100 GPa platen test cases. Stress was measured through a summation of unbalanced forces at the top and bottom of the system while axial strains were measured across the specimen and system, respectively.

According to instability theory, the strength of the specimen should be lost suddenly due to platen rebound while no added system displacements would be required to fail the specimen. The system stress-strain response would therefore appear as a vertical drop in stress. This expected system response was confirmed in $FLAC^{3D}$ for the system loaded under unstable 1.5 GPa platen conditions as is shown in Figure 4.11. The response of the specimen should then appear as a linear response identical to the platen elastic modulus during unstable unloading or rebound. This behavior was also confirmed in the specimen plot for the 1.5 GPa platen shown in Figure 4.12, while the specimen plot assumed a constant response between the comparatively stable tests of 10 and 100 GPa platens.

An additional test was conducted to further study the theoretically stable-unstable-stable case when a Young's modulus of 10 GPa was used for the platens. In this test the velocities at the model boundaries were set to very slow values, with pauses taking place between small

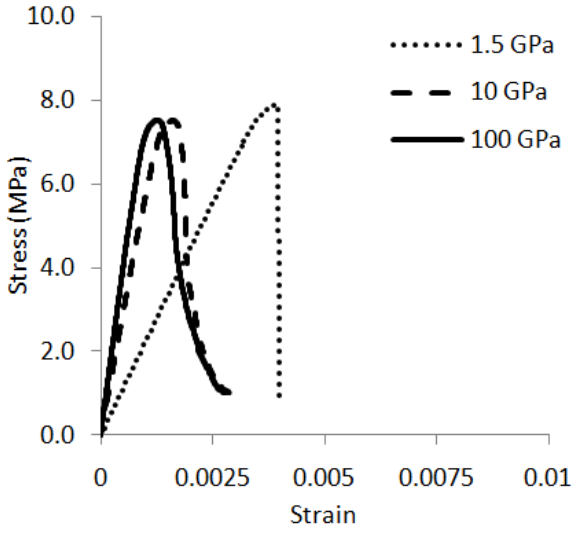

Figure 4.11: $FLAC^{3D}$ system stress-strain response for varying platen stiffnesses.

increments of total system strain. In this way it was possible to increase the load on the coal specimen in a controlled fashion and study the response of the specimen for indications of losses in stability. These individual loading steps may be observed in the incremental post-peak failure of the pillar shown in Figure 4.13. If an exceedingly small increment in system strain resulted in a large increase in specimen strain then it could be determined that stored strain energy in the platens was being converted to the unstable failure of the specimen.

4.3.4 Conclusions of Unstable UCS Tests

From the system and specimen stress-strain responses shown in Figure 4.12 and Figure 4.11 it can be seen that the brittle $FLAC^{3D}$ sample exhibited the behaviors expected from an unstable failure when a low elastic modulus of 1.5 GPa was used for the platens. In this test case the system stress-strain response was found to approach vertical as failure of the sample was propagated using strain energy stored within the system. No additional external loading was required to fully fail the specimen when unstable failure was first initiated. An equivalent effect was observed in the specimen stress-strain response during unstable failure which assumed the elastic behavior of the platen during unstable failure.

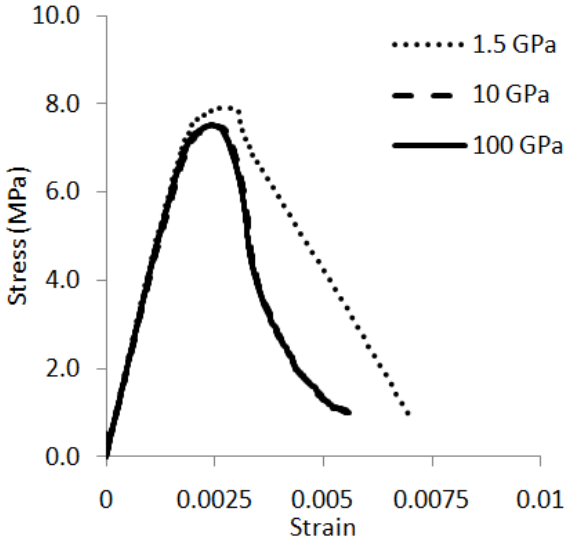

Figure 4.12: $FLAC^{3D}$ specimen stress-strain response for varying platen stiffnesses.

For the 100 GPa stable case, the post-peak slope of the system curve was found to remain non-vertical as the specimen was failed with the slow application of total system strain. The stress-strain response of the specimen in the stable case was found to assume a constant material response and remained unchanged from the calibrated response.

For the stable-unstable-stable failure case of 10 GPa platens the system curve was found to approach a vertical slope for a portion of the test. This relatively sudden loss of strength was an indication of unstable failure and additional pause tests were conducted to further explore this effect. The relative instability was found to occur between 5.3 and 4.4 MPa of the specimen's post-peak response and was exclusively a result of platen rebounding.

The combined results for the uniaxial compressive strength tests in $FLAC^{3D}$ showed that the explicit finite difference method was well suited for modeling brittle rock undergoing unstable, stable-unstable-stable, and stable type failure modes. The stress-strain response of the specimen and system were used to determine stability of the failure. Pause tests could be used for ambiguous cases of stability, such as stable-unstable-stable type failures, to determine the onset and duration of physical instability.

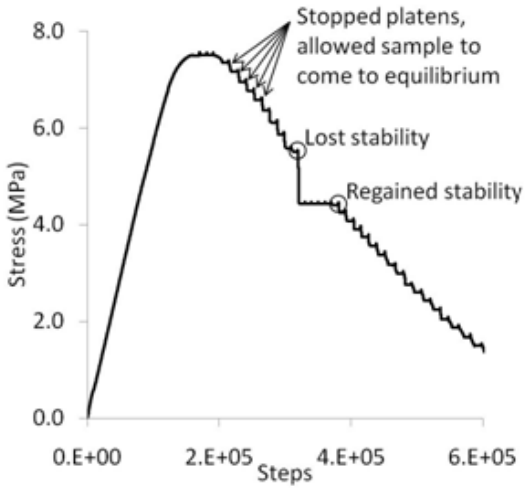

Figure 4.13: Stable-unstable-stable failure case of 10 GPa platens failing a specimen while using modified testing procedure with pauses during failure. The drop in strength corresponds to the duration of unstable failure in the $FLAC^{3D}$ model.

4.4 Triaixial Compressive Strength Tests in $FLAC^{3D}$

Failure was modeled in the $FLAC^{3D}$ UCS tests through an application of the Mohr-Coulomb strength criterion. An integral component of the Mohr-Coulomb model is the material strength's dependence on the confining stress state. This model is particularly well suited to account for the triaxial states of stress typically found in underground mining environments. Robust analyses of unstable failure must therefore take into account the effects of confining stresses on the ultimate strength and failure mode of rock.

A general analysis was conducted in $FLAC^{3D}$ on the failure mode and strength characteristics of a confined specimen failing under stable loading conditions. This analysis was then extended to include unstable loading conditions applied to the same specimens under varying levels of confinement. An assessment was made for the stability of each specimen using stress and strain measurements recorded during the tests.

4.4.1 Triaxial Test Procedure

A series of confined tests were conducted in $FLAC^{3D}$ on the brittle coal specimen calibrated for the previous UCS tests. Confining forces were applied onto the gridpoints across

the surface of the specimen to simulate radial confining pressures of 1, 2, 3, 4, 5, and 6 MPa. Small displacements of 6E-8 m/step were applied to the gridpoints at the top and bottom of the system until the resulting loads caused the specimen to fail. This loading procedure was continued until a specimen strain of 0.01 was achieved.

A local damping scheme was applied to the tests with a default damping of 0.8 on unbalanced forces at gridpoints. Additional damping was applied through a mass scaling technique applied to the gridpoints. These measures were installed to promote quasi-static solutions during the timestepping process.

For each level of confinement the specimen was caused to fail under both stable and unstable loading conditions. A high Young's modulus of 100 GPa was used for the platens to fail the specimen in a stable manner. Unstable failures were initiated using a low Young's modulus of 2 GPa for the platens during an identical series of tests. The behaviors of the brittle Mohr-Coulomb strain-softening model were then compared against a perfectly plastic Mohr-Coulomb model with a similar peak strength of 7.6 MPa and a friction angle of 30°. The inputs of the MCSS model matched those of the UCS test while the values for the Mohr-Coulomb specimens are shown below in Table 4.2.

Table 4.2: Input parameters of Mohr-Coulomb (plastic) $FLAC^{3D}$ coal specimen.

Model Inputs			
Density	1313 $\frac{kg}{m^3}$	System loading velocity	1e-7 $\frac{m}{s}$
Young's Modulus	4 GPa	Vertical gridpoint spacing	0.2 m
Poisson ratio	0.2	Radial gridpoint spacing	0.1 m
Cohesion	2.15 MPa	Specimen height	2 m
Friction angle	30°	System diameter	1 m
Dilation angle	5°	Total system height	4 m
Local damping	0.8		

4.4.2 Results of Triaxial Tests

The stress-strain results of the confined tests using $FLAC^{3D}$ are shown in Figure 4.14 with stable and unstable results marked accordingly.

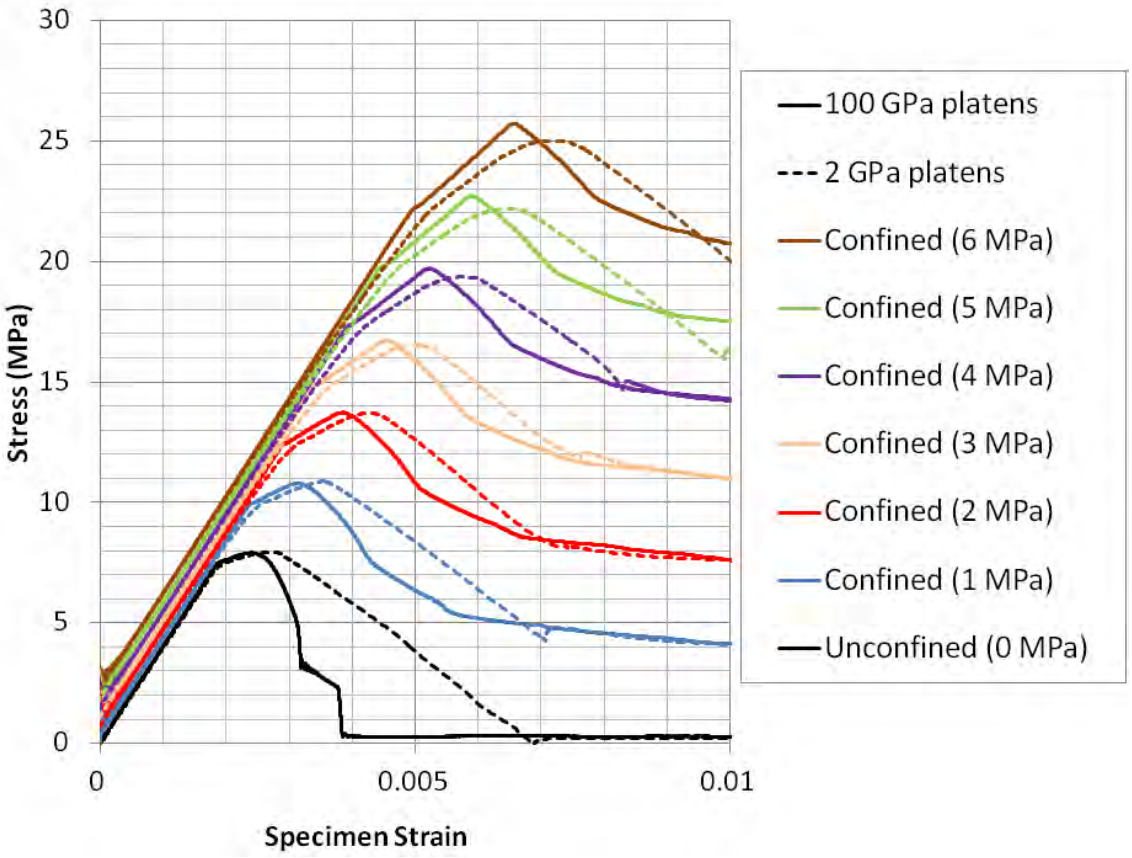

Figure 4.14: Stress-strain responses of triaxially confined brittle coal specimens undergoing failure under unstable (2 GPa) and stable (100 GPa) platen loading conditions.

It was found that the specimen assumed a cohesion of 2.3 MPa and a friction angle of 30° during the triaxial compressive strength tests. This behavior had been initially defined through the friction angle table (see Figure 4.8), yet was confirmed in these results. The specimen was found to assume a brittle yet hardening stress-strain behavior for increasing levels of confinement under stable loading. The post-peak slope assumed the stiffness of the soft 2 GPa platens for the unstable failure cases until a residual strength was reached. Due to the regaining of stability, the 2 GPa platens induced stable-unstable-stable type failures. The residual strength of the specimen was identical between stable and unstable failure tests. Note that each unstable test was readily distinguishable from its respective stable test through a review of stress-strain behavior with slow applications of load onto the system.

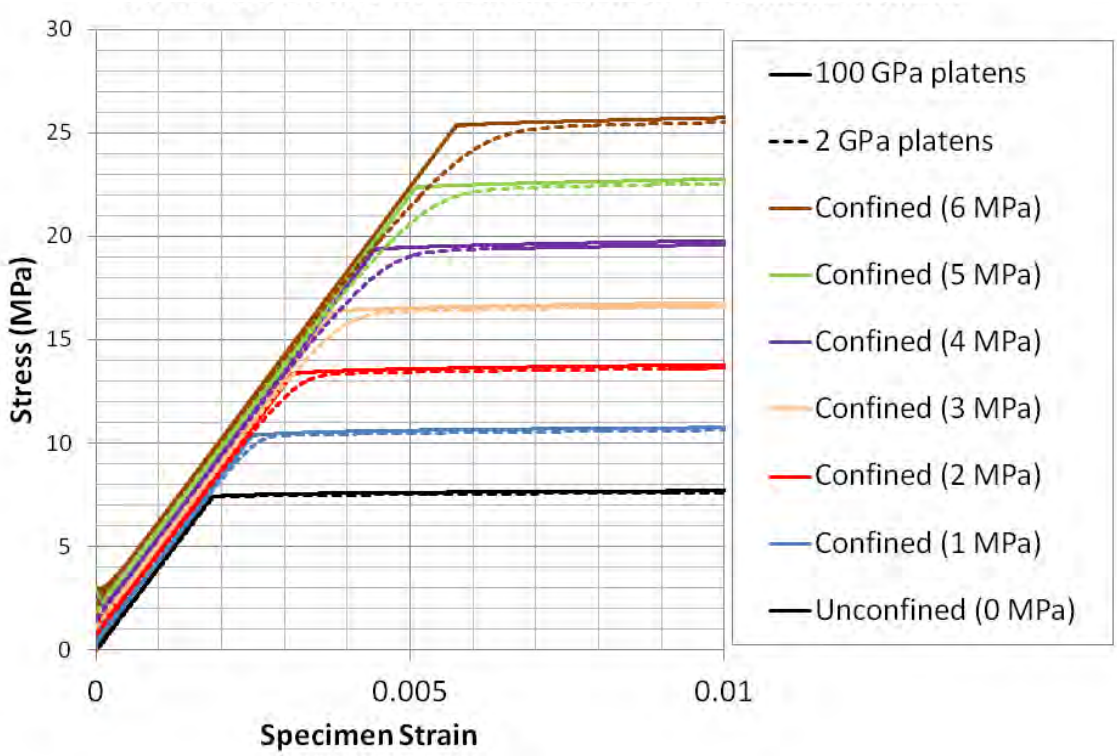

Figure 4.15: Stress-strain responses of triaxial compressive strength tests on plastic Mohr-Coulomb specimens under 2 GPa and 100 GPa platen loading conditions.

The results from the second series of triaxial compressive strength tests using plastic Mohr-Coulomb behavior for the specimen are shown in Figure 4.15. Some pre-peak failure was observed for the specimen when a Young's modulus of 2 GPa was used for the specimens. This behavior was thought to be caused by a slight reduction in confinement at the contact between the specimen and platen when greater radial strains were observed within the softer platen. Aside from the small deviation in strain at which the specimen reached peak strength, the Mohr-Coulomb constitutive model behaved as expected during the triaxial compressive strength tests while representing a perpetually stable specimen.

4.5 Dynamic Loading Effects on Model Response

An area of particular interest for simulating unstable failure which has not yet been discussed is the effect of dynamic loading on the finite difference model response. The explicit formulation of $FLAC^{3D}$ attempts to damp any large unbalanced forces which may

develop as a result of physical instabilities through both local and mass scaling methods as an approach to return the model to a quasi-static state. Unforeseen numerical effects may thereby result from the application of damping or due to the inherent construction of the calculation scheme.

The UCS test conditions for unstable loading were again applied in a repeated series of tests to record a more detailed response of the mode stress states across the principal loading direction. Elastic platens of 2 GPa were used to fail the specimen in a rapid and unstable manner. The increased spatial resolution of the stress-strain measurements allowed for the study of the localized dynamic response through discrete disc-shaped segments of the cylindrical coal specimen. The stress measurement of the specimen was divided along its principal axis at 0.2 m, or one-zone, increments. Stress measurements were therefore recorded for the specimen within 10 individual discs. Each discretized measurement volume was labeled from 11 to 20 in the manner shown in Figure 4.16.

The corresponding stress results for each segment are shown in Figure 4.17 with stress displayed as a function of the total axial strain of the specimen. The figure also includes results from the platen stresses (label '50') to compare this measurement technique with the previous method for determining the specimen response.

The averaged specimen were averaged for a stable UCS test with a quasi-static solution against the resulting specimen behavior under unstable and highly dynamic loading conditions. The results from these tests are shown in Figure 4.18 with a significant increase in internal stress measurements during unstable/dynamic loading.

These results showed a clear deviation of the specimen behavior from the observed quasi-static response. Dynamic loading from the platens increased the unbalanced forces acting at the gridpoints and therefore the strains and resulting stress increments. The model response was subsequently hardened as a result of dynamic loading from the elastic platens. Although this effect is an unintended consequence of the explicit solution scheme, the increased strength properties on dynamic loading reflect to some degree the strengthening observed during

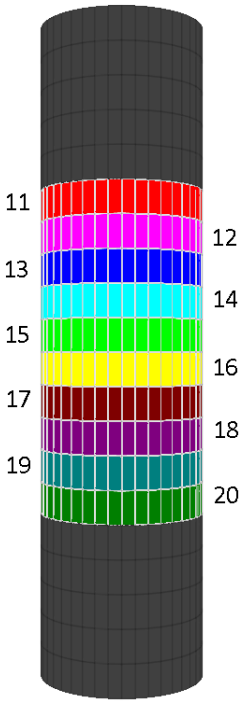

Figure 4.16: Labels applied to vertical stress measurement sections of the model which correspond with the numbering of plot Figure 4.17.

dynamic laboratory tests [60, 108, 110, 131]. This correlation should not be considered too deeply since the deviation from stable behavior is purely an effect of the numerical construction, however the effect provides a convenient extension of rock mechanics theory onto the numerical model.

4.6 Discussion of Finite Difference Method for Simulating Unstable Compression Failure in Rock

The calculation method which was incorporated in $FLAC^{3D}$ proved useful for simulating unstable failure in a continuum. Many aspects of brittle material failure were realistically modeled within the continuum. Unbalanced force initiated by unstable elastic rebound were effectively transferred to rapid plastic deformations of the Mohr-Coulomb strain-softening specimen in both uniaxial and triaxial confinement conditions. An approximate solution for the states of stress and strain were found during unstable failure calculations. Some

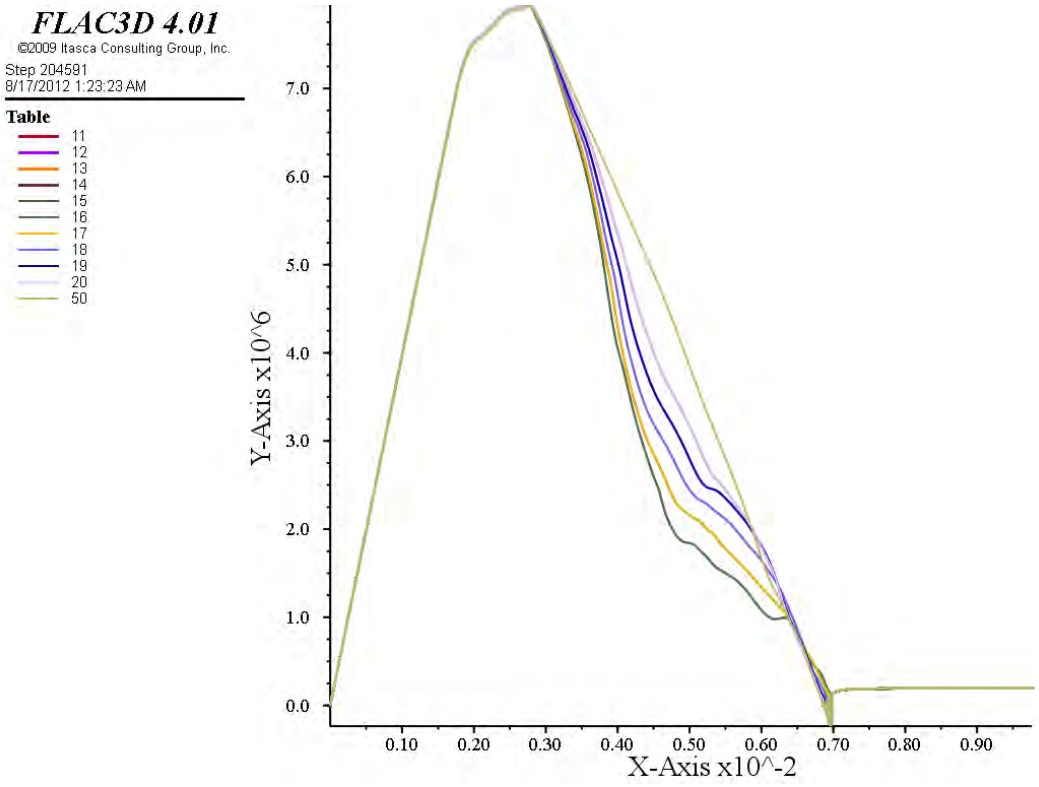

Figure 4.17: Specimen stress vs. strain plot with detailed assessment of stress in principal loading direction for unstable UCS test.

additional information could be extracted from these models regarding the dynamic motion of the model which provided a qualitative assessment of the relative speed of motion of gridpoints during failure.

The equations of motion applied in $FLAC^{3D}$ take a continuum form of a second order approximation to Newton's second law. Error is introduced into these calculations in the presence of rapid changes to accelerations which are typically assumed to be negligible in quasi-static solutions. Unstable loading conditions in rock may lead to large jerks applied to accelerations which would not be reflected in the models. The relevance of these errors would rely on the magnitude of changes to unbalanced forces as a function of time.

Special care should be taken when applying the MCSS model within $FLAC^{3D}$. Strain localization is shown to occur as element size is reduced. Problems evoked by strain localization cause great consternation when applying a strain-softening model, yet follow trends

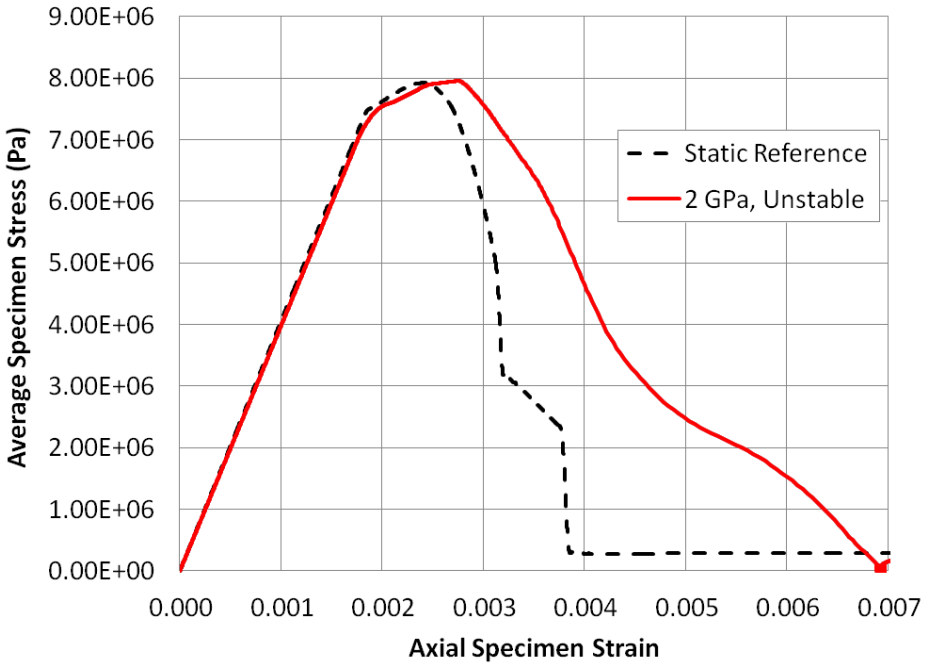

Figure 4.18: The internally measured specimen stress strain response in static vs. unstable (2 GPa) UCS tests.

witnessed in nature in that the widths of shear bands reduce in response to smaller grain sizes. An approach which accounts for the total energy consumed during failure may be used to assess the appropriateness of a zone size selection. This method may be extended to calculate the plastic energy consumed by affected volumes of plastically deformed rock. The response of the rockmass may therefore be analyzed against desired values of energy consumption during failure and for total affected volume of failed rock. Such precautions enable more reasonable approximations of the evolution of failure and provide quantitatively viable results for elastic and plastic energies.

Concluding remarks:

- $FLAC^{3D}$ was shown to provide a realistic approximation to physical instability through an explicit formulation through uniaxial and triaxial compressive strength tests.
- The continuum nature of the software is conducive for larger and more complex mining geometries.

- The Mohr-Coulomb strain-softening model may be applied directly to represent brittle behavior, however care should be made when selecting zone size in order to better approximate the localization of failure.

- The failure of a brittle material is path dependent, both in nature and in a MCSS representation; with this understanding it is possible to gain significant insight into the onset and development of failure in stable and unstable conditions.

- Errors may be introduced into these calculations through the quasi-static formulation and a quantitative assessment of the dynamic response of the model should not be made.

- The results of the UCS and triaxial confinement strength tests showed clear delineation between stable and unstable failure responses which adhered well to theoretical determinations of rock response to unstable equilibrium.

CHAPTER 5

IDENTIFIERS OF UNSTABLE FAILURE IN FINITE DIFFERENCE MODELS

Continuum and discrete explicit numerical methods have been shown to simulate the onset of unstable failure conditions in rock and have presented some estimation of the post-failure behavior of a brittle specimen. These numerical tools may be applied to analyze unstable failure conditions in both uniaxial and triaxial compression. With additional development these methods may be extended to study unstable failures in the context of realistic mining geometries and complex loading conditions.

The initiation of unstable failure was identified within the tests run in previous chapters by recording specimen stress-strain behavior and highlighting any deviations from idealized behavior. The investigative methods used to identify unstable failure were limited in the sense that an analysis could only be conducted along a single direction of loading and upon a pre-defined volume of the model. These limitations did not hinder an analysis of uniaxial or triaxial compressive strength tests due to a strongly dominant principal loading direction and clearly defined volumes of unstable rock (i.e., the specimen). However, an examination which relies solely on stress and strain is prohibitive for studies of unstable failure in the more complex model geometries and loading conditions found in typical mine models.

Several approaches have been taken by researchers to definitively identify unstable failure conditions in realistic mine models. One method is to apply small probing forces at every point in the model at every state of loading [107]. If a probing force results in a greater magnitude of energy released from the system than what was added in boundary work due to the probe, then the system is unstable in that direction of loading [104]. Finite element, finite difference, and boundary element simulations have been conducted in which a probing force is applied onto every point during every stage of mining while recording the resulting deformations of the system [1, 17]. A similar method was applied to $FLAC^{3D}$ in Chapter 4

in which a nominal strain was added to the system in a so-called "pause" test; if the strain increment led to large displacements and work performed on the specimen then the system was determined to be unstable. Such exhaustive approaches are difficult to put into practice and are typically infeasible to perform on any but the most simple of model geometries.

Less stringent yet more readily available methods may be available with which to study instability in complex rock models. Rather than directly identifying unstable failure conditions, it may be possible to analyze the secondary effects of instability as an informal indication of unstable failure. Explicit methods are practically suited for such a task in the sense that the dynamic effects which result from unstable failure are calculated at explicit timesteps throughout the simulation. Within the explicit finite difference software $FLAC^{3D}$, any instability will result in accelerations of the gridpoints which are analogous to Newton's second law of motion [57]. 5.1 demonstrates this concept in the simplified uniaxial compressive strength case shown in Figure 5.1 where F is the unbalanced force at point O due to a difference between the force applied by the spring and the force resisted by the rock.

$$F = F_S + F_R = m \cdot a \tag{5.1}$$

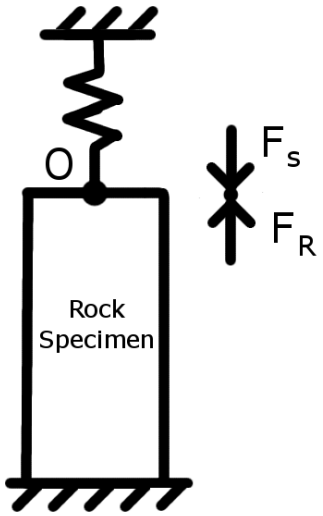

Figure 5.1: Representation of unbalanced force equilibrium which may develop at point O in uniaxial compression case.

Unbalanced forces resulting from unstable failure conditions will lead to accelerated motion within the models and to a general deviation from quasi-static behavior. This process takes a more complicated form in $FLAC^{3D}$ through the calculation steps outlined in Chapter 4. The formulations still approximate this Newtonian model within the continuum field and lead to increased accelerations at the onset of instability. The largest accelerations of point O will therefore correspond to the largest magnitudes of unbalanced forces, $max(F)$. Velocities continue to increase through the unstable failure if no viscous damping forces are applied to the system. Localized assessments of unstable failure conditions may be developed from these records of dynamic motion within the numerical simulation. Measurements applied at the gridpoints and particles could therefore provide valuable information on the location, duration, and magnitude of unstable failure. Additional measurements may then be applied to the zones within the continuum model as a means of incorporating the smallest volume of failable material in the studies. Effective identifiers for studying unstable failure in explicit models would focus on unbalanced forces, accelerations, and velocities within a simulated brittle failing rock.

5.1 FDM Identifiers of Instability in UCS Tests

Indicators of instability which are derived from explicit dynamic behaviors may be developed to identify the onset of unstable failure conditions, track the loss of stability, and determine relative magnitudes of energy released during simulated unstable failures. An exploration was made into the potential identifiers to be employed, and a series of tests was performed to determine the applicability of these methods. The basis for the explicit, time-dependent instability identifiers is derived from the concept that an initial unbalanced force which acts at a gridpoint under unstable equilibrium causes point O to move with a certain acceleration based on the point's apparent mass. If the instability criterion shown in 2.12 is met at any point during the simulation, then an unstable equilibrium will be initiated.

A series of uniaxial compression strength tests were conducted on stable and unstable platen-specimen-platen systems while recording potentially valuable dynamic indicators of

unstable failure. The $FLAC^{3D}$ specimen which was calibrated in Chapter 4 using a Mohr-Coulomb strain-softening model was again used within these tests. Specific identifiers which were measured were unbalanced forces, accelerations, velocities, and shear strain rates. The absolute magnitudes of these values did not reflect any physically realistic results due to the quasi-static nature of the calculations. The recorded identifier magnitudes could, however, be compared between known stable and known unstable tests on the system. In this way a qualitative assessment could be derived from an observed range of dynamic responses.

5.1.1 Testing Procedure

A simulated cylindrical rock specimen sized 1 m in diameter and 2 m in height was tested between two elastic platens each measuring 1 m in height. The combined system of platens and specimen is shown in Figure 5.2.

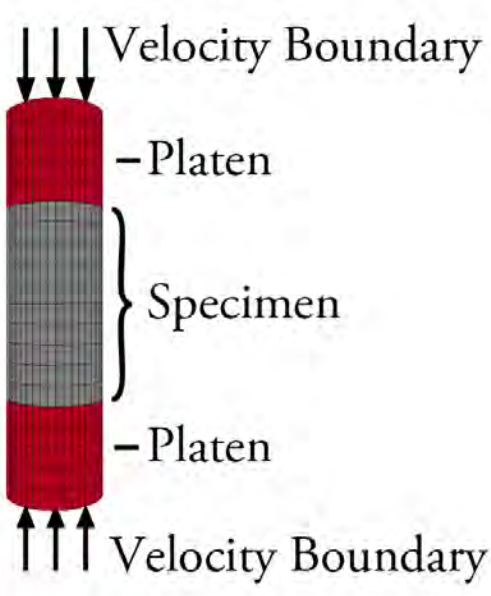

Figure 5.2: Uniaxial compressive strength test configuration in $FLAC^{3D}$ model.

The specimen was calibrated to generally represent coal using the Mohr-Coulomb strain-hardening/-softening (MCSS) constitutive law. The values provided from Chapter 4 were again used to define cohesion, friction angle, and dilation angle as functions of plastic strain.

A finite difference mesh identical to that found in the preliminary study was used for these continued tests. The specimen was calibrated to exhibit a peak strength of 7.9 MPa and a Young's modulus of 4.1 GPa. The specimen assumed a brittle failure response with a maximum post-peak drop of approximately -11 GPa.

The elastic modulus of the platens was controlled between tests and spanned the range of 2 to 100 GPa. According to the post peak response of the specimen, any platen with a stiffness greater than the maximum post-peak drop of -11 GPa should result in an unstable failure. The instability identifiers which were recorded consisted of unbalanced forces, accelerations, and velocities at the gridpoints, and shear strain rates of each zone. The maximum value of each identifier was recorded for all gridpoints and zones within the coal specimen using the FISH commands 'gp_extra' and 'z_extra', respectively. The specimen strain at which each maximum was recorded was also stored so as to provide a context for when these values were measured during the simulations. At the end of the analysis these values were then analyzed against the magnitude of relative instability present during each test due to elastic rebounding conditions for the platens.

The model was run in static solution mode with masses scaled artificially at the gridpoints. The ideal method for analyzing dynamic failure would be through a truly dynamic analysis, however uncertainties in the calibration of such a model and the length of time required to compute a dynamic solution made the static mode a more favorable option. The drawback of the static solution mode is that any measurements which are dependent on time hold little physical significance. Insight may still be gained by comparing a known stable failure case against an unknown, potentially unstable failure case. In this manner a measure of *relative* instability may be established.

A velocity boundary with a small rate of 6e-8 m/step was applied at the end of the platens to apply an increasing load onto the system until a specimen strain of 0.003 was achieved. At this point, the simulation was run for an additional 1000 steps and the system was allowed to come to static equilibrium. A second series of identical uniaxial compressive strength tests

was then run in which the coal specimen was modeled using a plastic Mohr-Coulomb (MC) constitutive law. These tests provided information on how loading system stiffness may directly affect the selected identifiers within the finite difference calculations. The specimen was calibrated with a cohesion of 2.15 MPa, dilation angle of 5 degrees, and friction angle of 30 degrees to undergo plastic flow at 7.9 MPa, or at a peak strength comparable to the Mohr-Coulomb strain-softening (MCSS) model which was calibrated in Section 4.3. The stable stress-strain response for the MCSS model is re-plotted as reference in Figure 5.3 along with the Mohr-Coulomb (MC) plastic model response as a comparison.

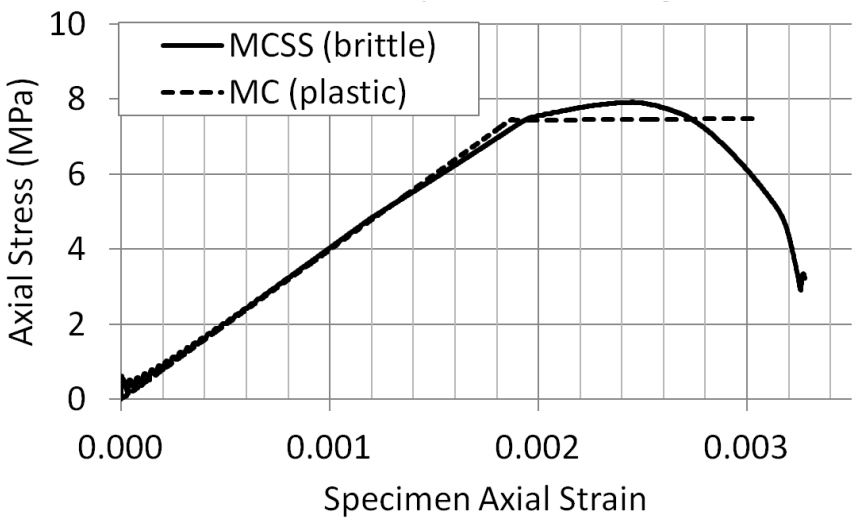

Figure 5.3: UCS specimen stress-strain response of Mohr-Coulomb Strain-Hardening/-Softening (MCSS) and Mohr-Coulomb (MC) models.

Axial stresses were calculated during the test from the sum of unbalanced forces applied at the boundaries divided by the cross-sectional area of the specimen. Strains were then recorded from the displacements at the specimen-platen contacts and from total displacements at the top and bottom of the system. The stress-strain responses of the specimens and loading systems were recorded from these values.

5.1.2 Identifier Results of UCS Tests

During the unstable uniaxial compressive strength tests, it was observed that the specimen failed along a linear stress-strain path which tracked the elastic modulus of the platens following the onset of unstable failure. These results are shown in Figure 5.4 in which the stress-strain behavior of the specimen was found to deviate from idealized behavior for any platen Young's modulus less than approximately 10 GPa.

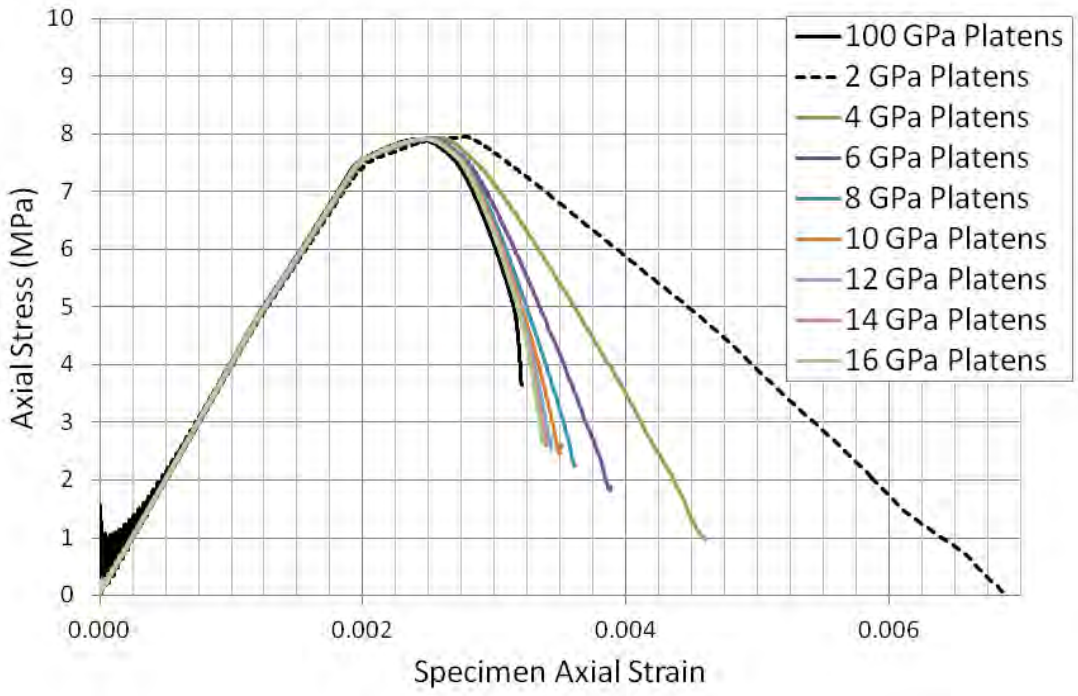

Figure 5.4: Stress-strain behavior of specimen showing rebound along elastic modulus of platens for unstable tests.

For systems with platen Young's moduli greater than approximately 10 GPa, the post-peak stress-strain response of the specimen was consistent between UCS tests. However, for lower elastic platen moduli, unstable failure conditions were initiated and large unbalanced forces resulted from the difference in stress applied by the rebounding platens and the remaining strength of the specimen. This is demonstrated for the stable 40 GPa and unstable 2 GPa loading cases shown in the first plot of Figure 5.5. The specimen in the unstable

failure case assumed a -2 GPa post-peak stress-strain response which was identical to the elastic modulus of the loading system. The second plot of Figure 5.5 compares the response of the maximum unbalanced force between the unstable and stable loading conditions. The onset of unstable loading conditions led to a dramatic increase in the maximum unbalanced force acting within the model.

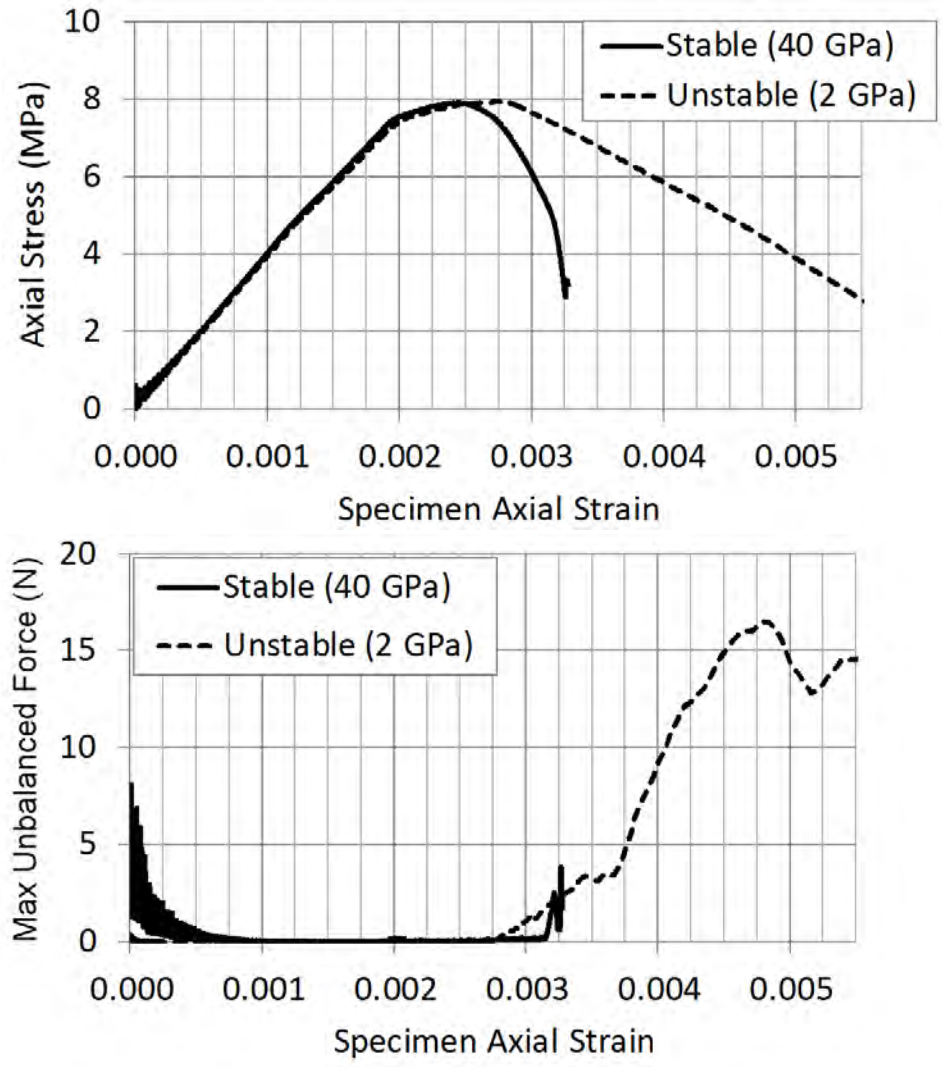

Figure 5.5: Stress vs. strain of Mohr-Coulomb strain-softening specimen during stable (40 GPa platens) and unstable (2 GPa platens) failures with corresponding histories of maximum unbalanced forces.

Low platen stiffnesses such as the 2 GPa case elicited an unstable failure response in the specimen as indicated by the stress-strain response and by the maximum unbalanced

force in the specimen. These unbalanced forces were carried through the model to cause large accelerations, velocities, and shear strain rates during unstable failure conditions. The maximum unbalanced force was large for high platen stiffnesses during initial loading due to the rapid application of forces on the specimen from a more stiff loading system. Identifier values were recorded only after the vertical specimen strain reached 0.001 in order to avoid recording the dynamic effects from the initial load application process.

The maximum values for the previously selected indicators were compared between the MC and the MCSS test cases to attempt to further isolate the unstable failure phenomenon from dynamic effects caused exclusively by changes to the loading system stiffness. The results from these tests are shown in semi-log plots in Figure 5.6 through Figure 5.9.

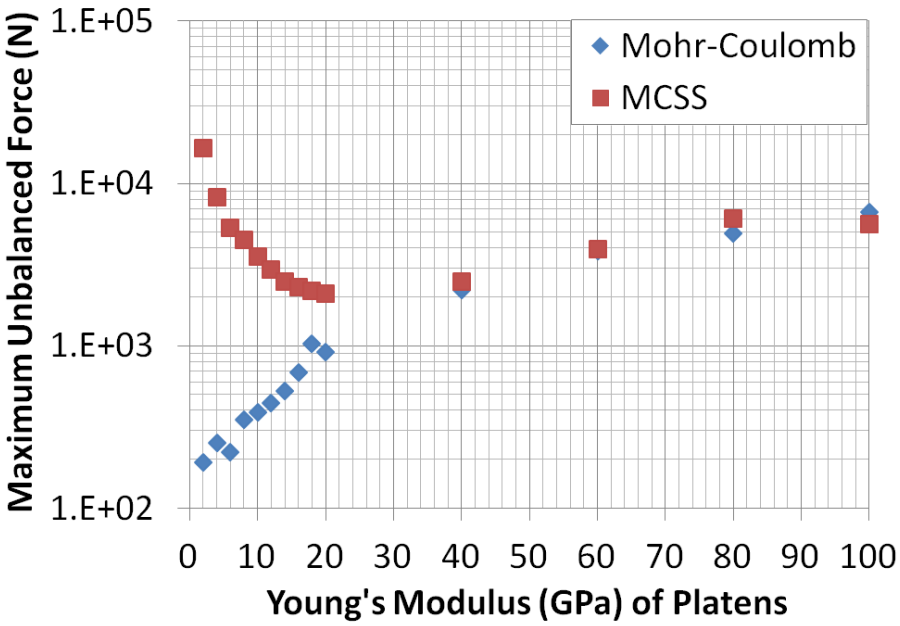

Figure 5.6: Maximum gridpoint unbalanced force (N) within specimen over a range of platen stiffnesses for both plastic Mohr-Coulomb and brittle Mohr-Coulomb strain-softening models.

Note that the behavior of the indicators diverge between the MCSS and the MC cases with platen stiffnesses less than approximately 10 GPa. This change in behavior corresponded well with other measures of unstable failure and the previously assumed initiation of unstable failure for platens softer than the steepest portion of the specimen's stress strain response,

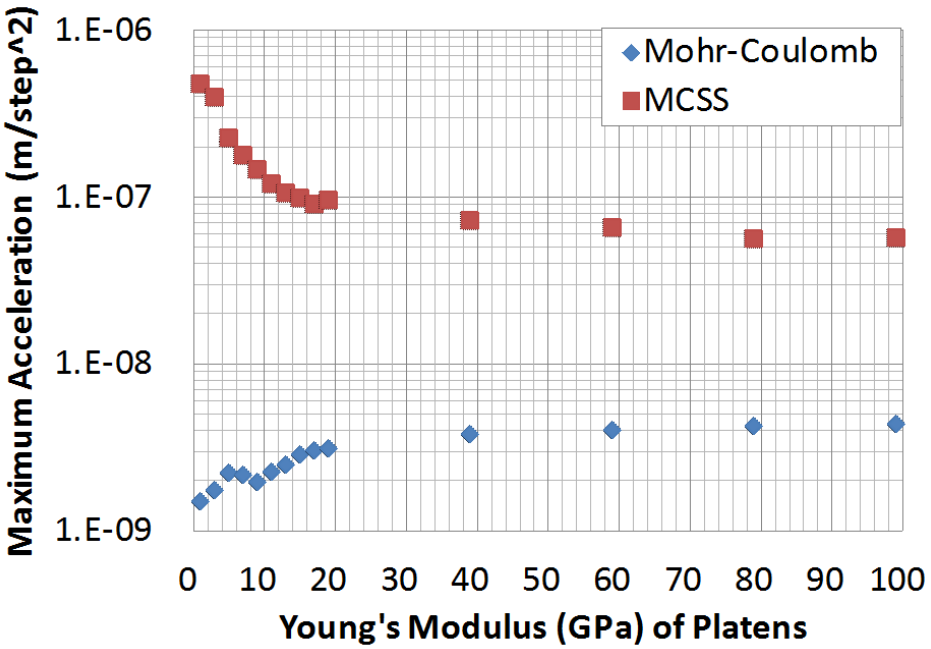

Figure 5.7: Maximum gridpoint accelerations (m/step^2) within specimen over range of platen stiffnesses for plastic Mohr-Coulomb and brittle Mohr-Coulomb strain-softening models.

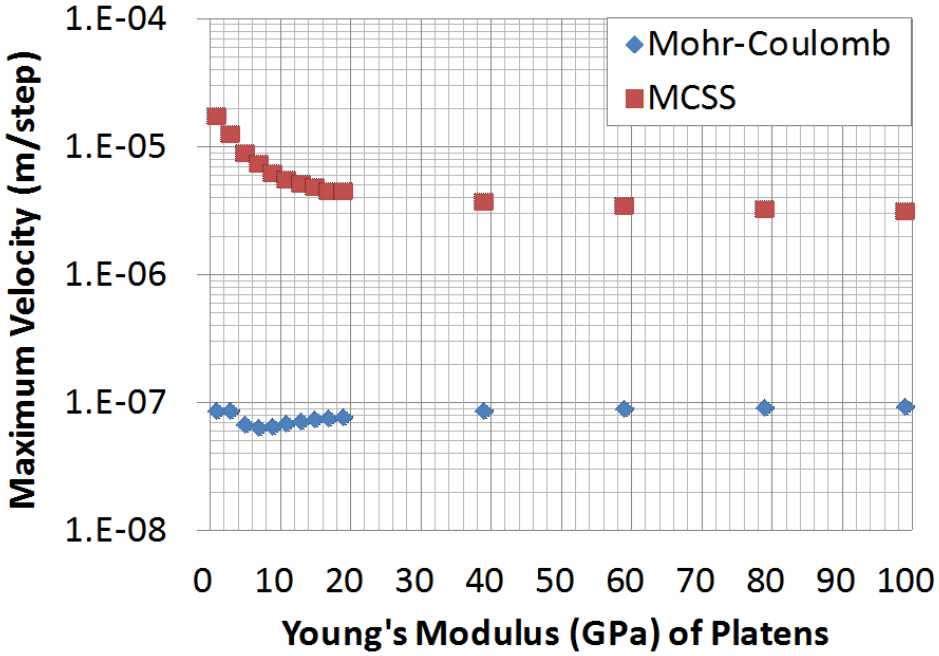

Figure 5.8: Maximum gridpoint velocity (m/step) within specimen over range of platen stiffnesses for plastic Mohr-Coulomb and brittle Mohr-Coulomb strain-softening models.

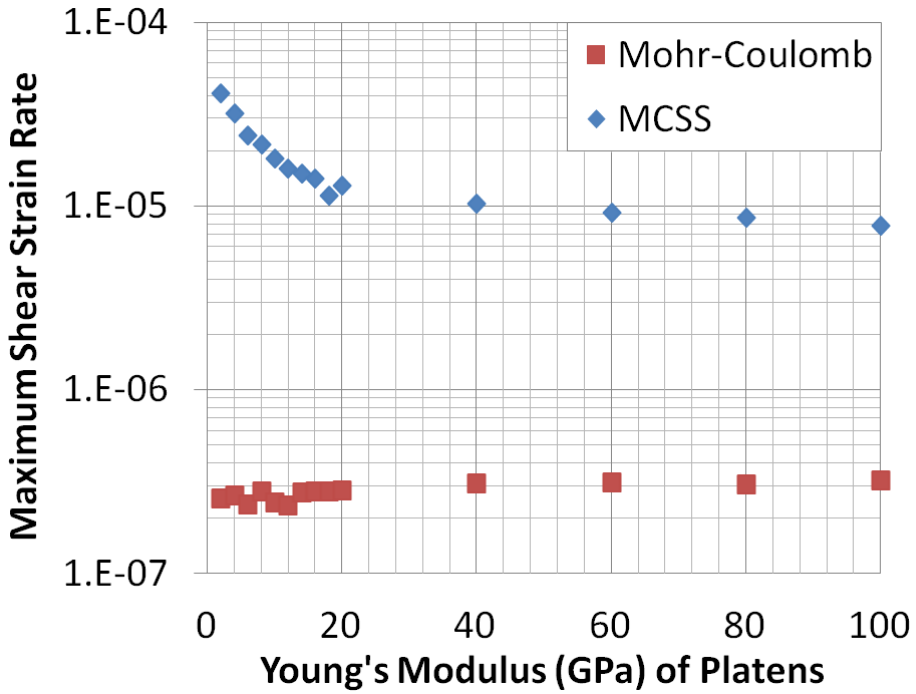

Figure 5.9: Maximum zone shear strain rate (step^{-1}) within specimen over range of platen stiffnesses for plastic Mohr-Coulomb and brittle Mohr-Coulomb strain-softening models.

which was approximately -11 GPa.

The results of the maximum shear strain rates were further split into a histogram covering the range of both 100 GPa and 2 GPa platen tests, shown as Figure 5.10. The histogram was split into 100 bins, with each bin representing an equal portion of the full range of values. The zones with maximum shear strain rates corresponding to each bin were tallied for either test. The maximum shear strain rates for the 100 GPa platen test and the 2 GPa platen test were 7.8e-6 and 4.1e-5, respectively, with these records marked accordingly in the figure.

Further insight was gained on the failure process by analyzing localized volumes of instability as determined by the gridpoint and zone identifiers. Each identifier was studied individually during the tests to determine the magnitude, location, and point in time at which physical instability was exhibited within the unstable coal specimens. Figure 5.11 shows a contour of the maximum unbalanced forces located at the gridpoints within the specimen during an unstable uniaxial compressive strength test using 2 GPa platens. The

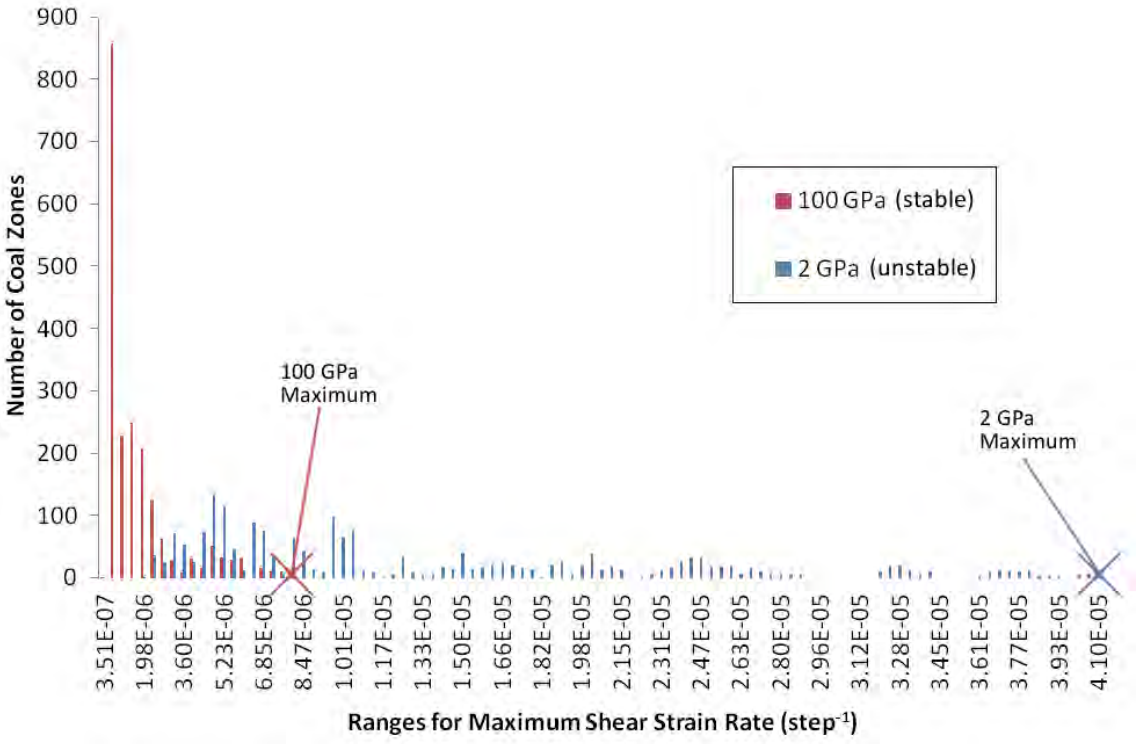

Figure 5.10: Histogram of maximum zone shear strain rate ($step^{-1}$) within specimen for 2 and 100 GPa platen tests of a brittle Mohr-Coulomb strain-softening model.

results have been filtered to exclude any unbalanced force which fell below the maximum unbalanced force recorded during the stable 100 GPa platen case. The specimen was found to undergo the largest unbalanced force at its core. Due to the mass scaling effects in the model, the gridpoints along the center of the specimen had the highest applied mass. These large unbalanced forces were therefore converted into large accelerations and velocities towards the least confined and lowest gridpoint masses at the perimeter of the specimen.

These large unbalanced forces were found to translate into large accelerations and velocities at the free boundary of the specimen. The lack of confinement at these locations propagated the dynamic effects of the unstable failure so that maximum accelerations and velocities were propagated along a ring around the outside perimeter at the center of the specimen. Figure 5.12 and Figure 5.13 show these results for the unstable UCS test which have been filtered to only include identifier values in excess to the maximum value recorded

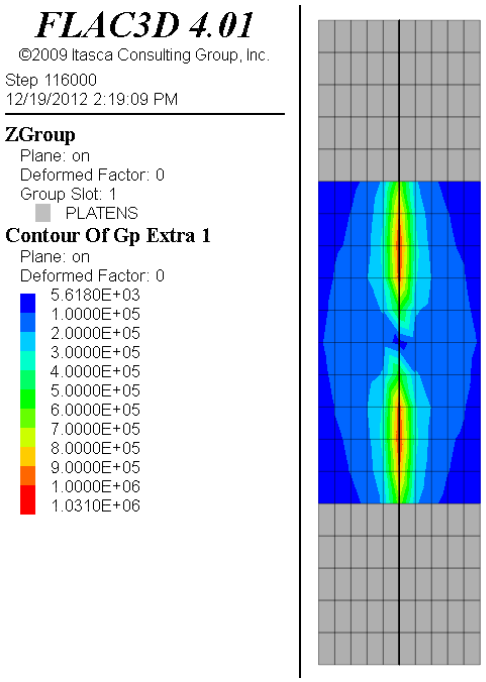

Figure 5.11: Maximum unbalanced forces (N) from 2 GPa UCS test that were in excess of stable unbalanced forces from 100 GPa test.

for the stable 100 GPa UCS test.

Shear strain rates were also analyzed as a method to assess the non-associated plastic flow rule which was applied to the Mohr-Coulomb strain-softening constitutive model. In this way the speed of deformation of the zones was calculated through combined elastic and plastic shear. The results of the shear strain rates during unstable uniaxial compressive failure case are shown in Figure 5.14 and have been filtered to only include values in excess to those recorded for the stable UCS test.

By analyzing the records of maximum shear strain rates for the zones it was possible to extrapolate the areas of the coal specimen which were most affected by instability during the unstable loading case. Rapid shear strains were observed across the horizontal centerline of the model where the largest plastic deformations were also observed. The unconfined zones at the sides of the specimen were found to fail in the most sudden and dynamic fashion during the tests.

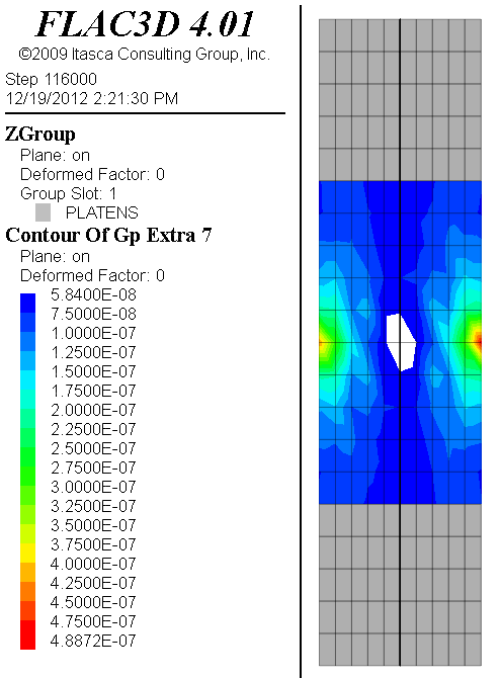

Figure 5.12: Maximum accelerations (m/step^2) from 2 GPa UCS test which were in excess of stable accelerations from 100 GPa test.

5.1.3 Conclusions on Unstable Failure Identifiers in UCS Tests

A series of uniaxial compressive strength tests were conducted in $FLAC^{3D}$ in which a brittle rock specimen was failed under a range of stable and unstable loading conditions. Several indicators of dynamic motion were recorded through the tests to better understand the dynamic behavior resulting from instability in the models. It was found that large magnitudes of unbalanced forces, accelerations, velocities, and shear strain rates were recorded within the specimens undergoing unstable failure as compared to the specimens failing under stable loading conditions. The maximum magnitudes of these indicators of instability were further shown to increase according to the relative magnitude of instability which was present during the tests. The dynamic measurements were further used to identify the localized volumes of the model which were most affected by instability.

The instability identifiers which have been proposed were shown to distinguish a stable from an unstable failure in the modeled specimen. The method was applied in a straight-

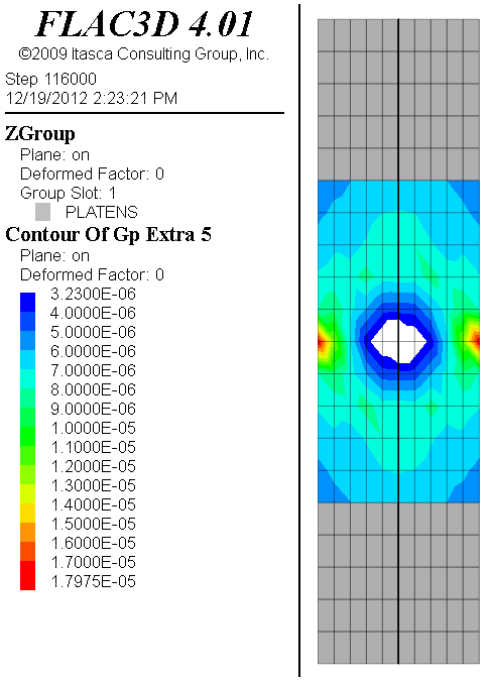

Figure 5.13: Maximum velocities (m/step) from 2 GPa UCS test which were in excess of stable velocities from 100 GPa test.

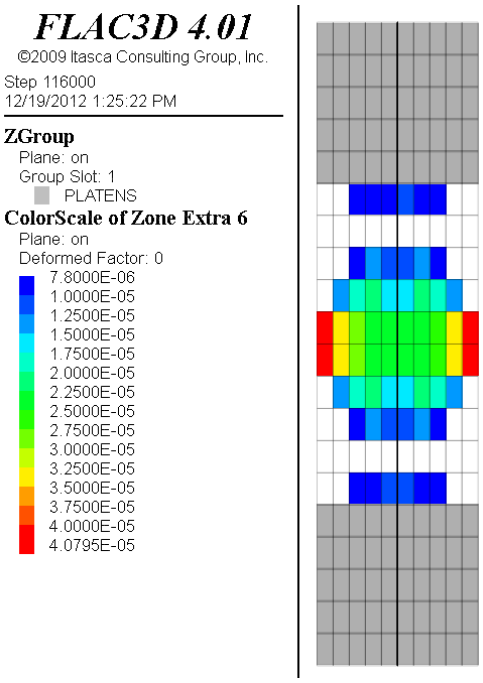

Figure 5.14: Maximum shear strain rates (step^{-1}) from 2 GPa UCS tests which were in excess of maximum stable shear strain rate from 100 GPa test.

forward manner for the uniaxial compressive strength case, however certain difficulties did arise. Steps were taken to reduce the dynamic effects of the initial load installation procedure for the system. Small increments of displacements were used to increase load to reduce potential dynamic loading effects. For extremely stiff platen systems it was additionally necessary to filter extraneous dynamic effects from the initial loading stage. The mass scaling procedure which was applied at the gridpoints to promote a more damped system also resulted in physically meaningless magnitudes for time-dependent processes in the models. To derive meaning from the dynamic motion of the model it was therefore necessary to relate the magnitudes of motion back to a known stable failure case. If more rapid motion was observed during a test than the known stable case, then this would be a good indication that some form of instability arose in the model due to unstable loading conditions.

5.2 FDM Identifiers of Instability in Triaxial Compressive Strength Tests

The triaxial compression strength tests which were conducted in Chapter 4 were repeated while recording potential identifiers of unstable failure. The primary role of these tests was to elucidate the role of an applied confinement boundary condition on the effects of dynamic behavior within an explicit finite difference model. The stress-strain response of the specimen is shown in Figure 5.15 for confining pressures ranging from 0 to 6 MPa.

A second series of tests was also repeated while using the plastic Mohr-Coulomb constitutive model to represent a perfectly stable specimen response. The stress-strain histories from these tests are shown in Figure 5.16.

5.2.1 Identifier Results of Triaxial Tests

The identifiers of unstable failure which were previously developed under uniaxial loading conditions were extended to triaxial compressive strength tests. These included the maximum unbalanced forces, accelerations, velocities, and shear strain rates. Identifiers were recorded for the specimen and the results from the tests are shown in Figure 5.17 through Figure 5.20. The results of plastic Mohr-Coulomb specimens failing during identical tests

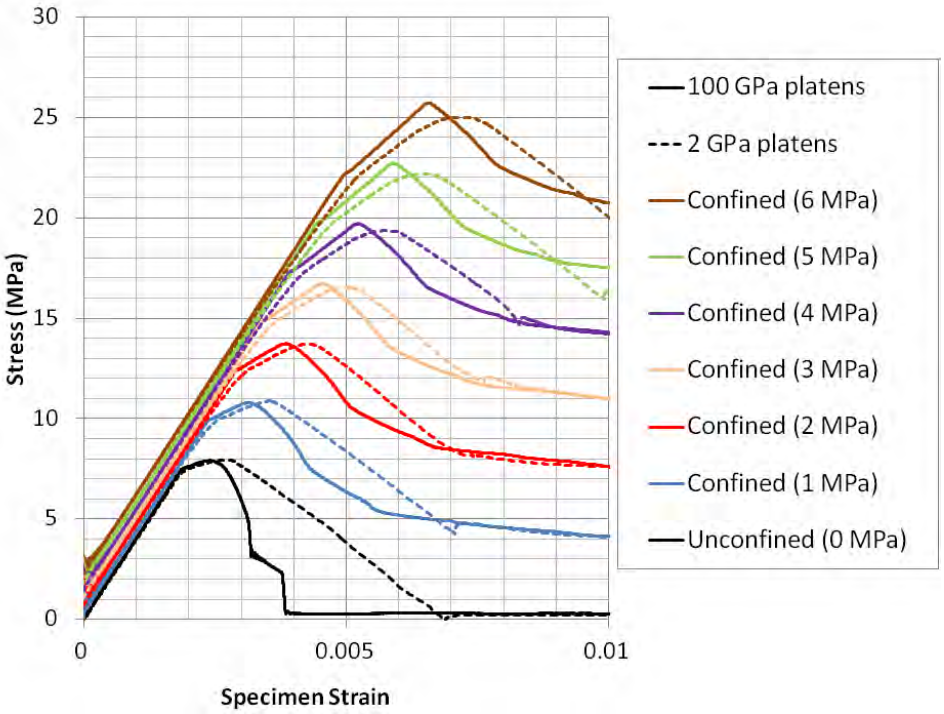

Figure 5.15: Stress-strain responses of triaxially confined brittle coal specimens undergoing failure under unstable (2 GPa) and stable (100 GPa) platen loading conditions.

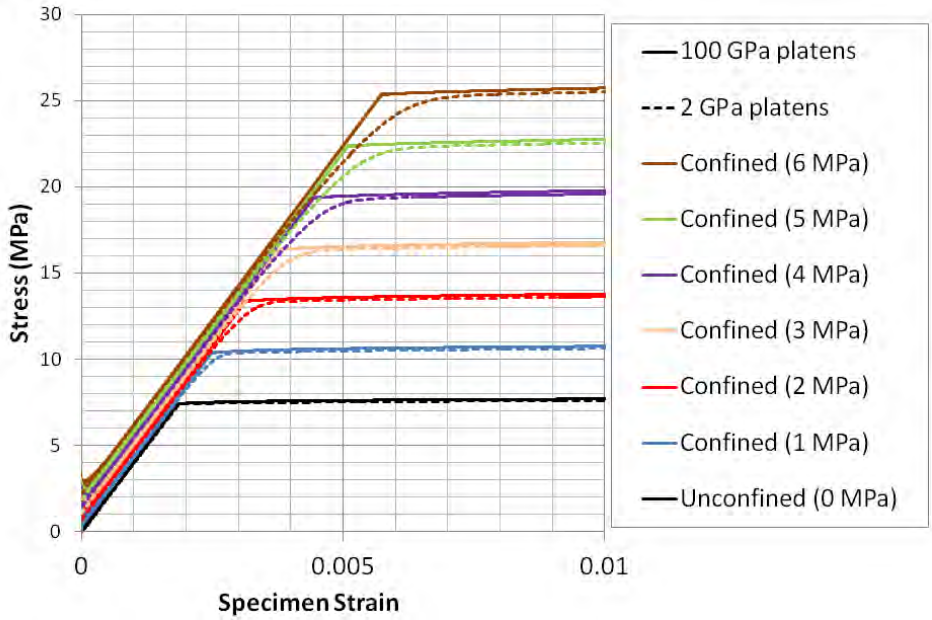

Figure 5.16: Stress-strain responses of triaxial compressive strength tests on plastic Mohr-Coulomb specimens under 2 GPa and 100 GPa platen loading conditions.

have been included to provide a reference for how a fully stable, plastic model responded to changing platen stiffnesses and confinements. Note that within these tests, gridpoints located at the surface of the specimen had a confining force applied onto them which was included within the measured output of unbalanced forces. Due to this convention in $FLAC^{3D}$, the identifier measurements of unbalanced force and resulting accelerations could not be accurately calculated at the confinement boundary. The unbalanced force and acceleration measurements were therefore not recorded at gridpoints located on the surface of the specimen. Other identifiers such as gridpoint velocity and shear strain rate were unaffected by the feature.

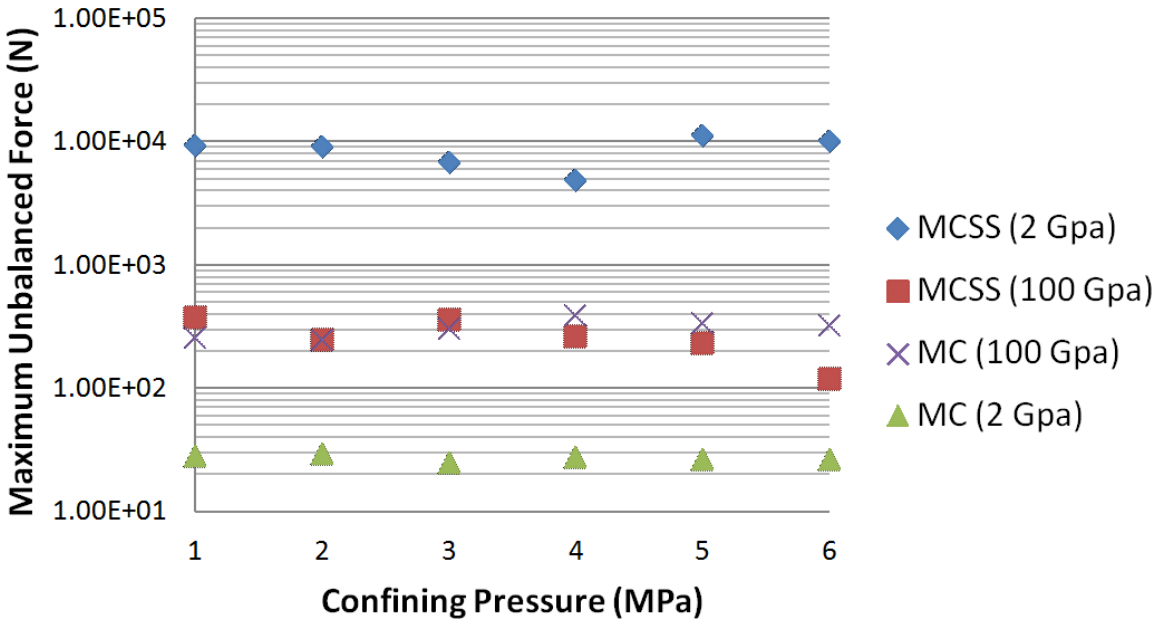

Figure 5.17: Maximum unbalanced forces (N) at gridpoints for triaxial strength tests ranging from 1 to 6 MPa confinement.

The maximum indicators of unstable failure show clear distinction in the magnitudes between stable and unstable test cases. Large unbalanced forces were observed at all levels of confinement for the soft loading condition as compared to the stiff, stable case at the same levels of confinement. Large unbalanced forces then led to increased accelerations, velocities, and shear strain rates in the model. The effect of physical instability in the specimen could

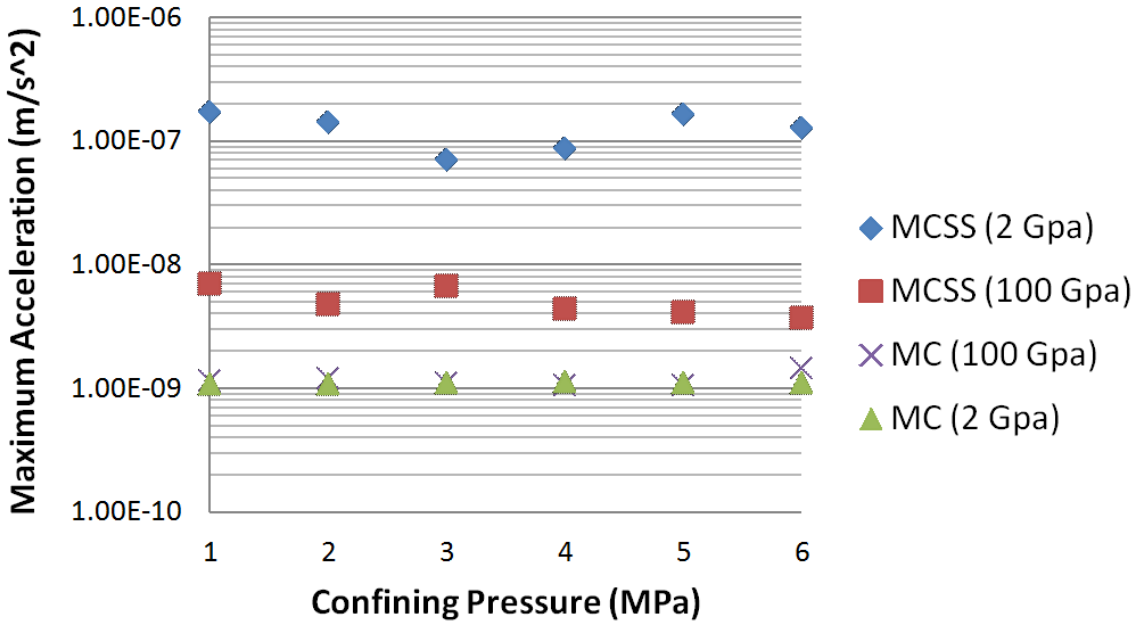

Figure 5.18: Maximum accelerations (m/step^2) at gridpoints for triaxial strength tests ranging from 1 to 6 MPa confinement.

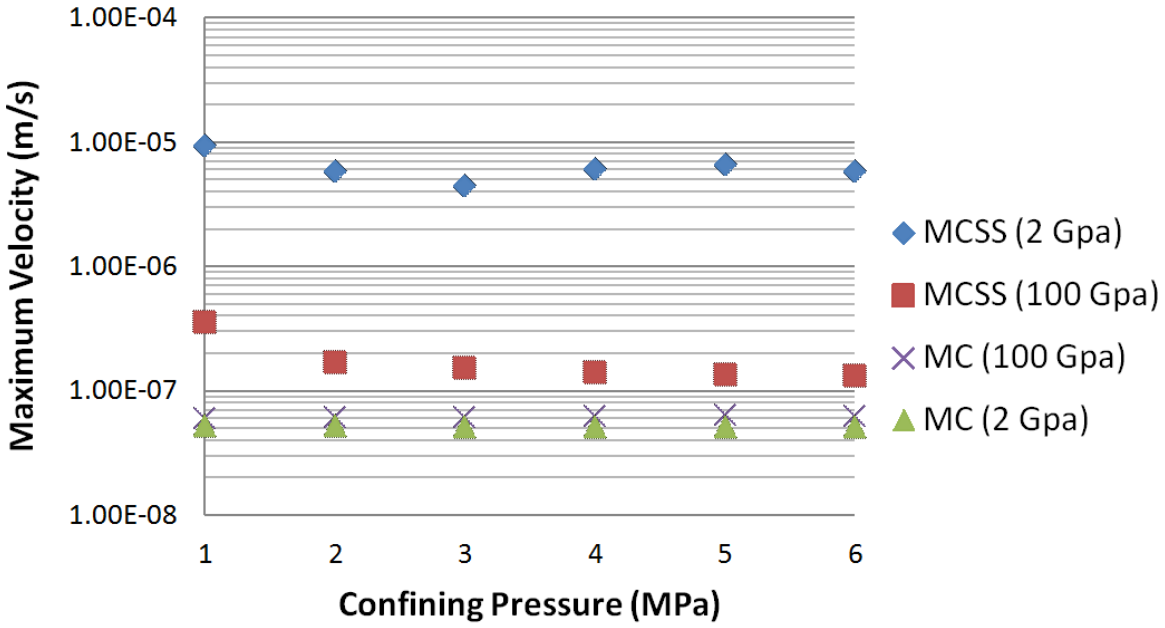

Figure 5.19: Maximum velocities (m/step) at gridpoints for triaxial strength tests ranging from 1 to 6 MPa confinement.

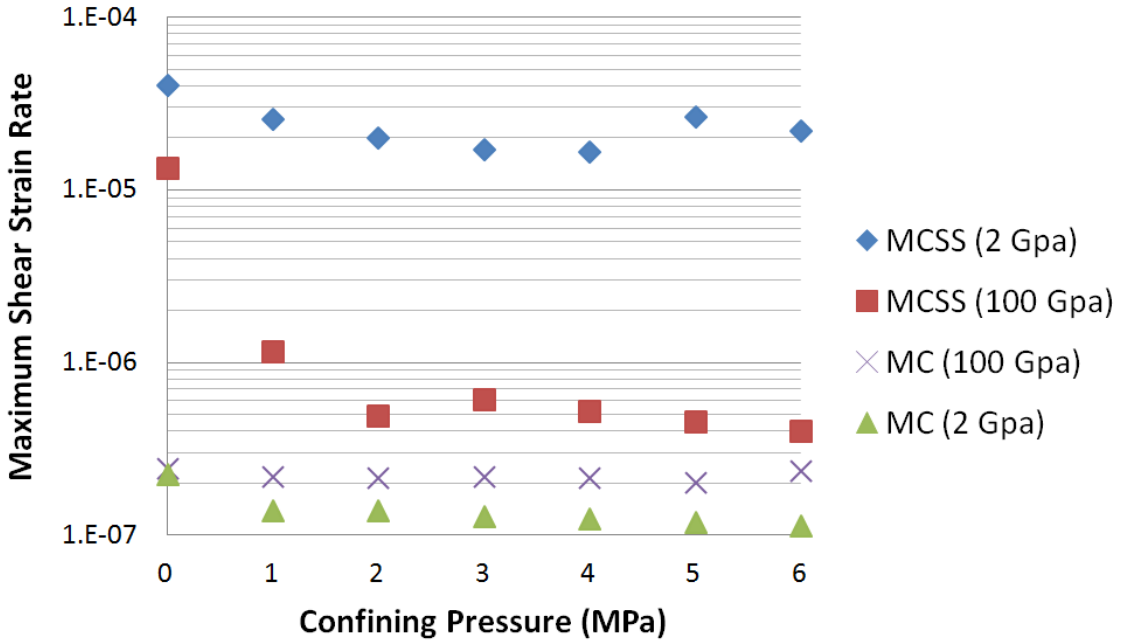

Figure 5.20: Maximum shear strain rate (step^{-1}) in zones for triaxial strength tests ranging from 1 to 6 MPa confinement.

be separated from direct changes to the loading system stiffness by comparing the Mohr-Coulomb strain-softening specimen results to the Mohr-Coulomb specimen results. It was found that the plastic Mohr-Coulomb specimen showed an opposite trend for dynamic effects in that the magnitudes of the indicators were slightly higher for the stiffer 100 GPa platen case than the softer 2 GPa platen case.

A histogram was generated from the results of the maximum shear strain rates recorded for the MCSS zones. Figure 5.21 shows a strong distinction between stable and unstable tests in that the largest result from the 100 GPa stable case was less than the smallest result from the 2 GPa unstable case, while their maximum values of 4.0-e7 and 2.2e-5 were separated by orders of magnitude.

A further assessment of the influence of confinement on the proposed instability measurements was conducted by analyzing the localization of failure of the 6 MPa confinement tests between the stable (100 GPa) and unstable (2 GPa) platen test cases. The results of the

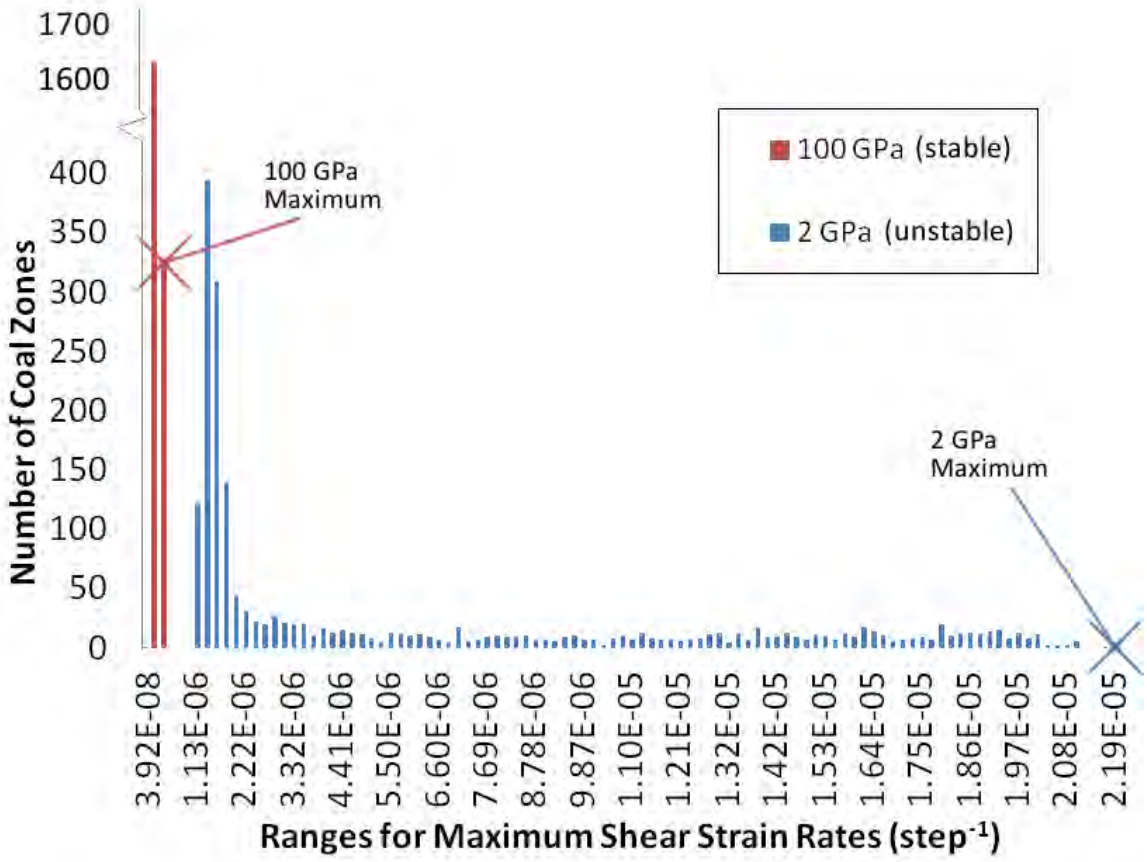

Figure 5.21: Histogram of maximum shear strain rates (step^{-1}) recorded for Mohr-Coulomb strain-softening zones for stable (100 GPa) and unstable (2 GPa) failures.

confined unstable failure are shown in Figure 5.22 to Figure 5.25. These figures do not include unbalanced force or acceleration data at the specimen boundary due to the difficulties in obtaining accurate unbalanced forces at a points of applied external loads. All maximum gridpoint identifiers which were recorded were greater in the unstable, 2 GPa platen case than the largest magnitude of identifier which was recorded in the stable, 100 GPa platen case. Large excess shear strain rates were seen to affect a localized shear band while all other zone shear strain rates fell below those values recorded during the stable 100 GPa test.

Maximum velocity measurements showed the bifurcation of two halves of the specimen concluding the unstable failure. The maximum shear strain rates further indicated that the unstable portion of the failure acted along an inclined shear band within the specimen. To

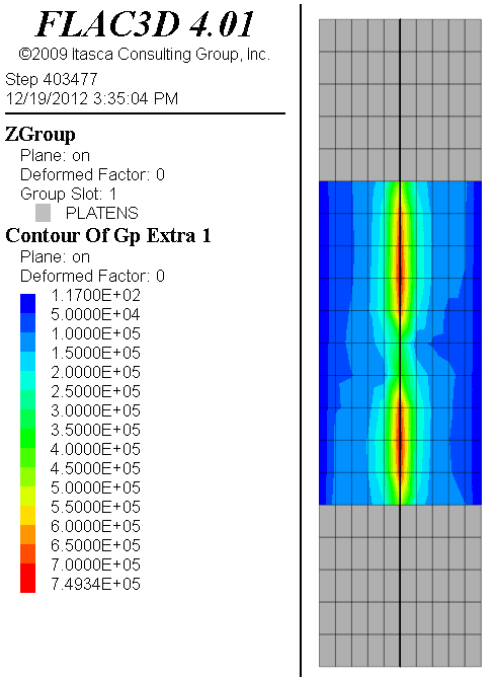

Figure 5.22: Maximum unbalanced force (N) recorded in MCSS specimen for 2 GPa platens at 6 MPa confinement.

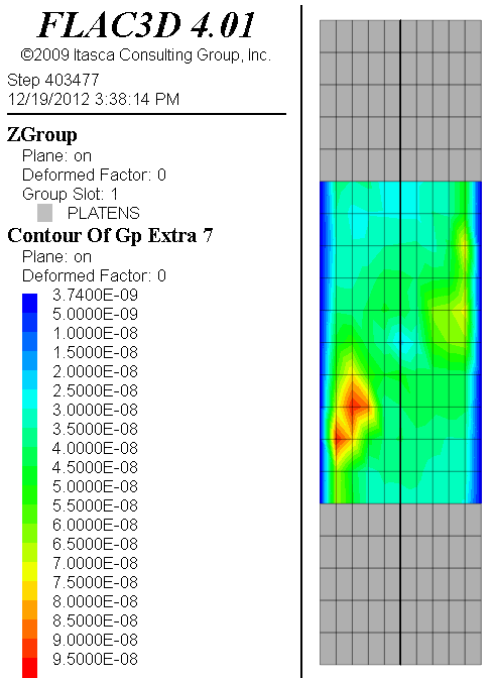

Figure 5.23: Maximum accelerations (m/step^2) recorded in MCSS specimen for 2 GPa platens at 6 MPa confinement.

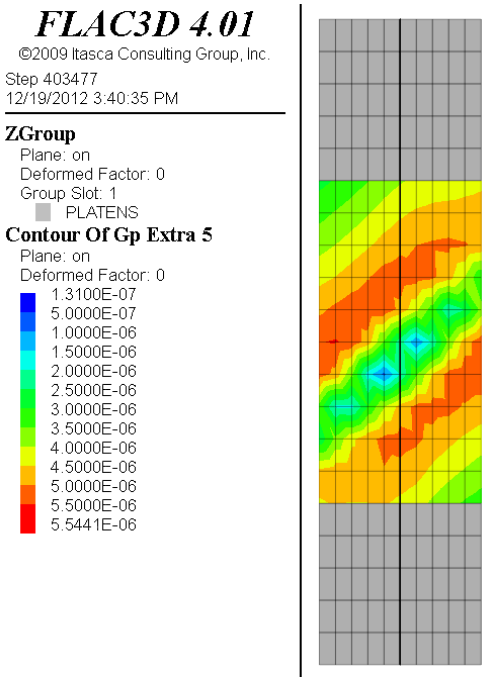

Figure 5.24: Maximum velocities (m/step) recorded in MCSS specimen for 2 GPa platens at 6 MPa confinement.

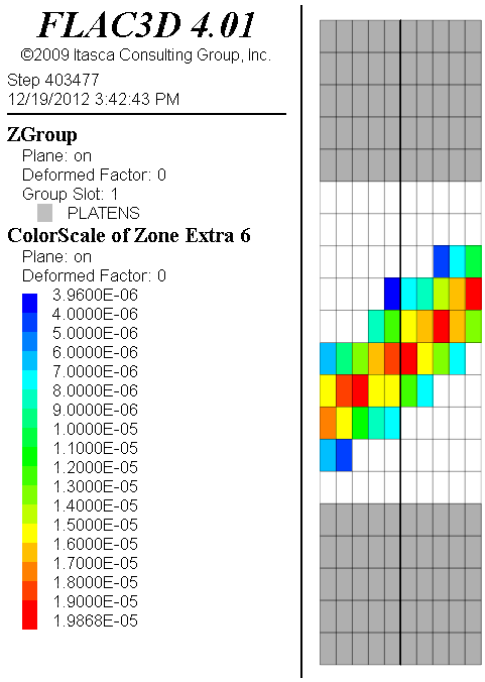

Figure 5.25: Maximum shear strain rates (step^{-1}) recorded in MCSS specimen for 2 GPa platens at 6 MPa confinement.

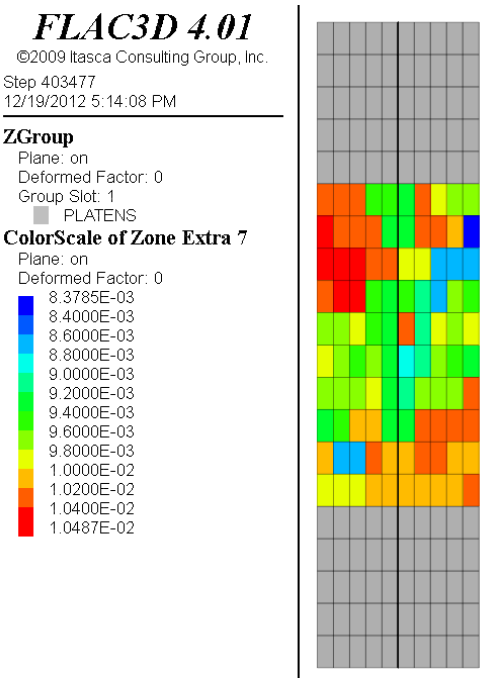

Figure 5.26: Specimen strain increment at which each respective zone reached its maximum shear strain rate for triaxial strength test with 2 GPa platens and 6 MPa confinement.

confirm that these strain rates corresponded with the unstable portion of the failure, an additional record was made of the time at which the maximum magnitudes of shear strain rates occurred, in terms of specimen strain. The resulting strain measurements from the 6 MPa confined test with 2 GPa platens are shown in Figure 5.26. The zones were seen to fail unstably from 0.0086 to 0.010 specimen strain during the test. This corresponded well with the expected range of unstable failure for specimen strain between 0.0075 and 0.010, as was determined from the specimen stress-strain response shown in Figure 5.15.

5.2.2 Conclusions on $FLAC^{3D}$ Identifiers of Unstable Failure in Triaxial Tests

Identifiers of unstable failure conditions were tested under triaxial conditions in $FLAC^{3D}$ as an extension of a previously conducted series of uniaxial compressive strength tests. It was found that the largest magnitudes of unbalanced forces, accelerations, velocities, and shear strain rates were all observed when unstable failure conditions were present in the models. The model was found to deform most quickly along an inclined shear band, and

the speed of this deformation was proportional to the magnitude and duration of unstable failure conditions. It was further observed that the maximum magnitudes of the instability identifiers occurred during periods of maximum physical instability.

5.3 Discussion of Dynamic Identifiers of Unstable Failure

Uniaxial and triaxial compressive strength tests were conducted in $FLAC^{3D}$ to determine an effective method of identifying the onset and duration of unstable failure conditions. Four identifiers of dynamic motion (unbalanced forces, accelerations, velocities, and shear strain rates) were recorded within stable and unstable testing environments to assess the presence of physical instability in the models. It was found that magnitudes of dynamic motion could be analyzed directly between tests to evaluate relative levels of instability.

The quasi-static formulation of $FLAC^{3D}$ yielded unrealistic values for dynamic motion in the models. Implementing local and mass damping further complicated this issue by changing the path dependency of the Mohr-Coulomb strain-softening brittle rock model during dynamic applications of load, such as those experienced after the onset of unstable failure conditions. A method was developed which relied not on the absolute magnitudes of dynamic motion but instead on the relative magnitudes between a known stable testing condition and an unknown, potentially unstable test. This approach was applied successfully to find the onset and duration of instability in the model. The method was then extended to study the propagation of instability by determining the total volume of rock failing under unstable conditions. These qualitative measurements provided a robust means for analyzing the loss of stability in explicit numerical simulations of unstable failure. This approach may be extended with little additional effort to analyze the effects of physical instability in models with complex geometries and combined forms of loading which would have previously been prohibitive for studies on unstable failure.

CHAPTER 6

ENERGY BALANCE OF UNSTABLE FAILURES IN CONTINUUM MODELS

A coal bump or rock burst is the result of damage caused by a release of excess energy from an unstable stress-strain equilibrium within a rockmass. Potential energy is rapidly converted into kinetic energy which initiates the motion of the rock. In stark contrast, stable forms of failure occur continuously through the mining process with the energy in the surrounding host rock being released during a controlled process of stable crack propagation and rock failure [15, 18]. A more rigorous definition of unstable failure may be developed through a formal analysis of these excess energies released during failure. The differences between stable and unstable forms of failures may then be isolated and applied to select numerical methods.

The absolute stability of a system may be considered in the force probing method outlined by [107]. The authors examined a volume of soil or rock under a set of applied loads as it is stressed from the surrounding loading system (shown in Figure 6.1). A fictitious force, or probing force, is applied onto the outer surface of the volume in question and the resulting release of energy is calculated. If the probing force results in a release of energy from the system which is greater than the work done by the probing force, then some excess energy has been released from the system due to instability. An unstable equilibrium is then derived in an absolute sense from the change in forces and displacements at every point on the surface of the enclosed volume. This concept is demonstrated in Figure 6.1 where there are i external node points on the surface with a resulting change in force $\Delta\bar{P}$ and displacement $\Delta\bar{U}$ from the application of a probe of a point on the surface. Note that the probing force is also included in this summation to account for the energy added to the system by the act of probing.

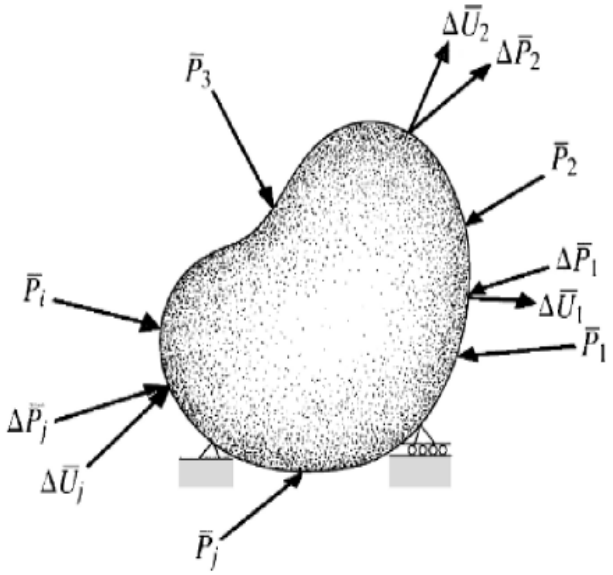

Figure 6.1: Probing forces applied onto a predefined volume of rock or soil. From [18].

The total energy released from the system may then be put in terms of resulting force and displacement changes at the system's surface. Any system which releases excess energy is therefore unstable, as shown in 6.1.

$$\sum \frac{1}{2} \cdot \Delta\bar{P}_i \cdot \triangle\bar{U}_i < 0 \quad (unstable) \tag{6.1}$$

While it is possible to perform near exhaustive checks to assess the instability criterion through applications of virtual work, this method is typically restricted to simplified numerical models because of the added complexities of determining absolute fitness at every point during the calculations. An alternative method of assessing the onset and propagation of unstable failures in the numerical models may be developed using the concepts of excess energy as a means of studying instability conditions.

In the example of the uniaxial compressive test of a coal specimen shown in Figure 6.2, the displacement at the top of the platen will contribute work to the system equal to the force at the boundary, P, multiplied by the distance the boundary is displaced, γ. This boundary work term, W_b, is calculated from the integral of $P(x)$ due to its dependence on

γ.

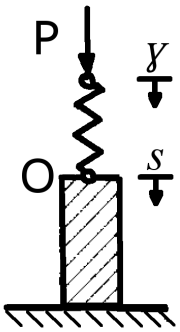

Figure 6.2: Demonstration of unstable failure energy balance in uniaxial compressive strength test.

$$W_b = \int P(\gamma) d\gamma \tag{6.2}$$

The boundary work directly contributes to three forms of static energy in the system: elastic strain energy in the spring/platen, U_s, elastic strain energy in the rock specimen, U_r, and dissipated plastic work performed by the rock during failure, W_r. This relation is shown in 6.3. The formula assumes that no kinetic energy is released from the system.

$$W_b = U_s + U_r + W_r \tag{6.3}$$

If the system is extended to include additional spatial dimensions, the total strain energy in the spring and rock may be calculated from the total strain energy density multiplied by the volume, V, as shown in 6.4. The assumption inherent in 6.4 is that the platen and rock material will continue to behave as a linear-elastic material throughout loading and unloading.

$$U = \frac{V}{2} \cdot \sigma_{ij} \cdot \varepsilon_{ij} \tag{6.4}$$

The elastic strain energy formula may alternatively be converted to the form in 6.5 using shear and normal stress components.

$$U = V \cdot \left[\left(\frac{1+\nu}{2 \cdot E} \right) \sigma_{ij} \sigma_{ij} - \left(\frac{\nu}{2 \cdot E} \right) \sigma_{kk} \sigma_{jj} \right] \tag{6.5}$$

An explicit timestepping numerical model allows the calculation of plastic work by taking the difference in the change in elastic strain energy from the change in total energy in the system over some duration of time. These energy relations are shown for the change in plastic work performed by the rock, ΔW_r, as shown in 6.6.

$$\Delta W_r = \Delta \left(\frac{V}{2} \cdot \sigma_{ij} \cdot \varepsilon_{ij} \right)_r - \Delta U_r \tag{6.6}$$

The total plastic work done by the rock is then found through a summation of all incremental changes in plastic work over the duration of the simulation as shown in 6.7.

$$W_r = \sum \Delta W_r \tag{6.7}$$

Energy is fully accounted for in the system through the static processes outlined in 6.3 as long as the static equilibrium conditions outlined in 2.12 are met. If these stability conditions are not met, then excess energy, E_e, is released from the system. The magnitude of excess energy may be found from the difference in boundary work and energy stored or consumed within the system, as shown in 6.8.

$$E_e = W_b - (U_s + U_r + W_r) \tag{6.8}$$

In the example of the idealized uniaxial compressive strength test, the unbalanced force acting at point O applies work onto the point which is equal to the excess energy caused by the presence of unstable loading condition. In rockbursts and coal bumps, kinetic energy is eventually damped out through dissipated seismic vibrations, collisions of broken rock if ejections were present, friction and heat losses, and additional work performed by supports, to name the primary contributors. An analogous damping mechanism may be applied in numerical models to dissipate excess kinetic energy, such as the local force damping employed in the static solution mode of $FLAC^{3D}$.

An additional energy term may be developed from the static assumptions where total excess energy is equivalent to the sum of current kinetic energy, E_k, and total dissipated kinetic energy, W_k. Current kinetic energy may then be calculated for any system from the displaced rock's mass and current velocity as shown in 6.10.

$$E_e = E_k + W_k \tag{6.9}$$

$$E_k = \frac{1}{2} \cdot m \cdot v^2 \tag{6.10}$$

The excess energy released as a result of dynamic instabilities may be calculated in numerical models through a static energy balance such as that outlined in 6.8 or directly through the kinetic energy and damping work, as shown in 6.9. Either method would be equally valid for use in dynamic numerical models and would result in separate determinations of excess energy released through physical instability. This excess energy may then be used as a quantitative method of studying simulated unstable failures in explicit models. However, for quasi-static models the formula in 6.8 is a complete determination of excess energy released as a consequence of unstable equilibria such as those experienced during unstable failure.

6.1 Extension of Energy Balance to FDM

The investigations made in previous chapters have shown that $FLAC^{3D}$ is capable of simulating the stress-strain behavior of a rockmass system failing under unstable loading conditions. It has also been shown that records of rapid dynamic motion are strong qualitative identifiers of instability conditions in the system. This current research hopes to extend these findings to explore the energy tracking capabilities of the program and to determine its usefulness in studying simulated unstable failures. The energy balance concepts for stable equilibrium which are shown in 6.3 may be adopted with little additional effort into $FLAC^{3D}$ v4.00.

Elastic strain and plastic work which are defined in a generalized sense in 6.4, 6.5, and 6.6 may be performed using existing $FLAC^{3D}$ calculations for stresses and strains. A method was adopted into $FLAC^{3D}$ v5.00 to compute these terms at each timestep [58]. This energy calculation procedure is described more fully in [58], but a comprehensive overview is included below.

The energy balance procedure implemented in $FLAC^{3D}$ first calculates the elastic energy for the tetrahedral subunits which make up the zones of the model. 6.11 shows the calculation for the current elastic energy, U, of a tetrahedron with volume, V. The elastic energy is calculated for shear and volumetric components from the *deviatoric*, σ_{ij}^{d}, and mean stress values, $\bar{\sigma}$. The shear and bulk moduli, marked G and K accordingly, are taken from the elastic material properties applied directly to the zone. Note that this equation is identical to the form previously derived for U as was shown in 6.5.

$$U = \frac{V}{2}\left(\frac{\sigma_{ij}^{d}\sigma_{ij}^{d}}{2G} + \frac{\bar{\sigma}\bar{\sigma}}{K}\right) \tag{6.11}$$

The plastic work is calculated at each timestep by tracking changes in shear and volumetric strain energy terms and comparing these values to the total work performed over a step. These changes to strain energy are calculated through Hooke's law applied to a continuum. The volumetric energy change in a single timestep, ΔW_v, is found for each tetrahedral subunit using 6.12 where $\bar{\sigma}'$ is the mean stress from the previous timestep and $\bar{\varepsilon}$ is the current mean strain.

$$\Delta W_v = \frac{3V}{2}\left(\bar{\sigma} + \bar{\sigma}'\right)\bar{\varepsilon} \tag{6.12}$$

The total shear energy change per timestep, ΔW_s, is then found from the *deviatoric* stresses and strains.

$$\begin{aligned}\Delta W_s = \frac{V}{2}\Big[&\left(\sigma_{11} + \sigma_{11}^{'}\right)\varepsilon_{11} + \left(\sigma_{22} + \sigma_{22}^{'}\right)\varepsilon_{22} + \left(\sigma_{33} + \sigma_{33}^{'}\right)\varepsilon_{33} \\ &+ 2\left(\sigma_{12} + \sigma_{12}^{'}\right)\varepsilon_{12} + 2\left(\sigma_{13} + \sigma_{13}^{'}\right)\varepsilon_{13} + 2\left(\sigma_{23} + \sigma_{23}^{'}\right)\varepsilon_{23}\Big]\end{aligned} \tag{6.13}$$

The total plastic work performed per step may then be calculated from the difference of the total energy change (as calculated by total deformations) and the elastic energy change due to changes in stress and strain. This is demonstrated in 6.14 below.

$$\Delta W_r = \left(\Delta W_s + \Delta W_v\right) - \Delta U \tag{6.14}$$

The plastic work performed through plastic deformation, W_r, is found through a cumulative summation of the change in plastic work calculated for n timesteps. This straightforward relation is shown in 6.15.

$$W_r = \sum_{i=1,n} (\Delta W_r)_i \tag{6.15}$$

The boundary work term may be calculated from the forces which develop at any displacement boundary. The change in boundary work at a gridpoint, ΔW_b, is found from the increase in boundary work performed over a time step, as shown in 6.16. Note that F_i is the unbalanced force in direction i while F_i' refers to the unbalanced force of the previous timestep. The variable d_i then corresponds to the displacement of the gridpoint where d_i' refers to the displacement recorded from the previous timestep.

$$\Delta W_b = \sum_{i=1,2,3} \left(\frac{F_i + F_i'}{2} \right) (d_i - d_i') \tag{6.16}$$

The total boundary work for the system may then be found through the cumulative summation of incremental boundary work across n timesteps as shown in 6.17.

$$W_b = \sum_{i=1,n} (\Delta W_b)_i \tag{6.17}$$

These terms may then be combined in the form of the static energy balance shown in 6.18. The total excess energy which is released is calculated as the difference between the boundary work applied to the system and the stored elastic strain energy plus the accumulated plastic work.

$$E_e = W_b - (U + W_r) \tag{6.18}$$

6.2 UCS Test with Energy Balance

A series of uniaxial compressive strength tests were performed on a $FLAC^{3D}$ coal specimen using variable elastic moduli for platens which were placed on either end of the specimen. These tests mimicked those previously conducted in Chapter 4 to determine a specimen's stress-strain behavior under unstable loading. A controlled loading rate of 1e-7 m/s was

applied to boundaries at the top and bottom of the platen-specimen-platen system. A Mohr-Coulomb strain-softening constitutive model was used to represent brittle material behavior of the specimen. A Mohr-Coulomb specimen was also prepared to demonstrate the purely plastic response of the model to different platen stiffnesses. The stress-strain behavior of the brittle and plastic material models are shown in Figure 6.3.

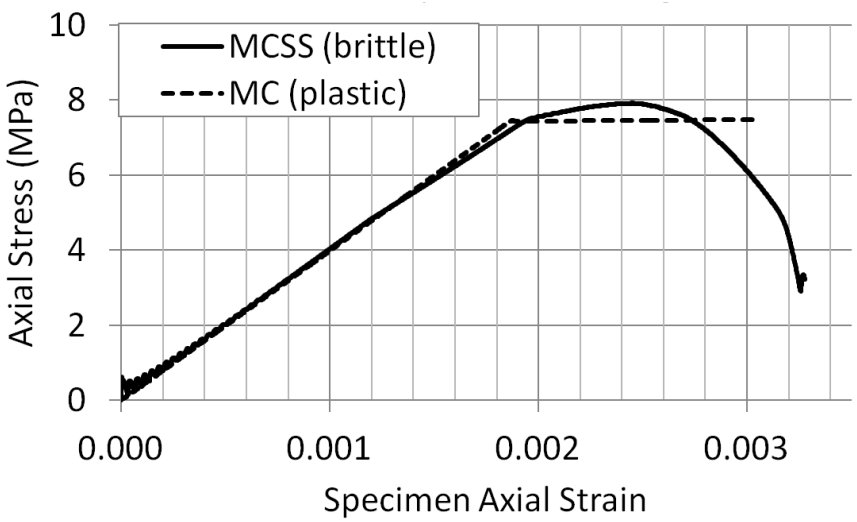

Figure 6.3: Uniaxial compressive stress vs. strain for Mohr-Coulomb (plastic) and Mohr-Coulomb strain-softening (brittle) material responses.

Input values were taken from the calibration efforts performed in Section 4.3.1 for the Mohr-Coulomb and Mohr-Coulomb specimen models. Strain measurements were taken for the system and the specimen was loaded through failure until its strength was reduced to a negligible value. Stress was recorded within the system through a record of reaction forces at the applied velocity boundaries.

A local damping scheme was applied to all gridpoints with a damping factor of 0.8. Mass scaling was applied while the simulations were run in "static" mode. Elastic and plastic energy terms were calculated every timestep. Excess energy was calculated from the time histories of the terms from the static equilibrium energy balance applied to finite difference models shown in 6.18.

Simulated uniaxial compressive strength tests were performed using elastic platens with Young's moduli ranging from 2 to 100 GPa. Due to their relative stiffness to the post-peak behavior of the specimen, the softer 2 GPa platens will elicit an unstable response while the more stiff platens (e.g., greater than 16 GPa) will fail the specimen stably. The results of these stable and unstable failures of the brittle MCSS specimen were compared against equivalent tests performed using a Mohr-Coulomb plasticity model for the specimen material behavior.

6.2.1 UCS Test Energy Balance Results

The final values of excess energy measured using static equilibrium energy balance are shown in Table 6.1 for the uniaxial compressive strength tests. The brittle Mohr-Coulomb strain-softening model resulted in a release of total dynamic energy ranging from 376 to 8,173 J, with larger excess energies for Young's modulus platens less than 16 GPa. The results for the specimen with a Mohr-Coulomb constitutive model is shown for the two test cases with platen Young's moduli of 2 and 100 GPa. The excess energies from these tests were smaller than those observed from the Mohr-Coulomb strain-softening model, and the softer platen resulted in a reduction of excess energy which was released.

The total energy histories taken during the duration of the tests are shown in Figure 6.4 through Figure 6.9, where the terms from the excess energy balance are further broken into the elastic strain energy of the spring/platen (U_s), elastic strain energy of the coal specimen (U_r), work performed in the plastic rock deformation of the coal specimen (W_r), and the boundary work applied to the system (W_b).

The series of uniaxial compressive strength tests revealed that the potentially unstable system of a brittle specimen and two elastic platens released increasing magnitudes of excess energy with increasing levels of physical instability in the system. Excess energy was calculated through the static energy balance developed in 6.8. Table 6.1 demonstrates a trend in the values of excess energy which matches previous trends established from the tests which focused on the dynamic instability identifiers of Chapter 5. The total excess energy which

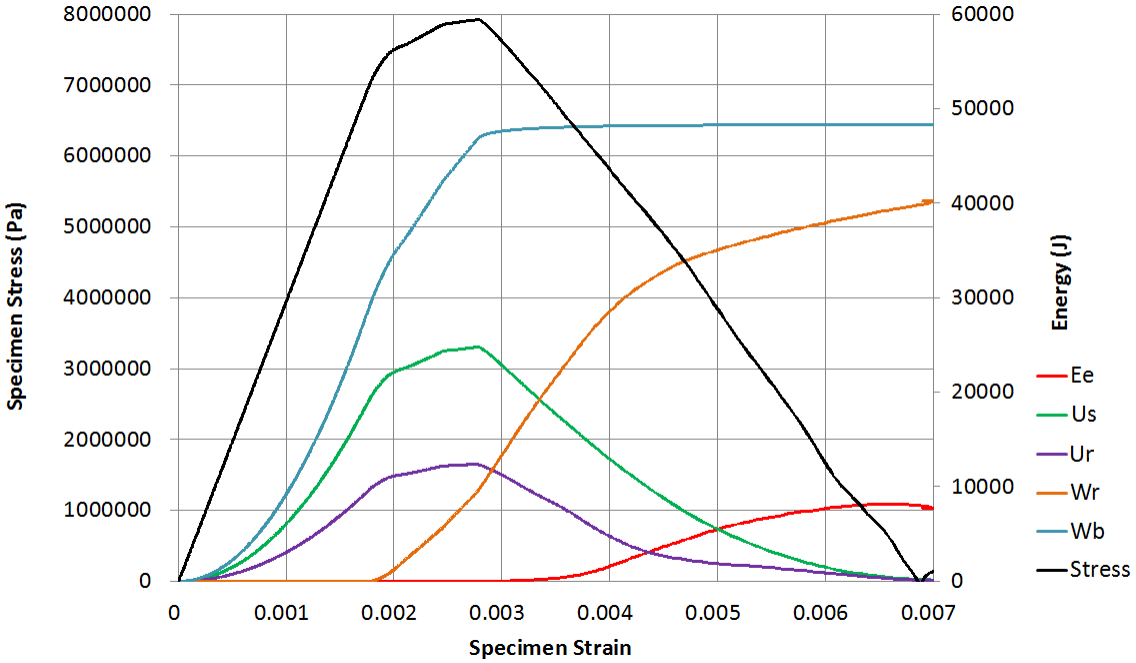

Figure 6.4: Specimen stress vs. strain for UCS test with 2 GPa platens, overlayed with the energy terms used to calculate excess energy.

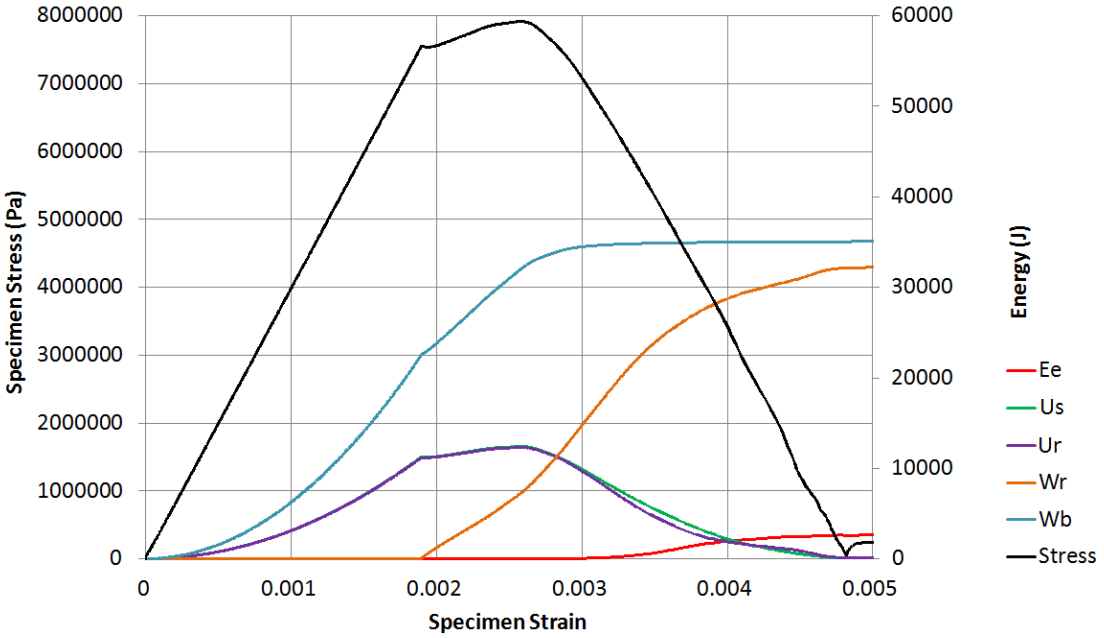

Figure 6.5: Specimen stress vs. strain for UCS test with 4 GPa platens, overlayed with the energy terms used to calculate excess energy.

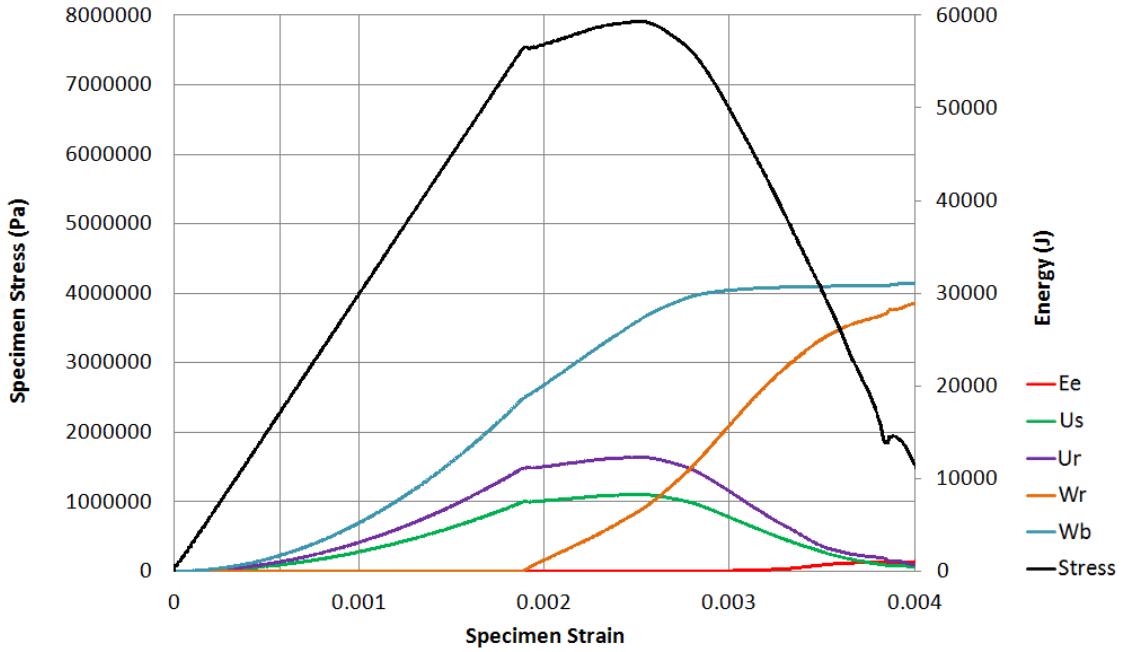

Figure 6.6: Specimen stress vs. strain for UCS test with 6 GPa platens, overlayed with the energy terms used to calculate excess energy.

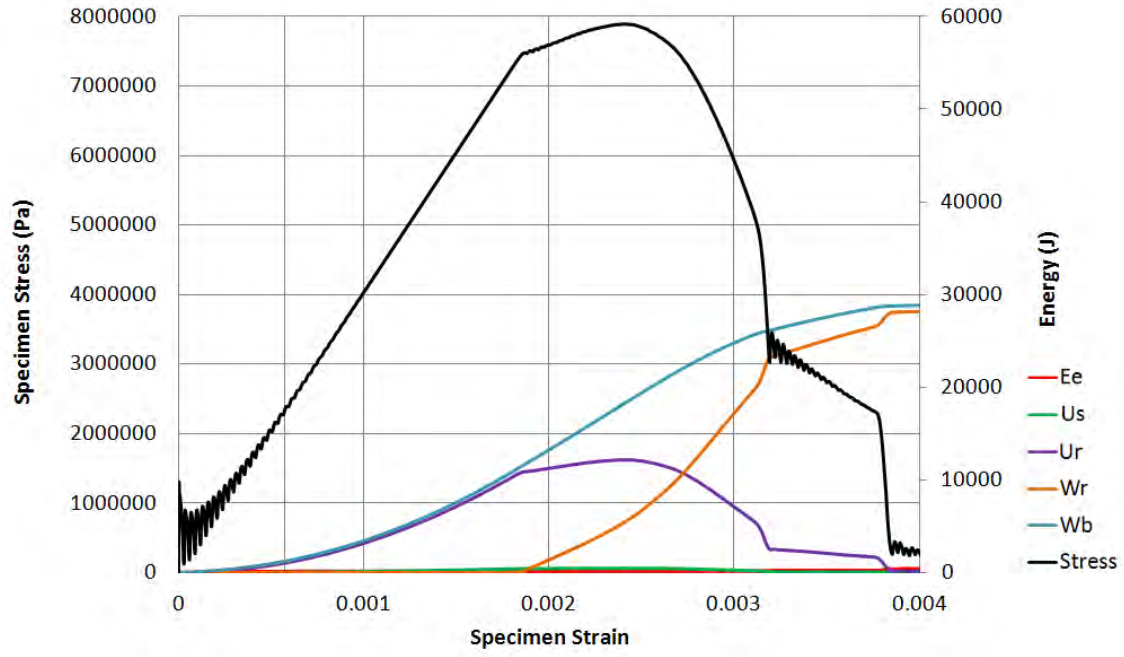

Figure 6.7: Specimen stress vs. strain for UCS test with 100 GPa platens, overlayed with the energy terms used to calculate excess energy.

Table 6.1: Total excess energy (E_e) released during UCS tests on Mohr-Coulomb strain-softening (MCSS) and Mohr-Coulomb (MC) coal specimens.

Platen Young's Modulus (GPa)	E_e of MCSS (J)	E_e of MC (J)
2	8,173	121
4	2,619	-
6	981	-
8	805	-
10	620	-
12	537	-
14	488	-
16	455	-
18	434	-
20	417	-
40	376	-
60	390	-
80	408	-
100	444	222

was released during the tests increased dramatically for platen Young's moduli less than 16 GPa.

The calculation procedure for determining excess energy was partially validated through tests conducted on a Mohr-Coulomb plastically failing specimen which was caused to fail under sets of 2 and 100 GPa Young's modulus platens. The energy histories of the plastic specimen, shown in Figure 6.8 and Figure 6.9, indicated only nominal values of excess energy released over the course of the tests. The total energy within these definitively stable systems was thereby shown to be accounted for through static processes.

A static calculation mode was assumed within $FLAC^{3D}$ for the tests. However, any system which required updates to the gridpoint position also required small velocities to be applied onto the gridpoints in order to bring them to their new equilibrium positions. This behavior was observed in the results of the energy balance when applying the static energy balance to stable failures. In cases of high platen stiffnesses or perfectly plastic specimens, a non-zero magnitude of excess energy was calculated which could be attributed to the modest dynamic energy required to update gridpoint positions through the simulation. A

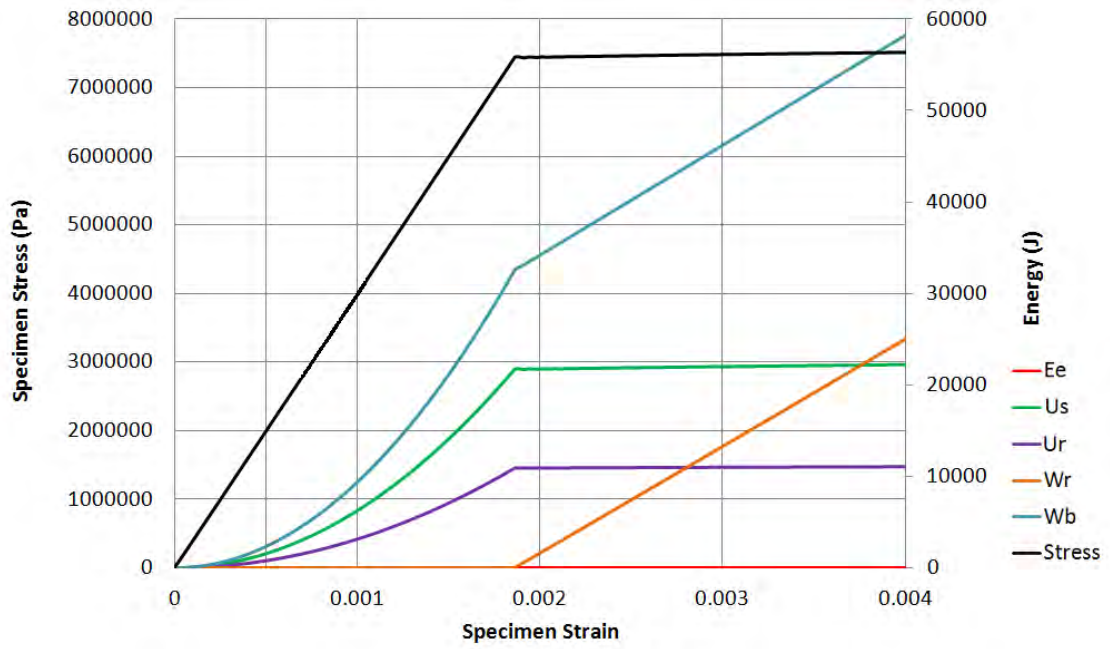

Figure 6.8: Specimen stress vs. strain for UCS test on Mohr-Coulomb specimen with 2 GPa platens, overlayed with the energy terms used to calculate excess energy.

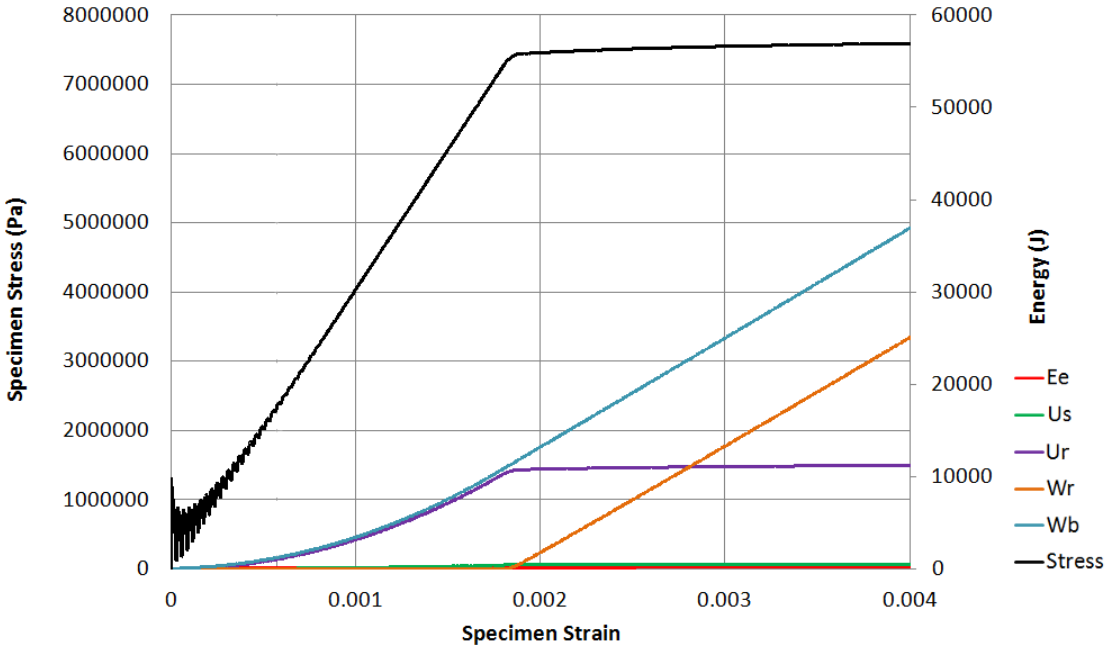

Figure 6.9: Specimen stress vs. strain for UCS test on Mohr-Coulomb specimen with 100 GPa platens, overlayed with the energy terms used to calculate excess energy.

baseline magnitude was established to determine the expected excess energy released during the laboratory style uniaxial compressive strength tests. Any deviations in excess to these baseline measures may therefore be attributed to additional dynamic energy released due to dynamic applications of load or due to the presence of unstable failure conditions.

6.3 Discussion on Energy Balance in Explicit Models of Unstable Failure

The energy balance which was developed at the beginning of this chapter was found to be a straightforward method for determining the excess energy released as kinetic energy due to the presence of unstable failure conditions. The calculations assume that a static energy balance can track the energy stored and consumed during brittle rock failure. Any energy which can not be accounted for through static processes is thereby summed to calculate the energy in excess to that which is required to satisfy static equilibrium. The imbalance in the static equation comes from the difference in total energy supplied to the system and the energy stored elastically or consumed through plastic work during zone failure.

Gravitational potential energy may also be considered for simulations of larger rock-masses in which gravity plays a significant role. The gravitational potential energy should be calculated from the volumetric mass of the rock distributed evenly through the gridpoints rather than from the numerically derived nodal masses which are assumed in the static solution mode of $FLAC^{3D}$. A more thorough discussion of how to adapt the static energy balance to realistic mine models follows in Chapters 8 and 9.

The calculation of elastic and plastic work terms assumes that the change in energy over a single timestep is small or that it follows a linear relationship over that timestep. Error may be introduced in the calculation of elastic strain energy changes and plastic work performed during periods of rapidly changing stresses and strains such as those experienced during instability. These assumptions are similar to those made in the second order finite difference scheme employed in $FLAC^{3D}$ however further reduce the calculations of energy to a first order equation. Errors may also be introduced in the calculation of plastic work through limitations of the plastic flow rule and and failure criterion to adequately describe the flow

of rock during periods of unstable failure, as has been discussed in previous chapters.

Each term of the static energy balance holds physical relevance within a rock mechanics context, in contrast to the instability identifiers which have been developed as a qualitative assessment of unstable failure. Determinations of excess energy represent the maximum magnitude of energy which may be released in the form of kinetic energy as a result of physical instability. Research on unstable failure has previously made some attempts to uncover the total kinetic energy released due to rockbursts or coal bumps, however these energy magnitudes are poorly understood even within the domain of idealized laboratory studies. The $FLAC^{3D}$ results were therefore not extended to direct energy measurements due to the lack of correlational data. The application of the energy balance was further restricted by a lack of experimental data for the plastic work performed by rock during unstable failure in a laboratory style uniaxial compressive strength test. However, historical records of large unstable mine failures have been shown to provide a few additional details on the kinetic energy released during unstable failures through the seismic records of these failures. A transition may therefore be made from the energy balance of rock failures in laboratory experiments to full-scale mining layouts and simulations of large excavations.

CHAPTER 7
COAL PILLAR MODELS

For most applications of numerical models in pillar design it is sufficient to capture a realistic pillar response using either elastic or plastic strength characteristics. However in some scenarios the post-peak response of a pillar plays an integral role in the design of a layout; notable examples of post-peak pillar design include retreat mining and the use of yield pillars. Studies which focus on rockbursts and coal bumps demand that even greater attention be given to the post-peak behavior of supportive rock structures in order to determine the magnitude and extent of dynamic energy released during unstable failures.

This chapter describes a series of pillar studies which were conducted in the finite difference method to develop models of coal pillars with realistic strength and post-peak failure responses. These pillars were caused in subsequent tests to fail under loading conditions which ranged from soft to stiff through an application of both strain energy and gravitational potential energy from the host rock. Note that the results and methods of these tests may be extended to common hard rock mine models, however the following models have been calibrated to the unique strength characteristics observed in coal.

7.1 Coal Pillar Strength Characteristics

Confinement and size effects drastically affect the ultimate strength and post-peak failure characteristics of *in situ* coal pillars. Research studies which have been conducted on full-sized coal pillars demonstrate a dramatically increased peak strength and hardening post-peak strength behavior with increasing width-to-height ratios. The coal at the edge of the pillar is shown to confine a much stronger central core which is more difficult to fail with increasing loads. Statistical analyses have been conducted on large databases of successful and unsuccessful pillar designs in attempts to derive appropriate strength criteria for pillar design across a range of mining conditions. These historical references were used in the

current finite difference calibration to develop appropriate strengths and strain-softening characteristics for smaller pillars ranging from width-to-height ratio 1:2 to 5:1.

Several different approximations of coal pillar strength have been developed from failed pillar case history. The Bieniawski strength formula [10] has gained widespread usage in the United States. An extension to this formula was made by Mark to include a second pillar dimension (i.e., length) for rectangular pillar geometries [73]. The original formula developed by Bieniawski is shown in 7.1 with the extension to a second width dimension shown as 7.2. The pillar strength, S_p, is derived from the cubic strength of coal, S_1, and the pillar's width, height, and length in the case of the Mark-Bieniawski formula. The cubic strength of coal for use in the these formulas was found through backanalyses to be approximately 6.2 MPa for coals typically found in the Eastern United States [76].

$$S_p = S_1 \left(0.64 + 0.36 \cdot \frac{w}{h}\right) \quad (Bieniawski\ Strength) \tag{7.1}$$

$$S_p = S_1 \left\{0.64 + \left[0.54 - 0.18 \left(\frac{w^2}{hL}\right)\right]\right\} \quad (Mark - Bieniawski\ Strength) \tag{7.2}$$

A similar statistical method was developed by Salamon and Munro [106] for use in South African collieries. Case histories of coal pillar failures indicated that the equation shown in 7.3 made a reasonable prediction of coal pillar strength when the constants for a and b were set to 0.46 and 0.66, respectively. The resulting Salamon-Munro strength formula has been applied with widespread success to deep South African coal mines [51].

$$S_p = S_1 h^a w^b \tag{7.3}$$

The Mark-Bieniawski and Salamon-Munro pillar strength formulas were selected to establish a range of allowable values for the ultimate pillar strengths within the finite difference model. These two strength criteria were adopted due to their widespread application in safe mine designs through independent methodologies for determining strength. The range in strengths between the two criteria thereby produced a workable range of strengths for the calibration of the numerical models.

No similarly clear-cut methodology exists for determining the post-peak modulus of coal pillars during failure. Tests conducted by Wagner and Van Herdeen have shown that pillars with width to height ratios up to 4:1 exhibit some form of softening behavior [118, 120]. With the increase of confinement, the pillar becomes less likely to reach a peak strength. At these and greater widths it is assumed that the pillar continues to harden with increasing loading. It is difficult to determine at what width a pillar will assume a hardening post-peak behavior. Backanalyses of massive collapses and cascading pillar failures indicate that pillars with a ratio of width-to-height greater than 3:1 tend to reduce the threat of massive collapse [73]. Pillars with a width to height ratio of 4 and greater are therefore thought to have a rapid increase in ultimate strength with increasing width as compared to their slightly smaller sized counterparts, and may be assumed to have an effectively plastic or hardening post-peak behavior. Additional evidence for a positive post-peak modulus comes from the pillar strength databases themselves, in which all of the pillar "failures" which have occurred for width-to-height ratio pillars greater than 3:1 have resulted from a gradual failure of the pillar or foundation leading to squeezing ground rather than in a collapse of the pillar itself. This fact is demonstrated from the chart shown in Figure 7.1 of pillar case histories used in the ARMPS (Analysis of Retreat Mining Pillar Stability) database of successful and unsuccessful pillar cases.

Numerical models which have been conducted using finite difference, finite element, and boundary element methods all lend substantial evidence to the idea that a pillar with a certain width and confining rock will become increasingly strong due to a confined core of strain-hardening frictional material. However, if unstable loading conditions are applied onto a wide pillar, excess energy may result in the *localized* unstable failure of the pillar rib. Many examples exist of unstable failures acting only at pillar ribs or sidewalls without extending deeper into the coal mass. Such behavior was observed in wide coal pillars during the recent Crandall Canyon failure in which pillars of width-to-height ratios greater than 8:1 were shown to violently eject material from their ribs into the entries, effectively filling

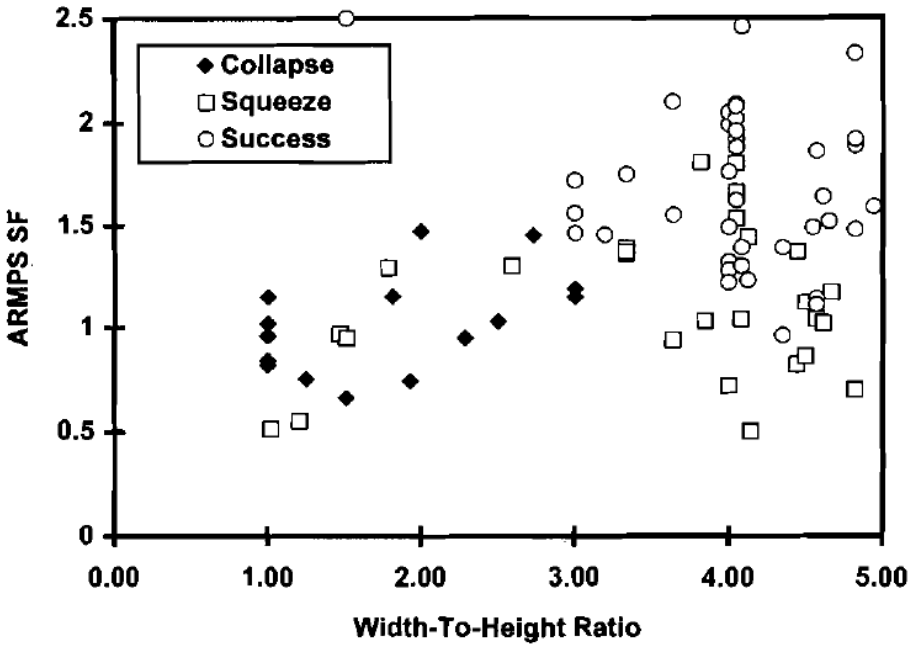

Figure 7.1: ARMPS database of pillar collapses and squeezes [73]. Note that no pillar collapses were found to occur at widths greater than 3:1.

the voids throughout the collapsed area of the mine [116]. A long mining history of violent ejections of coal from portions of pillars and sidewalls dictate that an analysis of unstable failure must also include these localized forms of instability in order to properly account for the safety of mining personnel.

The exact failure mode and extent of failure is difficult to assess from past case histories, primarily due to the speed of the coal bumps and amount of damage which is incurred by the ejected material. The micromechanical behavior of pillar failures are also not known for unstable failure conditions. For these reasons the discrete element method was not chosen as a primary tool for analysis of the unstable failure mechanism. The finite difference method with an assumed shear mode of failure was instead adopted for studying the onset and duration of instability within coal structures of varying geometries.

7.2 $FLAC^{3D}$ Calibration Procedure

A calibrated Mohr-Coulomb strain-softening (MCSS) constitutive model with a non-associated flow rule, which has been discussed in detail as an approximate model for simulating brittle rock in a continuum, has been shown by previous researchers to simulate realistic strength and deformation characteristics of coal pillars [2, 91]. The process of modeling appropriate pillar behavior was adopted from these previous studies and extended to a parametric analysis of the cohesion, friction, and dilatancy input parameters used to calibrate the MCSS model. The validity of the resulting pillar models were then assessed against established pillar strength formulas for width-to-height ratios ranging from 1:2 to 5:1.

Two- and three-dimensional models were developed within $FLAC^{3D}$ to record the stress-strain response of an *in situ* coal pillar as it was loaded through failure by a stiff loading system. The two-dimensional models assumed a plane strain condition to represent an infinite length pillar of set width. Zone sizes were restricted to 0.1 m cubes for the pillar and immediate roof and floor. Reduced zone resolution was then applied to the remainder of the model. A coal seam height of 2.4 m was assumed for all tests. Figure 7.2 shows the zone meshing used for a single pillar model. Loading was applied onto the system through displacement boundaries at the top and bottom of the model. Roller boundary conditions were applied to the sides of the model to make it a half symmetry plane strain model of a single pillar. The form of displacement loading which was applied to the stiff roof and floor reduced the potential of an unstable equilibrium developing as a result of potential energy being released from the loading system..

The three-dimensional pillar calibration model which was developed represented a 1/4 symmetry system with roller boundary conditions along four sides of the model to represent an infinite room of pillars. Displacements were again applied simultaneously at the top and bottom of the system to slowly apply load onto the pillar. The model boundaries were extended within the three-dimensional model to include the far-field roof and floor so as to reduce the effects of the boundary on the resulting pillar load-deformation characteristics.

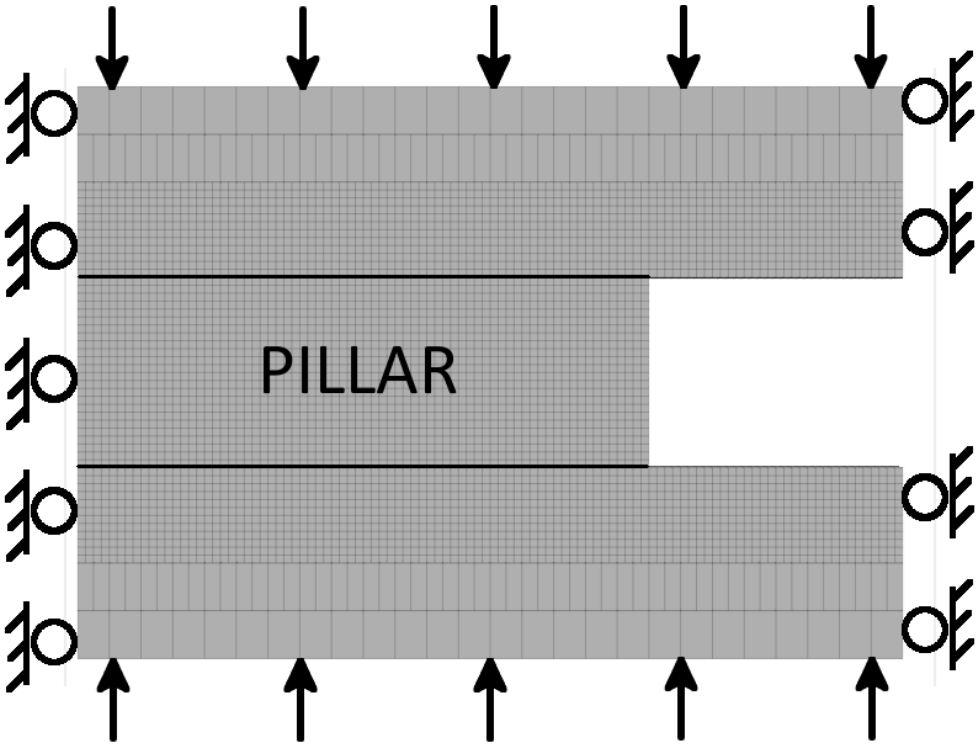

Figure 7.2: $FLAC^{3D}$ 2D pillar calibration model.

A zone size of 0.1 m^3 was again adopted for the pillar zones. The three-dimensional quarter symmetry model is shown in Figure 7.3.

A Young's modulus of 2.7 GPa and a Poisson ratio of 0.12 were applied to the elastic properties of the pillar in order to represent coal from the Hiawatha coal seam in Utah in which the Crandall Canyon mine disaster occurred. A Mohr-Coulomb strain-softening constitutive model was applied to the coal pillar in order to capture the reduction in strength inherent in brittle rocks. A calibration approach was taken which followed the method outlined by Badr [2] in which the peak and residual cohesion values are variable, along with the cohesion drop rate to determine the rate of cohesion decrease as a function of plastic strain. By steepening the cohesion drop rate it is thereby possible to increase the brittleness of the modeled rock. This concept is demonstrated in Figure 7.4.

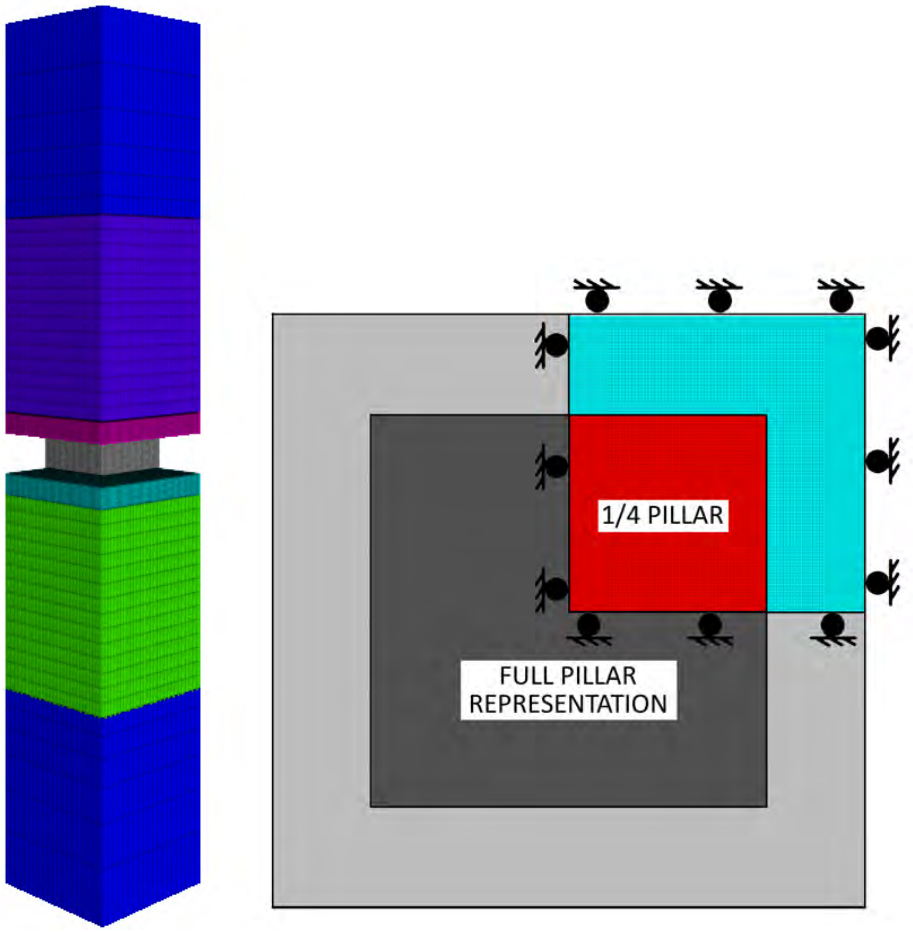

Figure 7.3: $FLAC^{3D}$ quarter-symmetry pillar calibration model.

Nine sets of tables were established for the cohesion, friction, and dilatancy inputs of the MCSS model. Coal pillars ranging from width-to-height ratios of 1:2 to 5:1 were then failed through the displacement boundary condition previously described. Cohesion was varied between 1.65 MPa and 0.1 MPa with cohesion drop rates of -6 MPa/ε_p to -400 MPa/ε_p. The friction angle was assumed to increase with the introduction of plastic deformation, as is seen in laboratory testing and took on values ranging from 23 to 35 degrees. The dilation angle played less of a role in the calibrations however values were taken from 0 to 30 degrees. The resulting pillar strengths were compared between tests in order to determine the closest fit to empirical pillar strength formulas. Figure 7.6 shows the results of these tests for the two dimensional model and compares the modeled pillar strengths to the desired

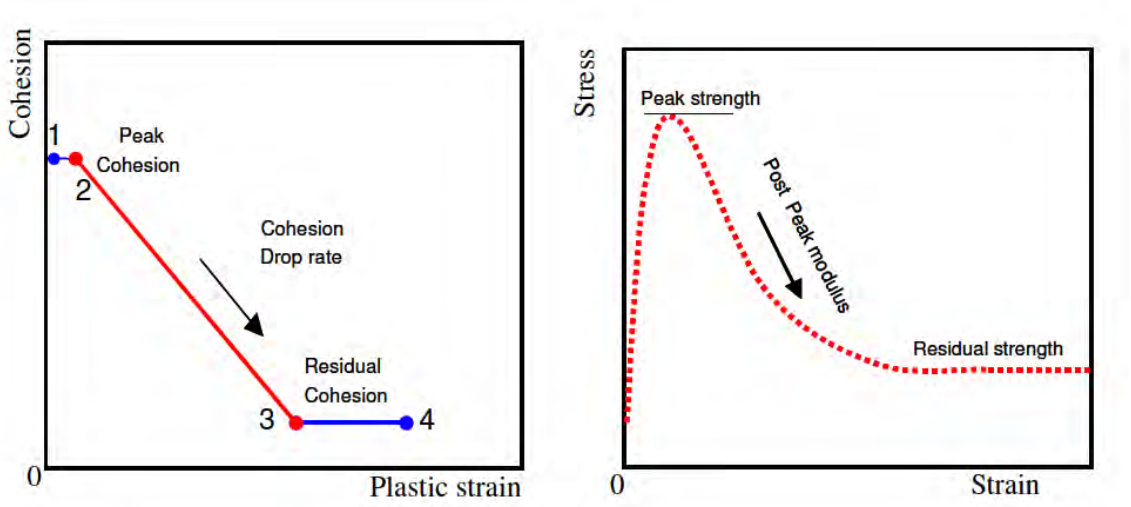

Figure 7.4: Cohesion drop rate as a method to control brittleness in the MCSS constitutive model [2, 41].

Mark-Bieniawski strength values.

The simulated pillar strengths which most closely matched the Mark-Bieniawski strength formula were adapted for use in a calibrated set of MCSS input parameters. The calibrated pillar strengths are further detailed in Figure 7.7 which showed good agreement with the Mark-Bieniawski formula. Figure 7.5 shows the record of the stress-strain characteristics of the two-dimensional pillars. The corresponding MCSS inputs for these models are plotted in Figure 7.8 to Figure 7.10.

The calibrated input parameters which were derived in two dimensions were extended to the three-dimensional pillar models. A Young's modulus of 21.4 GPa was applied to the roof and floor. An entry width of 6 m was assumed within the models. The resulting stress-strain results of the three-dimensional pillars are shown in Figure 7.11.

A weakening behavior was observed for pillars of width-to-height ratios 3:1 or less. The 4:1 pillar was seen to exhibit relatively plastic deformation while the widest 5:1 pillar continued to increase in strength with increasing strains. A practical limit was established at 1.5% strain at which point the 5:1 pillar had reached a stress of 15.3 MPa. If the tests were continued then the 5:1 pillar would continue to strengthen with increasing strains.

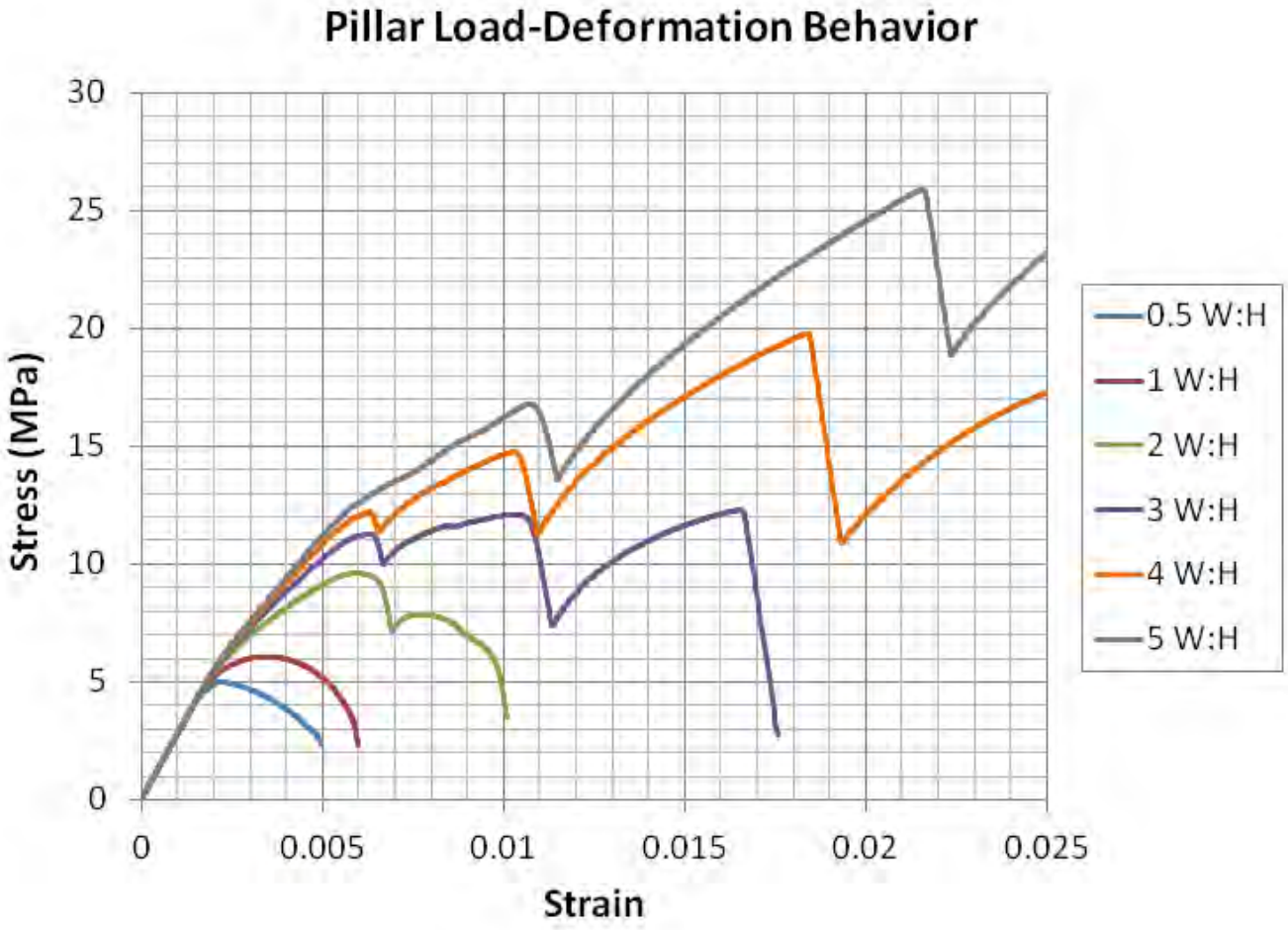

Figure 7.5: Stress-strain results of calibrated 2D pillar model.

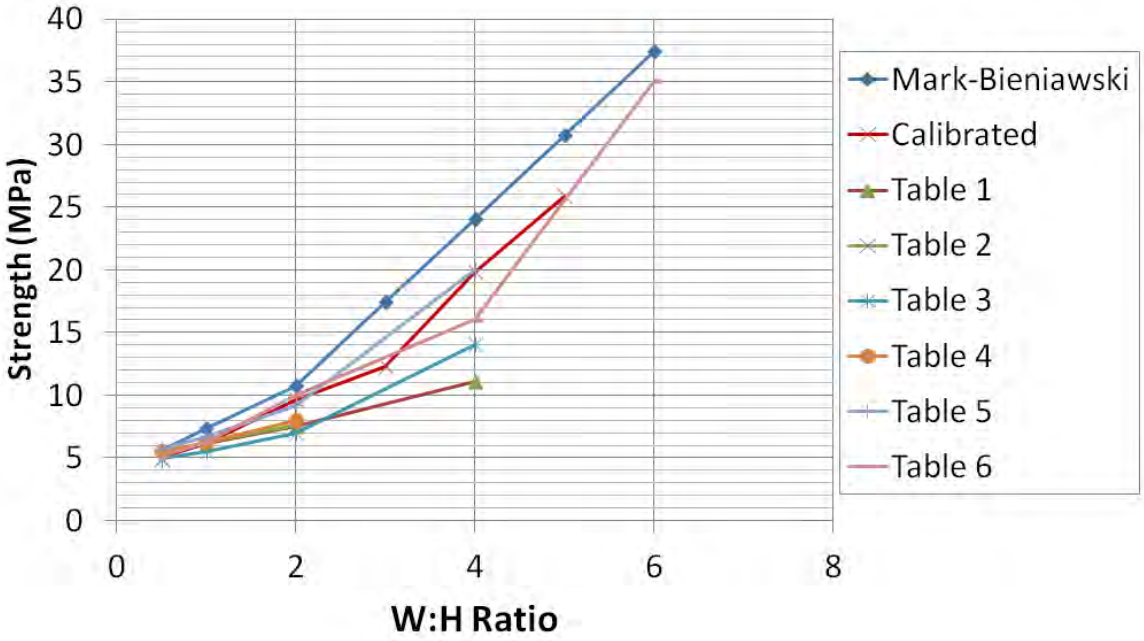

Figure 7.6: Ultimate strengths of 2D pillar model from calibration tables in $FLAC^{3D}$.

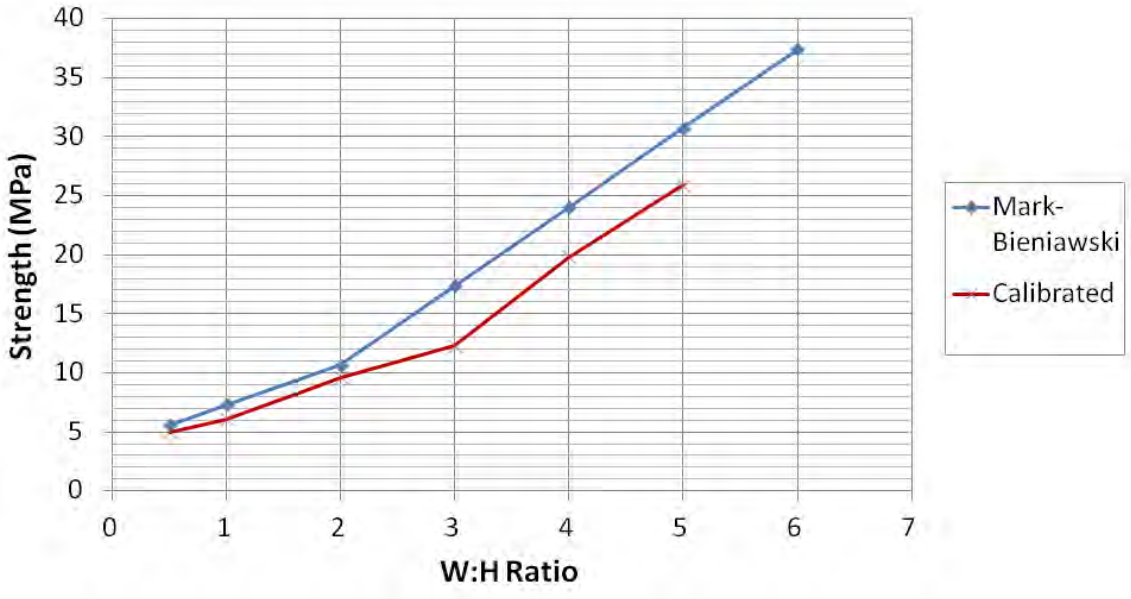

Figure 7.7: Pillar strengths of calibrated $FLAC^{3D}$ model compared to Mark-Bieniawski strength formula.

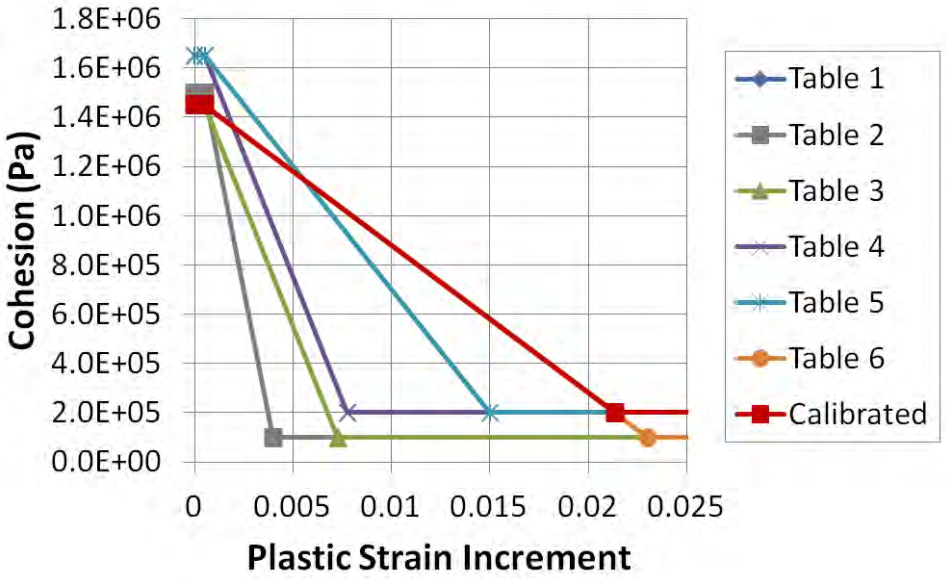

Figure 7.8: Cohesion input values for MCSS pillar models.

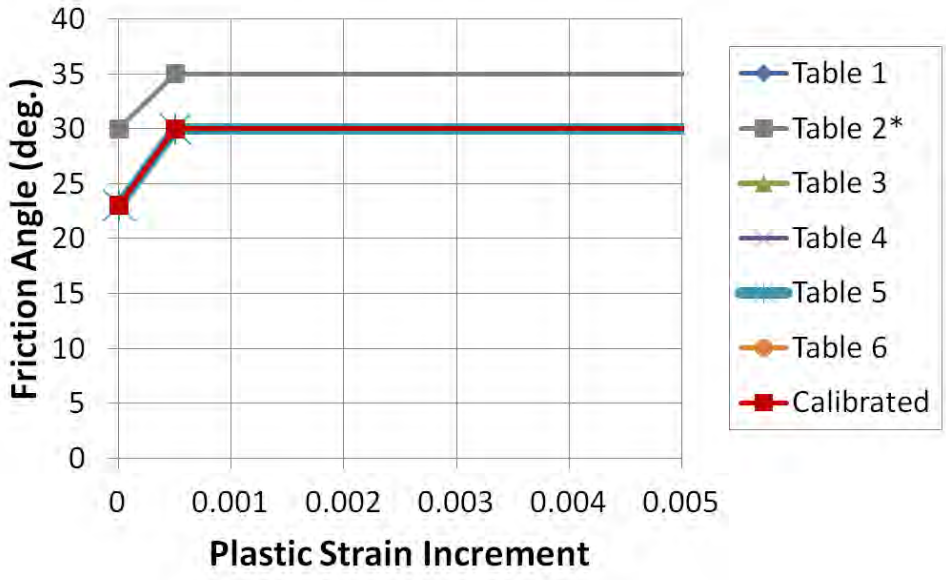

Figure 7.9: Friction angle input values for MCSS pillar models.

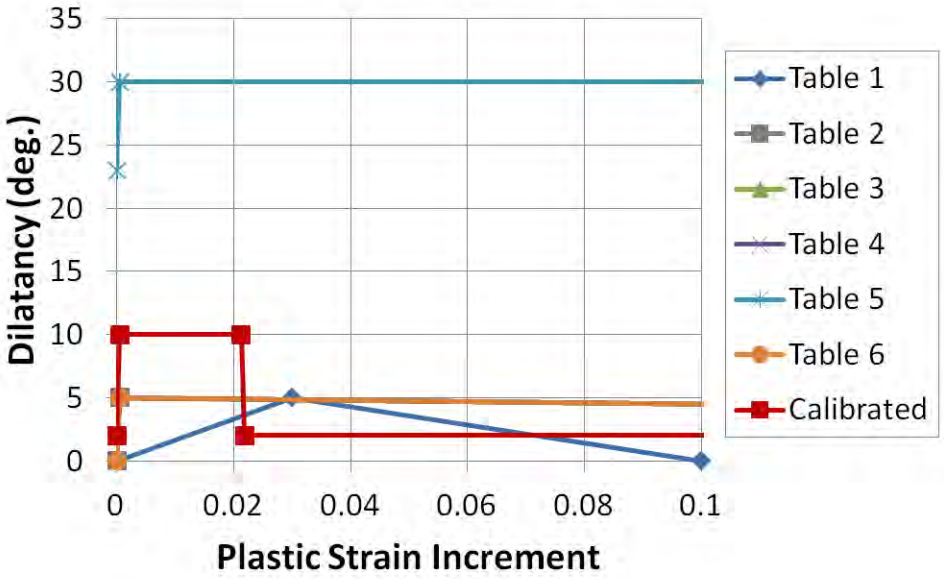

Figure 7.10: Dilation angle input values for MCSS pillar models.

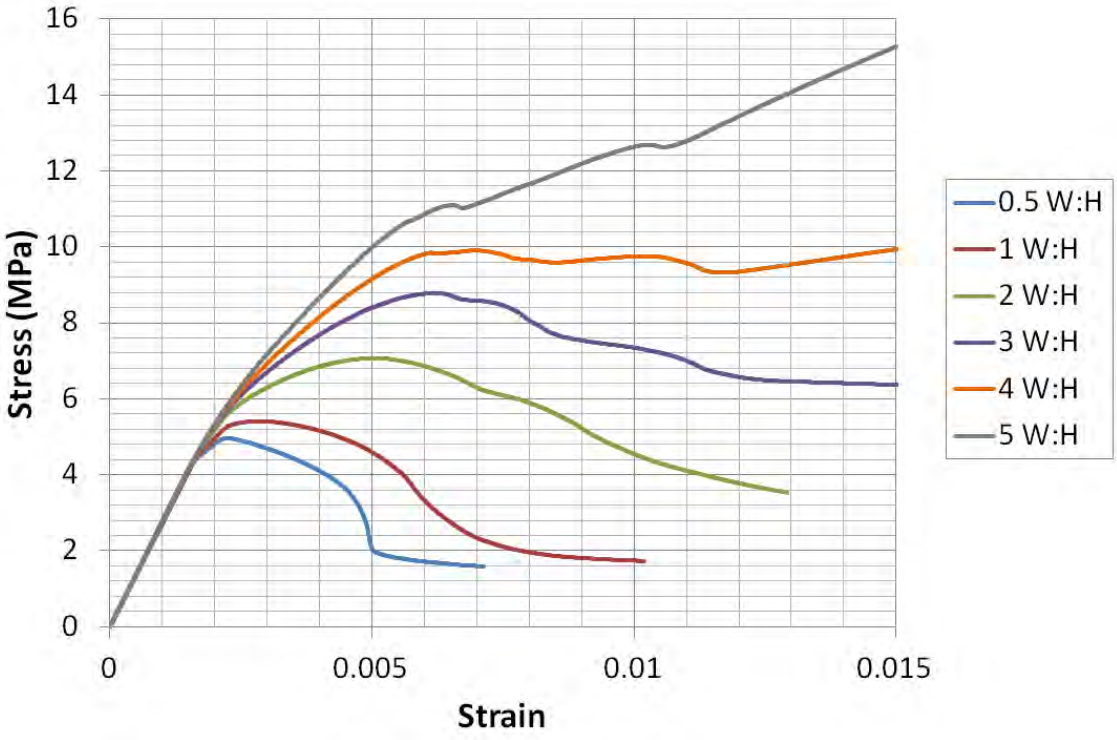

Figure 7.11: Stress-strain results of calibrated 3D pillar model.

The ultimate strength values were again compared against the Mark-Bieniawski strength formula, but in this instance a finite length dimension was applied. The Salamon-Munro strength formula, which is only applied to square pillars, could also be used to assess the pillar strengths in the three dimensional case. The pillar strengths recorded from these tests are shown in Figure 7.12 with the two selected pillar strength formulas included as references. The modeled pillar strengths fell close to the range established by the pillar strength formulas, however was found to lie slightly lower than the Salamon-Munro value for the 2:1 pillar and would greatly exceed the expected strength of the 5:1 pillar had the test not been stopped at the arbitrarily derived 1.5% strain limit.

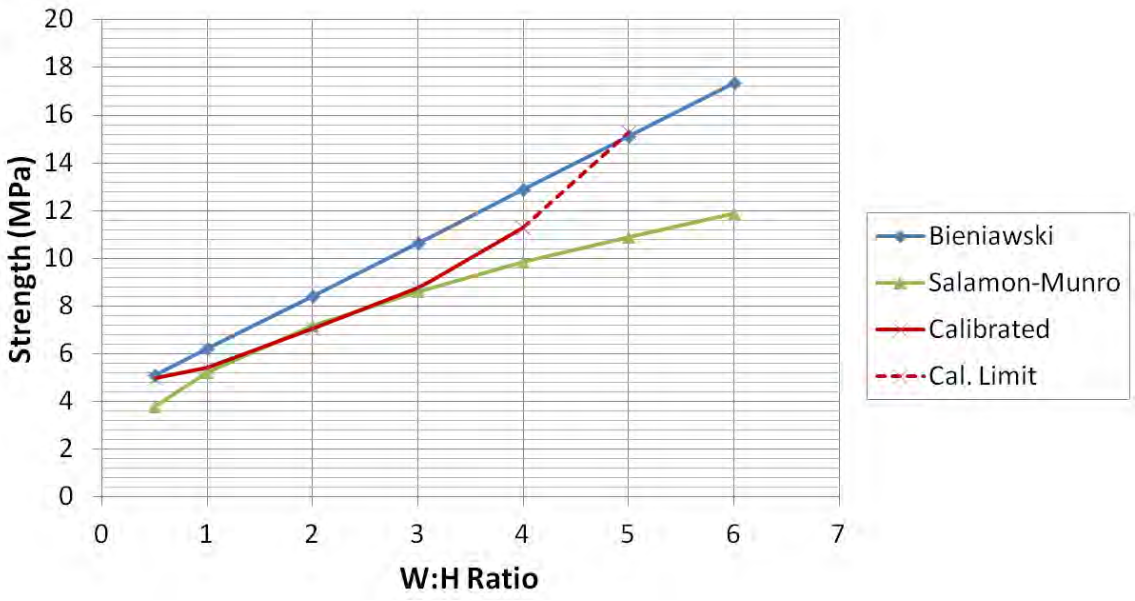

Figure 7.12: Calibrated strength values of pillars from 1:2 to 5:1 width-to-height as compared to empirical formulae.

The post-peak pillar responses of the three-dimensional model were also shown to be in good agreement with the *in situ* pillar tests conducted by Wagner and Van Herdeen. The values which Wagner obtained for the post-failure modulus of South African coal pillars are shown in Figure 7.13. The ranges, when marked, indicate the average and the maximum slope of the post-failure stress-strain response which were recorded at each width-to-height

ratio. The maximum values of the pillar post-failure modulus in the $FLAC^{3D}$ pillar models are projected onto this plot for the three width-to-height ratios within the scope of the Wagner study. Only the maximum slopes are presented because the residual strength of the continuum model prevented the calculation of average post-failure modulus from holding physical significance. The complete tabulated $FLAC^{3D}$ post-failure modulus results are listed in Table 7.1 and were within expected ranges.

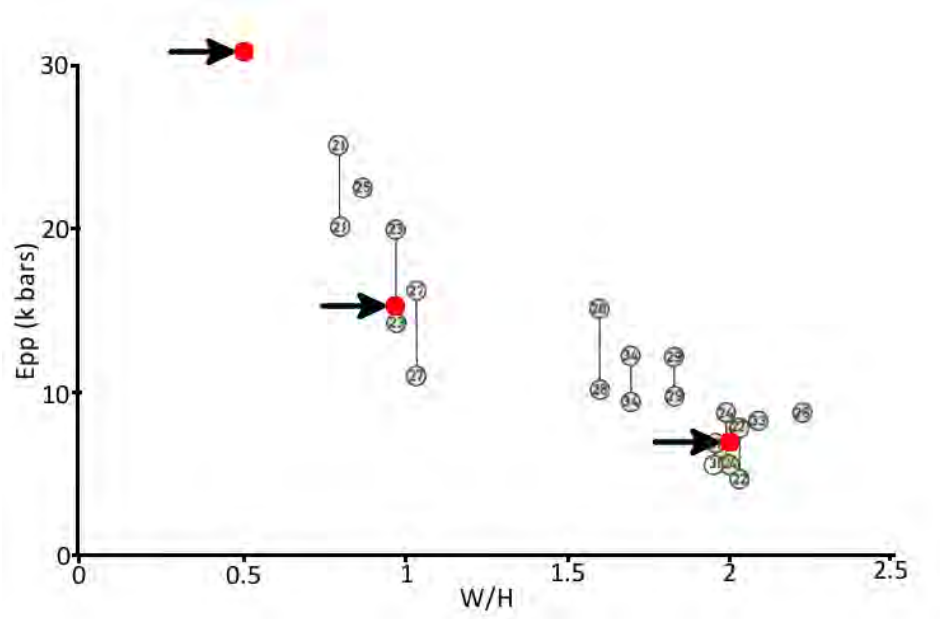

Figure 7.13: Wagner post-failure modulus from [120] with overlayed $FLAC^{3D}$ results at 0.5, 1, and 2. The range of post-failure moduli from Wagner represents the maximum and the average post-failure modulus while the $FLAC^{3D}$ results show the maximum modulus only.

Table 7.1: Steepest post-failure modulus (E_{pp}) of calibrated $FLAC^{3D}$ pillar trials.

W:H	Min. E_{pp} (GPa)
1:2	-3.14
1:1	-1.51
2:1	-0.67
3:1	-0.99
4:1	-0.45
5:1	+0.62 (avg.)

The calibrated $FLAC^{3D}$ pillar model was seen to match desired ultimate strength values as determined from the Mark-Bieniawski and Salamon-Munro pillar strength formulas. The post-failure modulus fell within the ranges established by the Wagner *in situ* pillar tests for width-to-height ratio pillars 2:1 or smaller. A rapid increase in post-failure modulus was also observed in the $FLAC^{3D}$ models for pillar sizes 4:1 and larger, as is supported by pillar collapse case history. From these results it was concluded that the pillar model was appropriately calibrated for continued testing under potentially unstable failure conditions.

CHAPTER 8

2D MODEL OF LOCAL LOADING STIFFNESS

A series of two-dimensional tests were conducted in $FLAC^{3D}$ to simulate a coal seam being loaded by an elastic rockmass. An excavation was made in the model to form a single pillar with a width-to-height ratio of between 1:1 and 5:1. Soft roof and floor conditions initiated unstable failure of the pillar when more elastic strain energy was released from the rockmass than could be statically stored or consumed. The instability identifiers developed in Chapter 5 were recorded during the tests to provide a method of identifying the occurrence of physical instabilities in the model. The static energy balance from Chapter 6 was used to quantify the magnitude of the simulated coal bumps. The identifiers and energy balance were used to analyze the expression of unstable failures and their applicability for studying physical instability was explored in the single pillar mine model.

8.1 Test Procedure

A mine-scale model was constructed to represent a single pillar being loaded past failure by an elastic rockmass. A velocity boundary condition was applied onto the top and bottom of the model in order to compress the rockmass and increase the stresses transmitted onto the pillar. The elastic properties of the rockmass were adjusted between tests to vary the loading stiffness which was applied onto the pillar. Soft rockmass properties were used to induce unstable failure within the brittle pillar.

The height of the pillar remained constant at 2.4 m between tests, however the width took on values ranging from 1.2 m to 6.0 m. A symmetry boundary condition was applied at the representative centerline of the pillar in order to then simulate mirrored width-to-height ratios ranging from 1:1 and 5:1. A 3 m entry was developed within the rockmass next to the pillar. An elastic sidewall was modeled outward for 80 m and was given elastic properties identical to those of the pillar. The roof and floor were given a height of 80 m. The resulting

model is shown as Figure 8.1. Note that gravitational forces were excluded for this analysis and did not play a role in the failure of the pillar.

A roller boundary condition was applied to the left and right sides of the mine model with displacement boundaries loading it from top and bottom. With the plane strain condition and the imposed symmetry condition, the system shown in Figure 8.1 was representative of an infinitely long barrier pillar with a 6 m entry on either side. The calibrated Mohr-Coulomb strain-softening model developed in Chapter 7 was applied to represent a characteristic coal pillar. The pillar was constructed of 0.1 m cubic zones in the model.

The velocity which was applied at the boundaries remained constant through each test but varied depending on the Young's modulus of the rockmass. Softer systems were loaded faster to reduce the overall run time of the tests. Stiff rockmasses were loaded slower to reduce the resulting unbalanced forces which were induced at the boundaries. Table 8.1 shows the complete listing of velocities applied for a given Young's modulus of the rockmass.

Table 8.1: Loading velocities applied to top and bottom of system for varying rockmass Young's moduli.

Rockmass E (GPa)	Boundary Velocity (m/step)
0.5	40e-8
1	20e-8
2	10e-8
5	10e-8
20	7.5e-8
40	4e-8

The initial loading of the model caused large unbalanced forces to be measured at the model boundaries. In turn, these unbalanced forces were factored into the calculation of boundary work in the static energy balance (see 6.2). Energy terms were therefore not recorded during the initial loading stages of the model, or until a vertical pillar strain of 0.002 had been reached.

Maximum velocities and accelerations were stored for the gridpoints and maximum shear strain rates were stored for the zones. The energy balance was calculated for the entire model

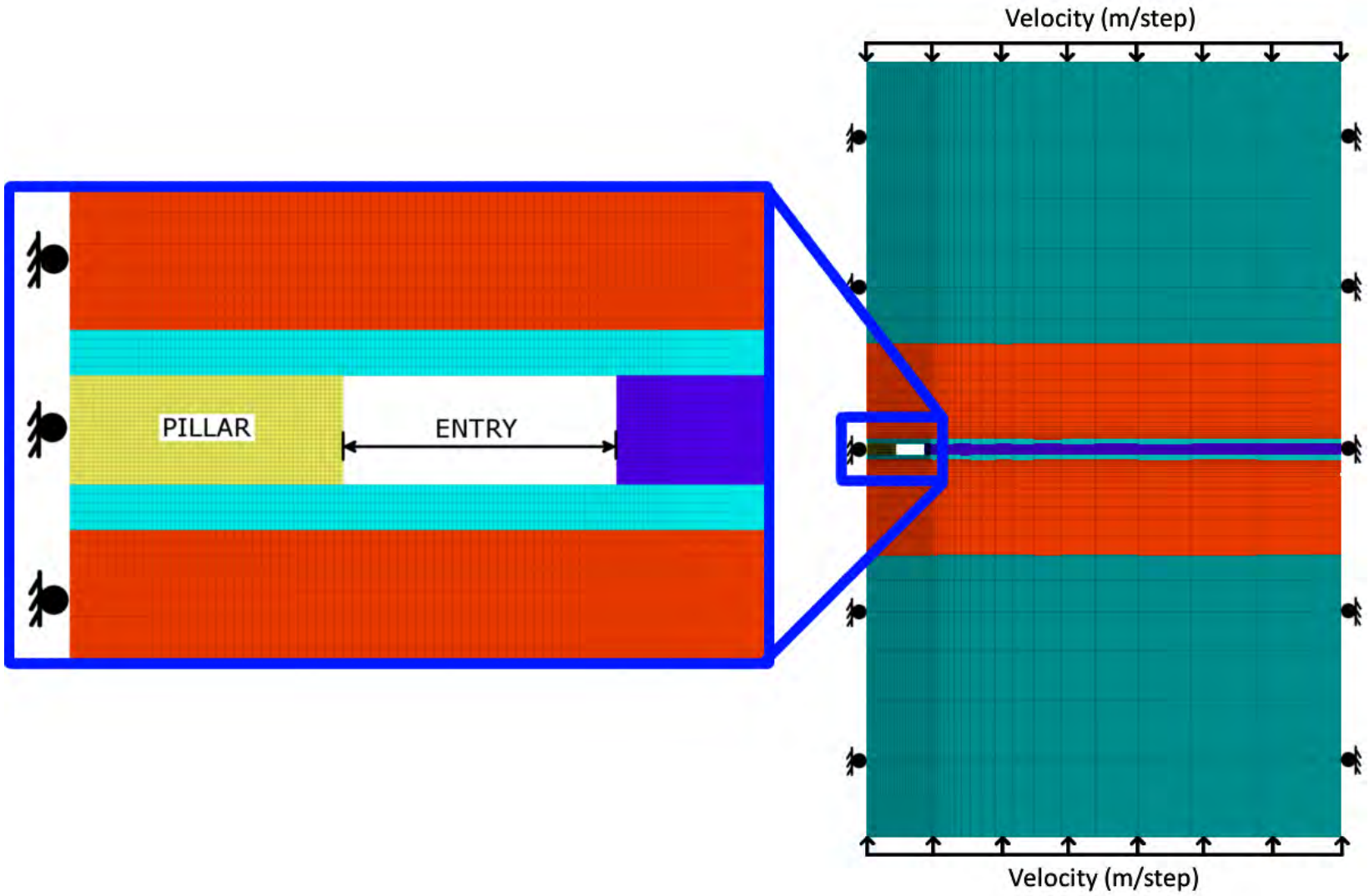

Figure 8.1: Two-dimensional pillar model with inset showing detail of pillar and entry.

at each history step and the unbalanced energy was recorded as excess energy. The boundaries were displaced inwards until an average vertical pillar strain of 0.0175 was reached. At this point the test was stopped and the calculation routine was cycled until the system came to equilibrium.

8.2 Results of 2D Pillar Behavior

The smaller width-to-height ratio pillars of 1:1 and 2:1 were seen to behave similarly to slender rock specimens in UCS tests. Wider pillars introduced significant complexities as a result of multi-stage failure modes. These complexities and the steps taken to analyze the pillar behavior are discussed later in this chapter when width-to-height ratio 3:1 pillars are introduced.

The 1:1 width-to-height ratio pillar was seen to fail in an unstable manner for the rockmass Young's moduli of 5 GPa and smaller. This determination of instability could be made directly from the pillar's stress-strain behavior, shown in Figure 8.2. The pillar deviated from calibrated stress-strain behavior in cases of unstable failure and assumed a reduced post-peak modulus.

The calibrated pillar strength of Figure 8.2 was reduced to 5.79 MPa and 5.28 MPa in the 1 and 0.5 GPa tests, respectively. An investigation of this strength reduction revealed that the pillar failure was more localized at the pillar rib for the softer rockmass conditions. A more complete discussion is given for the wider 3:1 and larger pillars in which this effect was more pronounced.

The maximum velocities, accelerations, and shear strain rates are shown in Figure 8.3. The horizontal axis of the plots has been set to the average vertical pillar strain at which each maximum identifier value was recorded in the simulations. These strains may be compared against the stress and strain histories to identify periods of instability in the simulations.

The maximum velocity and shear strain rate were recorded when the pillar reached its residual strength and again became stable. The maximum acceleration was recorded while the unstable failures were occurring, at the approximate point when the difference in

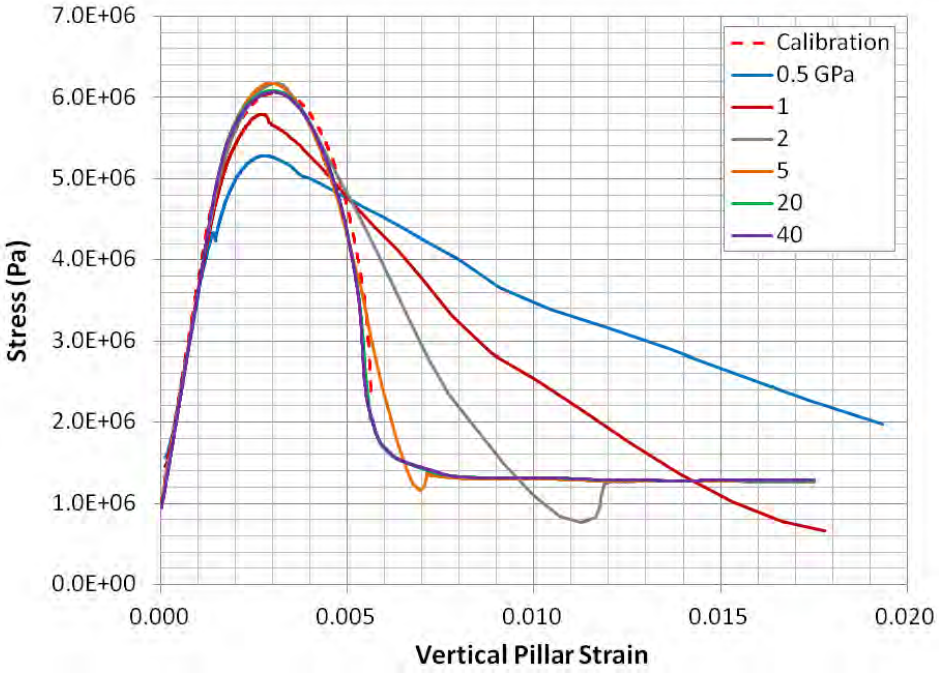

Figure 8.2: W:H=1, Pillar stress-strain response.

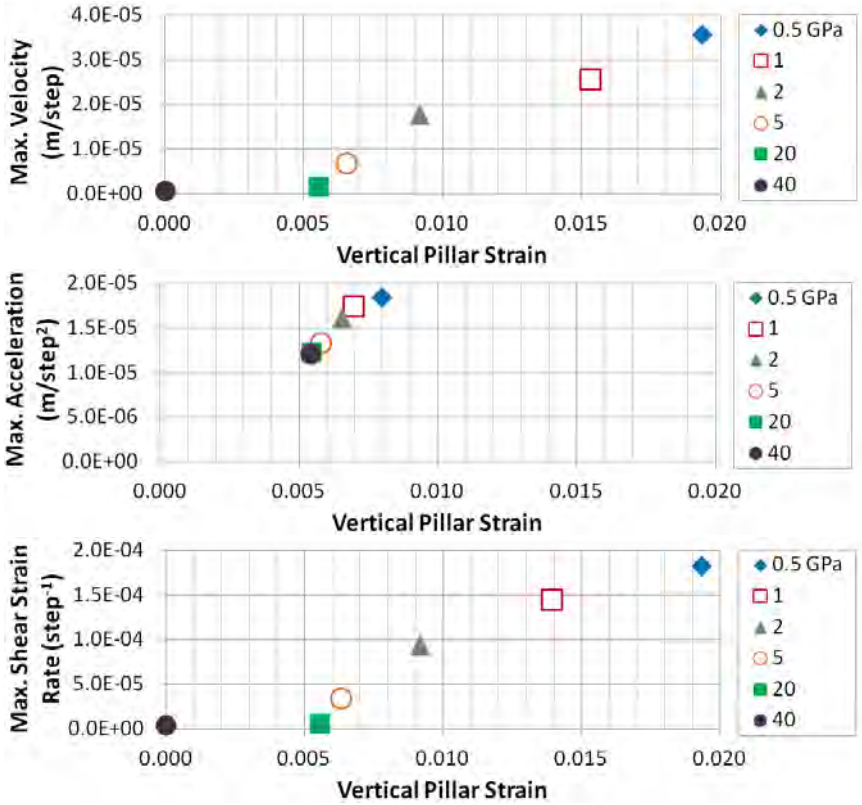

Figure 8.3: W:H=1, Maximum velocities, accelerations, and shear strain rates.

unbalanced force between rockmass and pillar reached its highest value. The results from the 1:1 pillar show a clear demonstration of the trends which were expected from the identifiers of instability.

The magnitudes of the identifiers were compared between tests to assess relative degrees of instability in the models. The magnitudes of velocity, acceleration, and shear strain rate were elevated for the lower stiffness rockmass cases of Young's moduli 5 GPa and less. The results showed a maximum shear strain rate of 1.83e-4 for the 0.5 GPa test and 4.58e-6 for the stable 40 GPa case. The 5 GPa rockmass, which caused only minor instability in the pillar, led to a maximum shear strain rate of 3.52e-5. In the 1:1 pillar the selected identifiers confirmed the presence of unstable failure in the models. The complete listing of maximum identifier magnitudes are shown in Figure 8.4.

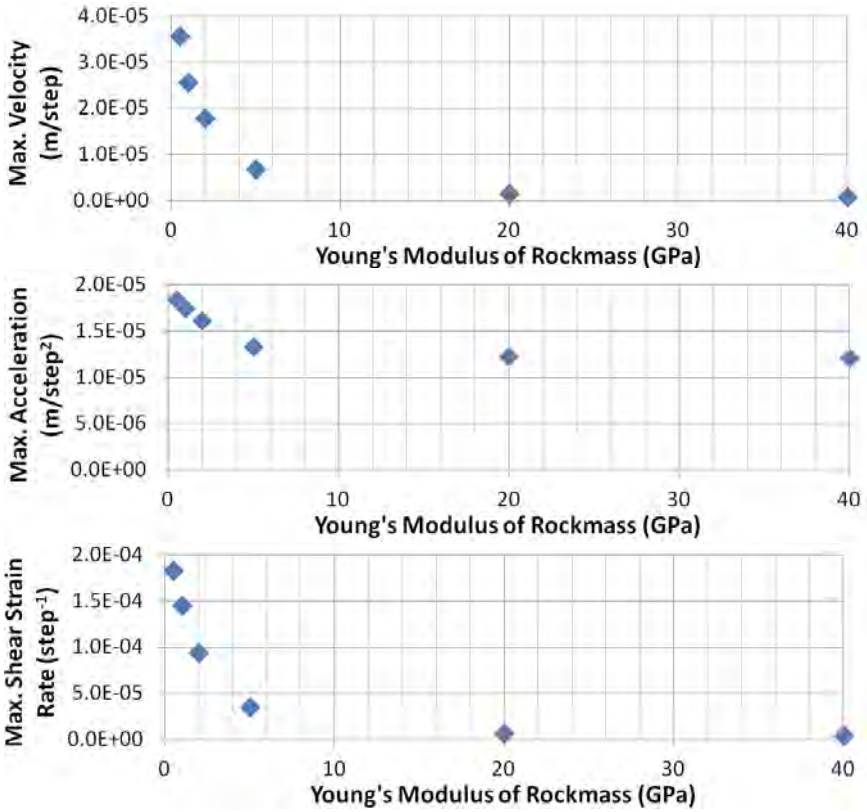

Figure 8.4: W:H=1, Maximum velocities, accelerations, and shear strain rates.

Greater interest was applied to the energy balance than the instability identifiers in the pillar model due to the continuum model's adherence to accurate static calculations of energy. The complete histories of excess energy are shown in Figure 8.5 for the 1:1 pillar tests.

A large excess energy was recorded during the initial application of strain at the boundaries of the model. The increase in excess energy was a result of gridpoint velocities increasing throughout the model until a constant, uniform strain rate was achieved at all points. Great effort was made to reduce the applied strain rate and to subsequently reduce these extraneous contributions to excess energy. Ultimately, a set of extremely slow loading velocities (see Table 8.1) was applied onto the top and bottom of the model and the excess energy was zeroed once a pillar strain of 0.002 was reached. The accounting of energy was then continued from that point.

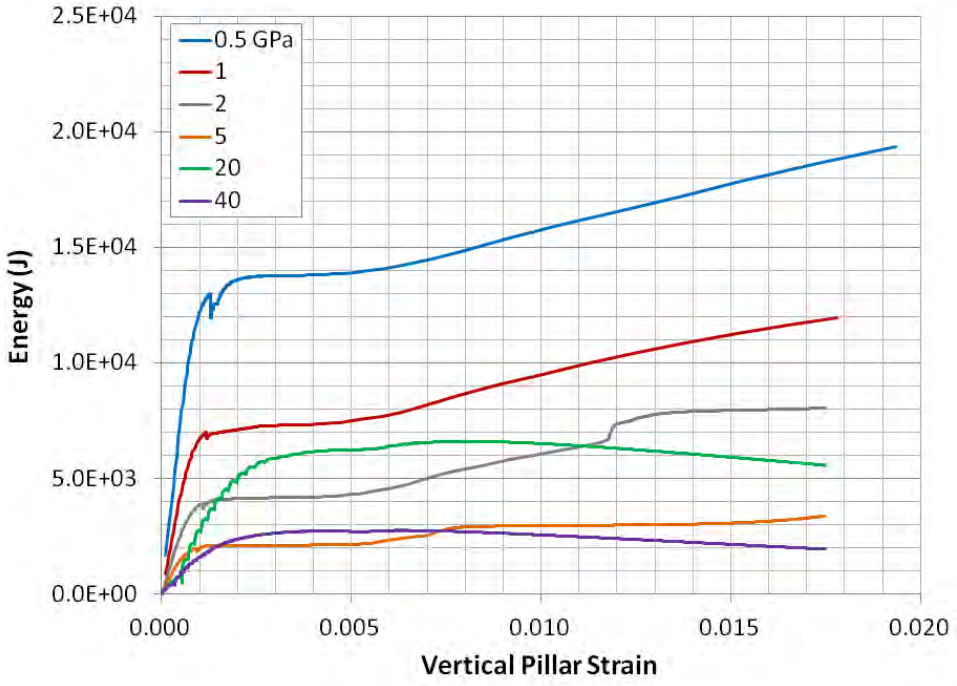

Figure 8.5: W:H=1, Pre-filtered histories of excess energy.

Figure 8.5 shows the complete histories of excess energy to demonstrate to the reader that a significant amount of excess energy is introduced into the energy balance during the initialization of the model. Figure 8.6 shows the filtered histories of excess energy as a clearer

demonstration of how excess energy may be used to calculate the magnitudes of unstable failures.

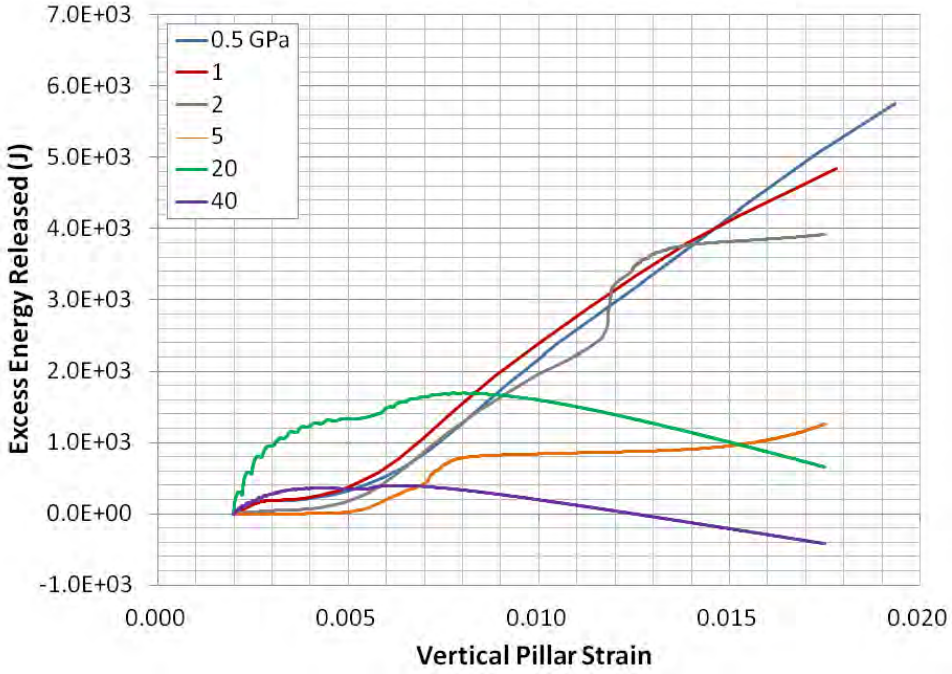

Figure 8.6: W:H=1, Cumulative excess energy.

The results of the tests showed some increases in excess energy at the beginning of the measurements due to initial loading effects. A more sizable increase of excess energy was seen for the 20 GPa test. Note that this energy may be reduced by reducing the strain rate applied to the models, however the simulations remained quasi-static during loading as measured by an unbalanced force mechanical ratio of 1e-5.

The excess energy reached the maximum magnitudes shown in Figure 8.7 during the tests. The excess energy of the 20 GPa test was elevated due to loading rate effects, however all other tests showed an increase in excess energy with a reduction in Young's modulus of the rockmass. The larger excess energies for smaller Young's moduli were caused as a consequence of more strain energy being released from the softer rockmasses than from the stiffer rockmasses during elastic rebound. The energy results from these tests matched the laboratory scale model, however the size of the mine model introduced significant noise into

the calculation of excess energy.

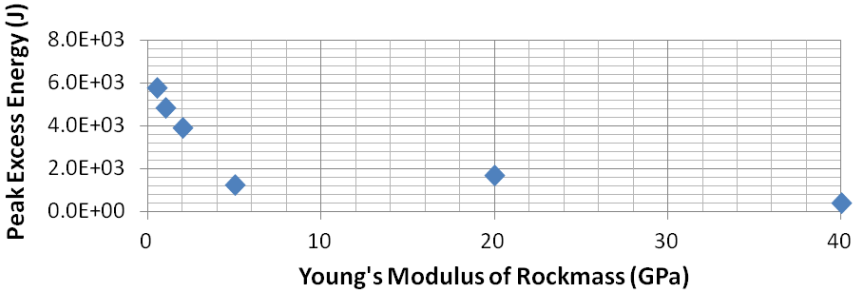

Figure 8.7: W:H=1, Maximum excess energy.

The results of the 2:1 pillar tests are shown in terms of the pillar's vertical stress and strain. Similar trends were observed as in the 1:1 tests. The strength of the pillar was reduced for rockmass Young's moduli of 5 GPa and less. This strength decrease was significant and was again a result of the localization of failure at the pillar rib. The post-peak modulus of the pillar in these cases assumed a reduced slope from the rebounding elastic rockmass.

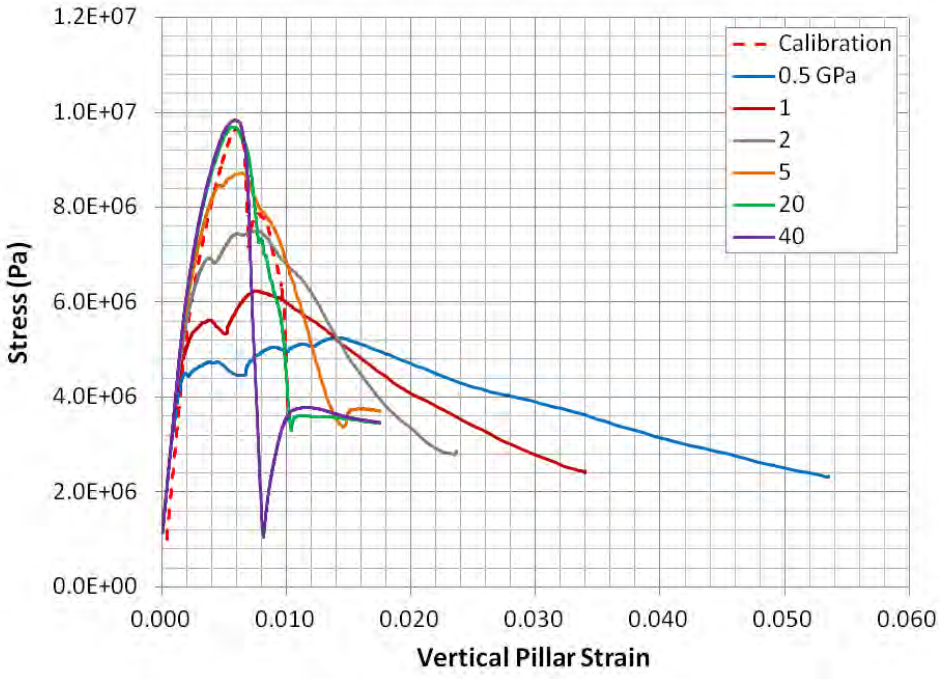

Figure 8.8: W:H=2, Pillar stress-strain response.

An unexpected result was obtained for the 40 GPa rockmass. The pillar stress-strain behavior greatly deviated from the calibrated pillar model and a sudden stress drop was observed at approximately 0.0065 strain. The sudden stress drop was caused by a favorable formation of shear planes within the pillar which initiated a kinematically favorable failure. Less energy was required for the failure and so the rockmass, even with stiff elastic properties, was capable of providing the energy required to unstably fail the pillar. This 40 GPa rockmass result for the width-to-height ratio 2:1 pillar was unique in the results of the 2D pillar strain models by providing an example of unstable failure initiated in stiff ground conditions. Figure 8.9 and Figure 8.10 display the maximum strains in the pillar following stable failure caused by the 20 GPa rockmass and the unexpectedly unstable failure caused by the 40 GPa rockmass.

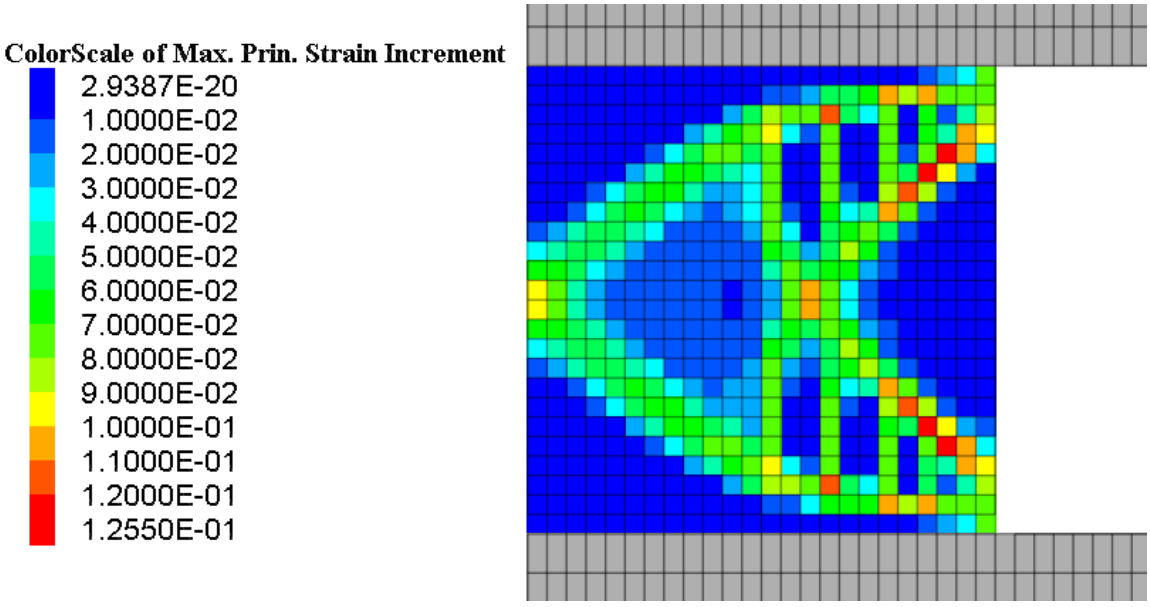

Figure 8.9: Maximum principal strains in W:H 2 pillar after stable failure in 20 GPa rock.

The maximum identifier values experienced in the 2:1 pillar model are shown in Figure 8.11. The velocity values followed expected trends with elevated velocities at the end of instability in the unstable soft rockmass conditions. The unstable 40 GPa results showed higher velocities as compared to the 20 GPa case. The 20 GPa rockmass provided the only

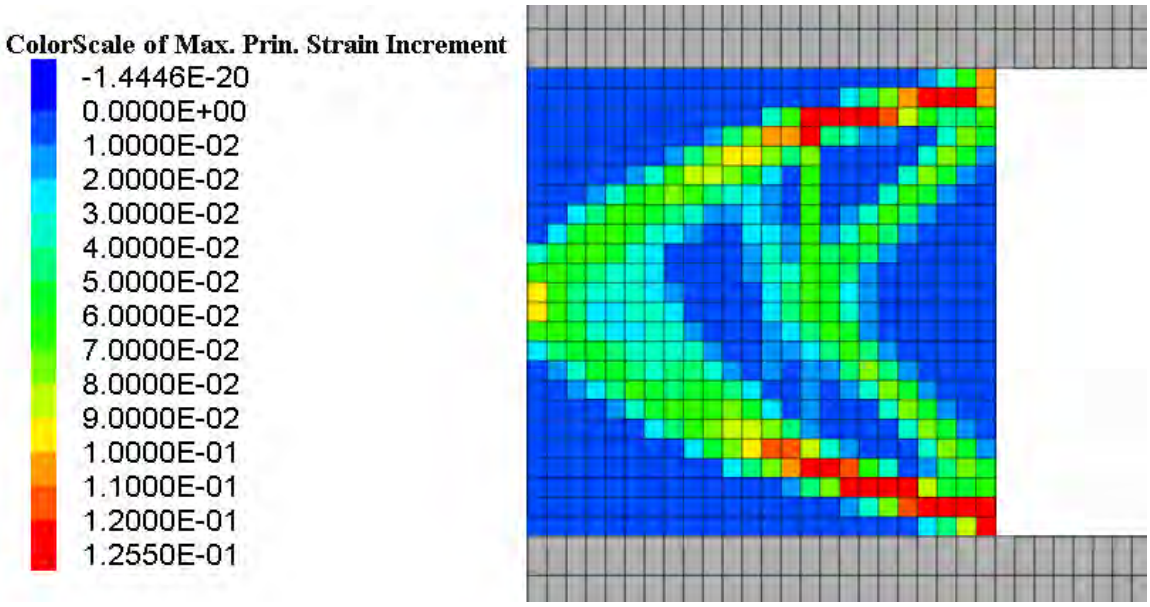

Figure 8.10: Maximum principal strains in W:H 2 pillar after unexpected unstable failure in 40 GPa rock.

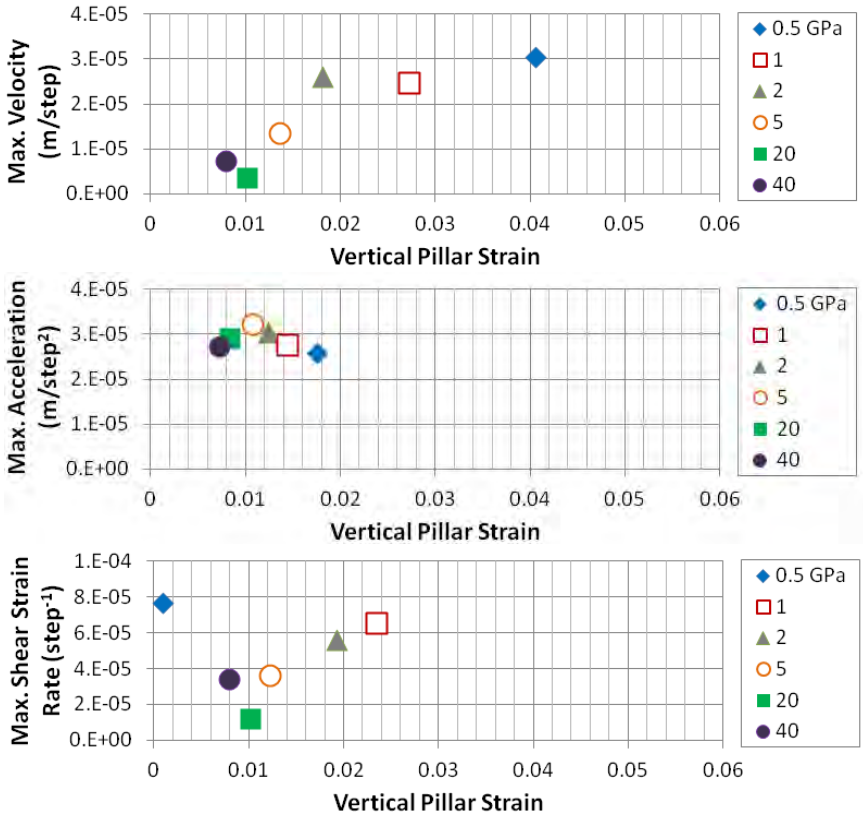

Figure 8.11: W:H=2, Maximum velocities, accelerations, and shear strain rates.

example of stable failure. Acceleration magnitudes were seen to be relatively constant between tests and were located along the pillar's post-peak response. The 0.5 GPa rockmass showed its maximum shear strain rate at the onset of failure which is good indication that the pillar became unstable at the first onset of failure.

The instability identifier magnitudes are listed as a function of the Young's modulus of the rockmass in Figure 8.12. The velocity magnitudes were seen to increase for the soft rockmasses and the stiff yet unstable 40 GPa case. The shear strain rates followed a similar trend with a more direct response to the rockmass Young's modulus.

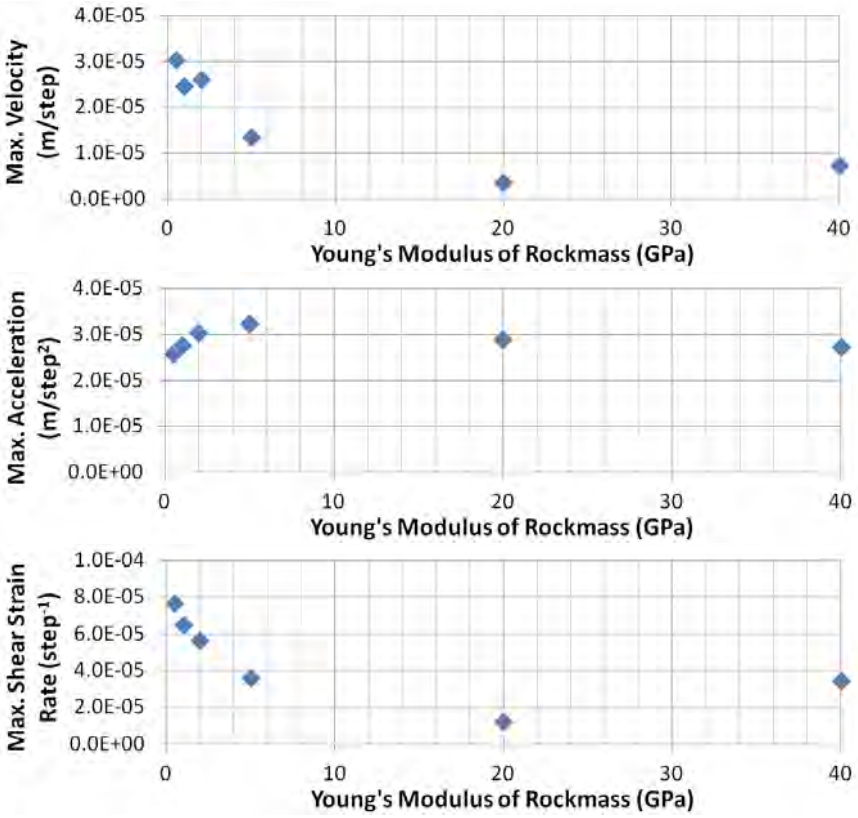

Figure 8.12: W:H=2, Maximum velocities, accelerations, and shear strain rates.

The filtered excess energy balance is shown in Figure 8.13 and the final values are plotted in Figure 8.14. The excess energy was found to be a reliable measure of the magnitude of energy released during the simulated unstable failures. Peak excess energy of 8220 J was recorded in the 0.5 GPa, as compared to 1860 J in the stable 20 GPa case. The 40 GPa

unstable failure also showed an elevated magnitude of 3720 J.

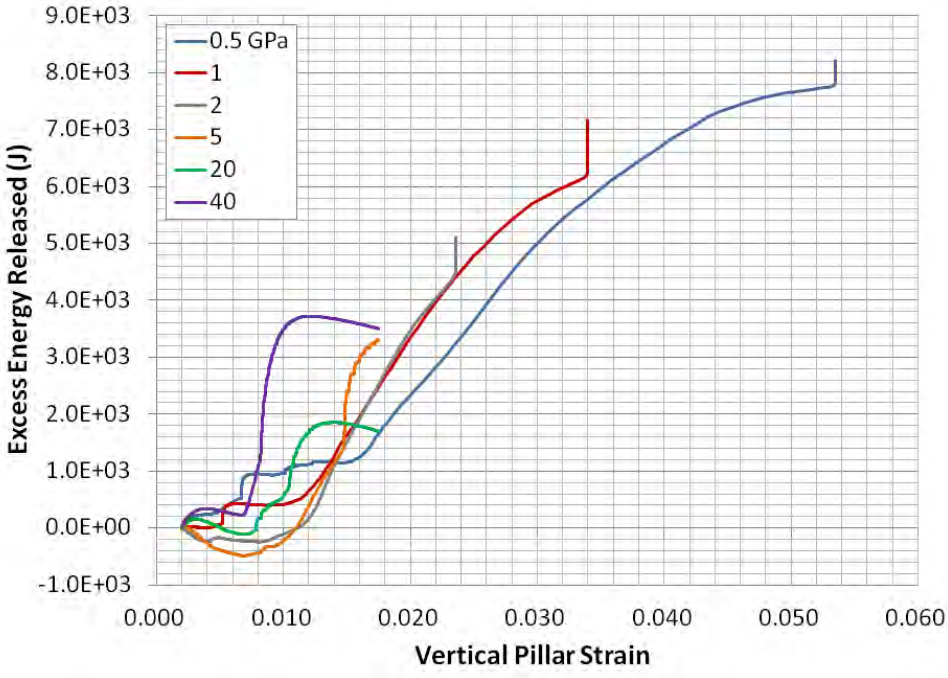

Figure 8.13: W:H=2, Cumulative excess energy.

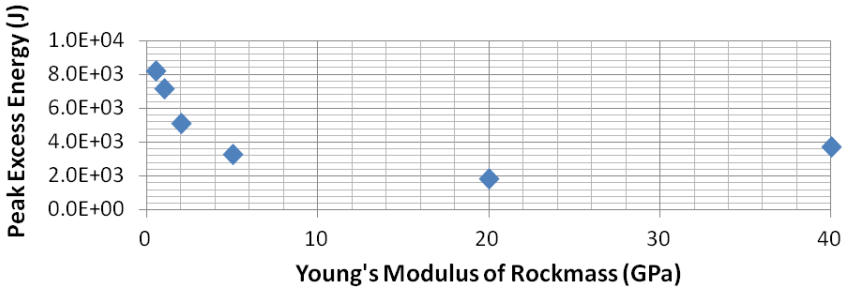

Figure 8.14: W:H=2, Maximum excess energy.

The 3:1 pillars showed a dramatic strength reduction with decreasing Young's modulus of the rockmass. Figure 8.15 shows the stress-strain behavior of the pillar and the plastic strengths of the pillars. A reduction of ultimate pillar strength with decreasing elastic rockmass properties matches rock mechanics theory for brittle rock, however the phenomenon is rarely discussed in practical mining literature. The reduction in strength was caused by higher stress concentrations at the pillar rib due to soft roof and floor conditions which led

to more localized failures. This trend was observed in the smaller pillars but the effects of rockmass stiffness on pillar strength became more pronounced with increasing widths of pillars.

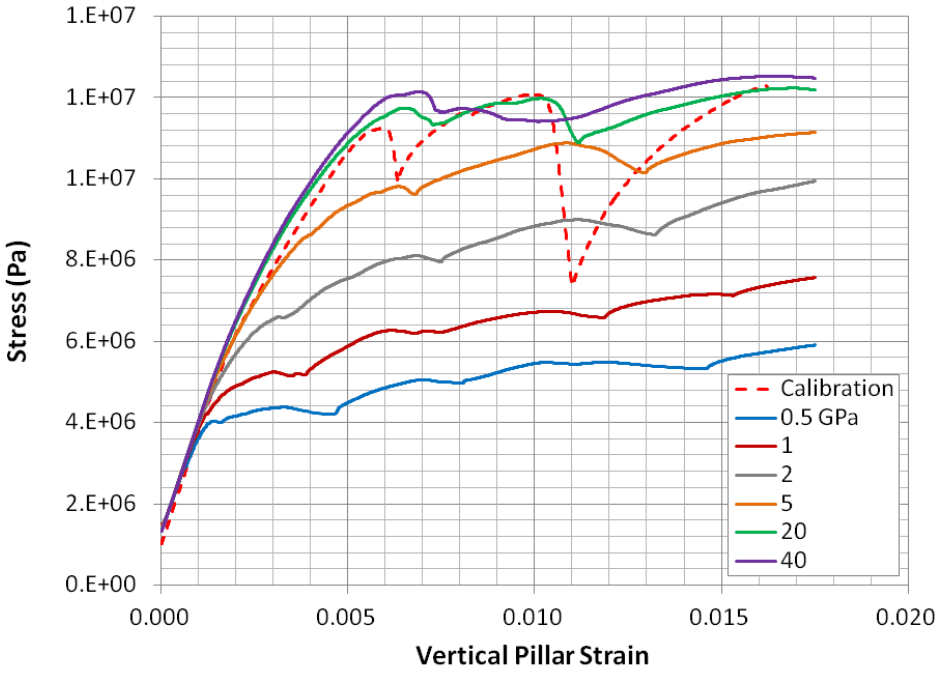

Figure 8.15: W:H=3, Pillar stress-strain response during failure.

Figure 8.16 shows the maximum principal strains which were calculated in the zones at the conclusion of the 0.5 and 40 GPa tests of a 3:1 pillars. These figures provide a good comparison of the localization of the pillar failure in the rib for the soft roof and floor. The figure shows that pillar failure was concentrated more closely to the pillar rib for the soft 0.5 GPa rockmass condition with zones in the rib experiencing larger strains.

The occurrence of unstable failure could not be identified directly through the stress-strain behavior of the pillar. An unstable failure at the rib of a wide pillar did not significantly affect the average pillar stress and strain response. The instability identifiers became useful for tracking the onset of instability in larger pillars where a stress-strain analysis would be unable to recognize unstable failures. The velocities and shear strain rates showed increased magnitudes for the 0.5 and 1 GPa rockmasses. These peak values were recorded at the onset

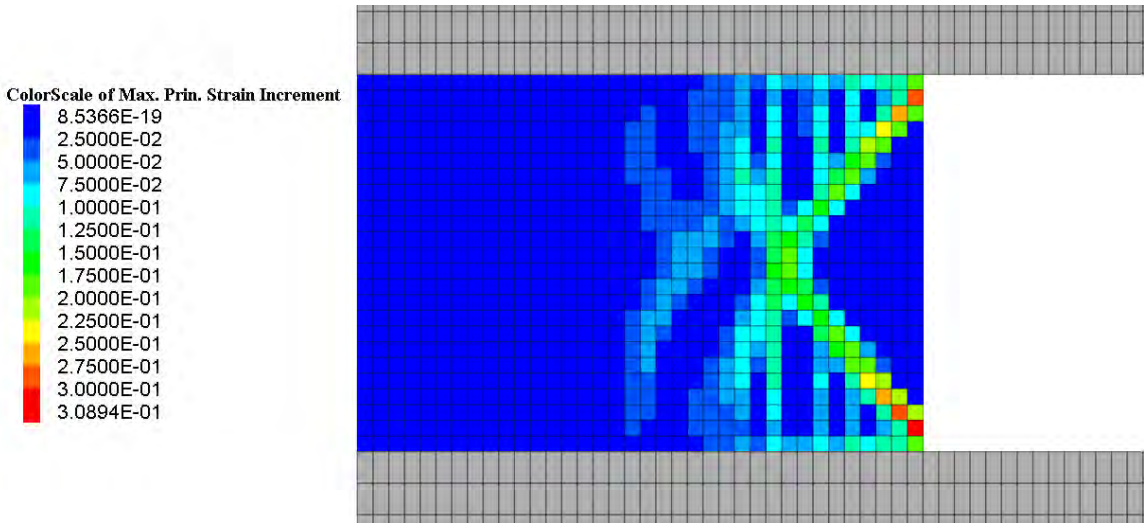

Figure 8.16: Maximum principal strain of 3:1 pillar in 0.5 GPa rock. Localized failure is observed at the pillar rib in the soft loading conditions.

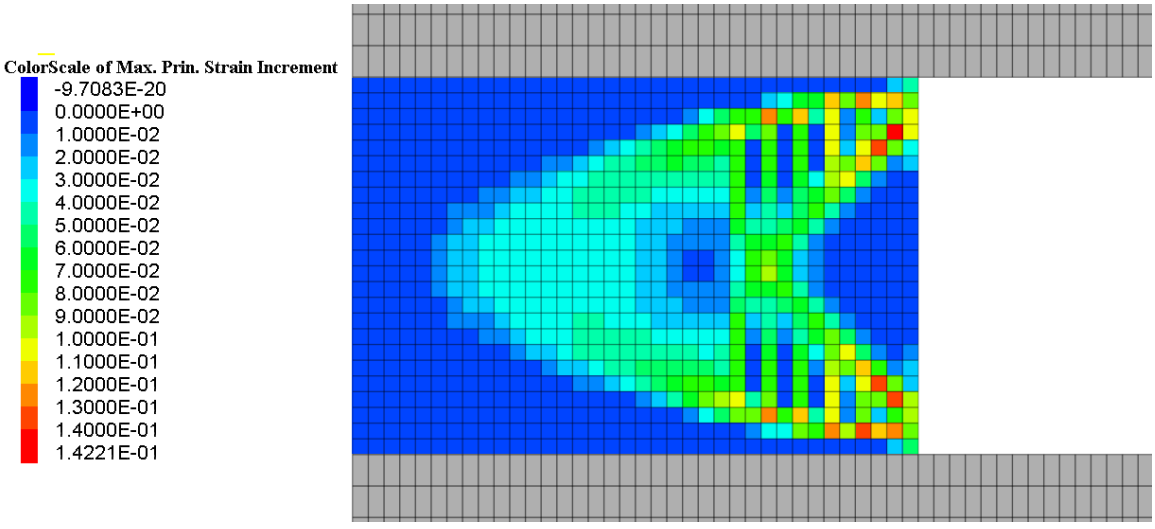

Figure 8.17: Maximum principal strain of 3:1 pillar in 40 GPa rock. A distributed failure extends over 3 m into the pillar in the stiff loading conditions.

of failure in the rib of the pillar (see Figure 8.18). The magnitudes of maximum accelerations showed no relation to unstable failure and a reduction of accelerations was observed for the more unstable test cases. This trend of reducing accelerations with increasing instability was contrary to that which was witnessed for the UCS tests and for smaller width-to-height ratio pillars.

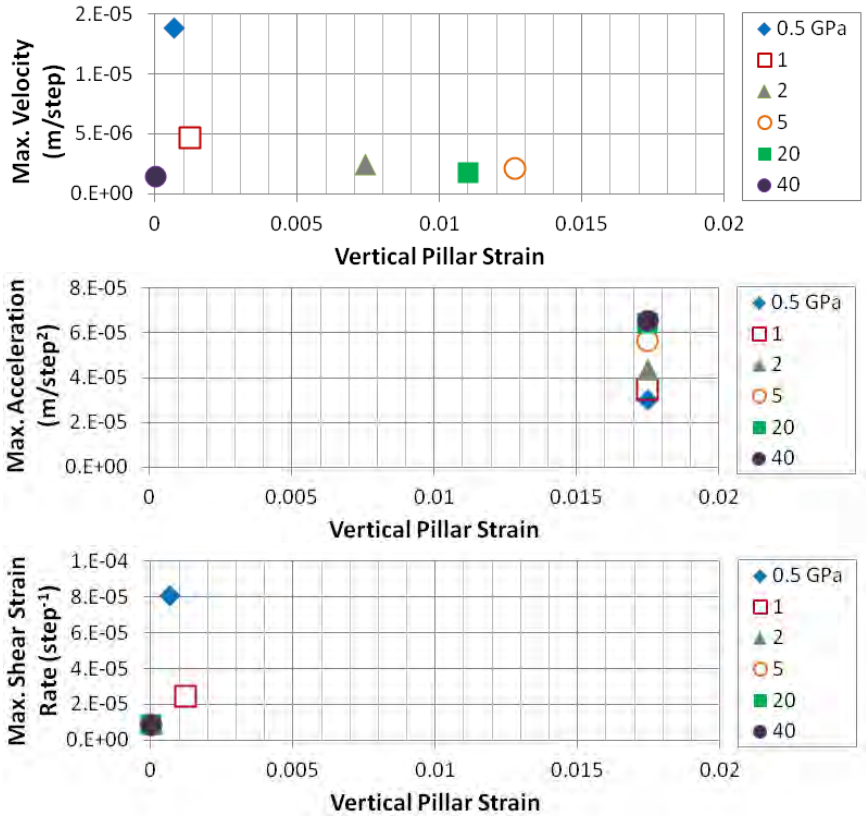

Figure 8.18: W:H=3, Maximum velocities, accelerations, and shear strain rates.

The excess energies shown in Figure 8.20 were released during the 3:1 pillar tests. The excess energies in the unstable failure cases of 0.5, 1, 2, and 5 GPa were greatly reduced from corresponding tests on smaller pillars. Two major increases in excess energy were recorded for the 2 GPa rockmass case. This two-stage increase in energy is thought to be the consequence of two major unstable failure events.

The peak magnitudes of excess energy are shown in Figure 8.21. The simulation of the 0.5 GPa rockmass showed no significant increase in excess energy from the stable 20 and 40

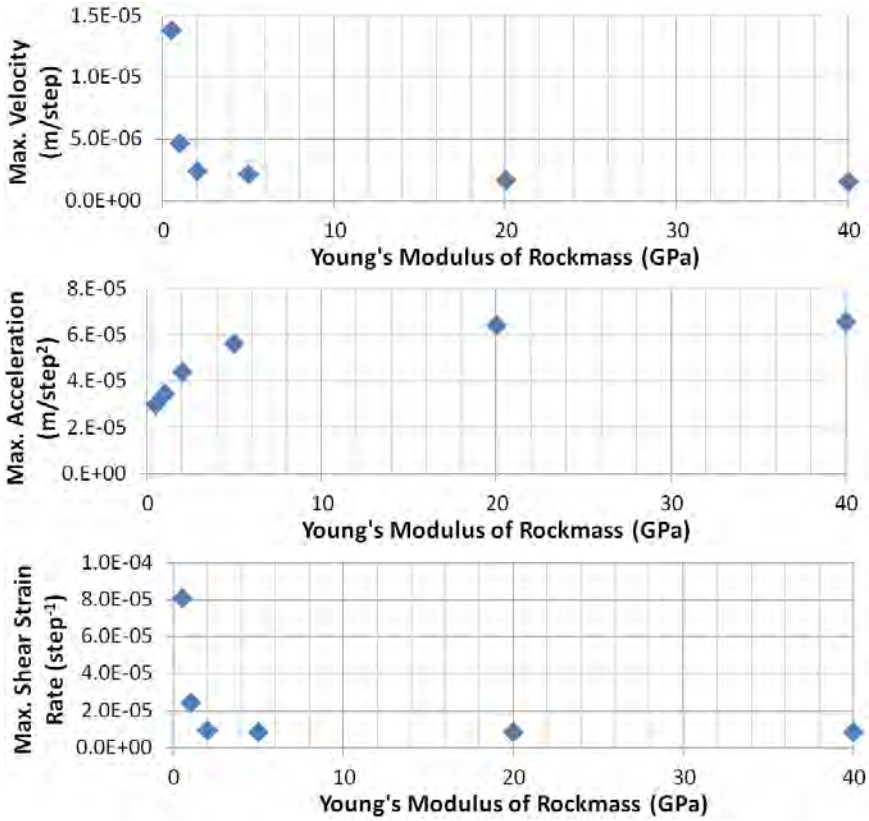

Figure 8.19: W:H=3, Maximum velocities, accelerations, and shear strain rates.

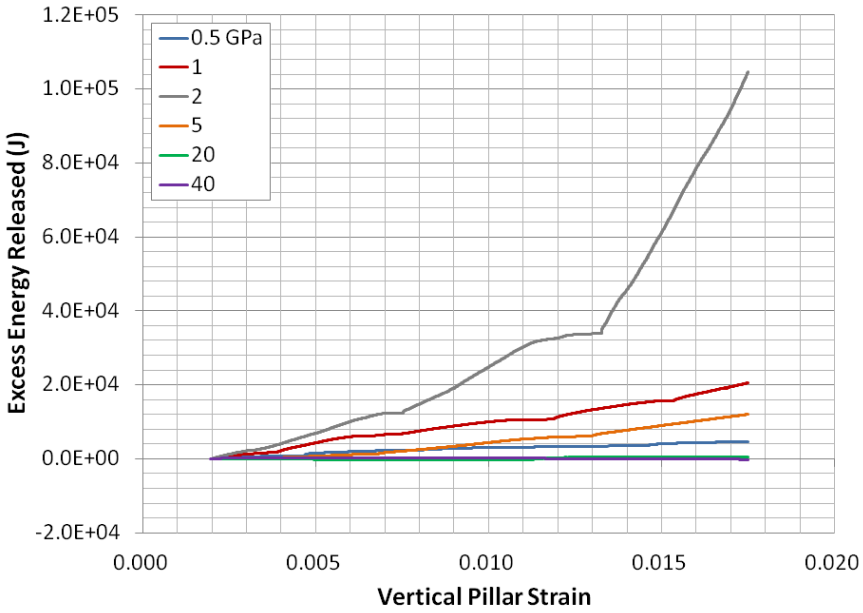

Figure 8.20: W:H=3, Cumulative excess energy after 0.002 pillar strain had been reached.

GPa cases. So, although the instability identifiers showed good indications of rapid motion in the 0.5 GPa case, the total release of energy was significantly smaller than other unstable failure cases due to a reduction in the pillar and rockmass areas which were affected by the instability. The true benefit of the excess energy balance in assessing instability was highlighted for the 3:1 pillar. Smaller localized unstable failures were readily distinguishable from larger unstable failures which affected the entire pillar stability through an assessment of excess energy.

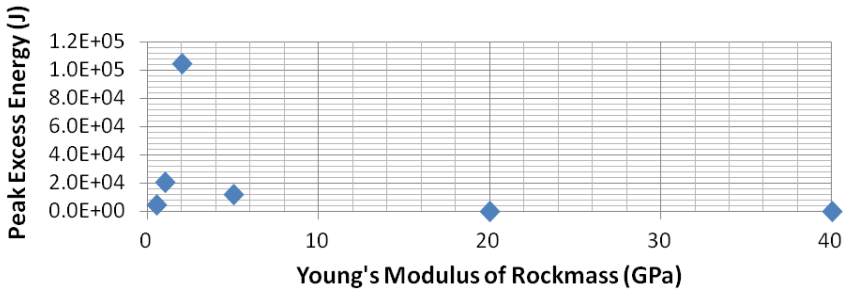

Figure 8.21: W:H=3, Maximum excess energy.

The stress-strain results of the 4:1 pillar cases showed a gradual strength increase with increasing strains due to a wide, highly confined pillar core. Figure 8.22 compares stress and strain histories against the calibrated pillar behavior.

Velocities and shear strain rates showed rapid motion of the pillar in the 0.5 GPa rockmass. Slightly elevated values were also recorded for the 1 GPa case, with all other tests resulting in comparable velocities and shear strain rates. The maximum accelerations, like in the 3:1 pillar case, showed no correlation to the expression of unstable failure in the 4:1 pillar model.

The excess energy balance of the 4:1 pillar in Figure 8.25 showed significant increases in the energy released from the 2 GPa system as compared to other rockmass stiffnesses. This increase was due to the combination of an increase in elastic energy released from the rockmass and a pillar failure mode which allowed large volumes of the pillar to fail in a sudden and brittle manner.

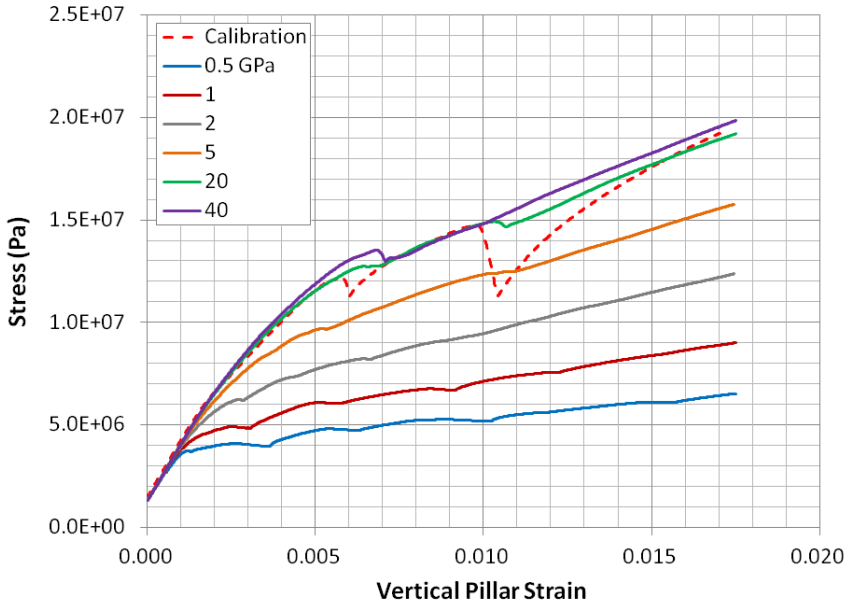

Figure 8.22: W:H=4, Pillar stress-strain response.

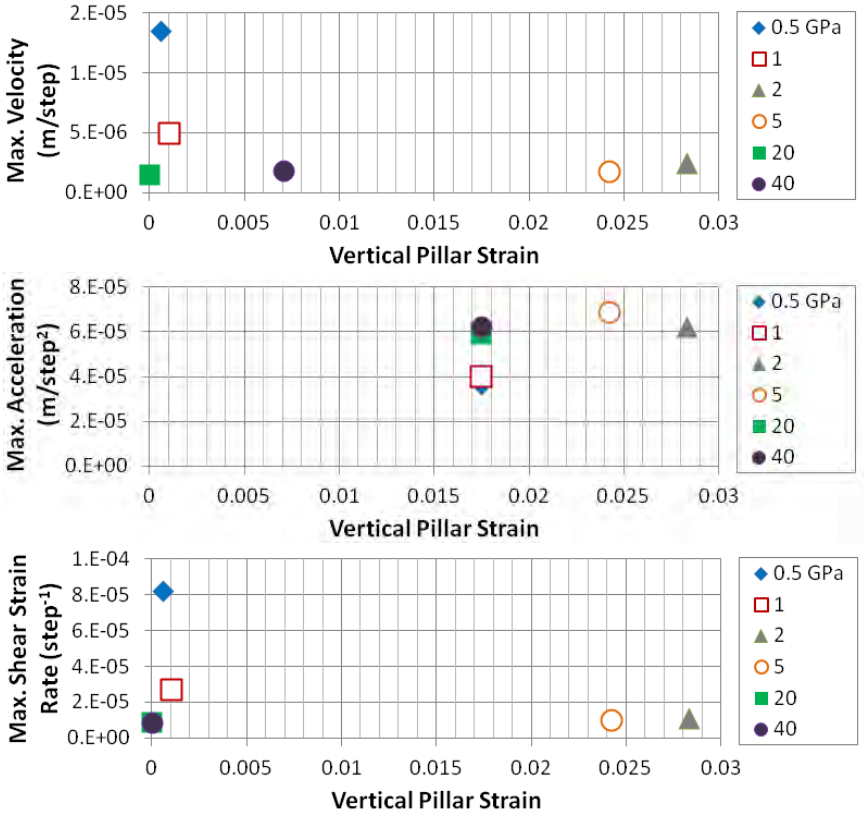

Figure 8.23: W:H=4, Maximum velocities, accelerations, and shear strain rates.

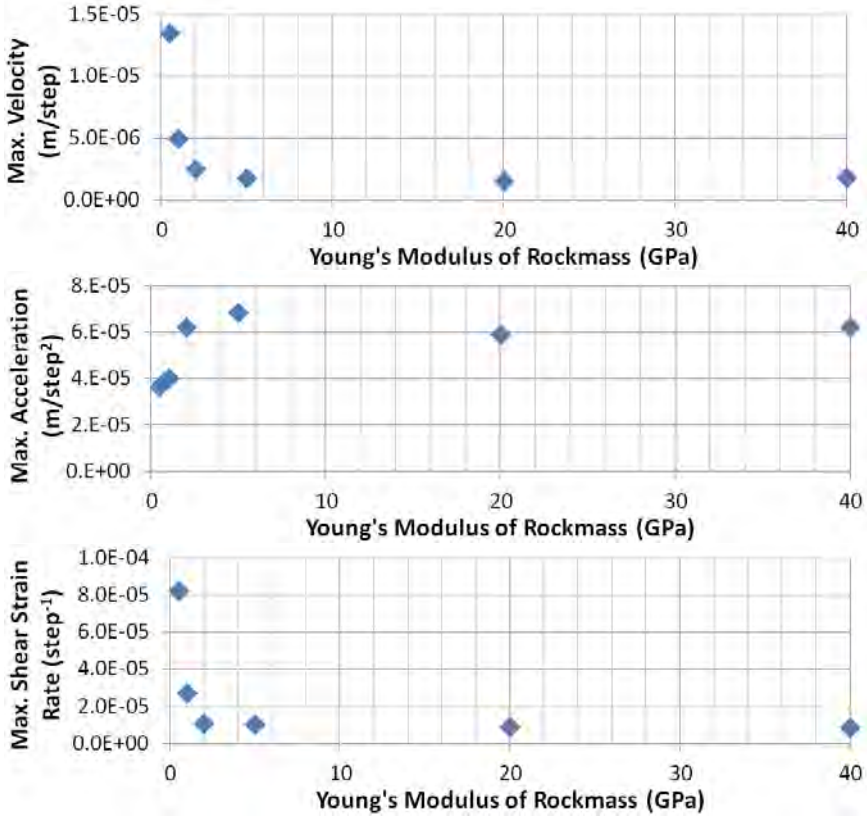

Figure 8.24: W:H=4, Maximum velocities, accelerations, and shear strain rates.

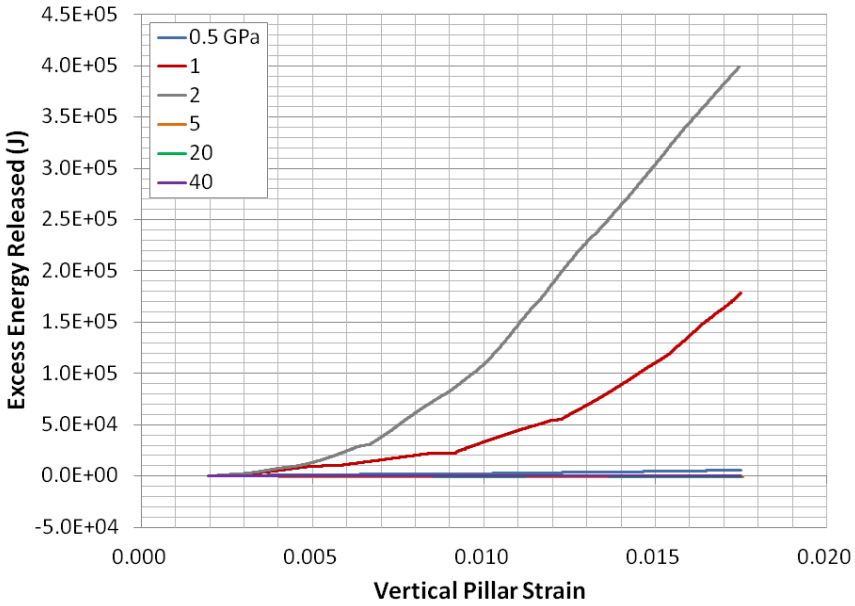

Figure 8.25: W:H=4, Cumulative excess energy.

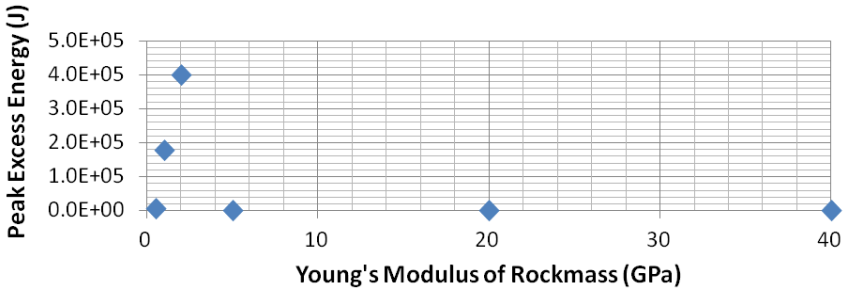

Figure 8.26: W:H=4, Maximum excess energy.

The results of the widest 5:1 pillar are shown in terms of stress and strain in Figure 8.27. The strength of the pillar was seen to increase with increasing Young's modulus of the rockmass. The pillar followed the approximate response of the calibrated pillar.

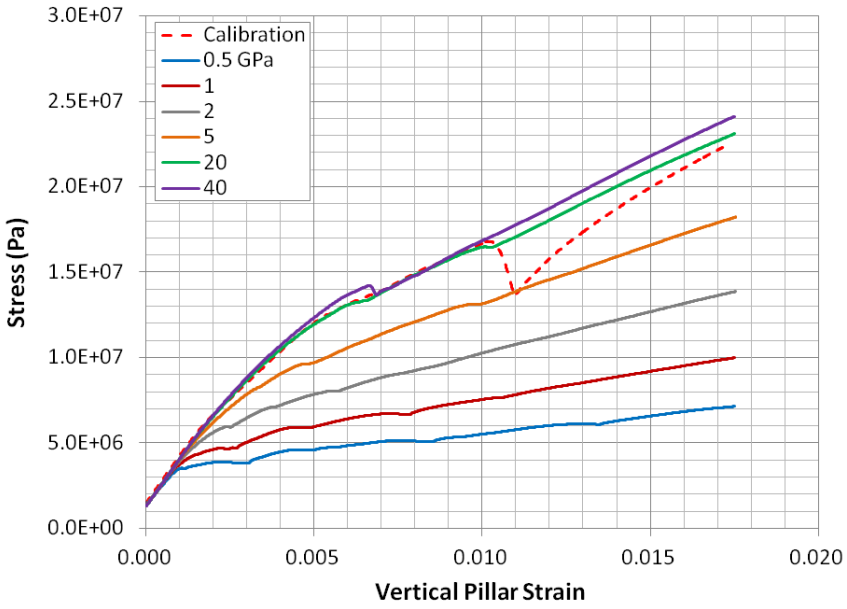

Figure 8.27: W:H=5, Pillar stress-strain response.

Instability identifier values of velocity and shear strain rate showed increases for the 0.5 GPa and 1 GPa rockmass cases. These maximum values and the strain at which they occurred may be used to show that the most rapid deformations of the pillar resulted from softest rockmass properties.

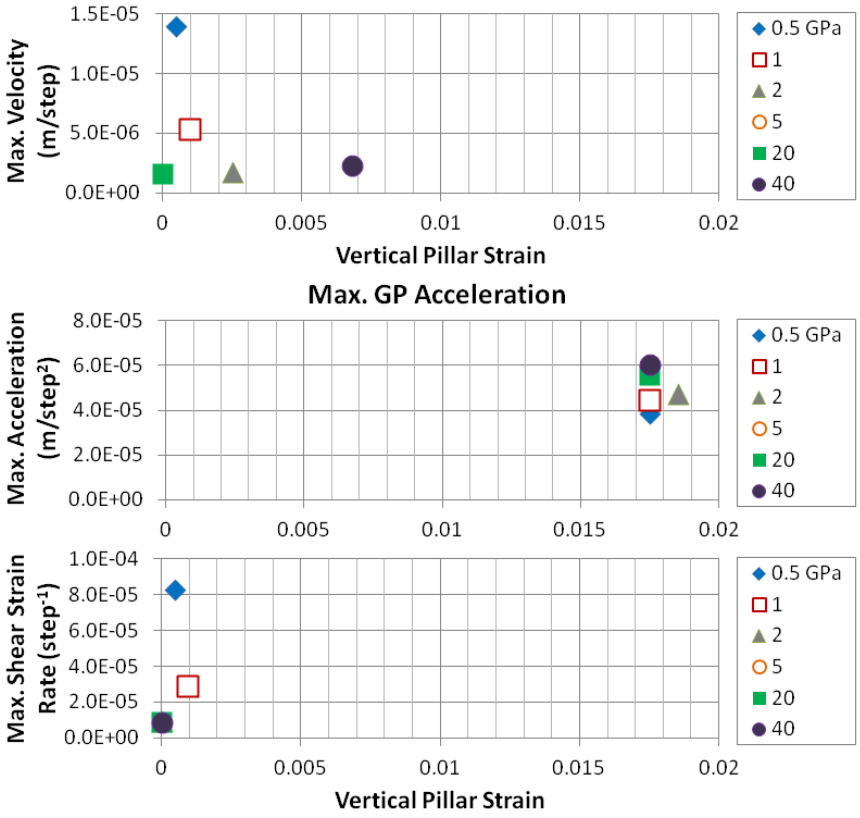

Figure 8.28: W:H=5, Maximum velocities, accelerations, and shear strain rates.

Figure 8.29 shows the maximum magnitudes of the instability identifiers for the 5:1 pillar tests. The response of the velocity and shear strain rate showed no increase in magnitudes for the 2 GPa case which was an unstable failure. In this instance the unstable failure of large portions of the pillar did not result in larger instability identifier magnitudes and unstable failure could not be identified directly from indicators of dynamic motion.

Excess energy histories showed a dramatic increase in energy released for the 1 and 2 GPa rockmass case as compared to all other stiffness values which were tested. These failures were highly unstable, and the amount of energy released from the system was greater than in the unstable tests of 4:1 pillars. The 0.5 GPa rockmass elicited a slightly increased excess energy due to the localized unstable failure at the rib.

The combined results of the energy balance calculation are shown in Table 8.2 and Figure 8.32. The 0.5 GPa rockmass caused unstable failure with elevated excess energies. The

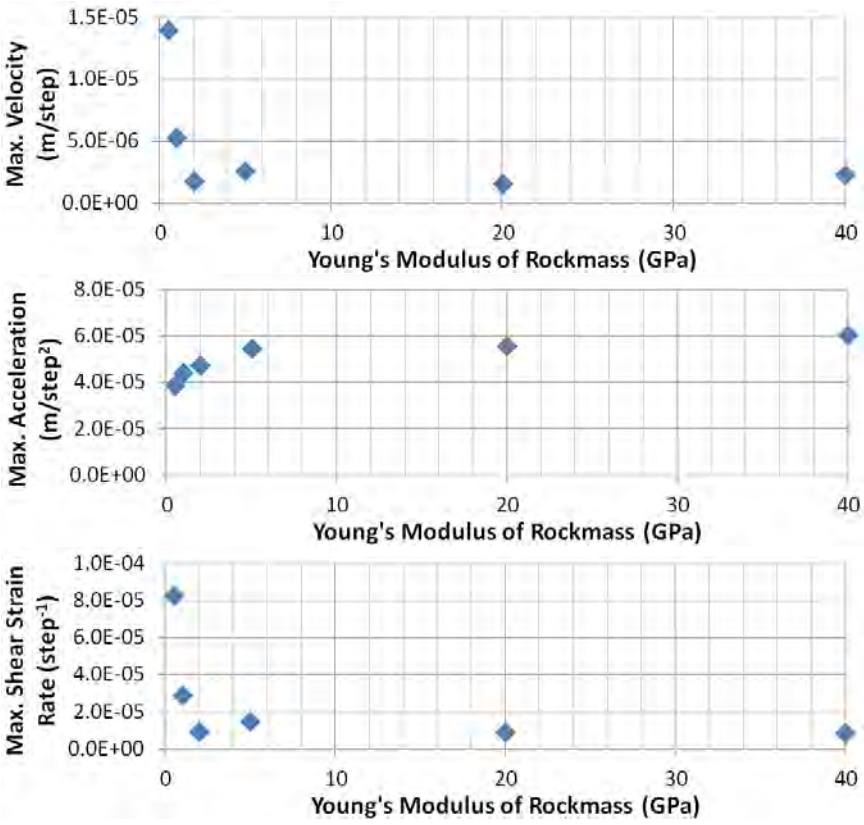

Figure 8.29: W:H=5, Maximum velocities, accelerations, and shear strain rates.

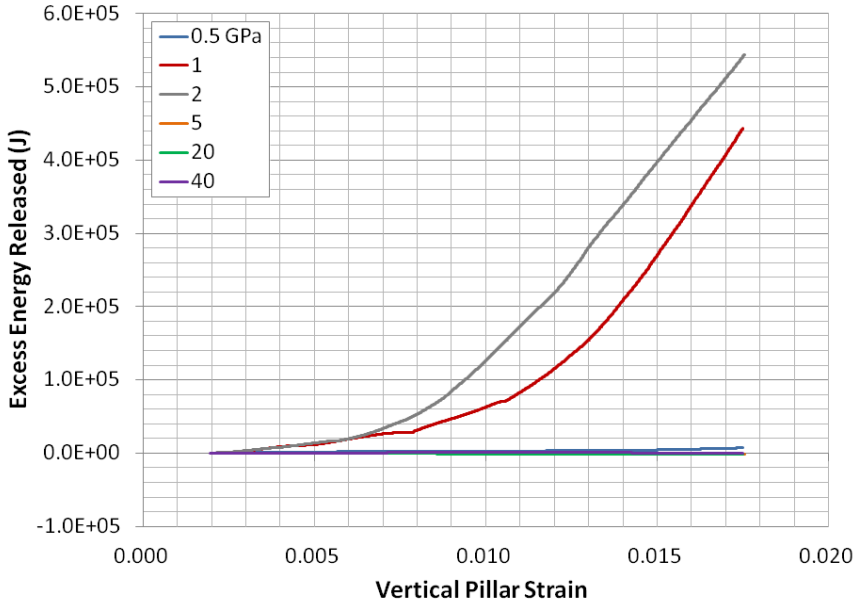

Figure 8.30: W:H=5, Cumulative excess energy.

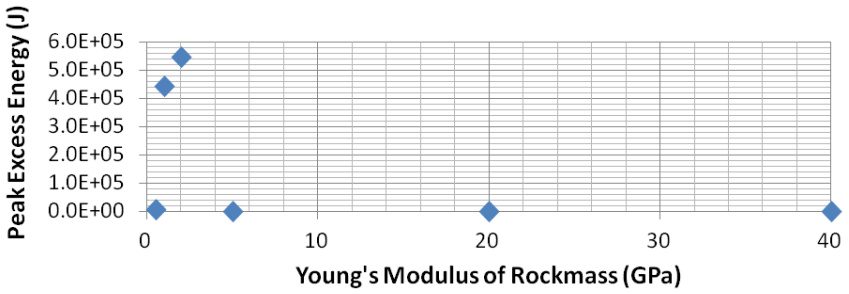

Figure 8.31: W:H=5, Maximum excess energy.

Table 8.2: Peak excess energy of 2D pillar studies.

Rockmass E (GPa)	Peak Excess Energy (J)				
	W:H 1	W:H 2	W:H 3	W:H 4	W:H 5
0.5	5.76e3	8.22e3	4.69e3	5.99e3	7.18e3
1	4.85e3	7.17e3	2.05e4	1.79e5	4.44e5
2	3.92e3	5.12e3	1.05e5	3.99e5	5.44e5
5	1.26e3	3.30e3	1.20e4	0.00	0.00
20	1.70e3	1.86e3	5.20e2	2.36e2	4.35e0
40	3.96e2	3.72e3	2.83e2	5.09e2	7.70e2

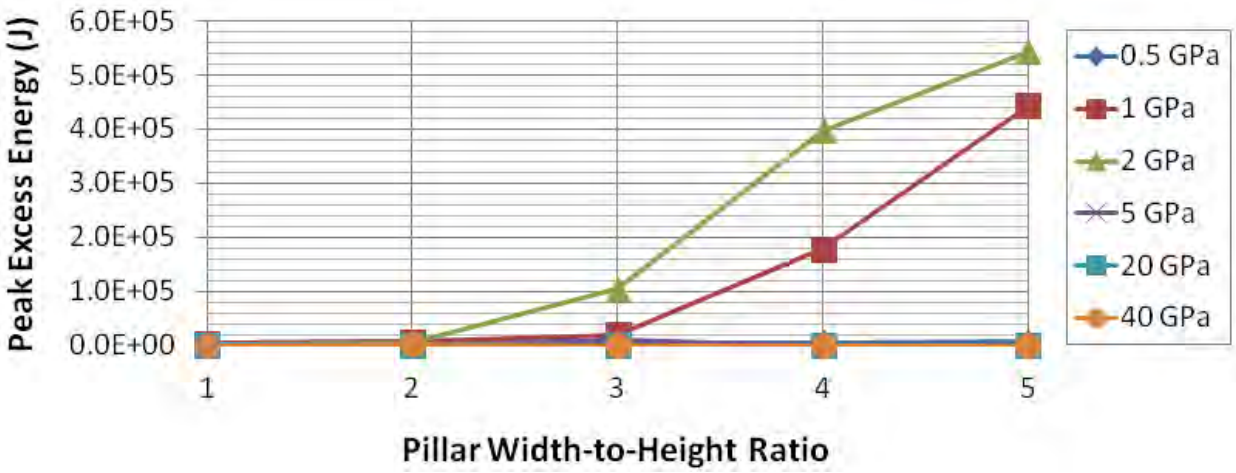

Figure 8.32: Excess energy released as a function of pillar width-to-height.

range of excess energies for different pillar widths showed a relatively small range of values for the 0.5 GPa rockmass as compared to other unstable Young's moduli which were tested. These results indicate that the unstable failure occurred locally in the pillar rib and did not extend deeper than the 1.2 m width which was modeled in the 1:1 pillar case. The 1 GPa rockmass showed an increase in excess energy between the 3:1 and the 4:1 pillar cases. This same behavior shift was observed between 2:1 and 3:1 pillars for the 2 GPa rockmass. The 5 GPa rockmass was shown to release reduced magnitudes of excess energy for the wider 4:1 and 5:1 pillars. This is thought to be a response to stabilization of the pillar with increasing widths. The results of the 20 GPa rockmass remained consistent between tests. The 40 GPa case showed an increase in excess energy for the 2:1 pillar in which an unexpected unstable failure had occurred.

8.2.1 Conclusions

The two-dimensional $FLAC^{3D}$ pillar models were tested under a range of elastic rockmass properties to elicit unstable failures for softer roof and floor conditions. The small pillars of widths 1:1 and 2:1 behaved similarly to a uniaxial compressive strength specimen. The failure of wider pillars brought added complexity into the simulation by allowing the pillar to fail in discrete vertical sections beginning at the pillar rib. This more localized view of pillar failure brought a nuance to the evaluation of unstable failure because unstable failures were allowed to occur in localized portions of the pillar without affecting total pillar stability.

In the case of the small pillars, the system released more excess energy with decreasing Young's modulus of the rockmass. The instability identifiers showed a similar trend and increased in magnitude with decreasing rockmass stiffness. The larger pillars with widths of 3:1 and greater showed a more complex failure response than their slender counterparts. Local unstable failures were observed at the ribs of the wide pillars for soft rockmass conditions. However, the propagation of the unstable failure into the confined core of the pillar was also dependent on the failure pattern which was initiated at the rib of the pillar. A striking feature of these tests was that if the material at the pillar rib was failed prior to the

more confined core, then less excess energy was released due to unstable failure. The softest rockmass of 0.5 GPa was seen to cause such high stress concentrations in localized areas of the pillar that the failure could not propagate significantly into the confined pillar core. The total magnitude of energy released was less than the more stiff 1 and 2 GPa rockmass trials.

Traditional methods of analyzing unstable failure which have been presented in the literature proved insufficient for addressing localized forms of instability in the larger pillar models. The instability identifiers developed in Chapter 5 and the excess energy balance developed in Chapter 6 were, shown to accommodate the additional complexities presented by wider pillar geometries. A few practical limitations were found for these numerical evaluation tools. Firstly, the maximum gridpoint accelerations did not correspond to systems of high instability for the pillars with widths of 3:1 and higher. Secondly, significant noise was introduced into the calculation of excess energy due to the application of strains onto the system. Modifications were made to the analysis to account for these deficits. The shear strain rates and velocities became the focus of the instability identifiers, and the energy balance was calculated after an initial application of strains. With these modifications the instability identifiers proved well suited for determining the onset of unstable failure and the presence of localized unstable failures at the pillar ribs. Larger unstable failures which affected the stability of the entire pillar could be assessed through magnitudes of excess energy released from the system.

CHAPTER 9

3D MODEL OF GLOBAL LOADING STIFFNESS

Chapter 8 previously explored the failure of large pillars through a two-dimensional pillar set in a local mine model. The instability identifiers and energy balance were employed to track and quantify the unstable failures which occurred in the pillars. In these tests, the energy which contributed to unstable failure came entirely from an elastically rebounding rockmass. These models did not include the effects of gravity and the energy to cause unstable failure came from the elastic strain energy of the rockmass. These two-dimensional tests were extended into three-dimensional models of pillars under gravitational loads in studies described within this chapter. Small modifications were made to the existing energy balance to account for the potential energy contribution made by body forces. Unstable failure was then analyzed in the context of the gravitational loading model.

The pillar, roof, and floor were modeled with a 1/4 symmetry condition to represent an infinite room-and-pillar layout with repeating pillar geometries. This scenario represents a massive collapse of a mine and defines the maximum excess energy which could be released for a given pillar geometry. If the peak strength is met and the pillar is weakened in any way, then a constant pressure would be applied onto the pillar regardless of the resulting strains. If the pillar could not increase its strength to its previous levels, then a complete crushing of the pillar would follow and the roof and floor would converge.

Width-to-height ratio pillars ranging from 1:1 to 5:1 were tested using calibrated values for the Mohr-Coulomb strain-softening constitutive model. The strain-softening material was used to represent a brittle coal pillar with increasing strength with confinement. The residual strength of the three-dimensional pillar was less dependent upon the formation of individual shear planes than the two-dimensional model and was therefore more representative of the true failure mode experienced by coal pillars.

9.1 Test Procedure

The three-dimensional model of a coal pillar was constructed in $FLAC^{3D}$ using 1/4 symmetry. The pillar height remained constant at 2.4 m between tests and its width was adjusted from 1.2 m to 12 m. An elastic overburden of height 30 m was modeled along with an equivalent height of the floor. The rockmass was given a Young's modulus of 20 GPa and a Poisson ratio of 0.26 to represent a soft sandstone. A roller boundary condition was employed to reflect the boundaries of the model to simulate pillars of width-to-height ratios ranging from 1:1 to 5:1. An entry of 3 m was modeled to simulate 6 m entries in an infinitely large room-and-pillar layout A slightly reduced entry width of 4.8 m was modeled for the 1:1 pillar case in which a 6 m entry caused failure of the pillar before a stress was applied to the top of the system. Figure 9.1 displays the total pillar model with a magnified view of the pillar and shows a plan view of the pillar and entry, along with the roller boundary conditions used to simulate a full pillar.

The rockmass had a density of 2,250 kg/m^3. The bottom of the system was fixed and a gravitational acceleration of 9.81 m/s^2 was given to the gridpoints in the model. An initial stress state was applied which corresponded to the pressure gradient caused by gravitational loading. A pressure boundary was applied to the top of the model after the system had come to static equilibrium. The downward pressure was increased at a rate of 1 kPa per 100 steps until the vertical pillar strain reached 0.02.

The excess energy balance was calculated for the model. A new energy term shown in 9.1 was introduced to account for gravitational potential energy changes in the rockmass. The change in potential energy due to downward displacements of mass was calculated for each zone in the model. Mass was determined from the pre-deformed volume of the zone, V, multiplied by its density, ρ. The gravitational acceleration, g, was set to -9.81 m/s^2 for these tests. Downward displacements, Δz, were calculated from the zone centers at each calculation step.

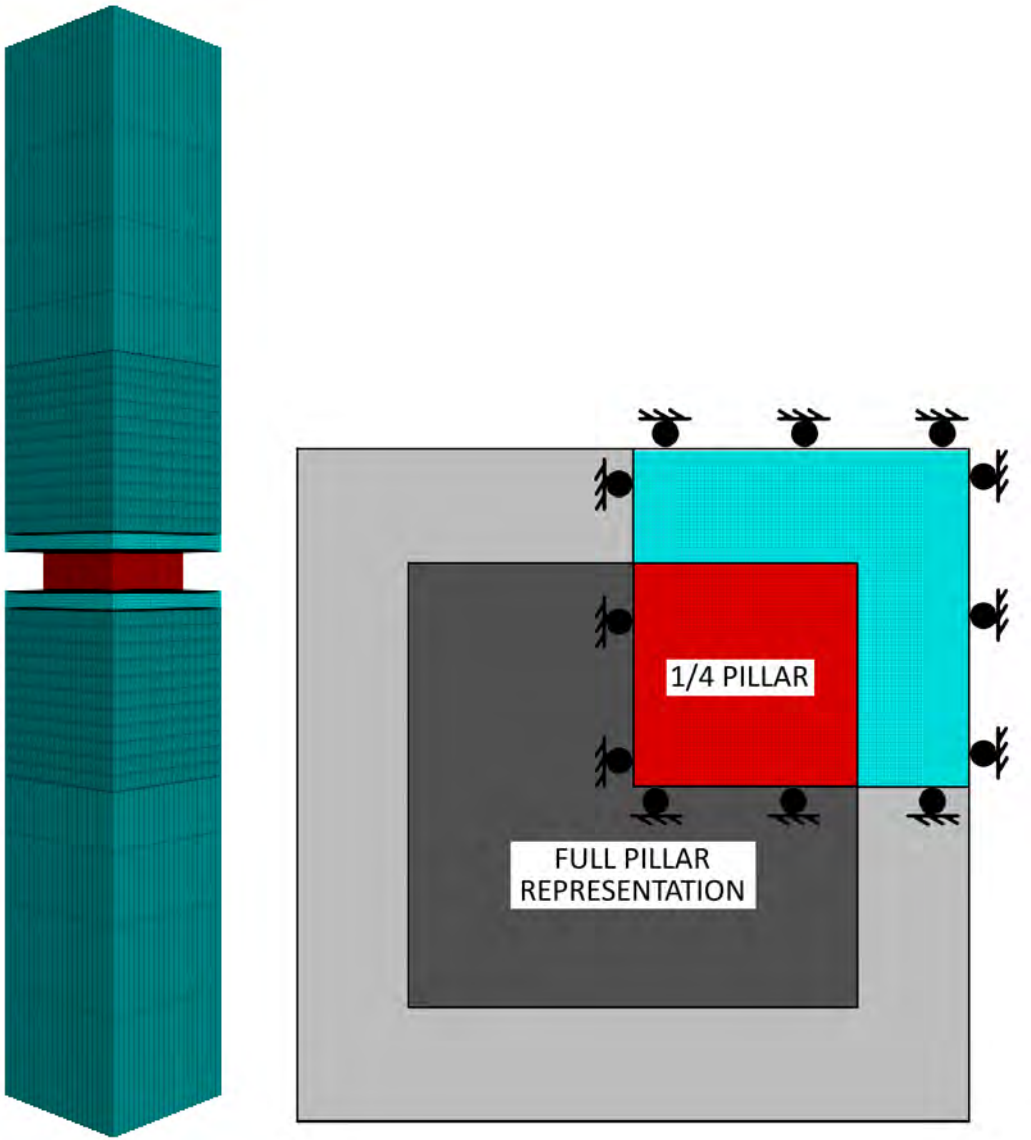

Figure 9.1: 3D global pillar model. Full model and zoomed view of pillar.

$$W_g = \sum_{i=1,n} \rho \cdot V_i \cdot g \cdot \triangle z_i \tag{9.1}$$

The potential energy contributions were introduced into the updated form of the excess energy calculation shown in 9.2. Note that U is the total elastic strain energy stored in the rock while W_r is the total work performed by the work during plastic deformation.

$$E_e = (W_b + W_g) - (U + W_r) \tag{9.2}$$

The maximum velocities, accelerations, and shear strain rates were recorded at the gridpoints and zones. Vertical pillar stress was calculated from an average of the vertical stress in the zones at the top and bottom of the pillar. An average of gridpoint displacements was at the top and bottom of the pillar was used to calculate vertical pillar strains.

9.2 Results of 3D Pillar Behavior

The 3D pillar model showed expected behaviors for the pillar and rockmass under gravitational loading. Plots of stress vs. strain are shown as Figure 9.2 for width-to-height ratios ranging from 1:1 to 5:1. The gravitational loading caused the 5:1 pillar to deviate from its calibrated behavior starting at 0.016 strain in which a large stress drop was observed in the pillar. Aside from this unexpected reduction in strength, the stress-strain behavior of the pillars remained in accordance with calibrated responses.

The energy balance was reset beginning at 0.002 strain to avoid excess energy being calculated from the initial application of stresses onto the model. Large increases in excess energy were observed in the cases of unstable failure for the small pillars 3:1 and smaller. These unstable failures represented total pillar collapse under gravitational loading. Absolute magnitudes of excess energy were seen to increase with increasing widths up to 3:1. The 4:1 pillar was then seen to result in very small releases of energy for the relatively plastic pillar. A large energy increase was observed in the 5:1 pillar during the unexpected strength drop of the pillar.

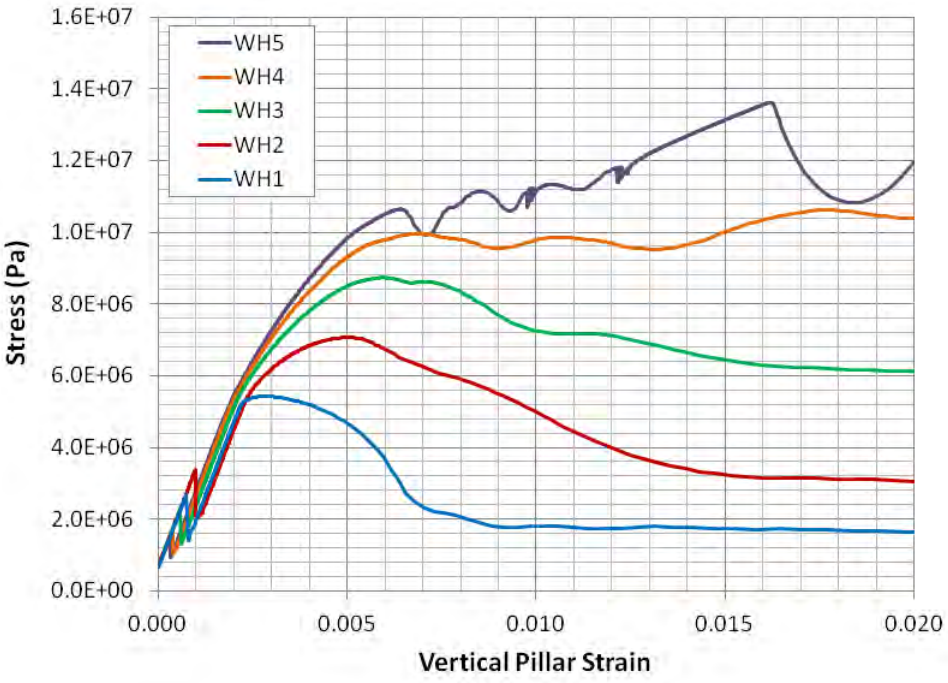

Figure 9.2: Stress vs. strain behavior of pillars under global loading.

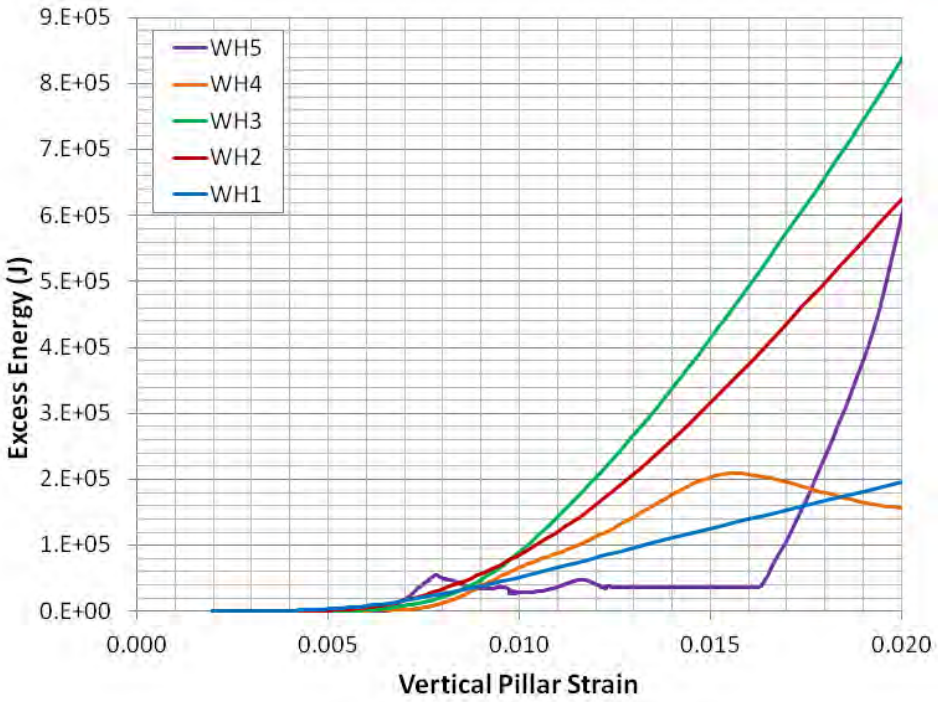

Figure 9.3: Excess energy of systems under global loading.

A more detailed view of the 1:1 pillar test is shown in Figure 9.4 as an example of total collapse. In this test the pillar reached a peak strength of 5.4 MPa at which point the pressure boundary and loading force remained constant as the pillar failed. The free-moving overburden collapsed the pillar and the system released excess energy which was recorded during the decidedly unstable failure.

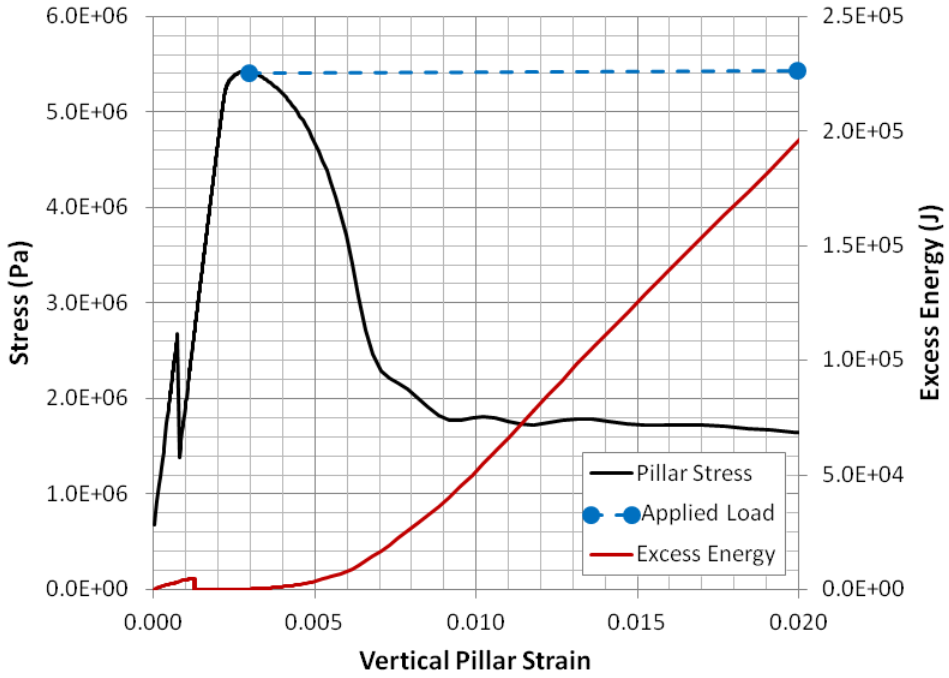

Figure 9.4: 1:1 pillar failing from global loading. Stress and excess energy are plotted against the pillar strain. The applied global load is also shown.

The 4:1 pillar trial is presented as a contrast to the 1:1 pillar failure. The 4:1 pillar maintained its peak strength of 10 MPa. The reductions in strength shown in the stress line of Figure 9.5 demonstrate that small unstable failures could still affect pillars with relatively plastic failure characteristics. The history of excess energy was shown to track periods of instability in the model.

A complete overview of the maximum excess energy values from the pillar simulations is shown in Figure 9.6. The absolute values hold little physical meaning due to the changing size of the model between tests. The total volume of overburden was greater for larger width-

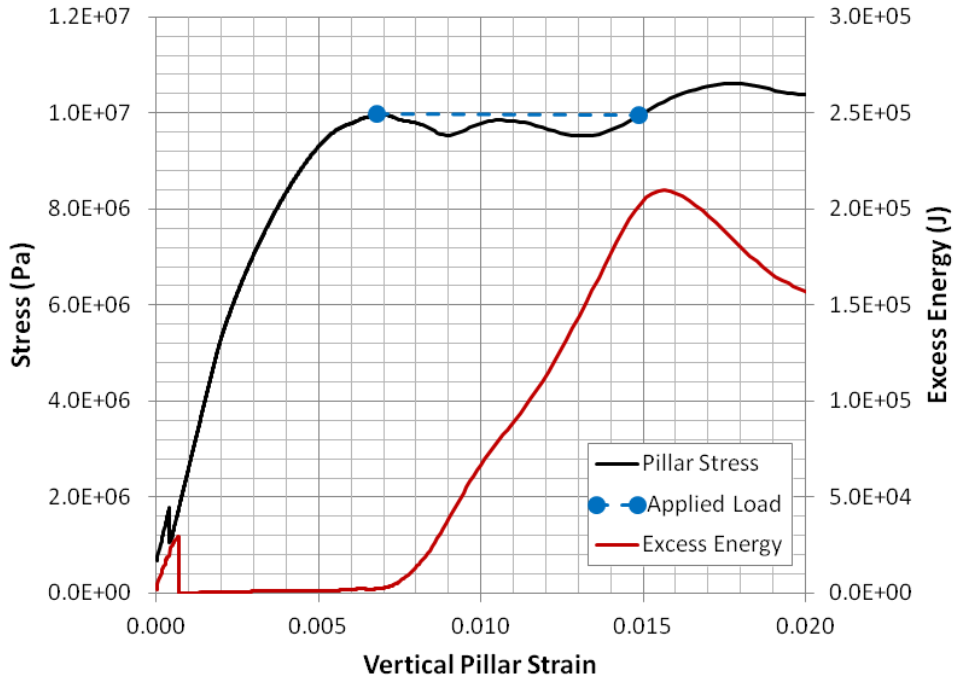

Figure 9.5: 4:1 pillar failing from global loading. Stress and excess energy are plotted against the pillar strain. The applied global load is also shown.

to-height ratio pillars. The excess energy magnitudes must therefore be normalized in some way to account for the difference in overburden volumes. The absolute magnitudes of excess energy were divided by the total plan area of the development to obtain the normalized values in Table 9.1 which are in terms of excess energy released per square meter of development.

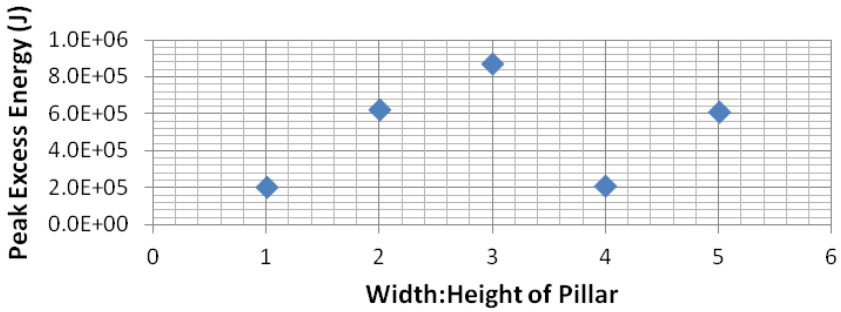

Figure 9.6: Peak magnitudes of excess energy.

The normalized results show dramatic increases in excess energy for the width-to-height ratios of 3:1 and smaller in which a total collapse of the overburden was allowed by the pillars

W:H	Max. Excess Energy (J)	Entry Half-Width (m)	Model Area (m^2)	Extraction Ratio	Excess Energy per Area (J/m^2)
1:1	2.04e5	1.2	5.8	0.75	3.54e4
2:1	6.28e5	3.0	29.2	0.80	2.15e4
3:1	8.72e5	3.0	43.6	0.70	2.00e4
4:1	2.09e5	3.0	60.8	0.62	3.44e3
5:1	6.15e5	3.0	81.0	0.56	7.59e3

Table 9.1: Excess energy released for global loading conditions, normalized by the development area being modeled.

with weakening post-peak responses. The smallest 1:1 ratio had the largest corresponding magnitudes of excess energy of 35.4 kJ/m^2. The predominantly plastic and hardening 4:1 and 5:1 pillars resulted in a significantly reduced value of excess energy per square meter of developed area. These normalized values are plotted in Figure 9.7 as a function of pillar widths with the normalized energy histories shown in Figure 9.8.

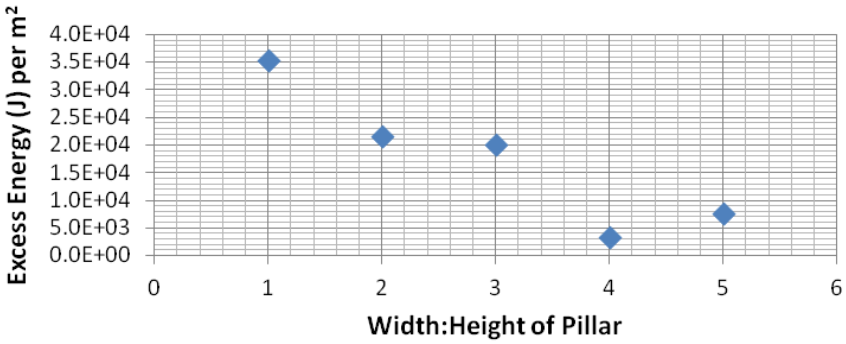

Figure 9.7: Peak magnitudes of excess energy per m^2 of development.

An analysis was conducted using the previously tested instability identifiers. The pillars of widths 3:1 and smaller experienced the largest accelerations at a point when the pillar reached its residual strength. These values correspond to the highest magnitudes of unbalanced forces which would exist between the applied load and the resisting load of the pillar. The large accelerations translated into an increasing velocity at the gridpoints which increased until the test was stopped. The maximum shear strain rates were found at the conclusion of the 1:1 through 3:1 pillar tests. For the wider pillars of 4:1 and 5:1

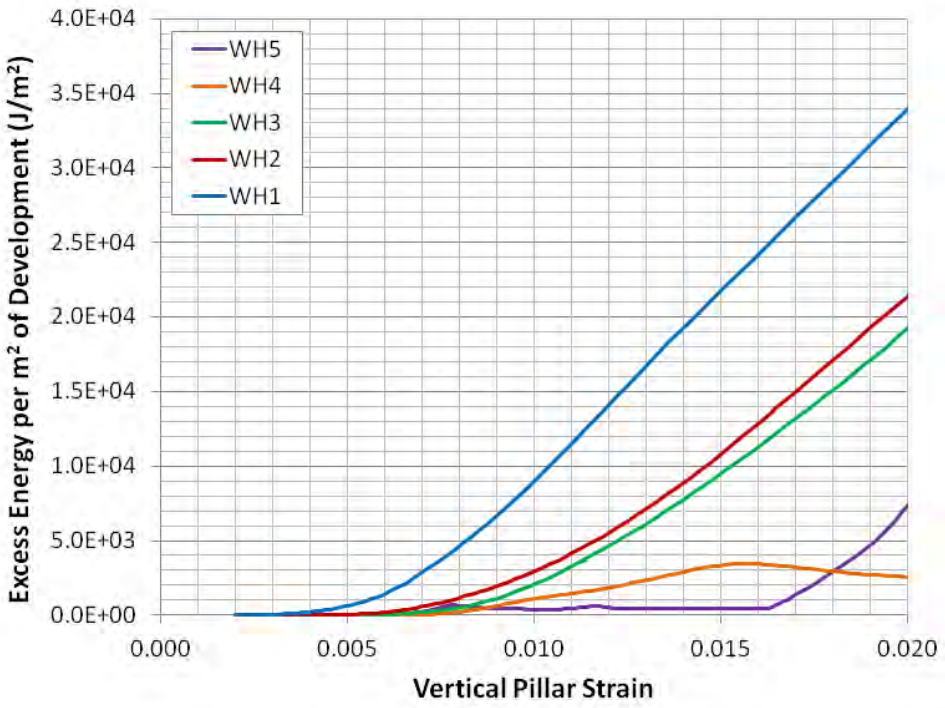

Figure 9.8: Excess energy released per square meter of development under global loading.

the maximum accelerations occurred in the middle of the small unstable portions of their post-peak responses. Maximum velocities were recorded at the end of these instabilities, as were maximum shear strain rates.

The three instability identifiers corresponded well to expected periods of rapid dynamic motion. These identifiers could be used in future tests to identify periods of highest instability within a mine model employing a gravitational loading scheme. Note that the ultimate magnitudes of the identifiers did not provide insight into the magnitudes of unstable failure due to the inherently non-dynamic calculation scheme which is solved in $FLAC^{3D}$. A fully dynamic simulation must be employed to capture the true dynamic response of a rock pillar under gravitational free fall of roof.

A demonstration of how the shear strain rate identifier may be used to identify the location of unstable failure in the model is shown in Figure 9.10 through Figure 9.12. The maximum shear strain rate reveals the area of greatest instability over the longest durations.

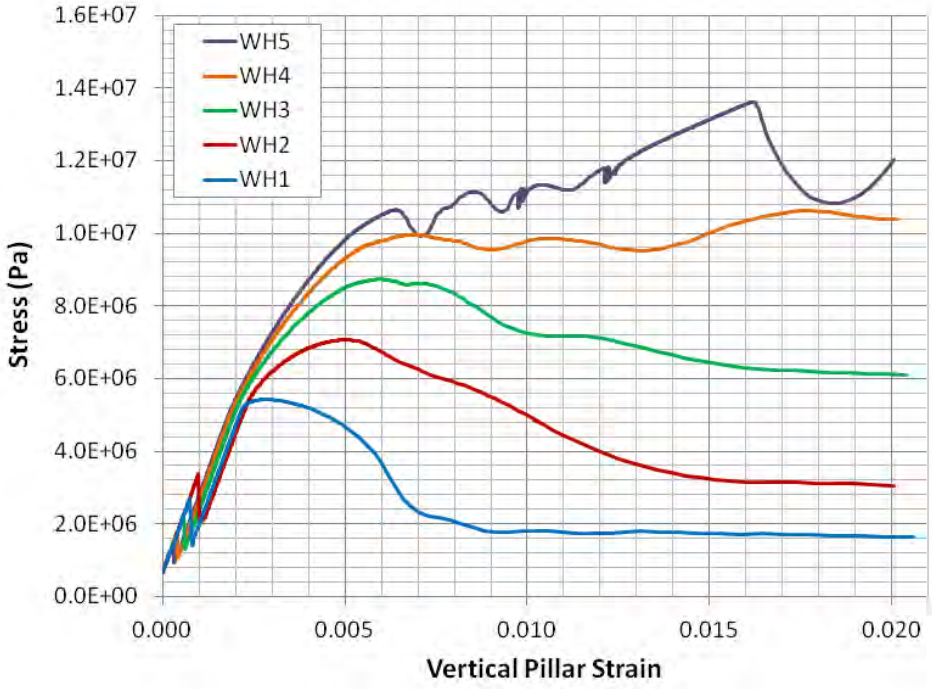

(a)

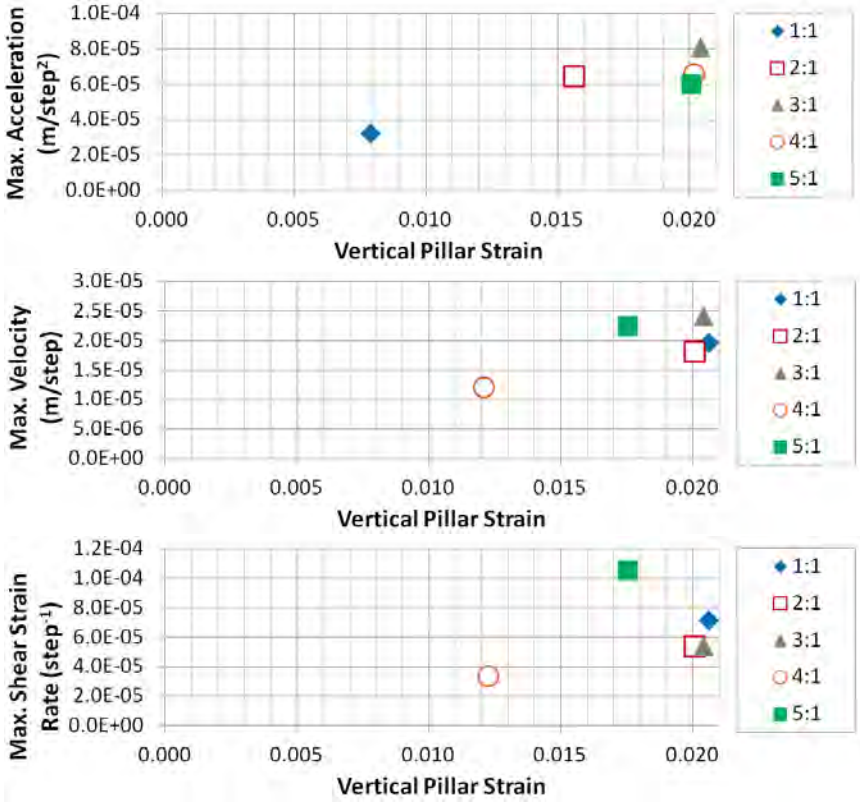

(b)

Figure 9.9: (a) Records of stress and strain for global loading models. (b) Maximum accelerations, velocities, and shear strain rates in the pillar plotted against pillar strain.

This indicator of shear deformation of the zones was most concentrated along the shear planes of failure which developed in the pillar. The least confined rock close to the rib was seen to experience the most rapid deformations and the lowest speeds of shear deformation were found in the pillar core.

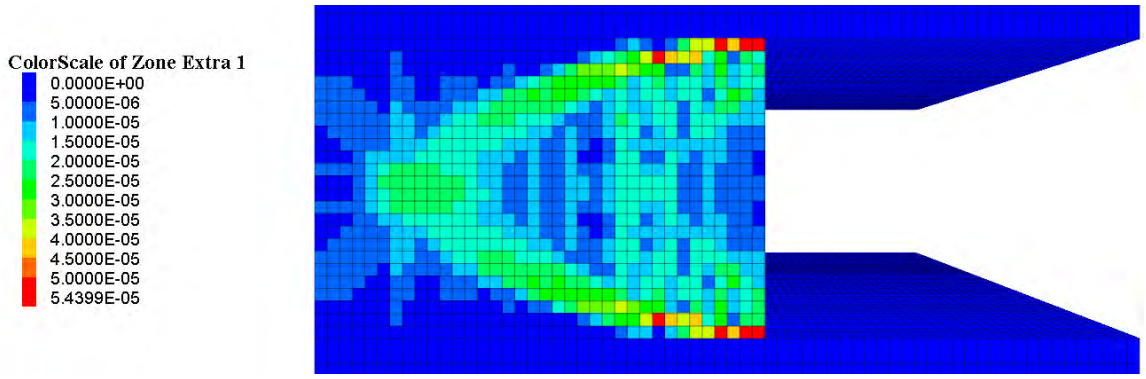

Figure 9.10: Projected elevation view of side of 3:1 pillar after unstable failure by gravitational loading. Zones colored by maximum shear strain rate show areas of highest instability.

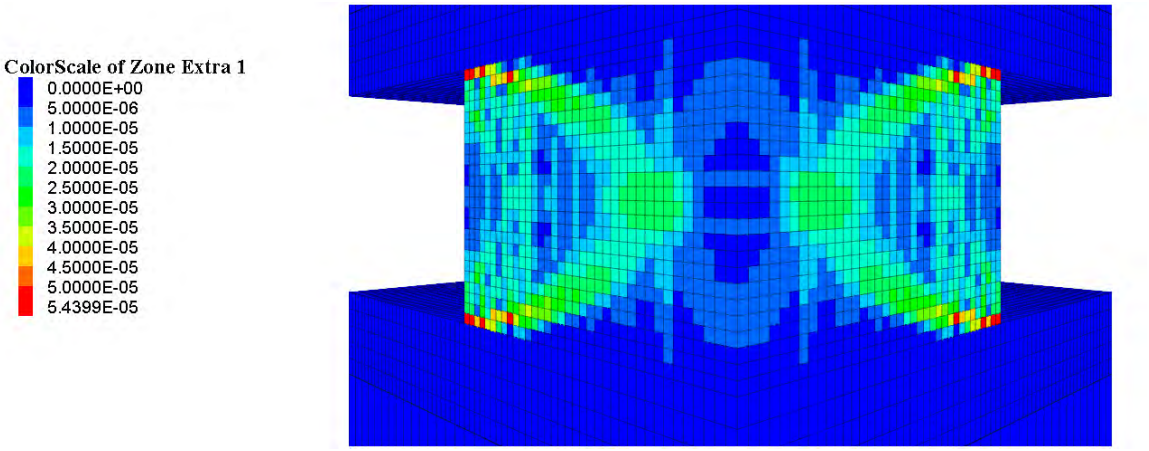

Figure 9.11: Internal view of innermost 3:1 pillar core after unstable failure by gravitational loading. Zones colored by maximum shear strain rate show areas of highest instability.

9.3 Conclusions

A series of tests was conducted over coal pillars of width-to-height ratios ranging from 1:1 to 5:1. An overburden transferred an applied pressure boundary and its own gravitational force onto the pillar. The pressure boundary was increased until the pillar achieved

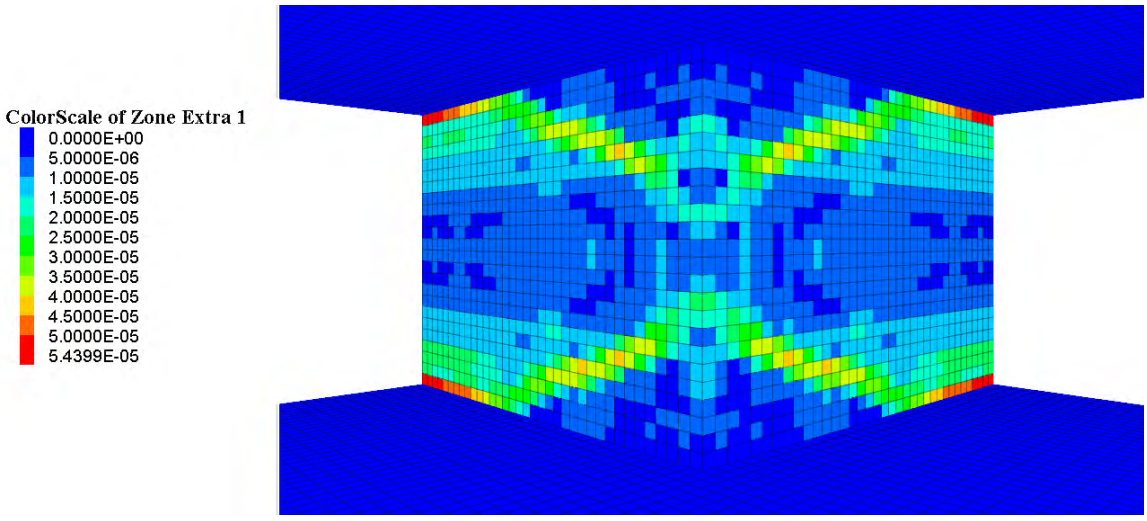

Figure 9.12: View of rib corner of 3:1 pillar after unstable failure by gravitational loading. Zones colored by maximum shear strain rate show areas of relative instability.

a 2% vertical strain. Roller boundary conditions were applied to the sides of the system to represent a large room-and-pillar layout on the verge of massive collapse.

The pillars with widths of 3:1 and smaller were seen to fail completely under the global loading scheme being represented. The smaller pillar saw a release of excess energy greater than 20 kJ per square meter of development. The 4:1 and 5:1 pillars maintained enough residual strength to resist complete collapse, yet increases in excess energy were still observed when the wide pillars experienced numerous failures of their zones. The normalized excess energy values of 3.4 and 7.6 kJ/m^2 were recorded for the 4:1 and 5:1 pillar as compared to the higher magnitudes observed for smaller pillars. Velocities, accelerations, and shear strain rates were recorded during the tests. These identifiers provided useful measures for the onset of unstable failure and pinpoint the locations at which they occurred in the models.

The global pillar model provided valuable insight into the residual strength bearing capacity of calibrated coal pillars. The excess energy balance was modified to include gravitational potential energy and was used to calculate the total release of energy in simulated massive collapses. Smaller pillars which had a negative post-failure modulus were seen to release high magnitudes of excess energy as compared to their larger counterparts. A study was

presented in which pillars of varying widths were analyzed for their burst-proneness and resulting magnitudes of unstable failure through the records of excess energy and instability identifiers.

CHAPTER 10
CONCLUSIONS

Great effort is made by modern mining operations to reduce the likelihood of unstable failures. Eliminating their occurrence is difficult in practice due to the uncertainty of rock stresses, strains, strengths, stiffnesses, and micromechanical characteristics. Numerical methods have been applied in attempts to mitigate the effects of unstable failures, however existing methods of analyzing unstable failures in numerical models suffer from several limitations. Most striking, most do not adequately identify localized forms of instability nor do they assess the release of energy as a consequence of unstable failure within complex geometries or large mine models. These limitations restrict computational analyses from being applied more widely to studies of unstable failure in realistic mine geometries.

Techniques were advanced in this doctoral research to calculate the magnitude of excess energy released as a consequence of unstable equilibria in continuum models. This calculation of excess energy is identical in magnitude to the total kinetic energy which is released during a dynamic failure and may be used as an ultimate assessment of a rock system's stability. Concepts of dynamic motion during unstable failure were also explored through identifiers of instability within explicit numerical models. By tracking instability identifiers and the release of excess energy it was shown that both local and global unstable failures could be straightforwardly assessed in large mine models. The concepts developed in this research provide a detailed methodology by which to study unstable failures in discrete element and finite difference models.

10.1 Summary of Conclusions

A methodology has been presented for studying unstable equilibia in brittle rock systems using discrete element and finite difference methods. Laboratory style compressive strength simulations showed that rapid dynamic motion could be used to identify the onset and

duration of instability in the explicit numerical models while providing some insight on the relative magnitudes of energy released during failure. Quasi-static assumptions made in the DEM software PFC^{3D} and the finite difference software $FLAC^{3D}$ prevented a detailed analysis from being performed on the dynamic response of the simulated rock and more suitable methods of analyzing unstable failure were sought within the quasi-static explicit models.

A static energy balance was derived to calculate the magnitude of excess energy released as a consequence of unstable equilibria in continuum finite difference models. The energy balance was applied to laboratory style uniaxial compressive strength tests to validate the approach within an idealized testing environment. The results of these tests showed good agreement to theoretical calculations of energy released from unstable systems. The UCS energy balance was then extended to two-dimensional coal pillars being loaded by an elastically rebounding rockmass and three-dimensional coal pillars being loaded by gravitational loading to simulate massive collapse. The stability of small width-to-height ratio pillars was assessed directly through their stress and strain responses during failure and the calculation of excess energy was confirmed within these more slender pillar geometries. For wider pillars the stress-strain determination of instability proved insufficient and alternative methods of analysis were required. The excess energy balance was used as the primary assessment tool for studying unstable failure conditions in the $FLAC^{3D}$ wide pillar models for which no other comprehensive methods of analysis existed. The total magnitudes of excess energy released from unstable rock systems were calculated as an ultimate assessment of instability in the two- and three-dimensional pillar and mine models.

The instability identifiers and excess energy balance provide a robust methodology with which to study unstable failure in explicit numerical models. These analysis techniques provide a means of assessing unstable equilibrium conditions within rock systems and mining geometries which have previously been too complex for numerical studies. The modeling techniques which have been developed may be applied in future research to design primary

and secondary supports in burst-prone conditions, evaluate retreat mining cut sequences, asses de-stressing techniques, or perform backanalyses of unstable failures in select mining layouts.

A more detailed listing of the conclusions is provided in relation to the Chapter in which each concept was developed:

Chapter 2 - Literature Review of Numerical Methods for Studying Unstable Rock Failures

- explicit numerical methods are well suited for assessing rock failure during unstable equilibrium conditions due to their ability to simulate progressive failure while approximating dynamic effects
- acoustic emissions and other signatures of large failures may be used to assess failure in numerical models but these measures neglect the role of instability on failures
- excess energy has previously been calculated by [124] for an elasto-brittle finite element simulation
- additional development of existing numerical methods is required to allow detailed studies of mining induced instability to be conducted within *in situ* models

Chapter 3 - Discrete Element Models of Rock Failure in Compression

- a genetic algorithm may be used to calibrate the many input parameters of DEM to achieve desired macroproperties through multi-objective optimization
- a proposed genetic algorithm required between 500 and 1000 trials to determine a set of 9 input parameters which yielded 4 specimen macroproperties to within 1% of desired values
- a brittle bonded-particle discrete element model mimics unstable failures observed in controlled laboratory UCS tests using DEM software PFC^{3D}

- the post-failure modulus of the bonded-particle model in PFC^{3D} was highly dependent on loading rate even for previously assumed quasi-static loading conditions; no characteristic post-peak strength behavior could be defined for the UCS specimen, even in cases of stable failure

- higher loading velocities of the BPM resulted in an increased number of cracks and signs of rupture during UCS tests

- long computation times, limited applicability to study large rock structures, and post-failure modulus load rate dependence of the bonded-particle model made its use infeasible for the intended studies on mine layouts and realistic underground mining conditions

Chapter 4 - Finite Difference Models of Rock Failure in Compression

- the Mohr-Coulomb strain-softening (MCSS) constitutive model may be used to simulate compression-induced brittle shear failure

- care is required when selecting zone size for the MCSS model to prevent failure from localizing along small-width bifurcation planes

- the explicit finite difference calculations in $FLAC^{3D}$ provide a realistic approximation to unstable failure of brittle rock in uniaxial and triaxial compressive strength tests

- dynamic loading increases the ultimate strength and the post-failure modulus of a $FLAC^{3D}$ specimen similarly to trends observed in physical dynamic loading tests

Chapter 5 - Identifiers of Unstable Failure in Finite Difference Models

- identifiers of unstable failure were used in$FLAC^{3D}$ to assess the onset, duration, and location of instability

  - maximum unbalanced forces and accelerations correspond to the point of greatest instability when the difference is highest between the applied stress and the residual strength of the specimen.
  - maximum velocities result from sustained accelerations during instability and correspond to the final point of instability as the rock system regains static equilibrium.
  - maximum shear strain rates are analogous to maximum velocities, however focus the analysis on a normalized calculation of zone deformations to allow a comparison to be made on the instability of differently sized zones within the same test

- the magnitudes of velocities and accelerations hold no physical relevance on their own within the quasi-static $FLAC^{3D}$ simulations, however a loose qualitative assessment of *relative* magnitudes of instability may be derived by comparing magnitudes between known stable and potentially unstable test cases

Chapter 6 - Energy Balance of Unstable Failures in Continuum Models

- an energy balance was derived to calculate the magnitude of excess energy released as a consequence of unstable equilibrium
  - $E_e = W_b - (U + W_r)$
  - where E_e is the excess energy released from an unstable equilibrium in the system, W_b is total boundary work added to the system during loading, U is the stored strain energy in the system, and W_r is the work consumed by plastic deformations during failure.

- a plastic Mohr-Coulomb specimen shows no increase in excess energy for changing platen stiffnesses due to its inherently stable, perfectly plastic failure characteristics

- the magnitudes of excess energy released in $FLAC^{3D}$ UCS tests match theoretical calculations of energy released due to unstable failure

Chapter 7 - Coal Pillar Models

- two- and three-dimensional coal pillar models were calibrated in $FLAC^{3D}$ using the MCSS constitutive model

- coal pillars ranging from width-to-height ratios of 1:2 to 5:1 were calibrated to match strength values obtained through the Mark-Bieniawski and Salamon pillar strength formulae; the post-peak modulus was calibrated to match the results of Wagner's *in situ* tests for the 1:2 to 2:1 pillars

Chapter 8 - 2D Model of Local Loading Stiffness

- width-to-height ratio pillars 1:1 and 2:1 behave similarly in failure to slender UCS test specimens; wider pillar geometries of 3:1 and greater introduced a more complex failure mode which progressed from the rib and propagated into the strong central core of highly confined rock

- unstable failure was observed in the 1:1 to 5:1 pillars for all rockmass cases in which the Young's modulus was 2 GPa or less

- the velocity and shear strain rate identifiers of instability showed increased magnitudes for the most unstable failure cases

- the maximum acceleration results matched expected trends for the 1:1 and 2:1 pillar cases however were shown to decrease as a function of decreasing rockmass stiffness; the cause of the unexpected reduction in accelerations could not be identified in these tests

- the excess energy balance provided a method of quantifying the magnitudes of energy released as a consequence of unstable equilibrium in the models

- normalized values of excess energy over the total developed area of the models provided a comparison of energy released between different pillar layouts
- excess energy was released in the systems with 4:1 and 5:1 pillars when the pillars had temporary reductions in strength during portions of their otherwise plastic or hardening strength behavior
- the calculation of excess energy and the identifiers of unstable failure provided a straightforward assessment of stability loss in coal pillars during simulated massive collapse

10.2 Contributions

1. Designed a genetic algorithm to calibrate a bonded-particle discrete element model. (Section 3.3.1)
2. Demonstrated unstable failures in controlled UCS tests using a bonded-particle discrete element model. (Section 3.3.3)
3. Showed that the bonded-particle model's failure mode and resulting brittleness was highly dependent on the rate of loading at the time of failure. (Section 3.3.4)
4. Demonstrated unstable failure in controlled uniaxial and triaxial compressive strength tests using a finite difference model. (Chapter 4)
5. Developed instability identifiers to study dynamic response of finite difference models as qualitative measures of unstable equilibria. (Chapter 5)
6. Developed static energy balance to calculate the excess energy released as a consequence of unstable failure. (Chapter 6)

7. Evaluated the unstable failure of coal pillars (i.e., coal bumps) using the finite difference method in $FLAC^{3D}$. Applied excess energy calculations and identifiers of instability to assess the onset, duration, location, and relative magnitudes of unstable failure in the models. (Chapters 8 and 9)

8. Calculated the excess energy released during massive collapses of room-and-pillar coal mine layouts using finite difference models. (Chapter 9)

10.3 Future Work

1. Develop a discrete element model whose post-failure response is independent of loading velocity during stable loading conditions.

2. Use discrete element models to study the role of confinement loss in the progression of failure when dynamic loading causes broken rock to be ejected from a free face.

3. Assess the appropriateness of the Mohr-Coulomb failure criterion to represent unstable failure of brittle rock or develop a more appropriate constitutive model for dynamic rock failure.

4. Assess the effects of heterogeneity on the failure of the Mohr-Coulomb strain-softening model and the subsequent expression of unstable failure.

5. Further assess the role of the coal/rock interface on coal pillar strength and post-failure characteristics in finite difference models.

6. Examine the effects of faults or discontinuities on the release of excess energy in unstable rock systems.

7. Modify energy balance to account for excavated material in active mining steps made within the finite difference models.

8. Calculate the excess energy which is released from isolated sections of a continuum numerical model in order to reduce the error introduced by boundary effects and small kinetic energies distributed across a large mine model.

9. Perform validation of energy balance through backanalyses of massive mine collapses, cascading pillar failures, and localized pillar bursts. Relate excess energy calculations to observed damage and seismic records in selected case studies.

REFERENCES CITED

[1] Adhikary, D.P., B. Shen, and M.E. Fama (2002) "A study of highwall mining panel stability." International Journal of Rock Mechanics and Mining Sciences 39, no. 5 (2002): 643-659.

[2] Badr, S. (2004) Numerical Analysis of Coal Yield Pillars at Deep Longwall Mines, PhD Dissertation, Colorado School of Mines.

[3] Bahrani, N., Valley, B., Kaiser, P.K., and Pierce, M. (2011) Evaluation of PFC2D grain-based model for simulation of confinement-dependent rock strength degradation and failure processes. Proceedings of the 45th U.S. Rock Mechanics / Geomechanics Symposium, June 26 - 29, 2011, San Francisco, California.

[4] Bahrani, N., D. Potyondy and M. Pierce (2012) Simulation of brazilian test using PFC2D grain-based model. 21st Canadian Rock Mechanics Symposium: RockEng12 — Rock Engineering for Natural Resources (Proceedings, CARMA, Edmonton, Canada, May 2012), pp. 485-493. Westmount, Quebec: CARMA, CIMICM.

[5] Bardet, J. (1989) Finite element analysis of rockburst as surface instability. Computers and Geotechnics, vol. 8, no. 3, pp. 177-193.

[6] Barenblatt, G. I. (1962) The mathematical theory of equilibrium cracks in brittle fracture. Advances in applied mechanics 7, no. 55-129 (1962): 104.

[7] Barton, N. (1995) The influence of joint properties in modeling jointed rock masses. pp. 1023-1032.

[8] Barton, N. (2007) Rock quality, seismic velocity, attenuation and anisotropy. p. 483-515, New York: Taylor & Francis.

[9] Bieniawski, Z.T. (1966) Stable and unstable fracture propagation in rock. Report of the South African Council of Scientific and Industrial Research No. MEG 493, October, 1966.

[10] Bieniawski, Z.T. (1967) An analysis of results from underground tests aimed at determining the *in situ* strength of coal pillars. CSIR Report MEG 569, Pretoria, South Africa, July, 1967; Rock Mechanics Division, National Mechanical Engineering Research Institute Council for Scientific and Industrial Research, Leipzig, 1967.

[11] Bieniawski, Z.T. (1967) Eine studie des bruchmechanismus von kohle in situ. CSIR Report MEG 598/D, Pretoria, South Africa, October, 1967; Rock Mechanics Division, National Mechanical Engineering Research Institute Council for Scientific and Industrial Research, Leipzig, 1967.

[12] Bieniawski, Z.T. (1967) Mechanism of brittle fracture of rock, Part 1: Theory of the fracture process. International Journal of rock Mechanics and Mining Sciences, vol. 4, pp. 395-406.

[13] Bieniawski, Z.T. (1967) Mechanism of brittle fracture of rock, Part 2: Experimental studies. International Journal of rock Mechanics and Mining Sciences, vol. 4, pp. 407-423.

[14] Bigoni, D. and Hueckel, T. (1991) Uniqueness and localization -I. Associative and non-associative elastoplasticity. International Journal of Solids and Structures. Vol. 28, No. 2, pp. 197-213, 1991.

[15] Blake, W. and Hedley, D.G.F. (2003) Rockbursts: case studies from North American hard-rock mines. Society for Mining, Metallurgy, and Exploration, Inc., Littleton, CO, 2003.

[16] Bolton, M.D., Nakata, Y., and Cheng, Y.P. (2008) Micro- and macro-mechanical behaviour of DEM crushable materials. Géotechnique, vol. 58, no. 6, August 1, 2008, pp. 471-480.

[17] Brady, B.H.G., and E.T. Brown (2006) "Energy, mine stability, mine seismicity and rockbursts." Rock Mechanics for underground mining (2006): 271-311.

[18] Brady, B.H.G. and Brown, E.T. (2007) Rock mechanics: for underground mining. Springer, 2007.

[19] Cai, M. et al. (2007) FLAC/PFC coupled numerical simulation of AE in large-scale underground excavations. International Journal of Rock Mechanics and Mining Sciences, vol. 44, no. 4, pp. 550-564.

[20] Caldwell, J. (2009) SME on Crandall Canyon and mining bumps. http://ithinkmining.com/2009/02/25/sme-on-crandall-canyon-and-mining-bumps/, Accessed on 2/20/2013.

[21] Chase, F., Zipf, Jr., K. and Mark, C. (1994) The massive collapse of coal pillars - case histories from the United States. Proc. 13th International Conference on Ground Control in Mining, pp. 69-80.

[22] Chen, Z. (1997) A double rock sample model for rockbursts. International Journal of Rock Mechanics and Mining Sciences, vol. 34, no. 6, pp. 991-1000.

[23] Cook, N.G.W. (1965) "The Failure of Rock," Int. Journal of Rock Mechanics and Mining Sciences, vol. 2, pp. 389-403.

[24] Cook, N.G.W., (1965) A note on rockburst considered as a problem of instability. Journal of the South African Institute of Mining and Metallurgy, 437-46.

[25] Cundall, P.A. (1989) Numerical experiments on localization in frictional materials. Ingenieur-Archiv 59 (1989) 148-159. Presented at the workshop on Limit Analysis and Bifurcation Theory, held at the University of Karlsruhe (FRG), February 22-25, 1988.

[26] Cundall, P.A. (2000) Numerical experiments on rough joints in shear using a bonded particle model. Aspects of Tectonic Faulting, pp. 1-9, eds. F.K. Lehner and J.L. Urai, Springer-Verlag, Berlin, 2000.

[27] de Borst, R. (2001) Some recent issues in computational failure mechanics. International Journal for Numerical Methods in Engineering. vol 52:63-95.

[28] Detournay, C., & Dzik, E. (2006) Nodal Mixed Discretization for tetrahedral elements. Proceedings of 4th international FLAC symposium, numerical modeling in geomechanics. Minnesota Itasca Consulting Group, Inc. Paper (No. 07-02).

[29] Esterhuizen, G.S. (2006) Evaluation of the strength of slender pillars. SME Annual Meeting and Exhibit, St. Louis, Missouri, pp. Preprint 06-003, 2006.

[30] Esterhuizen, G., Mark, C. and Murphy, M. (2010) The ground response curve, pillar loading and pillar failure in coal mines. 29th International Conference on Ground Control in Mining, pp. 19-27.

[31] Esterhuizen, G. and Mark, C. (2009) Three-dimensional modeling of large arrays of pillars for coal mine design. Proceedings of the International Workshop on Numerical Modeling for Underground Mine Excavation Design, pp. 37-46.

[32] Fairhurst, C. (2004) Fundamental considerations relating to the strength of rock. Report on the Workshop on Extreme Ground Motions at Yucca Mountain. U.S. Geological Survey, Menlo Park, California, August 23-24, 2004.

[33] Fakhimi, A. and Villegas, T. (2006) Application of dimensional analysis in calibration of a discrete element model for rock deformation and fracture. Rock Mechanics and Rock Engineering 40: 193-211.

[34] Garvey, R. and Ozbay, U. (2011) Computer-aided calibration of PFC3D coal samples using a genetic algorithm. Proceedings of the 2nd International FLAC/DEM Symposium, pp. 493-499.

[35] Garvey, R. and Ozbay, M.U. (2012) Identifying Unstable Failure in Brittle Rock using the Finite Difference Method. Proceedings of the 46th U.S. Rock Mechanics/Geomechanics Symposium, Chicago, IL, 2012.

[36] Gates, et al. (2008) Fatal underground coal burst accidents, August 6 and 16, 2007. USDOL, MSHA Report of Investigation, ID No. 42-01715. Arlington, Virginia, pgs 176.

[37] Goldberg, D. E. (1989). Genetic algorithms in search, optimization, and machine learning.

[38] Grady, D.E. (1990) Particle size statistics in dynamic fragmentation. Journal of Applied Physics, vol. 68, no. 12, 15 December 1990, pp. 6099-6105.

[39] Griffith A. A. (1921) The phenomena of rapture and flow in solids. Phil. Trans. Roy. Soc., A 221, 163-198.

[40] Griffith, A.A. (1925) Theory of rupture. Proceedings of the first international congress for applied mechanics, (Bienzeno and Burgess, eds.) pp. 53-64. J. Waltman Jr. Press, Delft (1925).

[41] Griffiths, D.V. (1981) Computation of strain softening behaviour. Symposium on Implementation of Computer Procedures and Stress-Strain Laws in Geotechnical Engineering, Chicago, U.S.A., (eds. C.S. Desai and S.K. Saxena), pp.591-604. Acorn Press (1981).

[42] Hajiabdolmajid, V., Kaiser, P., and Martin, C. (2002) Mobilization of strength in brittle failure of rock - in laboratory vs. in situ. Proceedings of the Fifth North American Rock Mechanics Symposium, pp. 227-234.

[43] Hajiabdolmajid, V., Kaiser, P., and Martin, C. (2002) Modelling brittle failure of rock. International Journal of Rock Mechanics and Mining Sciences, vol. 39, no. 6, pp. 731-741.

[44] Haramy, K.Y., Hanna, K. and McDonnell, J.F.T (1984) Investigations of underground coal mine bursts. Proceeding of the Fourth Conference on Ground Control in Mining (ICGCM).

[45] Hazzard, J. and Young, R. (2004) Dynamic modelling of induced seismicity. International Journal of Rock Mechanics and Mining Sciences, vol. 41, no. 8, pp. 1365-1376.

[46] Hill, R. (1958) A general theory of uniqueness and stability in elastic-plastic solids. Journal of the Mechanics and Physics of Solids, vol. 6, 1958, pp. 236-249.

[47] Hobbs, B.E., and Ord, A. (1989) Numerical simulation of shear band formation in a frictional-dilational material. Presented at the workshop on Limit Analysis and Bifurcation Theory, held at the University of Karsruhe (FRG), February 22-25, 1988, Ingenieur-Archiv, 1989.

[48] Hoek, E. and Bieniawski, Z.T. (1966) Fracture propagation mechanism in hard rock. Proceedings of the First Congress of the International Society of Rock Mechanics, Lisbon, September, 1966, Vol. I, pp. 243-249.

[49] Horii, H. and Nemat-Nasser, S. (1985) Compression-induced microcrack growth in brittle solids: axial splitting and shear failure. Journal of Geophysical Research, vol. 90, no. B4, pp. 3105-3125, March 10, 1985.

[50] Hsieh, Y., Li, H., Huang, T. and Jeng, F. (2008) Interpretations on how the macroscopic mechanical behavior of sandstone affected by microscopic properties - revealed by bonded-particle model. Engineering Geology, vol. 99, no. 1, pp. 1-10.

[51] Hustrulid, W.A. (1976) A review of coal pillar strength formulas. Rock Mechanics, Vol. 8, pp. 115-145.

[52] Hyder, Z., Ali, Z., Akram, M., Westman, E. and Karmis, M. (2011) Simulation and modeling of pillar stability and analysis of safety factor. SME Annual Meeting, Denver, CO, 2011.

[53] Iannacchione, A.T. and Tadolini, S.C. (2008) Coal mine burst prevention controls. 27th International Conference on Ground Control in Mining, pp. 20-28.

[54] Iannacchione, A.T. and Zelanko, J. (1995) Occurrence and remediation of coal mine bumps: a historical review. Proceedings of the Mechanics and Mitigation of Violent Failure in Coal and Hard-Rock Mines, vol. 01, pp. 27-68.

[55] Irwin, G.R. (1960) Fracture mechanics. Structural Mechanics, (Goodier and Hoff, eds.) pp. 557-592, Pergamon Press (1960).

[56] Itasca Consulting Group Inc. (2010b) 3DEC (3 Dimensional Distinct Element Code), Version 4.1. Minneapolis, MN.

[57] Itasca Consulting Group Inc. (2010) FLAC3D (Fast Lagrangian Analysis of Continua in 3 Dimensions), Version 4.0. Minneapolis, MN.

[58] Itasca Consulting Group Inc. (2012) FLAC3D (Fast Lagrangian Analysis of Continua in 3 Dimensions), Version 5.0. Minneapolis, MN.

[59] Itasca Consulting Group Inc. (2010c) PFC3D (Particle Flow Code in 3 Dimensions), Version 4.0. Minneapolis, MN.

[60] Khan, A.S., and Irani, F.K. (1987) An experimental study on stress wave transmission at a metallic-rock interface and dynamic tensile failure of sandstone, limestone, and granite. Mechanics of Materials, vol. 6, pp. 285-292.

[61] Kias, E.M.C., Gu, R., Garvey, R., and Ozbay, U. (2011) Modeling unstable rock failure during a uniaxial compressive strength test. Proceedings of 45th U.S. Rock Mechanics/Geomechanics Symposium, San Francisco, CA, 2011.

[62] Kias, E.M.C., Mustoe, G.G.W., and Ozbay, U. (2013) Evaluation of two discrete element models for studying unstable frock failure in compression. Proceedings of DEM6 Conference, Golden, CO, 2013.

[63] Kidybiński, A. (1981) Bursting liability indices of coal. International Journal of Rock Mechanics and Mining Science & Geomechanics, vol. 18, 1981, pp. 295-304.

[64] Koehler, J.R., DeMarco, M.J., and Wuest, W.J. (1995) The critical pillar concept in yield pillar-based longwall gate road design. SME Annual Meeting, March 6-9, 1995, Denver, CO.

[65] Koyama, T. and Jing, L. (2007) Effects of model scale and particle size on micro-mechanical properties and failure processes of rocks—A particle mechanics approach. Engineering Analysis with Boundary Elements 31: 458-472.

[66] Kripakov, N. and Kneisley, R. (1992) Pillar design in bump-prone deep western U.S. coal mines. 11th International Conference on Ground Control in Mining, The University of Wollongong, N.S.W., pp. 72-83.

[67] Lahaie, F., Bigarre, P., Al Heib, M., Josien, J. and Noirel, J. (2003) Large-scale 3D characterisation of in-situ stress field in a complex mining district prone to rockbursting. International Society for Rock Mechanics, vol. 2, no. 200309, p. 6, Sep. 2003.

[68] Liu, H.Y., Kou, S.Q., Lindqvist, P.-A., and Tang, C.A. (2004) Numerical studies on the failure process and associated microseismicity in rock under triaxial compression. Tectonophysics, vol. 384, no. 1-4, June 16, 2004, pp. 149-174.

[69] Lu, J., Ray, A., Morsey, K., and Peng, S. (2008) Effects of rock/coal interface property on coal pillar strength. 27th International Conference on Ground Control in Mining (ICGCM).

[70] Maleki, H., Olsen, R., Spillman, D., and Stevenson, M. (2003) Development of geotechnical procedures for the analysis of mine seismicity and pillar designs. Proc. 22nd International Conference on Ground Control in Mining, pp. 270-277.

[71] Maotian, L., Zhongchang, W. and Qing, Y. (2006) Study on damage bifurcation and instability of rock-like materials. Acta Mechanica Solida Sinica, vol. 19, no. 3, September, 2006.

[72] Mark, C. (1999) Pillar design methods for longwall mining. U.S. Dept. of the Interior, U.S. Bureau of Mines.

[73] Mark, C. (1999) The state-of-the-art in coal pillar design in Preprint 99-86.

[74] Mark, C. (2006) Extreme multiple seam mining in the central Appalachian coalfields. 2006 SME Annual Meeting March 27-29, St. Louis, Missouri, p. 7.

[75] Mark, C. (2009) Deep cover pillar recovery in the US. 28th International Conference on Ground Control in Mining, Morgantown, WV, pp. 1-9.

[76] Mark, C. and Barton, T.M. (1996) The uniaxial compressive strength of coal: should it be used to design pillars? 15th International Conference on Ground Control in Mining, Golden, CO, August 13-15, 1996.

[77] Marti, J. and Cundall, P. (1982) Mixed discretization procedure for accurate modelling of plastic collapse. International Journal for Numerical Methods in Engineering, vol. 4, pp. 153-177.

[78] McClintock, F.A. and Walsh, J.B. (1963) Friction on Griffith cracks in rocks under pressure. Proceedings of the Fourth U.S. Congress on Applied Mechanics, pp. 1015-1021. American Society of Mechanical Engineers, New York (1963).

[79] McGarr, A. (1997) A mechanism for high wall-rock velocities in rockbursts. Pure and Applied Geophysics, vol. 150, pp. 381-391.

[80] Morsy, K. and Peng, S. (2002) Numerical modeling of the gob loading mechanism in longwall coal mines. 21st International Conference on Ground Control in Mining, August 6-8, 2002, Morgantown, WV, pp. 58-67.

[81] Mortazavi, A., Hassani, F.P., and Shabani, M. (2008) A numerical investigation of rock pillar failure mechanism in underground openings. Computers and Geotechnics, vol. 36, pp. 691-697.

[82] Muller, W. (1991) Numerical simulation of rock bursts. Mining Science and Technology, vol. 12, no. 1, pp. 27-42.

[83] Nakata, Y., Bolton, M.D., and Cheng, Y.P. (2005) Relating particle characteristics to macro behavior of DEM crushable material. Powders and Grains, 2005, ed. A.A. Balkema, Rotterdam, Netherlands, pp. 1387-1391.

[84] Nemat-Nasser, S. and Deng, H. (1994) Strain-rate effect on brittle failure in compression. Acta Metallurgica et Materialia. vol. 42, no. 3, pp. 1013-1024.

[85] Ng, L.K.W., Swan, G., and Board, M. (1993) The application of an energy approach in fault models for support design. Rockbursts and Siesmicity in Mines, pp. 387-391.

[86] Notley, K. (1984) Rock mechanics analysis of the Springhill mine disaster (October 23, 1958). Mining Science and Technology, vol. 1, no. 2, pp. 149-163.

[87] Oliver, J. and Huespe, A. (2007) Continuum approach to material failure in strong discontinuity settings. Computer Methods in Applied Mechanics and Engineering, vol. 193, no. 30, pp. 3195-3220, Jul. 2007.

[88] Osterwald, F.W. (1962) USGS relates geologic structures to bumps and deformation in coal mine workings. Mining Engineering, vol. 14, pp. 63-68, Apr-1962.

[89] Ozbay, M.U., Salamon, M.D.G., and Lee, K. (2001) Rational design of yield pillars: improved understanding of yielding mechanism. SME Annual Meeting, Denver, CO, 2001.

[90] Ozbay, U. and Badr, S. (2010) Numerical modeling of yielding chain pillars in deep longwall coal mines. Workshop on Pillar Design. 29th International Conference on Ground Control in Mining, Morgantown, WV, 2010.

[91] Ozbay, U. and Rozgonyi, T.G. (2003) Numerical modeling of stress and deformations encountered in deep longwall coal mines usig strain softening failure criterion. International Conference on Safety and Environmental Aspects of Mining. University of Miskolc Series A. Mining, Vol. 63, 2003.

[92] Pariseau, W. (2011) Geomechanics of Crandall Canyon barrier pillar mining. SME Annual Meeting, Denver, CO, 2011.

[93] Park, E., Martin, C.D., and Christiansson, R. (2004) Simulation of the mechanical behavior of discontinuous rock masses using a bonded-particle model. Gulf Rocks 2004: Rock Mechanics Across Borders & Disciplines, pp. Paper no. ARMA/NARMS 04-480.

[94] Peperakis, J. (1958) Mountain bumps at the sunnyside mines. Transactions AIME, vol. 211, pp. 982-986, Sep-1958.

[95] Pierce, M., Cundall, P., Potyondy, D. and Mas Ivars, D. (2007) A synthetic rock mass model for jointed rock. In E. Eberhardt et al. (Eds) Rock Mechanics: Meeting Society's Challenges and Demands (1st Canada-U.S. Rock Mechanics Symposium, Vancouver, May 2007), Vol. 1: Fundamentals, New Technologies and New Ideas, pp. 341-349, London: Taylor & Francis Group.

[96] Pijaudier-Cabot, G. and Bažant, Z.P. (1988) Dynamic stability analysis with nonlocal damage. Computers and Structures, vol. 29, no. 3, pp. 503-507, 1988.

[97] Pijaudier-Cabot, G. and Benallal, A. (1993) Strain localization and bifurcation in a nonlocal continuum. International Journal of Solids and Structures, vol. 30, no. 13, pp. 1761-1775.

[98] Potyondy, D. and Cundall, P. (2004) A bonded-particle model for rock. International Journal of Rock Mechanics and Mining Sciences, vol. 41, no. 8, pp. 1329-1364.

[99] Potyondy, D.O. (2012) A flat-jointed bonded-particle material for hard rock. 46th US Rock Mechanics / Geomechanics Symposium, Chicago, IL, June 24-27, 2012, ARMA 12-501.

[100] Rabczuk, T. (2012) Computational methods for fracture in brittle and quasi-brittle solids: state-of-the-art review and future perspectives. ISRN Applied Mathematics, eds. S. Li and R. Samtaney. Pre-publication, accepted September 3, 2012.

[101] Rice, J.R. (1976) The localization of plastic deformation. Theoretical and Applied Mechanics, Proceedings of the 14th International Congress on Theoretical and Applied Mechanics, Delft, 1976, vol. 1, North-Holland Publishing Co., 1976, pp. 207-220.

[102] Roberts, D.K. and Wells, A.A. (1954) The velocity of brittle fracture. Engineering, no. 178, pp. 820-821 (1954).

[103] Rudnicki, J.W. and Rice, J.R. (1975) Conditions for the localization of deformation in pressure-sensitive dilatant materials. Journal of the Mechanics and Physics of Solids, vol. 23, pp. 371-394.

[104] Salamon, M. (1970) Stability, instability and design of pillar workings. International Journal of Rock Mechanics and Mining Science & Geomechanics Abstracts, 7(6), 613-631.

[105] Salamon, M., Badr, S. and Ozbay, M.U. (2003) Pillar failure in deep coal seams: numerical simulation. Technology Roadmap for Rock Mechanics, vol. 2, no. 10, pp. 1011-1018, Sep. 2003.

[106] Salamon M.D.G. and Munro, A.H. (1967) A study of the strength of coal pillars. J. S. Afr. Inst. Min. Metall. September 1967.

[107] Schofield, A.N. and Wroth, P. (1968) "Critical state soil mechanics" McGraw-Hill, pp. 310, ISBN 978-0641940484.

[108] Shan, R., Jiang, Y. and Li, B. (2000) Obtaining dynamic complete stress-strain curves for rock using the Split Hopkinson Pressure Bar technique. International Journal of Rock Mechanics and Mining Sciences, vol. 37, pp. 983-992.

[109] Shimizu, H., Koyama, T., Ishida, T., Chijimatsu, M., Fujita, T. and Nakama, S. (2010) Distinct element analysis for Class II behavior of rocks under uniaxial compression. International Journal of Rock Mechanics and Mining Sciences, vol. 47, no. 2, pp. 323-333.

[110] Shockey, D.A., Curran, D.R., Seaman, L., Rosenberg, J.T., and Petersen, C.F. (1974) Fragmentation of rock under dynamic loads. International Journal of Rock Mechanics and Mining Sciences & Geomechanics Abstracts, vol. 11, no. 8, August, 1974, pp. 303-317.

[111] Srinivas, M. and Patnaik, L.M. (1994) Adaptive probabilities of crossover and mutation in genetic algorithms. IEEE Transactions on Systems, Man and Cybernetics, vol. 24, no. 4, April 1994, pp. 656-667.

[112] Starr, A. T. (1928) "Slip in a Crystal and Rupture in a Solid Due to Shear," Proc. Camb. Phil. Soc., 24, 489-500.

[113] Tarasov, B. (2010) Superbrittleness of rocks at high confining pressure. Proceedings of the fifth International Seminar on deep and high stress mining, pp. 119-133.

[114] Tawadrous, A.S., DeGagné, D., Pierce, M. and Mas Ivars, D. (2009) Prediction of uniaxial compression PFC3D model micro-properties using artificial neural networks. International Journal for Numerical and Analytical Methods in Geomechanics 33: 1953-1962.

[115] Tiwari, R.P. and Seshagiri Rao, K. (2006) Post failure behaviour of a rock mass under the influence of triaxial and true triaxial confinement. Engineering Geology, vol. 84, pp. 112-129.

[116] United States Mine Health and Safety Administration. (2008) Report of investigation, underground coal mine: fatal underground coal burst accidents, August 6 and 16, 2007, Crandall Canyon Mine, Genwall Resources Inc., Huntington Emergy County, Utah, ID, Issues 42-1715. Mine Safety and Health Administration, Office of the Adminstrator, Coal Mine Safety and Health, 2008.

[117] van der Merwe, J.N. (1998) The role of overburden integrity in pillar failure. 2nd International Workshop on Coal Pillar Mechanics and Design, pp. 173-179.

[118] van Heerden, W.L. (1975) In situ complete stress-strain characteristics of large coal specimens. Journal of the South African Institute of Mining and Metallurgy, March 1975, pp. 207- 217.

[119] Vermeer, P.A. and de Borst, R. (1984) Non-associated plasticity for soils, concrete and rock. HERON, vol. 29, no. 3, January 1984, pp. 1-64.

[120] Wagner, H. (1974) Determination of complete load deformation characteristics of coal pillars. Proceedings of 3rd ISRM Congress, Denver, CO, pp. 1076-1081.

[121] Wang, Y. and Tonon, F. (2009) Calibration of a discrete element model for intact rock up to its peak strength. International Journal for Numerical and Analytical Methods in Geomechanics 34: 447-469.

[122] Wang, L. et al. (2010) Controlling the effect of a distant extremely thick igneous rock in overlying strata on coal mine disasters. Mining Science and Technology, China, vol. 20, no. 4, pp. 510-515.

[123] Wang, S.Y., Au, S., Lam, K. and Tang, C.A. (2005) A numerical study of pillar failure based on a cusp-type catastrophe model. Key Engineering Materials, vol. 297, pp. 2628-2635.

[124] Wang, S.Y., Lam, K.C., Au, S.K., Tang, C.A., Zhu, W.C., and Yang, T.H. (2005) Analytical and numerical study on the pillar rockbursts mechanism. Rock Mechanics and Rock Engineering, vol. 39, no. 5, pp. 445-467.

[125] Whitley, D. (1994) A genetic algorithm tutorial. Statistics and Computing (4):65-85, 1994.

[126] Whyatt, J. (2008) Dynamic failure in deep coal: recent trends and a path forward. Proceedings 27th International Conference on Ground Control in Mining, pp. 37-45.

[127] Whyatt, J.K. and Board, M.P. (1991) Numerical exploration of shear-fracture-related rock bursts using a strain-softening constitutive model. RI 9350, United States Department of the Interior, Bureau of Mines, 1991.

[128] Wu, F., Wu, J., & Qi, S. (2010). Phenomena and theoretical analysis for the failure of brittle rocks. Journal of Rock Mechanics and Geotechnical Engineering, 2(4), 331-337.

[129] Yavuz, H. and Fowell, R. (2001) FDM prediction of a yield pillar performance in conjunction with a field trial. Proceedings of the 20th International Conference on Ground Control in Mining, pp. 78-87.

[130] Yoon, J. (2007) Application of experimental design and optimization to PFC model calibration in uniaxial compression simulation. International Journal of Rock Mechanics and Mining Sciences 44: 871-889.

[131] Zhao, J. (2000) Applicability of Mohr-Coulomb and Hoek-Brown strength criteria to the dynamic strength of brittle rock. International Journal of Rock Mechanics and Mining Sciences, vol. 37, pp. 1115-1121.

[132] Zhi-ru, H., Yao-dong, J., Yi-xin, Z., and Qing,ji G. (2009) Study of crack propagation of bump-prone coal sample. Proceeding of the 6th International Conference on Mining Science and Technology, pp. 471-478.

[133] Zhu, Q., Lu, W., Sun, J., Luo, Y. and Chen, M. (2009) Prevention of rockburst by guide holes based on numerical simulations. Mining Science and Technology (China), vol. 19, no. 3, pp. 346-351.

[134] Zingano, A., Koppe, J. and Costa, J. (2004) Violent coal pillar collapse. 23rd International Conference on Ground Control in Mining, Morgantown, WV, pp. 60-67.

[135] Zipf Jr., R.K. and Mark, C. (1997) Design methods to control violent pillar failures in room-and-pillar mines. Transactions of the Institute of Mining and Metallurgy, vol. 106, pp. A124-A132.

[136] Zou, D., Miller, H. and Kaiser, P. (1989) Numerical study of violent rock failure by stick-slip on joints. Mining Science and Technology, vol. 9, no. 3, pp. 241-251.

[137] Zubelewicz, A. and Mróz, Z. (1983) Numerical simulation of rock burst processes treated as problems of dynamic instability. Rock Mechanics and Rock Engineering, vol. 16, no. 4, pp. 253-274, Nov. 1983.

SELECTED BIBLIOGRAPHY

Adhikary, D.P., B. Shen, and M.E. Fama (2002) "A study of highwall mining panel stability." International Journal of Rock Mechanics and Mining Sciences 39, no. 5 (2002): 643-659.

Adhikary, D.P. (2010) Shortcomings in the standard continuum based implicit joint model of layered rocks. Journal of Geology and Mining Research, vol. 2, no. 2, pp. 23-28, May, 2010.

Babić, M. (1997) Average balance equations for granular materials. International Journal of Engineering Sciences, vol. 35, no. 5, 1997, pp. 523-548.

Bäck, T. (1993) Optimal mutation rates in genetic search. Proceedings of the 5th International Conference on Genetic Algorithms, Urbana-Champaign, IL, USA, June 1993, pp. 2-8.

Bäck, T. and Schütz, M. (1996) Intelligent mutation rate control in canonical genetic algorithms. ISMIS '96 Proceedings of the 9th International Symposium on Foundations of Intelligent Systems, pp. 158 - 167.

Bäckström, A., Antikainen, J., Backers, T., Feng, X., Jing, L., Kobayashi, A., Koyama, T., Pan, P., Rinne, M., Shen, B., and Hudson, J.A. (2008) Numerical modelling of uniaxial compressive failure of granite with and without saline porewater. International Journal of Rock Mechanics and Mining Sciences, vol. 45, 2008, pp. 1126-1142.

Badr, S. (2004) Numerical Analysis of Coal Yield Pillars at Deep Longwall Mines, PhD Dissertation, Colorado School of Mines.

Badr, S. (2010) Simulation of macro and micro responses of yielding rock pillar. The First International Conference on Advances in Interaction & Multiscale Mechanics, Jeju, South Korea, May 31 - June 2, 2010.

Bahrani, N., Valley, B., Kaiser, P.K., and Pierce, M. (2011) Evaluation of PFC2D grain-based model for simulation of confinement dependent rock strength degradation and failure processes. Proceedings of the 45th U.S. Rock Mechanics/Geomechanics Symposium, San Francisco, CA, 2011.

Barczak, T.M., Esterhuizen, G.S., and Dolinar, D.R. (2005) Evaluation of the impact of standing support on ground behavior in longwall tailgates. Proceedings of the 24th International Conference on Ground Control in Mining, August 2-4, 2005, Morgantown, WV.

Bardet, J. (1989) Finite element analysis of rockburst as surface instability. Computers and Geotechnics, vol. 8, no. 3, pp. 177-193.

Barenblatt, G. I. (1962) The mathematical theory of equilibrium cracks in brittle fracture. Advances in applied mechanics 7, no. 55-129 (1962): 104.

Barron, K. (1971) Brittle fracture initiation in and ultimate failure of rocks. Part II-Anisotropic Rocks: Theory. International Journal of Rock Mechanics and Mining Sciences. vol. 8, pp. 553-663. Pergamon Press, Britain, 1971.

Barron, L.R. (1990) Longwall stability analysis of a deep, bump-prone western coal mine-case study. Ninth Conference on Ground Control Mining Proceedings (ICGCM), p. 8.

Barton, N. (1995) The influence of joint properties in modeling jointed rock masses. pp. 1023-1032.

Barton, N. (2007) Rock quality, seismic velocity, attenuation and anisotropy. p. 483-515, New York: Taylor & Francis.

Bažant, Z.P. (1988) Stable states and paths of structures with plasticity or damage. Journal of engineering mechanics 114, no. 12 (1988): 2013-2034.

Beck, D.A., Pfitzner, M.J., Arndt, S.M, and Fillery, B. (2009) Estimating rock mass properties and seismic response using higher order, discontinuous, finite element models. ROCKENG09: Proceedings of the 3rd CANUS Rock Mechanics Symposium, 2009.

Bétournay, M.C. and Mitri, H.S. (2003) Laboratory simulation of the behaviour of highly stressed mining fronts. International Society for Rock Mechanics, 10th Congress: Technology

Roadmap for Rock Mechanics, September, 2003.

Bahrani, N., D. Potyondy and M. Pierce (2012) Simulation of brazilian test using PFC2D grain-based model. 21st Canadian Rock Mechanics Symposium: RockEng12 — Rock Engineering for Natural Resources (Proceedings, CARMA, Edmonton, Canada, May 2012), pp. 485-493. Westmount, Quebec: CARMA, CIMICM.

Bahrani, N., Valley, B., Kaiser, P.K., and Pierce, M. (2011) Evaluation of PFC2D grain-based model for simulation of confinement-dependent rock strength degradation and failure processes. 45th U.S. Rock Mechanics / Geomechanics Symposium, June 26 - 29, 2011 , San Francisco, California.

Bhide, R.J., McLennan, J.D., Guilkey, J.E., and Green, S.J. (2011) Numerical modeling of quasi-static rock testing. Proceedings of the 45th U.S. Rock Mechanics/Geomechanics Symposium, San Francisco, CA, 2011.

Bieniawski, Z.T. (1966) Stable and unstable fracture propagation in rock. Report of the South African Council of Scientific and Industrial Research No. MEG 493, October, 1966.

Bieniawski, Z.T. (1967) An analysis of results from underground tests aimed at determining the *in situ* strength of coal pillars. CSIR Report MEG 569, Pretoria, South Africa, July, 1967; Rock Mechanics Division, National Mechanical Engineering Research Institute Council for Scientific and Industrial Research, Leipzig, 1967.

Bieniawski, Z.T. (1967) Eine studie des bruchmechanismus von kohle in situ. CSIR Report MEG 598/D, Pretoria, South Africa, October, 1967; Rock Mechanics Division, National Mechanical Engineering Research Institute Council for Scientific and Industrial Research, Leipzig, 1967.

Bieniawski, Z.T. (1967) Mechanism of brittle fracture of rock, Part 1: Theory of the fracture process. International Journal of rock Mechanics and Mining Sciences, vol. 4, pp. 395-406.

Bieniawski, Z.T. (1967) Mechanism of brittle fracture of rock, Part 2: Experimental studies. International Journal of rock Mechanics and Mining Sciences, vol. 4, pp. 407-423.

Bieniawski, Z.T. (1968) Fracture dynamics of rock. International Journal of Fracture Mechanics, vol. 4, no. 4, December 1968, pp. 415-430.

Bigoni, D. and Hueckel, T. (1991) Uniqueness and localization -I. Associative and non-associative elastoplasticity. International Journal of Solids and Structures. Vol. 28, No. 2, pp. 197-213, 1991.

Blake, W. and Hedley, D.G.F. (2003) Rockbursts: case studies from North American hard-rock mines. Society for Mining, Metallurgy, and Exploration, Inc., Littleton, CO, 2003.

Bolton, M.D., Nakata, Y., and Cheng, Y.P. (2008) Micro- and macro-mechanical behaviour of DEM crushable materials. Géotechnique, vol. 58, no. 6, August 1, 2008, pp. 471-480.

Brady, B.H.G., and E.T. Brown (2006) "Energy, mine stability, mine seismicity and rockbursts." Rock Mechanics for underground mining (2006): 271-311.

Brady, B.H.G. and Brown, E.T. (2007) Rock mechanics: for underground mining. Springer, 2007.

Cai, M. et al. (2007) FLAC/PFC coupled numerical simulation of AE in large-scale underground excavations. International Journal of Rock Mechanics and Mining Sciences, vol. 44, no. 4, pp. 550-564.

Caldwell, J. (2009) SME on Crandall Canyon and mining bumps. http://ithinkmining.com/2009/02/25/on-crandall-canyon-and-mining-bumps/, Accessed on 2/20/2013.

Campoli, A.A., Barton, T.M., van Dyke, F.C., and Gauna, M. (1990) Mitigating destructive longwall bumps through conventional gate entry design. Report of Investigations RI-9325, 1990, United States Department of the Interior, Bureau of Mines.

Campoli, A.A., Oyler, D.C. and Chase, F.E. (1989) Performance of a novel bump control pillar extracting technique during room-and-pillar retreat coal mining. U.S. Department of the Interior, Bureau of Mines, 1989.

Chen, Z. (1997) A double rock sample model for rockbursts. International Journal of Rock Mechanics and Mining Sciences, vol. 34, no. 6, pp. 991-1000.

Cheng, Y.P., Bolton, M.D., and Nakata, Y. (2005) Grain crushing and critical states observed in DEM simulations. In Powders and grains, vol. 2 (eds R. Garcia-Rojo, H. J. Herrmann & S. McNamara), pp. 1393–1397. London, UK: Taylor & Francis Group.

Chase, F., Zipf, Jr., K. and Mark, C. (1994) The massive collapse of coal pillars - case histories from the United States. Proc. 13th International Conference on Ground Control in Mining, pp. 69-80.

Cho, N., Martin, C.D., and Sego, D.C. (2007) A clumped particle model for rock. International Journal of Rock Mechanics and Mining Sciences 44: 997-1010.

Cook, N.G.W. (1965) "The Failure of Rock," International Journal of Rock Mechanics and Minining Sciences, vol. 2, pp. 389-403.

Cook, N.G.W., (1965) A note on rockburst considered as a problem of instability. Journal of the South African Institute of Mining and Metallurgy, 437-46.

Cook, N.G.W., Hoek, E., Pretorius, J.P.G., Ortlepp, W.D., and Salamon, M.D.G. (1966) Rock mechanics applied to the study of rockbursts. Journal of the South African Institute of Mining and Metallurgy, vol. 66, May 1966, pp. 435-528

Cundall, P.A. (1989) Numerical experiments on localization in frictional materials. Ingenieur-Archiv 59 (1989) 148-159. Presented at the workshop on Limit Analysis and Bifurcation Theory, held at the University of Karlsruhe (FRG), February 22-25, 1988.

Cundall, P.A. (2000) Numerical experiments on rough joints in shear using a bonded particle model. Aspects of Tectonic Faulting, pp. 1-9, eds. F.K. Lehner and J.L. Urai, Springer-Verlag, Berlin, 2000.

Das, M.N. (1986) Influence of width/height ratio on post-failure behaviour of coal. International Journal of Mining and Geological Engineering, vol. 4, pp. 79-87.

de Borst, R. (2001) Some recent issues in computational failure mechanics. International Journal for Numerical Methods in Engineering. vol 52:63-95.

Debasis, D., Park, DW, and Novak, T. (1996) Numerical modeling of progressive gob formation in a deep longwall mine. 2nd North American Rock Mechanics Symposium, June 19 - 21, 1996, Montreal, Quebec, Canada.

Deisman, N., Mas Ivars, D., Darcel, C., and Chalaturnyk, R.J. (2010) Empirical and numerical approaches for geomechanical characterization of coal seam reservoirs. International Journal of Coal Geology, vol. 82, pp. 204-212.

DeMarco, M.J., Koehler, J.R., and Lu, P.H. (1988) Characterization of chain pillar stability in a deep western coal mine - case study. SME Annual Meeting, Phoenix, Arizona, January 25-28, 1988, Pre-print 88-76.

Deng, H. and Nemat-Nasser, S. (1992) Dynamic damage evolution in brittle solids. Mechanics of Materials, vol. 14, no. 2, December 1992, pp. 83-103.

Detournay, C., & Dzik, E. (2006) Nodal Mixed Discretization for tetrahedral elements. Proceedings of 4th international FLAC symposium, numerical modeling in geomechanics. Minnesota Itasca Consulting Group, Inc. Paper (No. 07-02).

Dou, L., Lu, C., Mu, Z., and Gao, M. (2009) Prevention and forecasting of rock burst hazards in coal mines. Mining Science and Technology (China), vol. 19, no. 5, pp. 585-591.

Drzewiecki, J. (2009) The accuracy of forecast of mine tremors location. Mining Science and Technology (China), vol. 19, no. 15, September 2009, pp. 668-673.

Esterhuizen, G.S. (2006) Evaluation of the strength of slender pillars. SME Annual Meeting and Exhibit, St. Louis, Missouri, pp. Preprint 06-003, 2006.

Esterhuizen, G.S. and Karacan, C.O. (2005) Development of numerical models to investigate permeability changes and gas emission around longwall mining panel. Proceedings of the 40th U.S. Symposium of Rock Mechanics, ARMA/USRMS paper 05-744, Anchorage, Arkansas.

Esterhuizen, G.S., Dolinar, D.R. and Ellenberger, J.L. (2011) Pillar strength in underground stone mines in the United States. International Journal of Rock Mechanics and Mining Sciences, vol. 48, no. 1, January 2011, pp. 42-50.

Esterhuizen, G., Mark, C. and Murphy, M. (2010) The ground response curve, pillar loading and pillar failure in coal mines. 29th International Conference on Ground Control in Mining, pp. 19-27.

Esterhuizen, G. and Mark, C. (2009) Three-dimensional modeling of large arrays of pillars for coal mine design. Proceedings of the International Workshop on Numerical Modeling for Underground Mine Excavation Design, pp. 37-46.

Fairhurst, C. (2004) Fundamental considerations relating to the strength of rock. Report on the Workshop on Extreme Ground Motions at Yucca Mountain. U.S. Geological Survey, Menlo Park, California, August 23-24, 2004.

Fakhimi, A. and Villegas, T. (2006) Application of dimensional analysis in calibration of a discrete element model for rock deformation and fracture. Rock Mechanics and Rock Engineering 40: 193-211.

Garvey, R. and Ozbay, U. (2011) Computer-aided calibration of PFC3D coal samples using a genetic algorithm. Proceedings of the 2nd International FLAC/DEM Symposium, pp. 493-499.

Garvey, R. and Ozbay, M.U. (2012) Identifying Unstable Failure in Brittle Rock using the Finite Difference Method. Proceedings of the 46th U.S. Rock Mechanics/Geomechanics Symposium, Chicago, IL, 2012.

Gates, et al. (2008) Fatal underground coal burst accidents, August 6 and 16, 2007. USDOL, MSHA Report of Investigation, ID No. 42-01715. Arlington, Virginia, pgs 176.

Gill, D.E., Leite, M.H., and Labrie, D. (1994) Designing mine pillars with the convergence-confinement method. International Journal of Rock Mechanics and Mining Sciences and Geomechanics Abstracts, vol. 31, no. 6, pp. 687-698.

Goldberg, D. E. (1989). Genetic algorithms in search, optimization, and machine learning.

Grady, D.E. (1982) Local inertial effects in dynamic fragmentation. Journal of Applied Physics, vol. 53, no. 1, January 1982, pp. 322-325.

Grady, D.E. (1990) Particle size statistics in dynamic fragmentation. Journal of Applied Physics, vol. 68, no. 12, 15 December 1990, pp. 6099-6105.

Grady, D.E. and Kipp, M.E. (1979) The micromechanics of impact fracture of rock. International Journal of Rock Mechanics and Mining Sciences and Geomechanics Abstracts, vol. 16, no. 5, October 1979, pp. 293-302.

Griffith A. A. (1921) The phenomena of rapture and flow in solids. Phil. Trans. Roy. Soc., A 221, 163-198.

Griffith, A.A. (1925) Theory of rupture. Proceedings of the first international congress for applied mechanics, (Bienzeno and Burgess, eds.) pp. 53-64. J. Waltman Jr. Press, Delft (1925).

Griffiths, D.V. (1981) Computation of strain softening behaviour. Symposium on Implementation of Computer Procedures and Stress-Strain Laws in Geotechnical Engineering, Chicago, U.S.A., 1981, (eds. C.S. Desai and S.K. Saxena), pp.591-604. Acorn Press.

Haimson, B. (2006) True triaxial stresses and the brittle fracture of rock. Pure and Applied Geophysics, vol. 163, pp. 1101-1130.

Hajiabdolmajid, V., Kaiser, P., and Martin, C. (2002) Mobilization of strength in brittle failure of rock - in laboratory vs. in situ. Proceedings of the Fifth North American Rock Mechanics Symposium, pp. 227-234.

Hajiabdolmajid, V., Kaiser, P., and Martin, C. (2002) Modelling brittle failure of rock. International Journal of Rock Mechanics and Mining Sciences, vol. 39, no. 6, pp. 731-741.

Hao, S.W., Wang, H.Y., Xia, M.F., Ke, F.J., and Bai, Y.L. (2007) Relationship between strain localization and catastrophic rupture. Theoretical and Applied Fracture Mechanics, vol. 48, pp. 41-49.

Haramy, K.Y., Hanna, K. and McDonnell, J.F.T (1984) Investigations of underground coal mine bursts. Proceeding of the Fourth Conference on Ground Control in Mining (ICGCM).

Harvey S., and Ozbay, U. (2009) Review and applicability of yielding support systems for bump prone coal mines in the western United States - Preprint 09-027. Presented at the SME Annual Meeting, Denver, CO, pp. 1-7.

Hazzard, J. and Young, R. (2004) Dynamic modelling of induced seismicity. International Journal of Rock Mechanics and Mining Sciences, vol. 41, no. 8, pp. 1365-1376.

He, M.C., Miao, J.L., and Feng, J.L. (2010) Rock burst process of limestone and its acoustic emission characteristics under true-triaxial unloading conditions. International Journal of Rock Mechanics and Mining Sciences, vol. 47, no. 2, February, 2010, pp. 286-298.

Heasley, K. (1991) An examination of energy calculations applied to coal bump prediction. Presented at the 10th International Conference on Ground Control in Mining, Morgantown, WV, pp. 122-129.

Hill, R. (1958) A general theory of uniqueness and stability in elastic-plastic solids. Journal of the Mechanics and Physics of Solids, vol. 6, 1958, pp. 236-249.

Hino, K. (1956) Fragmentation of rock through blasting and shock wave theory of blasting. The 1st U.S. Symposium on Rock Mechanics (USRMS), April 23 - 25, 1956 , Golden, CO.

Hobbs, B.E., and Ord, A. (1989) Numerical simulation of shear band formation in a frictional-dilational material. Presented at the workshop on Limit Analysis and Bifurcation Theory, held at the University of Karsruhe (FRG), February 22-25, 1988, Ingenieur-Archiv, 1989.

Hoek, E. and Bieniawski, Z.T. (1966) Fracture propagation mechanism in hard rock. Proceedings of the First Congress of the International Society of Rock Mechanics, Lisbon, September, 1966, Vol. I, pp. 243-249.

Hoek, E., Kaiser, P.K., and Bawden, W.F. (1995) Support of underground excavations in hard rock. Taylor and Francis, New York, NY, 1995.

Horii, H. and Nemat-Nasser, S. (1985) Compression-induced microcrack growth in brittle solids: axial splitting and shear failure. Journal of Geophysical Research, vol. 90, no. B4,

pp. 3105-3125, March 10, 1985.

Hsieh, Y., Li, H., Huang, T. and Jeng, F. (2008) Interpretations on how the macroscopic mechanical behavior of sandstone affected by microscopic properties - revealed by bonded-particle model. Engineering Geology, vol. 99, no. 1, pp. 1-10.

Hustrulid, W.A. (1976) A review of coal pillar strength formulas. Rock Mechanics, Vol. 8, pp. 115-145.

Hyder, Z., Ali, Z., Akram, M., Westman, E. and Karmis, M. (2011) Simulation and modeling of pillar stability and analysis of safety factor. SME Annual Meeting, Denver, CO, 2011.

Iannacchione, A.T. and DeMarco, M.J. (1992) Optimum mine designs to minimize coal bumps a review of past and present U.S. practices. New Technology in Mining Health and Safety, ch. 24, pp. 235-247, Society for Mining, Metallurgy, and Exploration, 1992.

Iannacchione, A.T. and Tadolini, S.C. (2008) Coal mine burst prevention controls. 27th International Conference on Ground Control in Mining, pp. 20-28.

Iannacchione, A.T. and Zelanko, J. (1995) Occurrence and remediation of coal mine bumps: a historical review. Proceedings of the Mechanics and Mitigation of Violent Failure in Coal and Hard-Rock Mines, vol. 01, pp. 27-68.

Irwin, G.R. (1960) Fracture mechanics. Structural Mechanics, (Goodier and Hoff, eds.) pp. 557-592, Pergamon Press (1960).

Itasca Consulting Group Inc. (2010) FLAC3D (Fast Lagrangian Analysis of Continua in 3 Dimensions), Version 4.0. Minneapolis, MN.

Itasca Consulting Group Inc. (2012) FLAC3D (Fast Lagrangian Analysis of Continua in 3 Dimensions), Version 5.0. Minneapolis, MN.

Itasca Consulting Group Inc. (2010b) 3DEC (3 Dimensional Distinct Element Code), Version 4.1. Minneapolis, MN.

Itasca Consulting Group Inc. (2010c) PFC3D (Particle Flow Code in 3 Dimensions), Version 4.0. Minneapolis, MN.

Jaeger, J.C. (1966) Brittle fracture of rocks. The 8th U.S. Symposium on Rock Mechanics (USRMS), September 15 - 17, 1966 , Minneapolis, MN.

Jahanbakhshi, R., Keshavarzi, R., and Azinfar, M.J. (2011) Intelligent prediction of uniaxial compressive strength for sandstone. Proceedings of the 45th U.S. Rock Mechanics/Geomechanics Symposium, San Francisco, CA, 2011.

Jaiswal, A. and Shrivastva, B. (2009) Numerical simulation of coal pillar strength. International Journal of Rock Mechanics and Mining Sciences, vol. 46, no. 4, pp. 779-788.

Janach, W. (1976) The role of bulking in brittle failure of rocks under rapid compression. International Journal of Rock Mechanics and Mining Sciences and Geomechanics Abstracts, vol. 13, pp. 177-186.

Kao, C.S., Labuz, J.F., Ince, N.F., Kaveh, M., and Biolzi, L. (2011) Surface spalling experiments with damage observations. Proceedings of the 45th th U.S. Rock Mechanics/Geomechanics Symposium, San Francisco, CA, 2011.

Kelly, P.A. (2012) Solid mechanics - course notes. http://www.des.auckland.ac.nz/uoa/piaras-kelly, University of Auckland, pp. 234-243. Accessed on June 4, 2012.

Khan, A.S., and Irani, F.K. (1987) An experimental study on stress wave transmission at a metallic-rock interface and dynamic tensile failure of sandstone, limestone, and granite. Mechanics of Materials, vol. 6, pp. 285-292.

Kias, E.M.C., Gu, R., Garvey, R., and Ozbay, U. (2011) Modeling unstable rock failure during a uniaxial compressive strength test. Proceedings of 45th U.S. Rock Mechanics/Geomechanics Symposium, San Francisco, CA, 2011.

Kias, E.M.C., Mustoe, G.G.W., and Ozbay, U. (2013) Evaluation of two discrete element models for studying unstable frock failure in compression. Proceedings of DEM6 Conference, Golden, CO, 2013.

Kidybiński, A. (1981) Bursting liability indices of coal. International Journal of Rock Mechanics and Mining Science & Geomechanics, vol. 18, 1981, pp. 295-304.

Kim, H., Wagoner, M.P., and Buttlar, W.G. (2009) Micromechanical fracture modeling of asphalt concrete using a single-edge notched beam test. Materials and Structures, vol. 42, no. 5, 2009, pp. 677-689.

Koehler, J.R., DeMarco, M.J., and Wuest, W.J. (1995) The critical pillar concept in yield pillar-based longwall gate road design. SME Annual Meeting, March 6-9, 1995, Denver, CO.

Koyama, T. and Jing, L. (2007) Effects of model scale and particle size on micro-mechanical properties and failure processes of rocks—A particle mechanics approach. Engineering Analysis with Boundary Elements 31: 458-472.

Kneisley, R.O. (1989) Microseismic data analysis of failure occurrence in a deep, western U.S. coal mine: a case study. Report of Investigations RI-9228, United States Department of the Interior, Bureau of Mines, 1989.

Kripakov, N. and Kneisley, R. (1992) Pillar design in bump-prone deep western U.S. coal mines. 11th International Conference on Ground Control in Mining, The University of Wollongong, N.S.W., pp. 72-83.

Lahaie, F., Bigarre, P., Al Heib, M., Josien, J. and Noirel, J. (2003) Large-scale 3D characterisation of in-situ stress field in a complex mining district prone to rockbursting. International Society for Rock Mechanics, vol. 2, no. 200309, p. 6, Sep. 2003.

Larson, M. and Whyatt, J. (2009) Critical review of numerical stress analysis tools for deep coal longwall panels under strong strata. SME Annual Meeting, Denver, CO, pp. Preprint 09-011, 2009.

Liang, W., Yuanping, C., Yuckui, Y., Haidong, C., Peiquing, L., Jic, L., and Feng, W. (2010) Journal of Mining Science and Technology, vol. 20, 2010, pp. 0510-0515.

Liu, H.Y., Kou, S.Q., Lindqvist, P.-A., and Tang, C.A. (2004) Numerical studies on the failure process and associated microseismicity in rock under triaxial compression. Tectonophysics, vol. 384, no. 1-4, June 16, 2004, pp. 149-174.

Lu, J., Ray, A., Morsey, K., and Peng, S. (2008) Effects of rock/coal interface property on coal pillar strength. 27th International Conference on Ground Control in Mining (ICGCM).

Maleki, H., Olsen, R., Spillman, D., and Stevenson, M. (2003) Development of geotechnical procedures for the analysis of mine seismicity and pillar designs. Proc. 22nd International Conference on Ground Control in Mining, pp. 270-277.

Maotian, L., Zhongchang, W. and Qing, Y. (2006) Study on damage bifurcation and instability of rock-like materials. Acta Mechanica Solida Sinica, vol. 19, no. 3, September, 2006.

Mark, C. (1999) Pillar design methods for longwall mining. U.S. Dept. of the Interior, U.S. Bureau of Mines.

Mark, C. (1999) The state-of-the-art in coal pillar design in Preprint 99-86.

Mark, C. (2006) Extreme multiple seam mining in the central Appalachian coalfields. 2006 SME Annual Meeting March 27-29, St. Louis, Missouri, p. 7.

Mark, C. (2009) Deep cover pillar recovery in the US. 28th International Conference on Ground Control in Mining, Morgantown, WV, pp. 1-9.

Mark, C. and Barton, T.M. (1996) The uniaxial compressive strength of coal: should it be used to design pillars? 15th International Conference on Ground Control in Mining, Golden, CO, August 13-15, 1996.

Marti, J. and Cundall, P. (1982) Mixed discretization procedure for accurate modelling of plastic collapse. International Journal for Numerical Methods in Engineering, vol. 4, pp. 153-177.

McClintock, F.A. and Walsh, J.B. (1963) Friction on Griffith cracks in rocks under pressure. Proceedings of the Fourth U.S. Congress on Applied Mechanics, pp. 1015-1021. American Society of Mechanical Engineers, New York (1963).

McGarr, A. (1997) A mechanism for high wall-rock velocities in rockbursts. Pure and Applied Geophysics, vol. 150, pp. 381-391.

Mellinger, F.M. and Birkimer, D.L. (1966) Measurements of stress and strain on cylindrical test specimens of rock and concrete under impact loading. Technical Report No. 4-46, Department of the Army, Ohio River Division Laboratories, Corp of Engineers, Cincinatti,

OH, April, 1966.

Mohamed, K.M. (2003) Design considerations for longwall yield pillar stability. PhD Dissertation, West Virginia University, Morgantown, WV, 2003.

Mohammad, N., Lloyd, P.W., and Reddish, D.J. (1997) Longwall surface subsidence prediction through numerical modelling. Proceedings of the 16th International Conference on Ground Control in Mining, 1997, Morgantown, WV.

Mohan, G.M, Sheorey, P.R., and Kushwaha, A. (2001) Numerical estimation of pillar strength in coal mines. International Journal of Rock Mechanics & Mining Sciences, vol. 38, pp. 1185-1192.

Morsy, K. and Peng, S. (2002) Numerical modeling of the gob loading mechanism in longwall coal mines. 21st International Conference on Ground Control in Mining, August 6-8, 2002, Morgantown, WV, pp. 58-67.

Morsy, K. and Peng, S. (2001) Typical complete stress-strain curves of coal. 20th International Conference on Ground Control in Mining, pp. 210-217.

Mortazavi, A., Hassani, F.P., and Shabani, M. (2008) A numerical investigation of rock pillar failure mechanism in underground openings. Computers and Geotechnics, vol. 36, pp. 691-697.

Muller, W. (1991) Numerical simulation of rock bursts. Mining Science and Technology, vol. 12, no. 1, pp. 27-42.

Nagraja Rao, G.M., Udayakumar, S., Raju, D., and Jennifer, P.D. (2010) Post-failure deformation behavior of coal and rocks. International Society for Rock Mechanics International Symposium - 6th Asian Rock Mechanics Symposium, October 23-27, 2010, New Delhi, India.

Nakata, Y., Bolton, M.D., and Cheng, Y.P. (2005) Relating particle characteristics to macro behavior of DEM crushable material. Powders and Grains, 2005, ed. A.A. Balkema, Rotterdam, Netherlands, pp. 1387-1391.

Napier, J.A.L. (2011) Explicit discontinuity modeling of deep mine stope face and pillar foundation failure. 45th US Rock Mechanics / Geomechanics Symposium, San Francisco, CA, June 26-29, 2011.

Nemat-Nasser, S. and Deng, H. (1994) Strain-rate effect on brittle failure in compression. Acta Metallurgica et Materialia. vol. 42, no. 3, pp. 1013-1024.

Newman, D.A. (1989) In situ yield behaviour of a coal pillar. International Journal of Mining and Geological Engineering, vol. 7, no. 2, 1989, pp. 163-170.

Ng, L.K.W., Swan, G., and Board, M. (1993) The application of an energy approach in fault models for support design. Rockbursts and Siesmicity in Mines, pp. 387-391.

Notley, K. (1984) Rock mechanics analysis of the Springhill mine disaster (October 23, 1958). Mining Science and Technology, vol. 1, no. 2, pp. 149-163.

Oliver, J. and Huespe, A. (2007) Continuum approach to material failure in strong discontinuity settings. Computer Methods in Applied Mechanics and Engineering, vol. 193, no. 30, pp. 3195-3220, Jul. 2007.

Osterwald, F.W. (1962) USGS relates geologic structures to bumps and deformation in coal mine workings. Mining Engineering, vol. 14, pp. 63-68, Apr-1962.

Ozbay, M.U., Salamon, M.D.G., and Lee, K. (2001) Rational design of yield pillars: improved understanding of yielding mechanism. SME Annual Meeting, Denver, CO, 2001.

Ozbay, U. and Badr, S. (2010) Numerical modeling of yielding chain pillars in deep longwall coal mines. Workshop on Pillar Design. 29th International Conference on Ground Control in Mining, Morgantown, WV, 2010.

Ozbay, U. and Rozgonyi, T.G. (2003) Numerical modeling of stress and deformations encountered in deep longwall coal mines usig strain softening failure criterion. International Conference on Safety and Environmental Aspects of Mining. University of Miskolc Series A. Mining, Vol. 63, 2003.

Pan, Y., Yang, X. and Ma, S. (2002) Study on deformation localization of rock by white light digital speckle correlation method. Chinese Journal of Geotechnical Engineering, vol.

24, no. 1, Jan. 2002.

Pariseau, W. (2011) Geomechanics of Crandall Canyon barrier pillar mining. SME Annual Meeting, Denver, CO, 2011.

Park, DW and Vojtech, G. (1989) Supercomputer assisted three-dimensional finite element analysis of a longwall panel. Rock Mechanics as a Guide for Efficient Utilization of Natural Resources. Balkema, Rotterdam, 1989.

Park, E., Martin, C.D., and Christiansson, R. (2004) Simulation of the mechanical behavior of discontinuous rock masses using a bonded-particle model. Gulf Rocks 2004: Rock Mechanics Across Borders & Disciplines, pp. Paper no. ARMA/NARMS 04-480.

Passman, S.L. and Trucano, T.G. (1984) Stability, instability, and localization in materials with damage. Journal of Rheology, vol. 28, no. 6, pp. 779-798.

Patino, G.S., Saucedo, N.R., and Naveja, F.A. (2011) Use of a neural network to build a 3D rock property model for a geomechanical model to optimize multi-stage fracture design in Chicontepec Basin, Mexico. Proceedings of the 45th U.S. Rock Mechanics/Geomechanics Symposium, San Francisco, CA, 2011.

Peperakis, J. (1958) Mountain bumps at the sunnyside mines. Transactions AIME, vol. 211, pp. 982-986, Sep-1958.

Petukhov, I.M. and A.M. Linkov. (1979) The theory of post-failure deformations and the problem of stability in rock mechanics. International Journal of Rock Mechanics, Mineral Sciences & Geomechanics, Abstract 16: 57-76. Great Britain: Pergamon Press Ltd.

Pierce, M., Cundall, P., Potyondy, D. and Mas Ivars, D. (2007) A synthetic rock mass model for jointed rock. In E. Eberhardt et al. (Eds) Rock Mechanics: Meeting Society's Challenges and Demands (1st Canada-U.S. Rock Mechanics Symposium, Vancouver, May 2007), Vol. 1: Fundamentals, New Technologies and New Ideas, pp. 341-349, London: Taylor & Francis Group.

Pijaudier-Cabot, G. and Bažant, Z.P. (1988) Dynamic stability analysis with nonlocal damage. Computers and Structures, vol. 29, no. 3, pp. 503-507, 1988.

Pijaudier-Cabot, G. and Benallal, A. (1993) Strain localization and bifurcation in a nonlocal continuum. International Journal of Solids and Structures, vol. 30, no. 13, pp. 1761-1775.

Potyondy, D. and Cundall, P. (2004) A bonded-particle model for rock. International Journal of Rock Mechanics and Mining Sciences, vol. 41, no. 8, pp. 1329-1364.

Potyondy, D. (2007) Simulating stress corrosion with a bonded-particle model for rock. International Journal of Rock Mechanics and Mining Sciences 44: 677-691.

Potyondy, D.O. (2012) A flat-jointed bonded-particle material for hard rock. 46th US Rock Mechanics / Geomechanics Symposium, Chicago, IL, June 24-27, 2012, ARMA 12-501.

Prassetyo, S.H., Gamal, R., Yang, L., Luo, Y. and Peng, S.S. (2011) The influence of interface friction and W/H ratio on the violence of coal specimen failure - a comparison between a bump and non-bump probe mines. Proceedings of the 30th International Conference on Ground Control in Mining, Morgantown, WV, July 23-26, 2011.

Rabczuk, T. (2012) Computational methods for fracture in brittle and quasi-brittle solids: state-of-the-art review and future perspectives. ISRN Applied Mathematics, eds. S. Li and R. Samtaney. Pre-publication, accepted September 3, 2012.

Rice, J.R. (1976) The localization of plastic deformation. Theoretical and Applied Mechanics, Proceedings of the 14th International Congress on Theoretical and Applied Mechanics, Delft, 1976, vol. 1, North-Holland Publishing Co., 1976, pp. 207-220.

Roberts, M.K.C. and Brummer, R.K. (1988) Support requirements in rockburst conditions. Journal of the South African Institute of Mining and Metallurgy, vol. 88, no. 3, Mar. 1988, pp. 97-104.

Roberts, D.K. and Wells, A.A. (1954) The velocity of brittle fracture. Engineering, no. 178, pp. 820-821 (1954).

Rougier, E., Knight, E.E., Munjiza, A., Sussman, A.J., Broome, S.T., Swift, R.P. and Bradley, C.R. (2011) The combined finite-discrete element method applied to the study of rock fracturing behavior in 3D. 45th US Rock Mechanics / Geomechanics Symposium, San

Francisco, CA, June 26-29, 2011.

Roylance, D. (2001) Yield and plastic flow. Massachusetts Institute of Technology, pp. 1-19.

Rudnicki, J.W. and Rice, J.R. (1975) Conditions for the localization of deformation in pressure-sensitive dilatant materials. Journal of the Mechanics and Physics of Solids, vol. 23, pp. 371-394.

Sainsbury, B., Pierce, M., and Mas, Ivars, D. (2008) Simulations of rock mass strength anisotropy and scale effects using a ubiquitous joint rock mass (UJRM) model. Proceedings of the 1st International FLAC/DEM Symposium on Numerical Modelling, 25-27 August, Itasca Consulting Group, Minneapolis (2008), pp. 241-250 paper 06-02.

Salamon, M. (1984) Energy considerations in rock mechanics: fundamental results. Journal of South African Institute of Mining and Metallurgy, Aug. 1984, vol. 84, no. 8, pp. 233-246.

Salamon, M. (1970) Stability, instability and design of pillar workings. International Journal of Rock Mechanics and Mining Science & Geomechanics Abstracts, 7(6), 613-631.

Salamon, M., Badr, S. and Ozbay, M.U. (2003) Pillar failure in deep coal seams: numerical simulation. Technology Roadmap for Rock Mechanics, vol. 2, no. 10, pp. 1011-1018, Sep. 2003.

Salamon M.D.G. and Munro, A.H. (1967) A study of the strength of coal pillars. J. S. Afr. Inst. Min. Metall. September 1967.

Schofield, A.N. and Wroth, P. (1968) "Critical state soil mechanics" McGraw-Hill, pp. 310, ISBN 978-0641940484.

Scholtès, L. and Donzé, F.V. (2012) Modelling progressive failure in fractured rock masses using a 3D discrete element method. International Journal of Rock Mechanics and Mining Sciences, vol. 52, June 2012, pp. 18-30.

Shan, R., Jiang, Y. and Li, B. (2000) Obtaining dynamic complete stress-strain curves for rock using the Split Hopkinson Pressure Bar technique. International Journal of Rock

Mechanics and Mining Sciences, vol. 37, pp. 983-992.

Shen, B., Poulsen, B.A., and Qu, Q. (2011) Overburden strata movement and stress change induced by longwall mining. Proceedings of the 45th U.S. Rock Mechanics/Geomechanics Symposium, San Francisco, CA, 2011.

Shimizu, H., Koyama, T., Ishida, T., Chijimatsu, M., Fujita, T. and Nakama, S. (2010) Distinct element analysis for Class II behavior of rocks under uniaxial compression. International Journal of Rock Mechanics and Mining Sciences, vol. 47, no. 2, pp. 323-333.

Shockey, D.A., Curran, D.R., Seaman, L., Rosenberg, J.T., and Petersen, C.F. (1974) Fragmentation of rock under dynamic loads. International Journal of Rock Mechanics and Mining Sciences & Geomechanics Abstracts, vol. 11, no. 8, August, 1974, pp. 303-317.

Srinivas, M. and Patnaik, L.M. (1994) Adaptive probabilities of crossover and mutation in genetic algorithms. IEEE Transactions on Systems, Man and Cybernetics, vol. 24, no. 4, April 1994, pp. 656-667.

Starr, A. T. (1928) "Slip in a Crystal and Rupture in a Solid Due to Shear," Proc. Camb. Phil. Soc., 24, 489-500.

Sterpi, D. (1999) An analysis of geotechnical problems involving strain softening effects. International Journal for Numerical and Analytical Methods in Geomechanics, vol 23, pp. 1427-1454.

Stroisz, A.M. and Fjær, E. (2011) Nonlinear elastic wave propagation in Castlegate sandstone. 45th US Rock Mechanics / Geomechanics Symposium, San Francisco, CA, June 26-29, 2011.

Tarasov, B. (2010) Superbrittleness of rocks at high confining pressure. Proceedings of the fifth International Seminar on deep and high stress mining, pp. 119-133.

Tawadrous, A.S., DeGagné, D., Pierce, M. and Mas Ivars, D. (2009) Prediction of uniaxial compression PFC3D model micro-properties using artificial neural networks. International Journal for Numerical and Analytical Methods in Geomechanics 33: 1953-1962.

Tiwari, R.P. and Seshagiri Rao, K. (2006) Post failure behaviour of a rock mass under the influence of triaxial and true triaxial confinement. Engineering Geology, vol. 84, pp. 112-129.

Tulu, I.B. and Heasley, K.A. (2011) Investigating themechanics of pillar loading through the analysis of in-situ stress measurements. 45th US Rock Mechanics / Geomechanics Symposium, San Francisco, CA, June 26-29, 2011.

United States Mine Health and Safety Administration. (2008) Report of investigation, underground coal mine: fatal underground coal burst accidents, August 6 and 16, 2007, Crandall Canyon Mine, Genwall Resources Inc., Huntington Emergy County, Utah, ID, Issues 42-1715. Mine Safety and Health Administration, Office of the Adminstrator, Coal Mine Safety and Health, 2008.

van der Merwe, J.N. (1998) The role of overburden integrity in pillar failure. 2nd International Workshop on Coal Pillar Mechanics and Design, pp. 173-179.

van Heerden, W.L. (1975) In situ complete stress-strain characteristics of large coal specimens. Journal of the South African Institute of Mining and Metallurgy, March 1975, pp. 207- 217.

Varas, F., Alonso, E., Alejano, L.R., and Fdez-Manin, G. (2005) Study of bifurcation in the problem of unloading a circular excavation in a strain-softening material. Tunnelling and Underground Space Technology, vol. 20, pp. 311-322.

Vermeer, P.A. and de Borst, R. (1984) Non-associated plasticity for soils, concrete and rock. HERON, vol. 29, no. 3, January 1984, pp. 1-64.

Wagner, H. (1974) Determination of complete load deformation characteristics of coal pillars. Proceedings of 3rd ISRM Congress, Denver, CO, pp. 1076-1081.

Wang, F.D., Kelly, W.A., and Wolgamott, J. (1976) In-situ coal pillar strength study. Final report of contract no. H0242022, Excavation Engineering and Earth Mechanics Institute (EMI), Colorado School of Mines, Golden, CO.

Wang, J.A. and Park, H.D. (2001) Comprehensive prediction of rockburst based on analysis of strain energy in rocks. Tunnelling and Underground Space Technologies, vol. 16, pp. 49-57.

Wang, Y. and Tonon, F. (2009) Calibration of a discrete element model for intact rock up to its peak strength. International Journal for Numerical and Analytical Methods in Geomechanics 34: 447-469.

Wang, L. et al. (2010) Controlling the effect of a distant extremely thick igneous rock in overlying strata on coal mine disasters. Mining Science and Technology, China, vol. 20, no. 4, pp. 510-515.

Wang, S.Y., Au, S., Lam, K. and Tang, C.A. (2005) A numerical study of pillar failure based on a cusp-type catastrophe model. Key Engineering Materials, vol. 297, pp. 2628-2635.

Wang, S.Y., Lam, K.C., Au, S.K., Tang, C.A., Zhu, W.C., and Yang, T.H. (2005) Analytical and numerical study on the pillar rockbursts mechanism. Rock Mechanics and Rock Engineering, vol. 39, no. 5, pp. 445-467.

Wawersic, W.R. and Fairhurst, C. (1970) A study of brittle rock fracture in laboratory compression experiments. International Journal of Rock Mechanics and Mining Science and Geomechanics Abstracts, 7, 561-575.

Whitley, D. (1994) A genetic algorithm tutorial. Statistics and Computing (4):65-85, 1994.

Whyatt, J., Blake, W., Williams, T. and White, B. (2002) Sixty years of rock bursting in the Coeur d'Alene district of norther Idaho: Lessons learned and remaining issues, SME Transactions, Volume 312, 2002.

Whyatt, J. and Varley, F. (2010) Regional bumps: case studies from the 1958 bump symposium. Transactions of Society for Mining, Metallurgy, and Exploration. vol. 326, Jan. 2010, pp. 101-105.

Whyatt, J. (2008) Dynamic failure in deep coal: recent trends and a path forward. Proceedings 27th International Conference on Ground Control in Mining, pp. 37-45.

Whyatt, J.K. and Board, M.P. (1991) Numerical exploration of shear-fracture-related rock bursts using a strain-softening constitutive model. RI 9350, United States Department of the Interior, Bureau of Mines, 1991.

Whyatt, J. and Loken, M.C. (2009) Coal bumps and odd dynamic phenomena - a numerical investigation. Proceedings of the 28th International Conference on Ground Control in Mining, July 28-30, 2009, Morgantown, WV.

Wu, F., Wu, J., & Qi, S. (2010). Phenomena and theoretical analysis for the failure of brittle rocks. Journal of Rock Mechanics and Geotechnical Engineering, 2(4), 331-337.

Yasitli, N.E., and Unver, B. (2005) 3-D numerical modelling of stresses around a longwall panel with top coal caving. The Journal of the South African Institute of Mining and Metallurgy, vol. 105, May/June, 2005, pp. 287-300.

Yavuz, H. (2001) Yielding pillar concept and its design. 17th International Mining Congress and Exhibition of Turkey, 2001.

Yavuz, H. and Fowell, R. (2001) FDM prediction of a yield pillar performance in conjunction with a field trial. Proceedings of the 20th International Conference on Ground Control in Mining, pp. 78-87.

Yoon, J. (2007) Application of experimental design and optimization to PFC model calibration in uniaxial compression simulation. International Journal of Rock Mechanics and Mining Sciences 44: 871-889.

York, G. (1998) Numerical modelling of the yielding of a stabilizing pillar/foundation system and a new design consideration for stabilizing pillar foundations. The Journal of the South African Institute of Mining and Metallurgy, October 1998, pp. 281-296.

Zhao, J. (2000) Applicability of Mohr-Coulomb and Hoek-Brown strength criteria to the dynamic strength of brittle rock. International Journal of Rock Mechanics and Mining Sciences, vol. 37, pp. 1115-1121.

Zhao, C., Hobbs, B.E., Ord, A., and Peng, S. (2009) Critical contact stiffness concept and simulation of crack generation in particle models of large length-scales. Computers and Geotechnics, vol. 26, issue 1-2, January-March, 2009, pp. 81-92.

Zhi-ru, H., Yao-dong, J., Yi-xin, Z., and Qing,ji G. (2009) Study of crack propagation of bump-prone coal sample. Proceeding of the 6th International Conference on Mining Science and Technology, pp. 471-478.

Zhu, Q., Lu, W., Sun, J., Luo, Y. and Chen, M. (2009) Prevention of rockburst by guide holes based on numerical simulations. Mining Science and Technology (China), vol. 19, no. 3, pp. 346-351.

Zhu, W.C., Li, Z.H., Zhu, L., and Tang, C.A. (2010) Numerical simulation on rockburst of underground opening triggered by dynamic disturbance. Tunnelling and Underground Space Technology, vol. 25, no. 5, September 2010, pp. 587-599.

Zingano, A., Koppe, J. and Costa, J. (2004) Violent coal pillar collapse. 23rd International Conference on Ground Control in Mining, Morgantown, WV, pp. 60-67.

Zingano, A.C., Koppe, J.C. and Costa, J. (2005) Modeling the arc-effect of a coal mine roof. Proc. 24th International Conference on Ground Control in Mining, pp. 155-161.

Zipf Jr., R.K. (1996) Simulation of cascading pillar failure in room-and-pillar mines using boundary-element method. 2nd North American Rock Mechanics Symposium, June 19 - 21, 1996 , Montreal, Quebec, Canada, pp. 1887-1892.

Zipf Jr., R.K. (1999) Using a postfailure stability criterion in pillar design. Proceedings of the 2nd International Workshop on Coal Pillar Mechanics and Design.

Zipf Jr., R.K. (2006) Numerical modeling procedures for practical coal mine design. Proceedings of the 41st U.S. Rock Mechanics Symposium, Golden, CO, Paper no. 06-1119.

Zipf Jr., R.K. and Mark, C. (1997) Design methods to control violent pillar failures in room-and-pillar mines. Transactions of the Institute of Mining and Metallurgy, vol. 106, pp. A124-A132.

Zou, D., Miller, H. and Kaiser, P. (1989) Numerical study of violent rock failure by stick-slip on joints. Mining Science and Technology, vol. 9, no. 3, pp. 241-251.

Zubelewicz, A. and Mróz, Z. (1983) Numerical simulation of rock burst processes treated as problems of dynamic instability. Rock Mechanics and Rock Engineering, vol. 16, no. 4, pp. 253-274, Nov. 1983.

APPENDIX A - EXCESS ENERGY OF FLAC3D UCS TESTS

Figure A.1 through Figure A.10 display additional energy plots from Chapter 6 in which an energy balance is performed during a series of uniaxial compressive strength tests in FLAC3D v4.01. The Young's modulus of the simulated loading platens was adjusted between 2 and 100 GPa with the full results of these tests displayed below. Some plots have been omitted as having been provided in the text of Chapter 6.

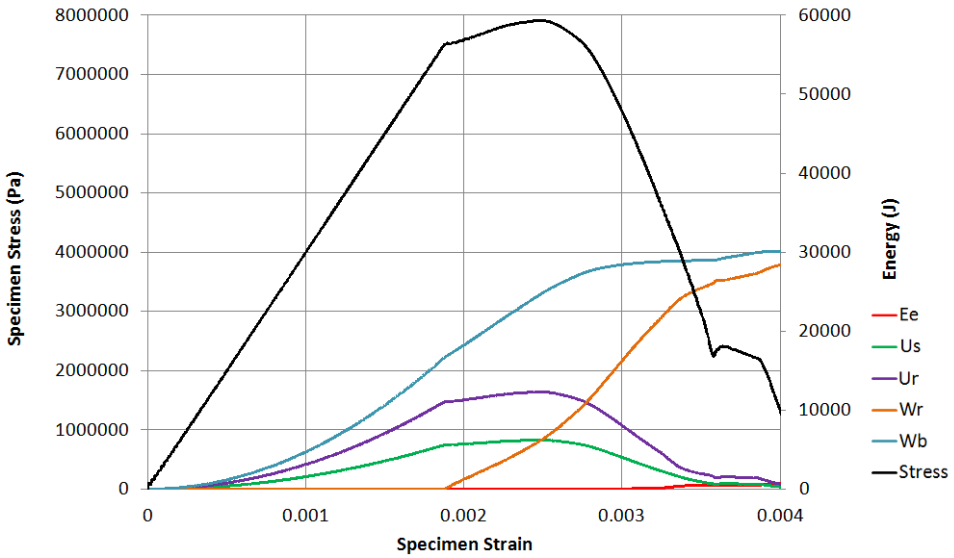

Figure A.1: Specimen stress vs. strain for UCS test with 8 GPa platens, overlayed with the energy terms used to calculate excess energy.

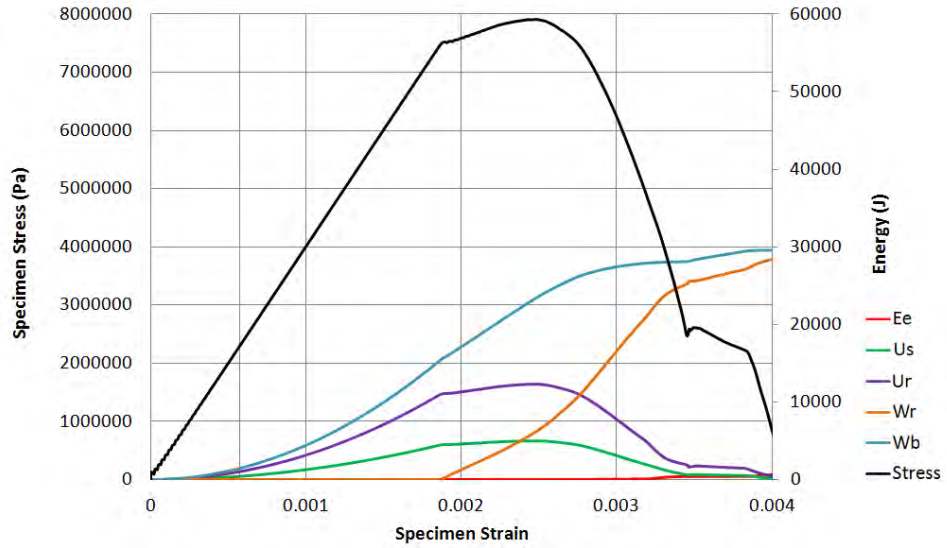

Figure A.2: Specimen stress vs. strain for UCS test with 10 GPa platens, overlayed with the energy terms used to calculate excess energy.

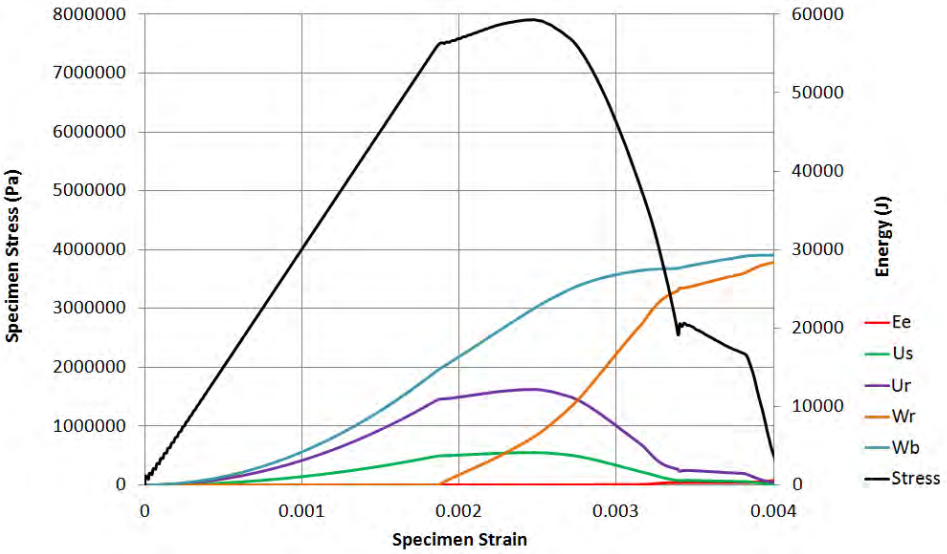

Figure A.3: Specimen stress vs. strain for UCS test with 12 GPa platens, overlayed with the energy terms used to calculate excess energy.

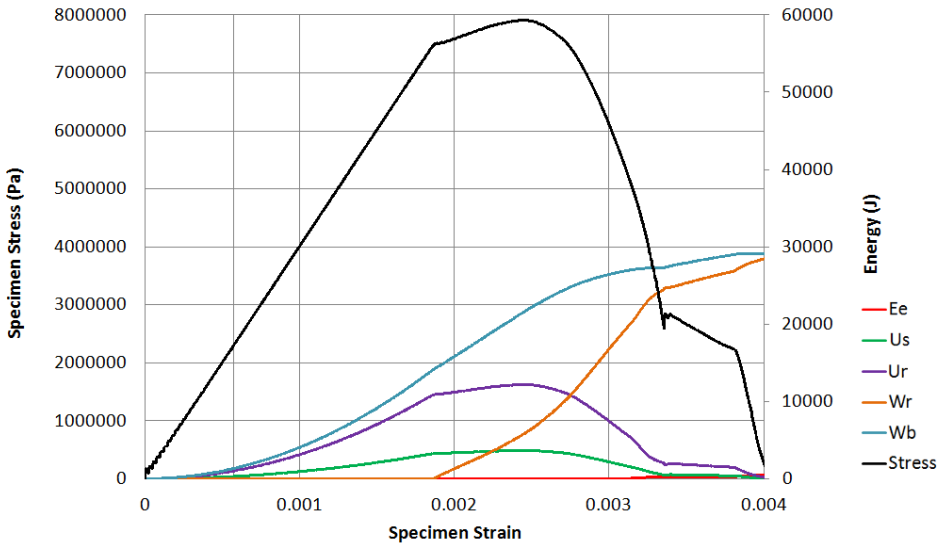

Figure A.4: Specimen stress vs. strain for UCS test with 14 GPa platens, overlayed with the energy terms used to calculate excess energy.

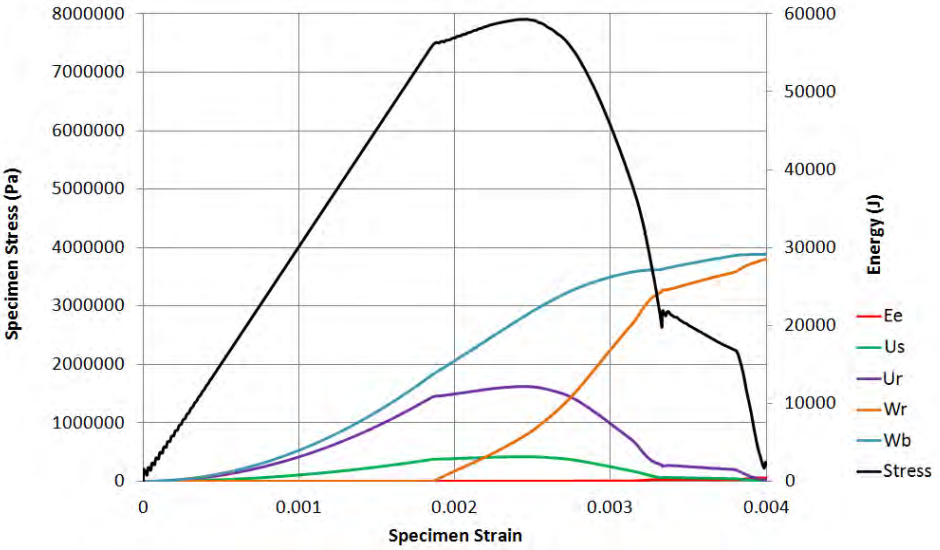

Figure A.5: Specimen stress vs. strain for UCS test with 16 GPa platens, overlayed with the energy terms used to calculate excess energy.

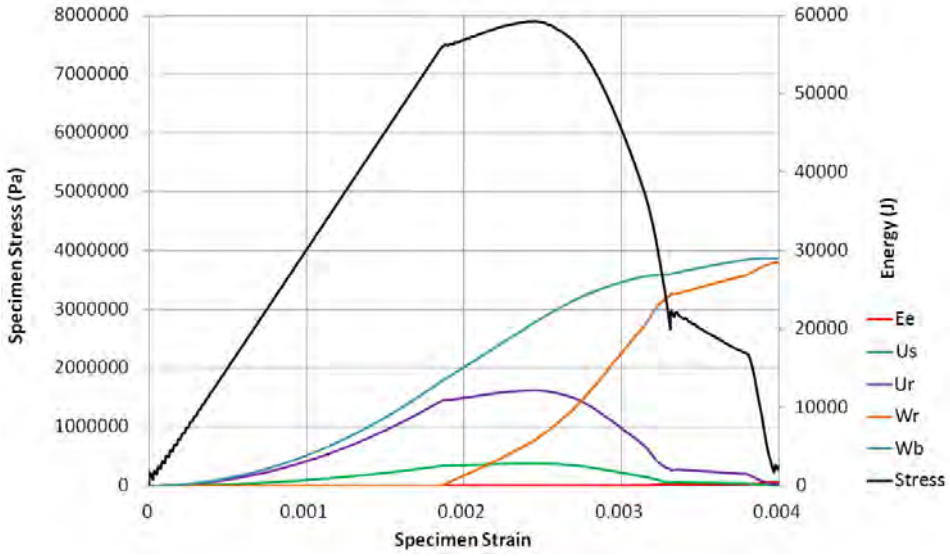

Figure A.6: Specimen stress vs. strain for UCS test with 18 GPa platens, overlayed with the energy terms used to calculate excess energy.

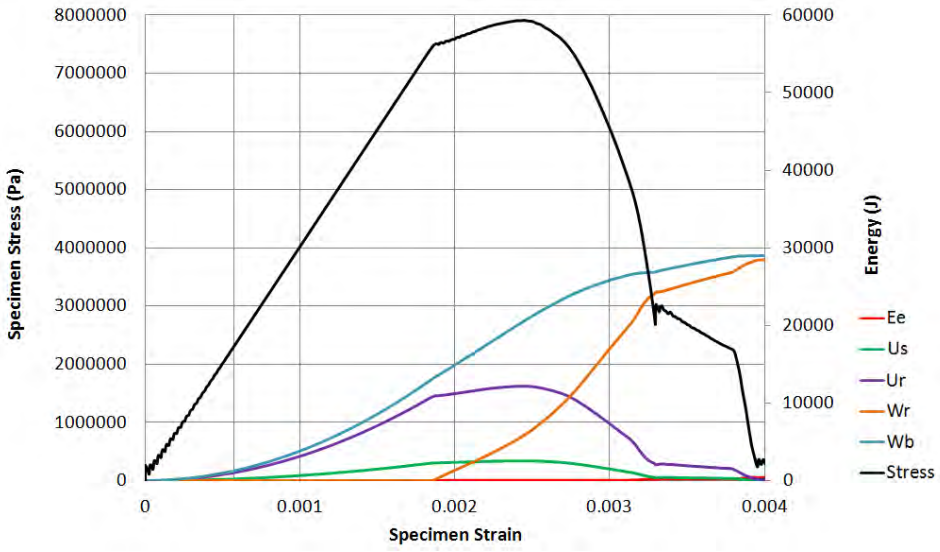

Figure A.7: Specimen stress vs. strain for UCS test with 20 GPa platens, overlayed with the energy terms used to calculate excess energy.

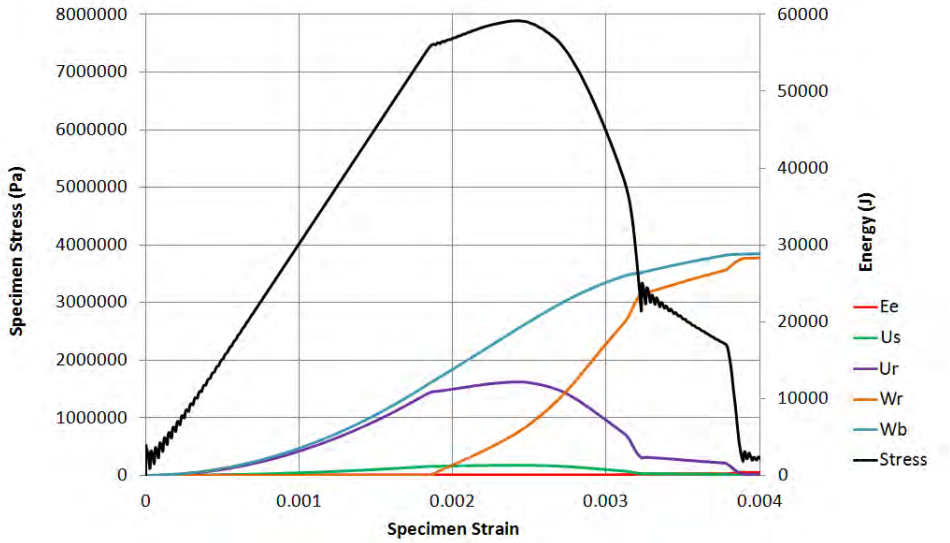

Figure A.8: Specimen stress vs. strain for UCS test with 40 GPa platens, overlayed with the energy terms used to calculate excess energy.

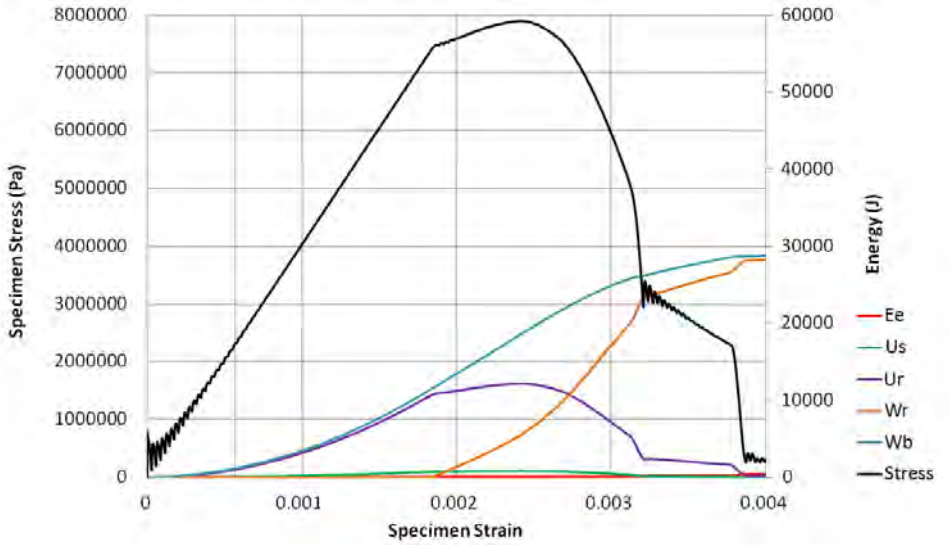

Figure A.9: Specimen stress vs. strain for UCS test with 60 GPa platens, overlayed with the energy terms used to calculate excess energy.

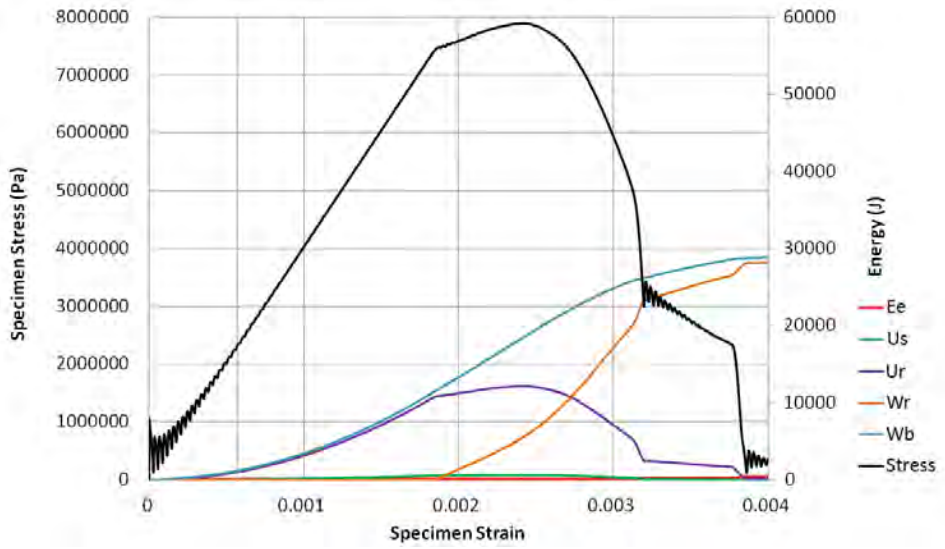

Figure A.10: Specimen stress vs. strain for UCS test with 80 GPa platens, overlayed with the energy terms used to calculate excess energy.

APPENDIX B - SUPPLEMENTAL ELECTRONIC FILES

FISH codes were developed within the PFC3D and FLAC3D modeling environments to conduct all numerical tests described within this document. Complete program listings are included as supplemental electronic files to this document. A summary of these codes is provided below with a reference to the section of the document in which they were used.

FISH Codes from Section 3.3.1	PFC3D v4.0
pb_cyl_driver.dvr	Primary batch file for running genetic algorithm calibrations.
pb_cyl_gen_v00.dvr	
_run_away.dvr	
pb_cyl_tAucs_v00.dvr	
_run_away_farther.dvr	
_run_ucs.dvr	
pb_cyl_tAucs_part2_v00.dvr	
_run_away_farther_still.dvr	
pb_cyl_tTriax_v00.dvr	
pb_cyl_tTriax2_v00.dvr	
_read_complete.dvr	
_find_top10.dvr	

FISH Codes from Section 3.3.2	PFC3D v4.0
cyl_sample_batch_driver.dvr	Primary batch file for performing a series of UCS tests.
cyl_sample_v00.dvr	

FISH Codes from Section 3.3.4	PFC3D v4.0
d.8_tA-tw_EV.dvr	Primary batch file for conducting dynamic UCS tests.
spc.dvr	
tAucs-param.dat	FISHTank inputs for UCS test.
param.dat	FISHTank inputs for BPM specimen.
2region-setup.dat	

FISH Codes from Section 4.3.2	FLAC3D v4.01
cyl_sample_batch_driver.dvr	Batch file for conducting UCS tests.
cyl_sample_v00.f3dat	

FISH Codes from Section 4.3.2 (Pause)	FLAC3D v4.01
cyl_sample_batch_driver.dvr	Batch file for conducting UCS pause tests.
cyl_sample_v00.f3dat	

FISH Codes from Sections 4.4.1 and 5.2	FLAC3D v4.01
cyl_sample_batch_driver.dvr	Batch file for triaxial compressive strength tests.
cyl_sample_v00.f3dat	

FISH Codes from Section 4.5	FLAC3D v4.01
cyl_sample_batch_driver.dvr	Batch file for dynamic UCS test.
cyl_sample_v00.f3dat	

FISH Codes from Section 5.1.1	FLAC3D v4.01
cyl_sample_batch_driver.dvr	Batch file for UCS tests with instability identifiers recorded during tests.
cyl_sample_v00.f3dat	

FISH Codes from Section 6.2	FLAC3D v4.01
cyl_sample_batch_driver.dvr	Batch file for UCS tests with energy balance and instability identifiers recorded during tests.
cyl_sample_v00.f3dat	

FISH Codes from Section 7.2 (2D)	FLAC3D v4.01
pillar_batch_vA00.fis	Batch file for calibration of 2D pillar with applied loading.
pillar_vA01.fis	

FISH Codes from Section 7.2 (3D)	FLAC3D v4.01
pillar_batch_vA00.fis	Batch file for calibration of 23D pillar with applied loading.
pillar_vA01.fis	

FISH Codes from Section 8.1	FLAC3D v4.01
wh1_pillar_batch_driver_v71_for_2D_pressure.f3dat	Batch file for running a series of 2D elastic rockmass tests for W:H = 1 pillar.
wh2_pillar_batch_driver_v71_for_2D_pressure.f3dat	
wh3_pillar_batch_driver_v71_for_2D_pressure.f3dat	
wh4_pillar_batch_driver_v71_for_2D_pressure.f3dat	
wh5_pillar_batch_driver_v71_for_2D_pressure.f3dat	
pillar_v73_for_2D_pressure.f3dat	
jacktest_batch_v51.f3dat	
jacktest_v51_nextrun.f3dat	

FISH Codes from Section 9.1	FLAC3D v4.01
pillar_batch_v74.f3dat	Batch file for running a series of 3D gravitational loading tests for W:H 1:1 to 5:1 pillars.
pillar_v74.f3dat	